

# UC Berkeley

## UC Berkeley Electronic Theses and Dissertations

### Title

First-Principles Approach to Materials Discovery, Design and Optimization: Applications to Transition-Metal Alloys and Functional Materials

### Permalink

<https://escholarship.org/uc/item/56w5r4wj>

### Author

De Jong, Maarten

### Publication Date

2015

Peer reviewed|Thesis/dissertation

First-Principles Approach to Materials Discovery, Design and Optimization:  
Applications to Transition-Metal Alloys and Functional Materials

by

Maarten de Jong

A dissertation submitted in partial satisfaction of the  
requirements for the degree of

Doctor of Philosophy

in

Engineering - Materials Science and Engineering

in the

Graduate Division

of the

University of California, Berkeley

Committee in charge:

Professor Mark Asta, Chair

Professor Daryl Chrzan

Professor Tarek Zohdi

Fall 2015

First-Principles Approach to Materials Discovery, Design and Optimization:  
Applications to Transition-Metal Alloys and Functional Materials

Copyright 2015

by

Maarten de Jong

## Abstract

First-Principles Approach to Materials Discovery, Design and Optimization:  
Applications to Transition-Metal Alloys and Functional Materials

by

Maarten de Jong

Doctor of Philosophy in Engineering - Materials Science and Engineering

University of California, Berkeley

Professor Mark Asta, Chair

This dissertation broadly describes efforts related to materials discovery, design and optimization using a first-principles approach based on density functional theory (DFT). The two main application areas comprise transition-metal alloys and functional materials. The research involving transition-metal alloys aims at finding cost-effective replacement strategies for rhenium (Re). Elemental Re exhibits profuse deformation twinning under mechanical loads and has a high ductility. It is shown that the twinning characteristics of Re and its ductility are correlated with its anomalously low  $\{11\bar{2}1\}$  twin-boundary energy. The origin of this twin-energy anomaly is related to the presence of icosahedral structural units on the  $\{11\bar{2}1\}$  twin boundary. These structural units are stabilized near  $d$ -band fillings corresponding to Re. The  $\{11\bar{2}1\}$  twin-boundary energy can be lowered further by decreasing the  $d$ -band filling with respect to elemental Re. This increases the intrinsic ductility according to three independent ductility parameters employed in this work: i) Pugh's ratio of bulk to shear modulus, ii) Yoo's ratio of surface to twin energy and iii) an ideal-strength criterion. Based on new insights in the relation between  $d$ -band filling, defect energies and intrinsic ductility, several candidate alloys for Re replacement are proposed. Ru-based alloys with additions of Ta, W and Re are shown to be potential replacement candidates. The last part of this dissertation describes high-throughput calculations that have culminated in the two largest databases of elastic and piezoelectric tensor properties available to-date. The workflow for doing such calculations is described, along with various checks to ensure the accuracy of the calculated physical properties. The database with elastic-tensor properties is expected to be of use in a number of fields where discovery of new materials with desired values of elastic stiffness or (lattice) thermal conductivity are of interest. Further, data mining and machine learning can be applied to better understand elastic properties and their physical descriptors. Several novel piezoelectric materials are discovered as part of this work. Some of these exhibit a high intrinsic piezoelectric response and may serve as a starting point for a process in which the piezoelectric response is optimized by alloying and microstructure engineering. As such, this database can support a



search for future replacement candidates of the widely used piezoelectric materials such as  $\text{Pb}(\text{Zr}_x\text{Ti}_{1-x})\text{O}_3$  (PZT) that contain lead.

To my wife Doohee and everyone else who supported me.

# Contents

|  |           |
|--|-----------|
| <b>List of Figures</b>   | <b>vi</b> |
| <b>List of Tables</b>  | <b>x</b>  |
| <b>I Introductory Material</b>                                       | <b>1</b>  |
| <b>1 Introduction and Background</b>                                 | <b>2</b>  |
| 1.1 Hexagonal Close Packed Rhenium . . . . .                         | 4         |
| 1.2 High-Throughput Calculations of Materials Properties . . . . .   | 6         |
| 1.3 Overview of Dissertation . . . . .                               | 6         |
| <b>2 Basic Theory and Methodology</b>                                | <b>9</b>  |
| 2.1 Density Functional Theory . . . . .                              | 9         |
| 2.1.1 Problem definition . . . . .                                   | 9         |
| 2.1.2 The Hohenberg-Kohn theorems . . . . .                          | 10        |
| 2.1.3 The Kohn-Sham Equations . . . . .                              | 11        |
| 2.1.4 Spin-Polarization . . . . .                                    | 12        |
| 2.1.5 Exchange-Correlation Functional . . . . .                      | 13        |
| 2.1.6 Pseudopotentials . . . . .                                     | 15        |
| 2.1.7 Structural relaxations . . . . .                               | 18        |
| 2.1.8 Density Functional Perturbation Theory . . . . .               | 19        |
| 2.1.9 Polarization and Berry Phases . . . . .                        | 20        |
| 2.2 Disorder in solids . . . . .                                     | 22        |
| 2.2.1 Special Quasirandom Structures . . . . .                       | 23        |
| 2.2.2 Virtual Crystal Approximation . . . . .                        | 24        |
| <b>II Results and Discussion</b>                                     | <b>26</b> |
| <b>3 Rhenium and its Alloys: Structure, Elasticity and Ductility</b> | <b>27</b> |

|          |   |           |
|----------|---|-----------|
| 3.1      | Foreword . . . . .  | 27        |
| 3.2      | Review of Intrinsic Ductility . . . . .   | 29        |
|          | 3.2.1 Pugh's criterion . . . . .  | 29        |
|          | 3.2.2 Yoo's criterion . . . . .   | 30        |
|          | 3.2.3 Ideal Strength-Based . . . . .  | 30        |
| 3.3      | Methodology . . . . .   | 31        |
|          | 3.3.1 DFT Calculations . . . . .  | 31        |
|          | 3.3.2 Elastic Constant Calculations . . . . .   | 32        |
|          | 3.3.3 Supercell Models for Alloys . . . . .   | 33        |
| 3.4      | Results . . . . .   | 34        |
|          | 3.4.1 Structural and Elastic Properties of Pure Rhenium . . . . .   | 34        |
|          | 3.4.2 Structural properties of Re-based transition metal alloys . . . . .                                   | 37        |
|          | 3.4.3 Energetics of Re-based transition metal alloys . . . . .  | 39        |
|          | 3.4.4 Elastic properties of Re-based transition-metal alloys . . . . .                                      | 41        |
| 3.5      | Discussion . . . . .  | 43        |
| 3.6      | Summary and Conclusions . . . . .   | 46        |
| <b>4</b> | <b>Twinning Energetics in HCP Transition Metals and Alloys</b>  | <b>48</b> |
| 4.1      | Foreword . . . . .  | 48        |
| 4.2      | Crystallography of Twinning . . . . .   | 50        |
| 4.3      | Twinning and Twinning Energetics in Elemental HCP Transition Metals . .                                     | 51        |
|          | 4.3.1 Computational Methodology . . . . .   | 51        |
|          | 4.3.2 Experimental Methodology and Results . . . . .  | 53        |
|          | 4.3.3 Results . . . . .   | 54        |
| 4.4      | Twinning Energetics: Effect of Alloying and <i>d</i> -band Filling . . . . .                                | 56        |
| 4.5      | Origin of the Twin Energy Anomaly . . . . .   | 62        |
| 4.6      | Rhenium Replacement Scenarios . . . . .   | 64        |
| 4.7      | Conclusions and Summary . . . . .   | 67        |
| <b>5</b> | <b>Calculations of Planar Defect Energies in Substitutional Alloys Using Special-Quasirandom-Structures</b> | <b>68</b> |
| 5.1      | Foreword . . . . .  | 68        |
| 5.2      | Methodology . . . . .   | 70        |
|          | 5.2.1 Supercell Geometries . . . . .  | 71        |
|          | 5.2.2 SQS Generation . . . . .  | 74        |
|          | 5.2.3 Computational Methods . . . . .   | 76        |
| 5.3      | Results and Discussion . . . . .  | 77        |
|          | 5.3.1 Embedded Atom Method Results . . . . .  | 77        |
|          | 5.3.2 Density Functional Theory Results . . . . .   | 83        |
| 5.4      | Summary and Conclusions . . . . .   | 86        |

|            |   |            |
|------------|---|------------|
| <b>6</b>   | <b>Ideal-Strength Calculations on Hexagonal Close Packed Metals and Alloys</b>                            | <b>87</b>  |
| 6.1        | Foreword . . . . .  | 87         |
| 6.2        | Introduction . . . . .  | 87         |
| 6.3        | Methodology . . . . .   | 89         |
| 6.3.1      | Wallace formalism and elastic instabilities in HCP materials . . . . .                                    | 89         |
| 6.3.2      | Calculation of second and third-order elastic constants . . . . .   | 91         |
| 6.3.3      | DFT-calculations . . . . .  | 93         |
| 6.4        | Results and Discussion . . . . .  | 94         |
| 6.4.1      | Elastic instabilities in HCP materials: A comparison of direct DFT and analytical model results . . . . . | 94         |
| 6.4.2      | Elastic instabilities and <i>d</i> -band filling . . . . .  | 97         |
| 6.5        | Summary and Conclusions . . . . .   | 99         |
| 6.6        | Appendix A . . . . .  | 100        |
| 6.7        | Appendix B . . . . .  | 102        |
| <b>III</b> | <b>High-Throughput Approach to Materials Science</b>  | <b>104</b> |
| <b>7</b>   | <b>High-Throughput Elastic Properties</b>   | <b>105</b> |
| 7.1        | Foreword . . . . .  | 105        |
| 7.2        | Background & Summary . . . . .  | 106        |
| 7.3        | Methods . . . . .   | 107        |
| 7.3.1      | Generation of elasticity data . . . . .   | 107        |
| 7.3.2      | Workflow . . . . .  | 110        |
| 7.3.3      | Code availability . . . . .   | 114        |
| 7.4        | Data Records . . . . .  | 114        |
| 7.4.1      | File format . . . . .   | 115        |
| 7.4.2      | Properties . . . . .  | 115        |
| 7.4.3      | Graphical representation of results . . . . .   | 116        |
| 7.5        | Technical Validation . . . . .  | 116        |
| 7.5.1      | Verification of computational methodology . . . . .   | 116        |
| 7.5.2      | Validation through comparison to experimental measurements . . . . .                                      | 119        |
| 7.6        | Usage Notes . . . . .   | 122        |
| <b>8</b>   | <b>High-Throughput Discovery of New Piezoelectrics</b>  | <b>124</b> |
| 8.1        | Foreword . . . . .  | 124        |
| 8.2        | Background & Summary . . . . .  | 124        |
| 8.3        | Methods . . . . .   | 127        |
| 8.3.1      | Definitions & computational settings . . . . .  | 127        |
| 8.3.2      | Compound selection and generation of piezoelectricity data . . . . .                                      | 131        |

|           |  |            |
|-----------|--|------------|
| 8.3.3     | Workflow . . . . .   | 131        |
| 8.3.4     | Code availability . . . . .  | 134        |
| 8.4       | Data records . . . . .   | 134        |
| 8.4.1     | File format . . . . .  | 134        |
| 8.4.2     | Properties . . . . .   | 135        |
| 8.4.3     | Graphical representation of results . . . . .                        | 138        |
| 8.5       | Technical validation and verification . . . . .                      | 138        |
| 8.5.1     | Verification of computational methodology . . . . .                  | 138        |
| 8.5.2     | Validation through comparison to experimental measurements . . . . . | 140        |
| 8.6       | Usage Notes . . . . .  | 143        |
| <b>IV</b> | <b>Concluding Remarks</b>  | <b>144</b> |
| <b>9</b>  | <b>Summary, Conclusions and Future Work</b>                          | <b>145</b> |
| 9.1       | Summary and Conclusions . . . . .                                    | 145        |
| 9.2       | Directions of Future Work . . . . .                                  | 150        |
| 9.2.1     | High-Entropy alloys for Rhenium replacement . . . . .                | 150        |
| 9.2.2     | Data Mining and Machine Learning . . . . .                           | 150        |
|           | <b>Bibliography</b>  | <b>152</b> |

# List of Figures

|     |  |    |
|-----|--|----|
| 1.1 | Different computational modeling techniques sorted by time and length scales: First-principles, Molecular Dynamics (MD), Monte Carlo (MC), Phase Field (PF), Thermo Chemical (TC) / Thermo Physical (TP) models and the Finite Element Method (FEM). . . . .   | 5  |
| 2.1 | An illustration of the self-consistency loop used in DFT to calculate the ground state electron density. . . . .   | 13 |
| 2.2 | Jacob's ladder showing different functionals as used in DFT, and their relative rankings in terms of (perceived) accuracy. . . . .   | 16 |
| 3.1 | The cost of elemental Re in US \$ per gram, with time. . . . .   | 28 |
| 3.2 | Schematic of the alloying strategy for Re replacement in this chapter. . . . .   | 29 |
| 3.3 | Volume solute expansion coefficient as a function of $3d$ , $4d$ or $5d$ solute element for alloy composition $\text{Re}_{15}\text{X}_1$ . . . . .   | 39 |
| 3.4 | Variation in $c/a$ as a function of $3d$ , $4d$ or $5d$ solute element for alloy composition $\text{Re}_{15}\text{X}_1$ . . . . .  | 40 |
| 3.5 | Heat of solution as a function of $3d$ , $4d$ or $5d$ solute element for alloy composition $\text{Re}_{15}\text{X}_1$ . . . . .  | 41 |
| 3.6 | Variation of (a) $K$ , (b) $G$ and (c) $K/G$ as a function of $3d$ , $4d$ or $5d$ solute element for alloy composition $\text{Re}_{15}\text{X}_1$ . . . . .  | 43 |
| 3.7 | Variation of the elastic anisotropy parameters $f_E$ (a) and $f_G$ (b) as a function of $3d$ , $4d$ or $5d$ solute element for alloy composition $\text{Re}_{15}\text{X}_1$ . . . . .  | 44 |
| 3.8 | Canonical $d$ -band heat of solution as a function of various $5d$ solute elements for alloy composition $\text{Re}_{15}\text{X}_1$ . . . . .  | 47 |
| 4.1 | An illustration of twinning elements. . . . .  | 50 |
| 4.2 | Projection-view of 5 twin boundaries considered in this work: (a) $K_1 = \{10\bar{1}1\}$ (projection along $[1\bar{2}10]$ ), (b) $K_1 = \{10\bar{1}2\}$ (projection along $[1\bar{2}10]$ ), (c) $K_1 = \{10\bar{1}3\}$ (projection along $[1\bar{2}10]$ ), (d) $K_1 = \{11\bar{2}1\}$ (projection along $[1\bar{1}00]$ ), (e) $K_1 = \{11\bar{2}2\}$ (projection along $[1\bar{1}00]$ ). . . . . | 52 |

|      |   |    |
|------|---|----|
| 4.3  | a) Inverse pole figure map of the deformed Re showing extensive twinning behavior. All twins present in the scan are $\{11\bar{2}1\}$ - type. b) $(0001)$ - Pole figure constructed from the data shown in (a) showing that the microstructure is weakly textured orthogonal to the $(0001)$ -orientation. The legend is in terms of times random. . . . .                                      | 54 |
| 4.4  | Bright-field TEM images showing twin deformation in a) pure Re and b) Re-10 at. % W. . . . .  | 55 |
| 4.5  | Calculated $\{10\bar{1}1\}$ and $\{11\bar{2}1\}$ twin boundary energies versus calculated values of the $G\Omega^{1/3}$ , where $G$ and $\Omega$ are shear modulus and atomic volume, respectively. Dashed lines are least-squares fits excluding the data for Re and Tc. . . . .   | 56 |
| 4.6  | Electron back-scattered diffraction scans of a) pure Re deformed 6.8 % and b) a Re-10 at. % W alloy deformed 7.8 %. The colors represent crystallographic orientation as described by the legend top right. Black areas represent regions that were unable to be indexed due to surface pitting. . .  | 57 |
| 4.7  | For Re-9.8 at. % X alloys, variations as a function of solute X, for (a) the $\{11\bar{2}1\}$ TB energy as calculated from SQS, VCA and KKR-CPA, (b) $\{0001\}$ surface energy calculated from SQS and (c) ductility parameter, $D = \gamma_s/\gamma_t$ . . . . .   | 59 |
| 4.8  | The energy of the $\{11\bar{2}1\}$ and $\{10\bar{1}1\}$ twin boundary in pure Re and Re-X alloys as a function of band filling, as calculated from the VCA. The composition of the alloys is Re- 10 at. % W and Re- 10 at. % Os. . . . .  | 60 |
| 4.9  | Calculated energies for $\{11\bar{2}1\}$ and $\{10\bar{1}1\}$ TBs for all 5d transition metals, including those stable in bcc and hcp crystal structures. . . . .   | 61 |
| 4.10 | Electronic DOS for the $\{11\bar{2}1\}$ and $\{10\bar{1}1\}$ TB and HCP Re. The inset shows that the DOS of the $\{11\bar{2}1\}$ TB is lower than the $\{10\bar{1}1\}$ TB DOS just left of the Fermi-level, with the opposite behavior to the right of the Fermi-level. . . . .   | 62 |
| 4.11 | (a) The $\{11\bar{2}1\}$ TB, viewed in projection along an $[1\bar{1}00]$ direction, highlighting a distorted icosahedron on the TB plane, (b) detailed view of the distorted icosahedron as found in the $\{11\bar{2}1\}$ TB, (c) an undistorted Z12 icosahedron, and (d) the calculated bimodality parameter $s$ as a function of distance relative to the TB plane. . . . .                  | 64 |
| 4.12 | A depiction of rhenium replacement strategies pursued in this section: create alloys . . . . .  | 65 |
| 5.1  | Example supercell geometry for (a) a bulk alloy with an appropriate orientation for defect calculations and (b) a $\{11\bar{2}1\}$ twin boundary cell, formed from the bulk after an appropriate combination of shear and shuffle. This figure shows a projection along the $[\bar{1}100]$ -direction. The twin-plane is inserted in the center of the bulk cell and is also indicated. . . . . | 72 |



|     |   |     |
|-----|---|-----|
| 5.2 | Supercell geometry for (a) a bulk cell with an appropriate orientation for defect calculations (b) calculation of the generalized stacking-fault energy and (c) calculation of free-surface energies. These figures show a projection along the [0001]-direction. . . . .   | 74  |
| 5.3 | Illustration of an SQS and configurational averaging-procedure used to compute the $\{11\bar{2}1\}$ TB energy. For the TB-calculations, a configurational average over 8 configurations within a single SQS-cell is employed. This figure shows a projection along the $[1\bar{1}00]$ -direction. . . . .   | 76  |
| 5.4 | $\{11\bar{2}1\}$ twin boundary energies ( $\gamma_t$ ) in $\text{Ti}_{1-x}\text{Al}_x$ alloys calculated using EAM potentials with two different supercell models: the benchmark Random-1M supercell, and the SQS-64 supercell. For the 64-atom SQS supercell, the results are an average over 8 planes in one SQS, and the error bars are standard deviations. The line through the benchmark Random-1M results is a guide to the eye. . . . . | 78  |
| 5.5 | Unstable stacking fault energies in $\text{Ti}_{1-x}\text{Al}_x$ alloys calculated using EAM potentials with two different supercell models: the benchmark Random-1M supercell, and the SQS-72 supercell. For the 72-atom SQS supercell, the results are an average over 6 planes in one SQS, and the error bars are standard deviations. The line through the benchmark Random-1M results is a guide to the eye. . . . .                       | 80  |
| 5.6 | $\{1\bar{1}00\}$ surface energies in $\text{Ti}_{1-x}\text{Al}_x$ alloys calculated using EAM potentials with two different supercell models: the benchmark Random-1M supercell, and the SQS-72 supercell. For the 72-atom SQS supercell, the results are an average over 6 planes in one SQS, and the error bars are standard deviations. The line through the benchmark Random-1M results is a guide to the eye. . . . .                      | 81  |
| 5.7 | The distribution of $\ corr^{SQS} - corr^{Random}\ $ over a million substitutional configurations for an hcp $\text{Ti}_{56}\text{Al}_8$ bulk alloy. A $\beta$ -distribution is fit to the data and plotted by the solid (red) line in the histogram. . . . .   | 83  |
| 5.8 | Probability of reproducing the Random-1M twin energies to within 10 % as a function of the metric $\ corr^{SQS} - corr^{Random}\ $ . The curve indicates a second order polynomial, fit to the calculated data. . . . .   | 84  |
| 5.9 | $\{11\bar{2}1\}$ twin boundary energy $\gamma_t$ in $\text{Ti}_{1-x}\text{Al}_x$ alloys calculated with 64-atom SQS supercells by DFT and EAM. The results plotted are averaged over 8 planes per supercell, with error bars denoting standard deviations. The lines are guides to the eye. . . . .   | 85  |
| 6.1 | Ideal failure mode-diagram vs. $d$ -band filling in HCP metals and alloys . . .   | 98  |
| 7.1 | High-Throughput calculation scheme. Workflow for calculating and filtering the elastic constants. . . . .   | 111 |

|     |  |     |
|-----|--|-----|
| 7.2 | Distribution of calculated volume per atom, Poisson ratio, bulk modulus and shear modulus. Vector field-plot showing the distribution of the bulk and shear modulus, Poisson ratio and atomic volume for 1,181 metals, compounds and non-metals. Arrows pointing at 12 o'clock correspond to minimum volume-per-atom and move anti-clockwise in the direction of maximum volume-per-atom, which is located at 6 o'clock. Bar plots indicate the distribution of materials in terms of their shear and bulk moduli. . . . .   | 117 |
| 7.3 | Plot of experimental vs. calculated bulk moduli. Comparison of experimental and calculated bulk moduli for a selected set of systems, with calculated Pearson correlation coefficient $r$ and Spearman correlation coefficient $\rho$ reported. . . . .  | 121 |
| 7.4 | Plot of experimental vs. calculated shear moduli. Comparison of experimental and calculated shear moduli for a selected set of systems, with calculated Pearson correlation coefficient $r$ and Spearman correlation coefficient $\rho$ reported. . . . .  | 122 |
| 8.1 | Part of a Heckmann diagram, showing the relation between mechanical and electrical properties of solids. . . . .   | 126 |
| 8.2 | Piezoelectric tensors and symmetry classes considered in this work, part I. Typical representations of the longitudinal piezoelectric modulus in 3D are also shown for each crystal point group. . . . .   | 129 |
| 8.3 | Piezoelectric tensors and symmetry classes considered in this work, part II. Typical representations of the longitudinal piezoelectric modulus in 3D are also shown for each crystal point group. . . . .  | 130 |
| 8.4 | Flowchart showing a schematic of the HT-infrastructure for calculating piezoelectric constants, including error-checking steps and database insertions. . . . .  | 132 |
| 8.5 | Visualization of the piezoelectric tensor: directional dependence of the longitudinal piezoelectric constant in cubic LaOF. Note that the maximum and minimum piezoelectric constants, $\ e_{ij}\ _{\max}$ , occur for the $\langle 111 \rangle$ family of crystallographic directions. . . . .  | 133 |
| 8.6 | A graphical representation of the piezoelectric dataset, currently comprising of 941 materials. A series of concentric circles indicate constant values of the maximum longitudinal piezoelectric modulus, $\ e_{ij}\ _{\max}$ . Concentric circles corresponding to moduli $\ e_{ij}\ _{\max}$ of 1, 2.5, 5, 10 and 20 C/m <sup>2</sup> are indicated explicitly in the figure. The compounds are broken up according to the crystal system and the different point group symmetry-classes considered in this work. . . . . | 139 |
| 8.7 | Comparison of experimental and calculated piezoelectric constants ( $\ e_{ij}\ _{\max}$ ) for a selected set of systems, with calculated Pearson correlation coefficient $r$ and Spearman correlation coefficient $\rho$ reported. . . . .   | 141 |

# List of Tables

|     |  |    |
|-----|--|----|
| 2.1 | Physical quantities that can be calculated from DFPT by taking first and second order derivatives with respect to atomic positions $\mathbf{R}$ , homogeneous strains $\eta$ and electric fields $\mathcal{E}$ . . . . .   | 20 |
| 3.1 | Structural and elastic properties of hcp Re, based on the computational and experimental (Exp.) methods listed in the first column. The units for the reported values of lattice constants ( $a$ and $c$ ), atomic volume ( $\Omega$ ), and elastic moduli ( $C_{ij}$ ) are Å, Å <sup>3</sup> , and GPa, respectively. For the lattice parameters and atomic volume, experimental values extrapolated to zero temperature, using reported thermal expansion coefficients, are given in parentheses. . . .    | 36 |
| 3.2 | Calculated solute lattice expansion coefficients $\eta_a$ and $\eta_c$ and heat of solution $\Delta H_{\text{sol}}$ (kJ / mol solute) of solutes in rhenium in the dilute limit for full structural relaxations. . . . .   | 38 |
| 3.3 | Independent elastic constants of hcp $\text{Re}_{15}\text{X}_1$ alloys. The unit of the reported values is GPa. . . . .  | 42 |
| 4.1 | Twinning elements of the 5 twin boundaries studied in this work. . . . .   | 51 |
| 4.2 | Calculated twin boundary energies for selected HCP metals ( $mJ/m^2$ ), twin boundary with the lowest energy and $G\Omega^{1/3}$ ( $J/m^2$ ) in $mJ/m^2$ , where $G$ is the Voigt-Reuss-Hill averaged shear modulus, and $\Omega$ is the atomic volume. For each metal, an asterisk denotes the twin boundary with the lowest energy.  | 57 |
| 4.3 | {11 $\bar{2}$ 1} twin boundary energies, calculated for several Ru-bases substitutionally disordered alloys. . . . .   | 66 |
| 5.1 | Concentration dependence of planar defect energies in hcp $\text{Ti}_{1-x}\text{Al}_x$ solid solutions, $\eta_\gamma = (\partial\gamma/\partial x)/\gamma_0$ , as calculated with EAM interatomic potentials, using benchmark Random-1M and SQS-72/64 supercell models. For the twin boundary, 64-atom SQS supercells are employed, and for the surface and stacking fault energies, 72-atom SQS supercells are employed. The Al atomic fraction is denoted by $x$ for the {1 $\bar{1}$ 00} surface. . . . . | 79 |

|     |  |     |
|-----|--|-----|
| 6.1 | Calculated SOEC's, TOEC's and ideal-failure characteristics for 12 HCP metals. Failure modes are characterized as either shear (S) or tension (T). . . | 96  |
| 7.1 | Properties derived from the elastic constant matrix in this work, and their corresponding JSON keys and datatypes. . . . .                             | 109 |
| 7.2 | JSON keys for metadata and their descriptions. . . . .   | 115 |
| 8.1 | JSON keys for metadata and their descriptions. . . . .   | 135 |
| 8.2 | Properties related to the piezoelectric tensor in this work, and their corresponding JSON keys and datatypes. . . . .                                  | 137 |

## Acknowledgments

I would like to thank all friends and family for their support during my time at Berkeley. I would like to thank my advisor Mark Asta for his guidance, for suggesting interesting research topics, for teaching me how to use hyphens properly and for always making sure adequate research funding was available for me. Many thanks of course also goes to the many people I have collaborated with over the past years: Wei Chen (Illinois Institute of Technology, USA), Marcel Sluiter (Delft University of Technology, The Netherlands), Josh Kacher (Georgia Tech, USA), David Olmsted (UC Berkeley, USA), Liang Qi (University of Michigan, USA), Randy Notestine (UC San Diego, USA), Anthony Gamst (UC San Diego, USA), Andrew Minor (UC Berkeley, USA) Kristin Persson (UC Berkeley, USA), Anubhav Jain (Lawrence Berkeley National Laboratory, USA), Gerbrand Ceder (Massachusetts Institute of Technology, USA) and Axel van de Walle (Brown University, USA).

Further I would like to pay specific thanks to Daryl Chrzan, Tarek Zohdi, Kristin Persson and Andrew Minor for taking the time to serve in my qualifying-exam committee and/or thesis committee and for the interesting discussion we have had about science and life in general.

Finally, I would like to acknowledge the following agencies for providing financial and/or computing resources:

- The US Office of Naval Research under Grant No. N00014-11-1-0886
- The Extreme Science and Engineering Discovery Environment (XSEDE) program supported by National Science Foundation Grant No. OCI-1053575
- The Materials Project Center, supported by the Basic Energy Sciences (BES) Department of Energy (DOE) Grant No. EDCBEE.
- The Assistant Secretary for Energy Efficiency and Renewable Energy, under Contract No. DE-AC02-05CH11231
- The National Energy Research Scientific Computing Center (NERSC), supported by the Office of Basic Energy Sciences of the U.S. DOE under Contract No. DE-AC02-05CH11231.

**Part I**

**Introductory Material**

## Chapter 1

# Introduction and Background

An alloy can be defined as a mixture of at least 2 elements, of which at least 1 is a metallic element. The atoms can be distributed more or less randomly over the lattice sites and yield a solid solution, certain atoms can cluster together, forming different phases, embedded in a matrix or ordering can take place, creating an intermetallic compound. For solid solutions, the alloy properties, such as mechanical strength and ductility, are in part determined by the chemical composition. The field of alloy design and alloy physics is very rich and includes an extremely large space of possible alloy compositions and phases, giving rise to a wide variety of distinct properties, ranging from mechanical to electrical and thermal to optical properties. Desired material properties can be designed by carefully tuning the alloying elements present and their respective compositions. This is not an easy task due to the enormous amount of potential alloy compositions and the lack of simple rules to translate alloy compositions directly into properties of interest. For this reason, research in the field of alloy design has historically been very active and remains so up to now.

The field of alloy design and materials science and engineering in general, has experienced a surge of new computational methods and algorithms in the past 2 decades to calculate various materials properties. Many of the underlying theories on which these modern techniques hinge, have been around since the 1960's or even earlier. J.W. Gibbs laid out his theory on thermodynamics and applied it to alloys in 2 pivotal papers published in 1876 and 1878 [1, 2]. In the decades after, important progress was made in the field of alloy kinetics and diffusion. M. Von Laue, W.H. Bragg and W.L. Bragg made important contributions to X-ray diffraction and confirmed the crystalline nature of metals and alloys [3, 4]. In the 1930's, W.L. Bragg and E.J. Williams for the first time discussed long and short range ordering and their relation to atomic interaction energies [5]. W. Hume-Rothery made important contributions to the field of *s-p* bonded and transition metal alloys specifically in 1926-1927, when he showed - among other things - that the *d*-electron count per atom plays a crucial role in the solubility of these metals into each other [6]. In

the 1940's, 1950's and 1960's, several important theoretical concepts for studying alloys were introduced such as the Monte Carlo method by N. Metropolis and S. Ulam in 1949 [7] and the cluster variation method by R. Kikuchi in 1950 [8]. Of particular importance to this work were the theories by P. Hohenberg and W. Kohn (1964) [9] and by W. Kohn and L.J. Sham (1965) [10] which led to the introduction of density functional theory (DFT). This provided a starting point for ab-initio quantum-mechanical calculations on materials.

Even though modern theories such as DFT have been around for over 50 years, recent advances in computer science, algorithms and technology have only recently made the practical implementation of some of these state-of-the-art techniques possible. This has allowed computation to help contribute recently to a great increase in the understanding of alloys and the physics governing their behavior. Examples can be found in several fields, such as aluminum alloys [11], magnesium alloys [12], shape memory alloys [13], and superconductors [14]. A very new subfield within materials science is that of high-throughput (HT) calculations [15, 16], in which the power of large-scale supercomputers is harnessed to calculate material properties on large, unprecedented scales. By applying modern techniques such as data mining and machine learning to the generated datasets, it is hoped that the fundamental descriptors underlying a given material property can be revealed, which can aid in the optimization and design of novel materials.

In the first part of this work, transition metal alloys are studied, with an emphasis on elastic properties, ductility, ideal strength and planar defects. Transition metals and alloys have the potential to exhibit attractive properties such as high melting temperatures, high strength, high stiffness, high ductility, high fracture toughness and superior corrosion and erosion resistance. However, unfortunately the attractive properties are usually not simultaneously present in an alloy. For example, a trade-off often exists between alloy strength on one hand and ductility on the other hand. Low ductility can be a limiting factor especially in hexagonal closed packed (HCP) transition metals and alloys, in which the limited number of slip systems can inhibit dislocation slip and plastic flow [17]. This leads to complications in both the manufacturing process of components made out of such materials and during the operational lifetime of the component. For this reason, the literature includes an extensive body of experimental and computational research, aimed at identifying alloying strategies that increase a material's ductility while maintaining its other attractive properties.

The difficulty of modeling ductility is in part that this property spans multiple length and time scales, see Fig. 1.1. On an electronic and atomic level, the Peierls barrier represents the energy barrier a dislocation has to overcome to glide along its slip plane and contribute to plastic flow and ductility. The Peierls barrier is related to shear modulus, which is a property that also finds its roots on the electronic and atomic level. This is the domain in which DFT typically operates. On a higher lengthscale, ductility is governed



by the interaction of dislocations with each other and with other defects such as grain boundaries, twin boundaries, impurities and second phase particles. Such phenomena are modeled for example with molecular dynamics (MD), Monte Carlo (MC) [18] or discrete dislocation dynamics (DDD) [19]. On a yet higher length and time-scale are continuum models that typically use approximations and constants from lower length scales to build models that disregard the discrete nature of materials and approximate their behavior by continuum laws. One such technique is the finite element-method (FEM) [20], another is Crystal Plasticity Modeling (CPM) [21, 22]. The microstructure of an alloy plays a big role in establishing its ductility is a function of many variables, such as the material's chemical composition and the details of its processing history. At the mesoscale level, techniques are available to predict microstructural features an alloy. Phase field (PF) [23] models allow for the simulation of microstructure evolution at the mesoscale, while accounting for arbitrarily complex grain morphologies. On the same level of time and length scales, Thermo Physical (TP) and Thermo Chemical (TC) models provide access to various thermodynamic properties of different phases of an alloy. A popular approach is the Calculation of Phase Diagrams (CALPHAD) formalism [24]. This class of models collects and assesses experimental and theoretical information on phase equilibria and thermochemical properties for a given alloy system. The Gibbs free energy is used to describe the thermodynamics of each phase and the resulting mathematical models are combined to calculate phase diagrams, often including metastable phases. Such models provide valuable insights into the attainable microstructure of alloys with a given composition. Also, manufacturing avenues may be suggested to create alloys with targeted microstructures.

## 1.1 Hexagonal Close Packed Rhenium

Much of the work in this thesis is devoted to the HCP transition metal rhenium (Re). Interest in this metal stems from observations that it exhibits unique mechanical properties such as the absence of a ductile-brittle transition and a high ductility at room temperature [25, 26]. The high ductility of Re, in combination with other attractive properties such as high strength and a high melting temperature, cause Re to be a potentially interesting structural material. Unfortunately, the exceptionally high cost and limited worldwide reserves of elemental Re have resulted in a limited use of Re-based alloys [27, 28]. Rhenium is currently being used in some applications where extremely demanding operating conditions are involved, such as rocket nozzles and nuclear reactors. It is clear that there exists a need for finding cost-effective replacement strategies for Re, without significantly altering its attractive mechanical properties, including the ductility [25].

In this dissertation, the first chapters will present results of an in-depth computational investigation into the elements that are feasible replacements candidates for Re. The aim is to retain or improve the ductility of Re by alloying in either of 2 ways. The first

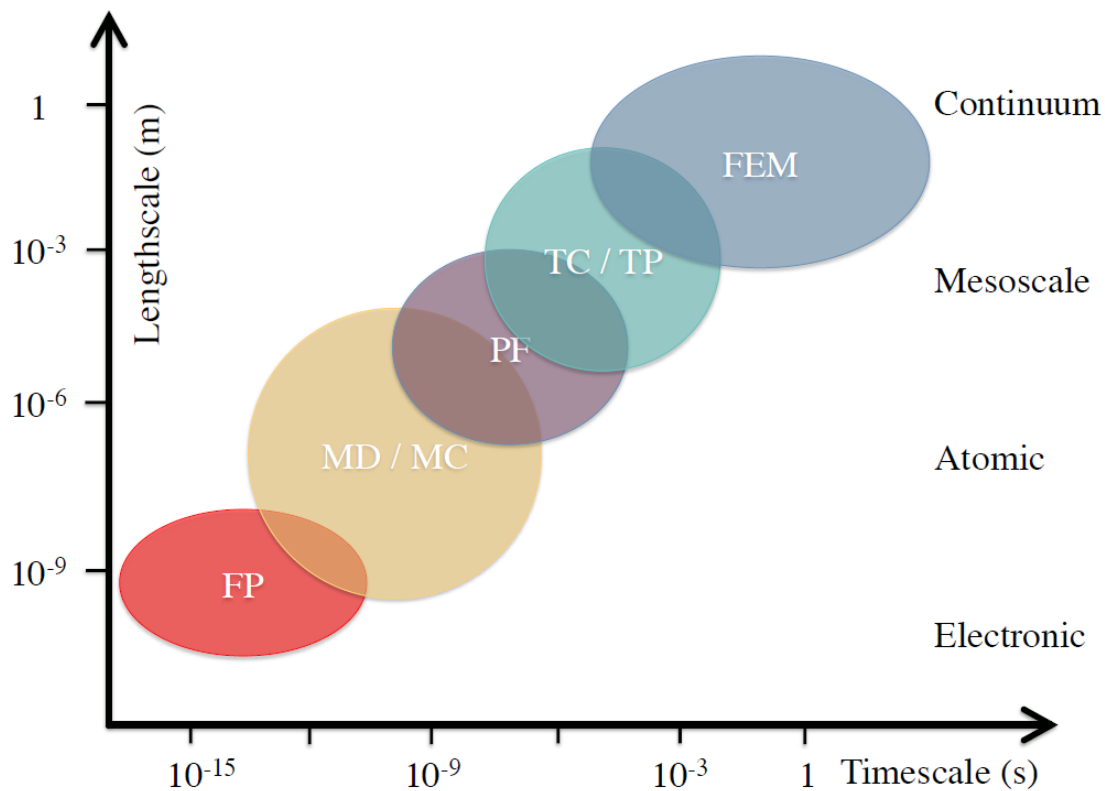


Figure 1.1: Different computational modeling techniques sorted by time and length scales: First-principles, Molecular Dynamics (MD), Monte Carlo (MC), Phase Field (PF), Thermo Chemical (TC) / Thermo Physical (TP) models and the Finite Element Method (FEM).

approach is to start with Re and identify less-expensive and more abundant solutes that it can be alloyed with, while maintaining or improving upon the ductility of the original material. This will yield a Re-based alloy that is somewhat less costly than pure Re. In the second approach, we seek to identify materials where Re is replaced completely and a new Re-free alloy is designed with elements that are less expensive and more abundant, while yielding comparable properties.

## 1.2 High-Throughput Calculations of Materials Properties

In the second part of this dissertation, we describe the results of HT-calculations for elastic properties and piezoelectric properties of inorganic crystalline compounds. This work is motivated by the observation that even though over 50,000 inorganic crystalline compounds are known to exist in nature, only for a fraction of those (typically 0.1 % - 0.3 %), important material properties such as elastic constants, piezoelectric constants, band gaps and dielectric constants are known, either from experiments or computationally. This lack of data represents a problem in a number of ways. First, it complicates the selection of materials with a set of desired properties for a given application, for example a certain stiffness to weight-ratio. Second, it hinders the development and optimization of current materials and the discovery of new materials. Third, the available materials property data in the literature is rather scattered and finding information can be rather time-consuming. Also, the materials property data in the literature is often obtained under different experimental conditions, which makes comparisons sometimes difficult. HT-calculations can alleviate these problems by making available large, searchable databases of materials properties calculated in a consistent manner.

## 1.3 Overview of Dissertation

The outline of this dissertation is as follows. In Chapter 2, the basic theory and methodology underpinning most of the work presented in this dissertation is presented. In particular, the “nuts and bolts” of density functional and density functional perturbation theory are reviewed. Density-functional-theory calculations are commonly performed on relatively small unit cells in combination with periodic boundary conditions, which complicates the simulation of disorder in materials. In Chapter 2, methods are reviewed that can be used to approximate substitutionally disordered solids in small unit cells with periodic boundary conditions.

Chapter 3 starts with a review of intrinsic ductility parameters, based on elasticity, defect energetics and ideal strength. Only the intrinsic ductility parameter based on elasticity will be studied in the remainder of Chapter 3, the other formulations are considered in later chapters. Subsequently, the methodology and computational details pertaining to Chapter 3 are described. In the results section, the structural and elastic properties of pure rhenium are first presented. Subsequently, the elastic and structural properties of Re-rich transition-metal alloys are presented. Trends in the intrinsic ductility and lattice constants as a function of solute type are revealed and in the following section, the energetics of Re-rich alloys are presented. Finally, in the discussion section, the obtained results are interpreted and put in the physical context of *d*-band filling and canonical *d*-band theory.

In Chapter 4, the energetics of twin boundaries in HCP metals and alloys are investigated. The crystallography of twinning and the accompanying nomenclature is introduced first. A study of twin boundaries in elemental HCP metals is presented next and interesting behavior of the twin energies with  $d$ -band filling is discussed and particular attention is paid to the twin-energy anomaly that occurs near half  $d$ -band fillings. The effect of alloying is presented next, followed by an explanation of the twin-energy anomaly in terms of structural stabilities and icosahedral building blocks that are present on certain types of twin boundaries. Some avenues towards rhenium-replacement are discussed next. The chapter ends with a discussion and conclusion.

Chapter 5 is closely related to Chapter 4 and discusses in more detail some of the methodologies developed as part of this work to study the energetics of planar defects in substitutionally disordered HCP alloys. After the introduction, the methodology is laid out, including discussions on the geometry of the twin boundary cells, unstable stacking faults and surfaces. The generation of the supercells is discussed next, followed by a discussion of the computational methods. Subsequently, the discussion and results sections are presented, first for the classical simulations and then for the quantum-mechanical simulations. This chapter ends with a summary and conclusions.

In Chapter 6, intrinsic ductility is studied from the perspective of ideal strength. After the introduction, the methodology is discussed, with particular focus on elastic instabilities in HCP metals under stress and the Wallace formalism. Also discussed are the formalism to calculate higher-order elastic constants and the computational methodology. In the results and discussion section, the occurrence of elastic instabilities is discussed and the analytical model is compared to the DFT results. The effect of  $d$ -band filling is discussed next, followed by conclusions.

Chapter 7 is dedicated to high-throughput calculations of elastic properties of inorganic crystalline compounds. This chapter comprises recent research efforts that culminated in the creation of the largest database of elastic properties to-date, consisting of full elastic information of over 2,200 (at the time of writing) inorganic crystalline compounds. After first presenting a background and summary of the work, the methods are described in detail, together with the high-throughput workflow. The results including a graphical representation are presented next, followed by a detailed verification of the computational methodology and an extensive comparison to experimental measurements of elastic properties.

Chapter 8 describes a computational high-throughput study of piezoelectric properties of compounds and is motivated by the lack of information on piezoelectric material properties, which hinders the development and discovery of new piezoelectric materials.

This chapter starts with describing the background of this work. The computational methodology, the compound selections and workflow is subsequently described. The next section describes the data records and gives a broad overview of the results and presents several newly discovered, high potential-piezoelectrics that were unveiled in this study. The final section in this chapter describes the verification of the computational methods employed in the piezoelectricity-calculations and presents comparison with selected experimental results.

Chapter 9 provides a summary and conclusions of the work presented in this dissertation. Further, suggestions for future work are made.

## Chapter 2

# Basic Theory and Methodology

Density Functional Theory (DFT) has now become one of the standard tools for the first-principles modeling of materials. In this chapter, a review of DFT is laid out, discussing the basic theorems, algorithms and approximations. Also included are short discussions of the virtual crystal approximation and density functional perturbation theory, as these methods have been used in part of the work presented in this dissertation.

## 2.1 Density Functional Theory

### 2.1.1 Problem definition

Consider an ensemble of  $N$  nuclei at positions  $(R_1, R_2, \dots, R_{N-1}, R_N)$  and  $n_e$  electrons located at  $(r_1, r_2, \dots, r_{n-1}, r_{n_e})$ . The energy of such a system follows from the Schrödinger equation in Eq. 2.1, in which  $H$  is the Hamiltonian,  $\Psi$  the wave function and  $E$  the total energy of the system [29].

$$H\Psi = E\Psi \quad (2.1)$$

The Hamiltonian is comprised of the sum of the kinetic energy and the potential energy:

$$H = \underbrace{-\frac{\hbar^2}{2m_e} \sum_i \nabla_i^2 - \frac{\hbar^2}{2M_\alpha} \sum_\alpha \nabla_\alpha^2}_{T} + \underbrace{\frac{1}{2} \sum_{i \neq j} \frac{e^2}{|r_i - r_j|} - \sum_{\alpha, i} \frac{e^2 Z_\alpha}{|r_i - R_\alpha|} + \frac{1}{2} \sum_{\alpha \neq \beta} \frac{e^2 Z_\alpha Z_\beta}{|R_\alpha - R_\beta|}}_V \quad (2.2)$$

In Eq. 2.2, the term  $T$  represents the kinetic energy, broken up in electron ( $T_e$ ) and nucleus parts ( $T_n$ ). The term  $V$  represents the potential energy, including electron-electron interactions ( $V_{ee}$ ), electron-nuclei interactions ( $V_{en}$ ) and nuclei-nuclei interactions ( $V_{nn}$ ).

Finally,  $m_e$  denotes the electron mass,  $M_\alpha$  denotes the nucleus mass and  $e$  and  $Z_\alpha e$  represent (minus) the electron charge and nuclear charge, respectively, where  $Z_\alpha$  is the atomic number for nucleus  $\alpha$ .

The Born-Oppenheimer approximation [30] is based on the fact that the protons and neutrons that make up the nucleus have a mass that is approximately 3 orders of magnitude larger than the electron mass. Hence, the electrons are much more agile than the nuclei and will almost instantaneously adapt to the motion of nuclei. This leads to the Born-Oppenheimer approximation and simplifies the Hamiltonian to Eq. 2.3.

$$H = T_e + V_{ee} + V_{en} \quad (2.3)$$

In the Born-Oppenheimer approximation, one can compute the energy of the electron subsystem using a Hamiltonian that is defined by a set of fixed nuclei, which provide an external electrostatic potential that the electrons feel. The total energy thus determined is only for the electron-electron and electron-nuclear interactions, and the total energy for a crystal must add to this the energy associated with the nucleus-nucleus interactions.

Even with the simplifications associated with the Born-Oppenheimer approximation, solving Eq. 2.1 is still an intractable problem for most systems of practical interest due to the electron-electron interaction. In the 1960's, several important theorems and simplifications were introduced that made solving 2.1 eventually possible, given certain approximations. This will be discussed next.

### 2.1.2 The Hohenberg-Kohn theorems

The roots for DFT were laid out in the 60's by Hohenberg and Kohn by the introduction of 2 important theorems. The first states that for a system consisting of  $n$  interacting electrons and an external potential  $V_{ext}(\vec{r})$ , the total energy is a unique functional of the electron density  $n(\vec{r})$ , see Eq. 2.4, in which  $F[n(\vec{r})]$  is some unknown functional of  $n(\vec{r})$  [9].

$$E[n(\vec{r})] = F[n(\vec{r})] + \int n(\vec{r})V_{ext}(\vec{r}) \quad (2.4)$$

Note that  $V_{ext}(\vec{r})$  is the potential felt by the electrons due to the nuclei, assumed to have fixed positions in accordance with the Born-Oppenheimer approximation introduced in the previous section. Eq. 2.4 is essentially an existence theorem of the functional, but does not say anything about how to calculate  $F[n(\vec{r})]$ .

The second theorem by Hohenberg and Kohn is expressed in Eq. 2.5. It states that for a given  $V_{ext}(\vec{r})$ , the ground state electron density  $n_0(\vec{r})$  and ground state energy  $E_0$  correspond to the minimum value of the functional  $E$  [9]:

$$E_0 = E [n_0(\vec{r})] = \min \{E [n(\vec{r})]\} \quad (2.5)$$

### 2.1.3 The Kohn-Sham Equations

The theorems by Hohenberg and Kohn have introduced a major simplification: they allow one to go from a wave-function based solution of the Schrodinger Equation to a variational problem written in terms of a single spatially varying function. However, these theorems have not resolved the fundamental difficulty of dealing with a many-body system consisting of  $N$  interacting nuclei and  $n$  interacting electrons. Kohn and Sham [10] proposed a formally exact reformulation in 1965 and replaced the full many-body problem with an approximation of non-interacting electrons, embedded in an effective external potential  $V_{eff}$ . Kohn and Sham broke up the functional  $F [n(\vec{r})]$  in Eq. 2.4, which is a function of the electron density  $n(\vec{r})$ , into 3 parts. The energy functional can then be expressed according to their formulation as in Eq. 2.6 [10].

$$E [n(\vec{r})] = T_s [n(\vec{r})] + E_H [n(\vec{r})] + E_{xc} [n(\vec{r})] + \int n(\vec{r})V_{ext}(\vec{r}) \quad (2.6)$$

In Eq. 2.6, the term  $T_s [n(\vec{r})]$  denotes the kinetic energy of the non-interacting electrons, which can be calculated from the Kohn-Sham orbitals  $\phi(\vec{r})$  according to Eq. 2.7, where the asterisk denotes a complex conjugate. Note that in Eq. 2.7, (Hartree) atomic units are employed, which is different from those in Eq. 2.2.

$$T_s [n(\vec{r})] = -\frac{1}{2} \sum_{i=1}^{n_e} \phi_i^*(\vec{r}) \nabla^2 \phi_i(\vec{r}) d\vec{r} \quad (2.7)$$

Note that the energy  $E$  in Eq. 2.6 is not the total energy: to obtain the total energy, the contribution from ion-ion interactions has to be added. The electron density  $n(\vec{r})$  is calculated from the Kohn-Sham orbitals according to Eq. 2.8.

$$n(\vec{r}) = -e \sum_{i=1}^{n_e} |\phi_i(\vec{r})|^2 \quad (2.8)$$

In Eq. 2.6, the term  $E_H [n(\vec{r})]$  represents the Coulomb-energy term, calculated from the Hartree-approximation as in Eq. 2.9.

$$E_H [n(\vec{r})] = \frac{1}{2} \int \frac{n(\vec{r})n(\vec{r}')}{|\vec{r} - \vec{r}'|} \quad (2.9)$$

Finally, the last term is the exchange-correlation energy defined in Eq. 2.10.

$$E_{xc} [n(\vec{r})] = (\langle T \rangle - T_s [n(\vec{r})]) + (\langle E_H \rangle - E_H [n(\vec{r})]) \quad (2.10)$$



The quantities  $\langle T \rangle$  and  $\langle E_H \rangle$  denote the energies associated with the true, interacting electrons and  $T_s [n(\vec{r})]$  and  $E_H [n(\vec{r})]$  relate to the approximated energies of non-interacting electrons. Hence, the exchange-correlation energy is a measure of the error in the energy that is introduced when making the approximation of non-interacting electrons. An effective potential is now introduced,  $V_{eff}(\vec{r}) = V_H(\vec{r}) + V_{xc}(\vec{r}) + V_{ext}(\vec{r})$ . The Kohn-Sham equations follow and are given in Eq. 2.11, where the terms  $\epsilon_i$  represent the Kohn-Sham energy eigenvalues, where again atomic units are employed.

$$\left[ -\frac{1}{2}\nabla^2 + V_{eff}(\vec{r}) \right] \phi_i(\vec{r}) = \epsilon_i \phi_i(\vec{r}) \quad (2.11)$$

The Kohn-Sham equations are exact and have not introduced new physical approximations. The practical implementation of these equations however, requires a known functional form of the exchange-correlation functional. In general, this is not known and approximations have to be made. The accuracy of DFT-calculations is often limited primarily by how accurate the approximation of the exchange-correlation functional is. The exchange-correlation energy functional is often split up in an exchange ( $E_X [n(\vec{r})]$ ) and correlation ( $E_C [n(\vec{r})]$ ) part such that  $E_{XC} [n(\vec{r})] = E_X [n(\vec{r})] + E_C [n(\vec{r})]$ . To calculate the effective potential  $V_{eff}$ , the electron density  $n(\vec{r})$  is required, but to calculate  $n(\vec{r})$ , the Kohn-Sham orbitals are required, which is what we are trying to solve for to compute  $n(\vec{r})$ . This type of problem is solved self-consistently as shown in Fig. 2.1.

### 2.1.4 Spin-Polarization

In the above treatment of the Kohn-Sham equations, the electron spin has not been explicitly taken into account. For spin-polarized systems, an extension of the Kohn-Sham equations is required to calculate the ground-state electron density. The extension of the Kohn-Sham equations for spin-polarized systems entails [31] i) a decomposition of  $n(\vec{r})$  into spin up ( $n(\vec{r}, \uparrow)$ ) and spin down ( $n(\vec{r}, \downarrow)$ ) parts:  $n(\vec{r}) = n(\vec{r}, \uparrow) + n(\vec{r}, \downarrow)$  and ii) a decomposition of the spin density  $s(\vec{r})$  such that:  $s(\vec{r}) = n(\vec{r}, \uparrow) - n(\vec{r}, \downarrow)$ . The Kohn-Sham equations for a spin-polarized system can be recast as in Eq. 2.12.

$$\left[ -\frac{1}{2}\nabla^2 + V_{eff}^\delta(\vec{r}) \right] \phi_i(\vec{r})^\delta = \epsilon_i^\delta \phi_i^\delta(\vec{r}) \quad (2.12)$$

In this equation,  $\delta$  represents either spin up ( $\uparrow$ ) or spin down ( $\downarrow$ ). These spin densities are coupled, and their effects are lumped into the effective potential  $V_{eff}$ . In this work, DFT calculations are performed on some systems containing magnetic elements and in those cases, the spin-polarized ground state may have a lower energy than the non spin-polarized ground state.

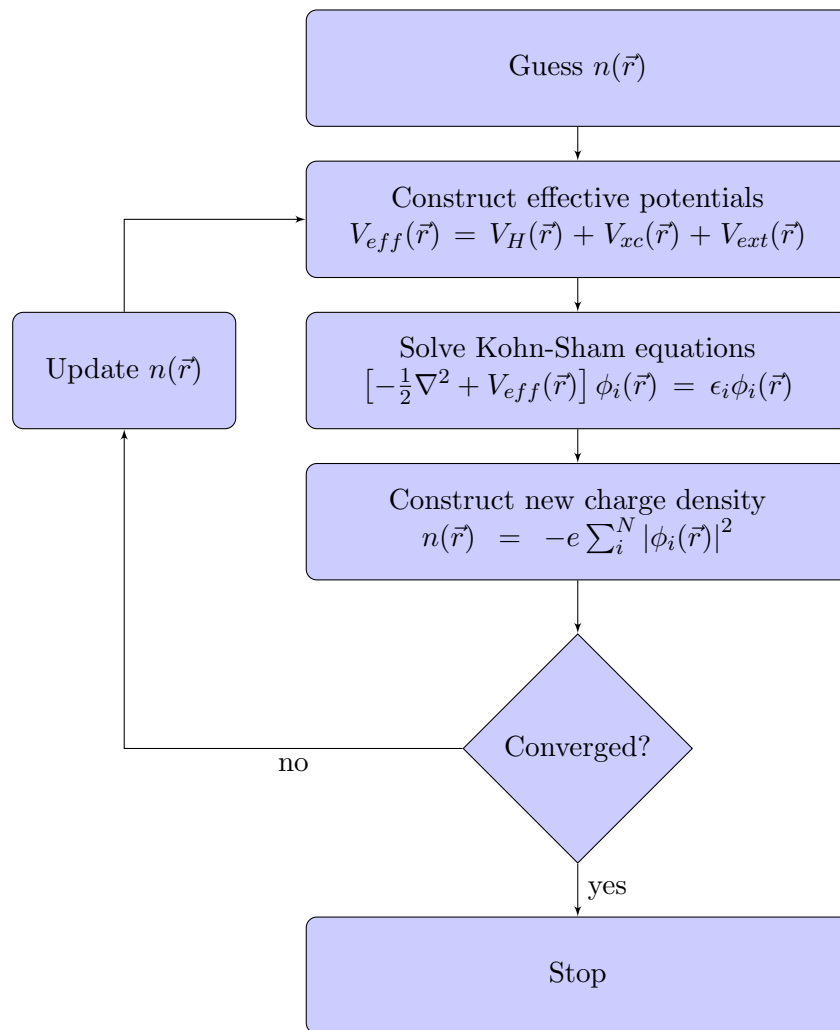


Figure 2.1: An illustration of the self-consistency loop used in DFT to calculate the ground state electron density.

### 2.1.5 Exchange-Correlation Functional

With the Kohn-Sham equations, the exchange-correlation energy  $E_{xc} = E_{xc}[n(\vec{r})]$  was introduced. This quantity is a functional of the electron density and is generally unknown. Several approximations to  $E_{xc}$  exist, each with different degrees of sophistication. In essence, the various approximations differ primarily by the number of terms included in the electron density. The simplest approach is the local density approximation (LDA), in which  $E_{xc}$  depends only on the electronic density at each point in space [31]. In this

approach,  $E_{xc}$  is obtained as in Eq. 2.13.

$$E_{xc}^{LDA} [n(\vec{r})] = \int n(\vec{r}) \epsilon_{xc} [n(\vec{r})] d\vec{r} \quad (2.13)$$

In Eq. 2.13,  $\epsilon_{xc} [n(\vec{r})]$  represents the exchange-correlation energy potential, which is approximated to be equal to that of a locally homogeneous electron gas, with an electron density of  $n(\vec{r})$ .

Within LDA, the exchange-energy potential,  $\epsilon_x [n(\vec{r})]$ , can be expressed analytically using the Hartree-Fock approach as a function of  $n(\vec{r})$ , see Eq. 2.14 [32], where atomic units are employed as before.

$$\epsilon_x [n(\vec{r})] = -\frac{3}{4} \left( \frac{3}{\pi} n(\vec{r}) \right)^{1/3} \quad (2.14)$$

Whereas for the exchange-energy potential, an analytic expression can be derived, this has presently not yet been achieved for the correlation-energy potential in the general case. Only for systems in the limit of infinitely weak or strong correlations, asymptotic analytical expressions exist. Correlation-energies have been obtained for the homogeneous electron gas by Ceperley and Alder, who employed quantum Monte Carlo-simulations at several intermediate values of the electron density [33]. By interpolation, correlation energies can then be obtained at any electron density [34]. The LDA tends to work well for systems in which the charge density behaves rather smoothly in space. In the case of large gradients in the charge density, the assumption of a locally homogeneous electron gas breaks down and other models may have to be used for the exchange-correlation energy.

One such approximation is the generalized gradient approximation (GGA), which takes into account not only the electron density but also the gradient of the electron density on the exchange-correlation energy. This can be expressed mathematically as in Eq. 2.15 .

$$E_{xc}^{GGA} [n(\vec{r})] = \int n(\vec{r}) \epsilon_{xc} [n(\vec{r})] F_{XC} [n(\vec{r}), \nabla n(\vec{r})] d\vec{r} \quad (2.15)$$

The functional  $F_{XC} [n(\vec{r}), \nabla n(\vec{r})]$  serves as a correction factor to the LDA exchange-correlation energy potential. In the literature, it is often expressed as a function of the Wigner-Seitz radius  $r_s$  and the reduced density gradient  $s(\vec{r})$ , defined in Eq. 2.16, where  $k_F$  denotes the Fermi momentum at position  $\vec{r}$ .

$$s(\vec{r}) = \frac{|\nabla n(\vec{r})|}{2k_F(\vec{r})n(\vec{r})} \quad (2.16)$$

Different expressions for  $F_{XC}$  have been proposed in the literature giving rise to different functionals, such as by Perdew-Wang (PW91) [35, 36] and Perdew, Burke and Ernzerhof

(PBE) [37]. There exist other functionals than just LDA and GGA and these are sometimes ranked in terms of relative accuracy in a Jacob's ladder as shown in Fig. 2.2 [38]. As one moves up the ladder, the accuracy of the functionals generally improves, at the cost of involving more analytical terms in the expressions and hence, greater computational cost. The term  $\tau$  in Fig. 2.2 involves both  $\nabla^2 n$  and the Kohn-Sham orbital kinetic energy densities. The functional by Tao, Perdew, Staroverov and Scuseria (TPSS) [39] is an example of a meta-GGA functional in which  $\tau$  is used instead of  $\nabla^2 n$ . Details can be found in the work by Perdew and others [38]. Hybrid methods such as by Becke, Lee, Yang and Parr (BLYP) [40, 41] approximate the exchange-correlation functional by a combination of on one hand the exact-exchange that is obtained from the Hartree-Fock approximation and a standard LDA or GGA-functional on the other hand [41]. Other commonly used hybrid functionals in the literature are PBE0 [42] and HSE06 [43, 44].

As a general rule of thumb, LDA functionals are known to overbind whereas GGA functionals tend to underbind. This often leads to an underestimation of lattice constants in LDA and an overestimation of cohesive energy, elastic constants and defect energies [45, 46].

### 2.1.6 Pseudopotentials

In most solids at ambient temperatures and pressures, it is the valence electrons that most participate in the bonding of a solid and establish its properties. The core electrons are effectively screened by the valence electrons and do not strongly interact with the valence electrons or the chemical environment in which a given atom is embedded. In terms of the electronic structure of a material, one can think of two types of occupied Kohn-Sham states. The first are core states that lie very deep in energy and are spherically localized around the nuclear core. The second are valence states that are closer to the Fermi-level and form bands, showing considerably more dispersion than the core states. When the core states of an atom in a solid are compared to those of the isolated atom, often no significant differences in their spectrum and distribution are found. This implies that the chemical environment plays only a limited role in establishing the core states. Including states close to the core explicitly in DFT-calculations may prove problematic, since the requirement of orthogonality leads to rapid oscillations of wavefunctions near the nucleus.

Although there exist methods that treat all electrons (both core and valence) explicitly, another approach is to only consider the valence electrons explicitly and lump the effect of the core electrons into an effective potential. In this formalism the wave functions of the core electrons,  $\psi_i^c(\vec{r})$ , and those of the valence electrons,  $\psi_i^v(\vec{r})$ , are considered separately. Both these are solutions to the Kohn-Sham equations with respective eigenvalues  $\epsilon_i^c$  and  $\epsilon_i^v$ . The wave functions of the valence electrons can be expressed as in Eq. 2.17 [47].

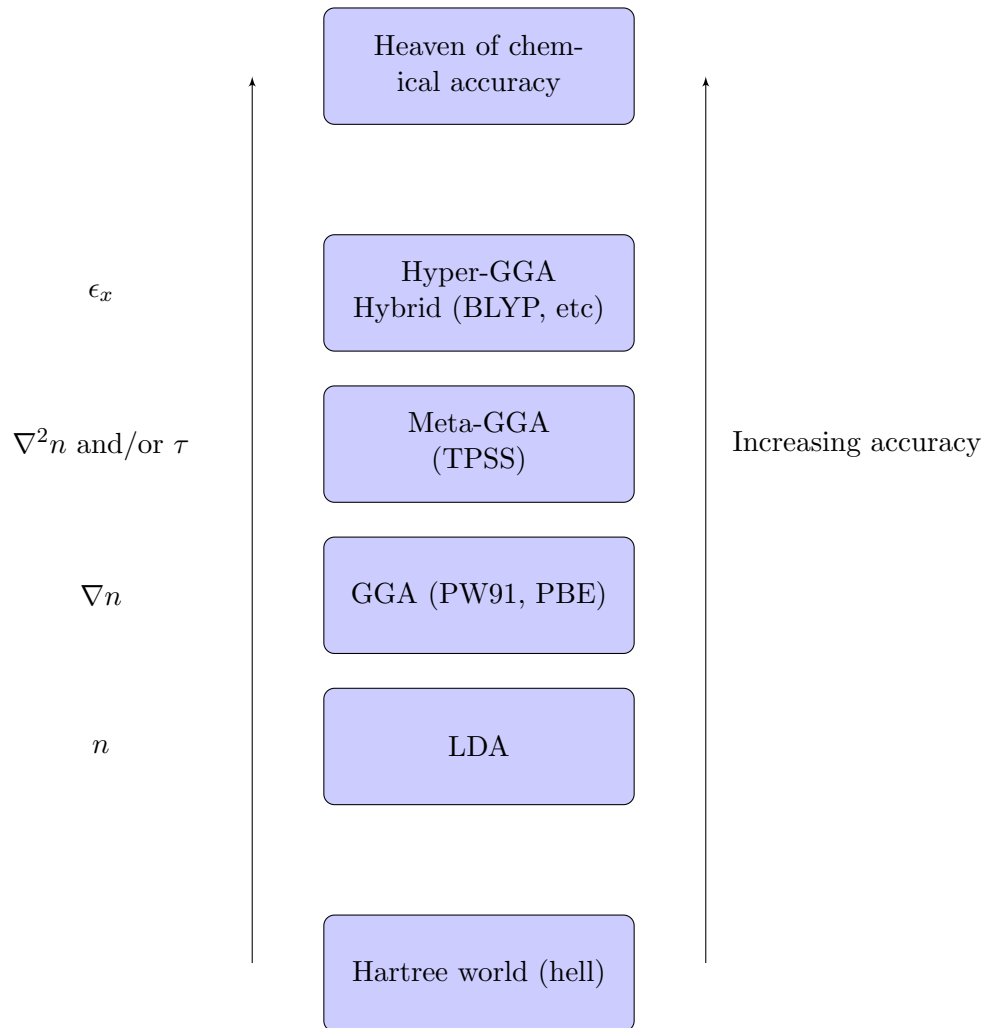


Figure 2.2: Jacob's ladder showing different functionals as used in DFT, and their relative rankings in terms of (perceived) accuracy.

$$\psi_i^v(\vec{r}) = \tilde{\psi}_i^v(\vec{r}) - \sum_j \langle \psi_j^c | \tilde{\psi}_i^v(\vec{r}) \rangle \psi_j^c(\vec{r}) \quad (2.17)$$

Further, a pseudo external wave function for the valence electrons can be defined as in Eq. 2.18. In Eq. 2.18, an effective pseudopotential is defined which applies to the valence electrons outside the core region.

$$V_{ext}^{ps} \tilde{\psi}_i^v(\vec{r}) = V_{ext} \tilde{\psi}_i^v(\vec{r}) + \sum_j (\epsilon_i^v - \epsilon_j^c) \langle \psi_j^c(\vec{r}) | \tilde{\psi}_i^v(\vec{r}) \rangle \psi_j^c(\vec{r}) \tilde{\psi}_i^v(\vec{r}) \quad (2.18)$$

The valence electrons are governed by their own pseudo wavefunctions,  $\tilde{\psi}_i^v$ , which are solutions to the Kohn-Sham equations, see Eq. 2.19.

$$\left[ -\frac{1}{2} \nabla^2 + V_{ext}^{ps} \right] \tilde{\psi}_i^v(\vec{r}) = \epsilon_i \tilde{\psi}_i^v(\vec{r}) \quad (2.19)$$

Within the general class of pseudopotentials, different formalisms have been developed such as norm-conserving pseudopotentials (NCPP's) and Kleinman-Bylander pseudopotentials [48]. In part of the work presented in this dissertation, NCPP's are employed [49].

NCPP's aim at approximating the all-electron wave functions,  $\psi_{ae}$  by imposing a number of constraints on the pseudo wave functions,  $\psi_{pp}$  [50, 51]. The requirements are i) the valence pseudo wave functions should contain no nodes, ii) beyond a cut-off radius  $r_c$ ,  $\psi_{ae}$  and  $\psi_{pp}$  are identical, iii) the charge enclosed within  $r_c$  should be equal for both  $\psi_{ae}$  and  $\psi_{pp}$ , which is referred to as the norm-conserving conditions, see Eq. 2.20 and iv) the eigenvalues of  $\psi_{ae}$  and  $\psi_{pp}$  must be equal.

$$\int_0^{r=r_c} \psi_{ae}^* \psi_{ae} dr = \int_0^{r=r_c} \psi_{pp}^* \psi_{pp} dr \quad (2.20)$$

If a pseudopotential meets these 4 requirements, it is referred to as an NCPP. Another approach that is used in this work is the projector-augmented-wave (PAW) [52, 53] method. This is an all-electron method, which maps the true all-electron wave functions onto smooth pseudo waves via a linear transformation that acts in a region close to the nucleus (the augmentation sphere). Outside the sphere (in the interstitial regions), the smooth pseudo waves reduce to the true all-electron waves. The core wave functions are usually represented on a spherical grid and the valence wave functions on a Cartesian grid, which are matched smoothly at the augmentation-sphere boundary. The pseudo waves are characterized by slow spatial variations, which leads to good convergence properties of their Fourier-coefficients to zero for short wavelengths.

Within the PAW-formalism, a common approximation is the frozen-core approximation [52, 53]. This approximation relies on the observation that core states are rather inert to the chemical environment of the atom. Hence in the frozen-core approximation, the core states are pre-computed only once in an all-electron calculation and their densities are stored. This approximation is very computationally efficient, as the core states are considered frozen and do not have to be recomputed. The core electrons are computed fully relativistically using the Dirac equation whereas the valence electrons are treated in a scalar relativistic approximation, including mass and Darwin relativistic corrections, but

not spin-orbit-coupling terms. These relativistic corrections are important for many of the systems under investigation in this work, such as  $5d$  transition-metals and alloys.

### 2.1.7 Structural relaxations

Structural relaxations in DFT aim to minimize the energy of a given configuration of atoms with respect to their position. Different types of structural relaxations can be performed such as internal coordinates only, constant volume, constant shape and full relaxations. The ionic forces and stress tensor are typically used by the structural relaxation-algorithm to find the minimum-energy configuration.

The ionic force can be calculated from DFT by applying the Hellmann-Feynman theorem [54, 55]. It states that for any perturbation  $\lambda$ , the energy change is given by a rather simple expression, see Eq. 2.21, where  $\phi$  denotes the ground-state wave function.

$$\frac{\partial E}{\partial \lambda} = \langle \phi | \frac{\partial H}{\partial \lambda} | \phi \rangle \quad (2.21)$$

Here, we have introduced bra-ket notation, where in general  $\langle \phi | v | \phi \rangle$  represents the expectation value of a physical quantity  $v$  in an arbitrary state  $\phi$ . Eq. 2.21 can be employed to calculate the ionic forces and stress tensor from DFT. In particular, given an ion at position  $\mathbf{R}$ , the ionic forces follow from Eq. 2.22.

$$\mathbf{F} = -\frac{\partial E}{\partial \mathbf{R}} = -\langle \phi | \frac{\partial H}{\partial \mathbf{R}} | \phi \rangle \quad (2.22)$$

The force on ion  $\alpha$  at position  $\mathbf{R}_\alpha$ , surrounded by ions at positions  $\{\mathbf{R}\}$  can be expressed in more detail as in Eq. 2.23, where the terms  $V_{en}$  and  $V_{nn}$  were defined in Eq. 2.2.

$$\mathbf{F} = \int_{\mathbf{r}} n(\mathbf{r}) \frac{V_{en}(\mathbf{r} - \mathbf{R}_\alpha)}{\partial \mathbf{R}_\alpha} d\mathbf{r} - \frac{\partial V_{nn}(\{\mathbf{R}\})}{\partial \mathbf{R}_\alpha} \quad (2.23)$$

The stress tensor  $\sigma_{\alpha\beta}$ , can be described in terms of strain-derivatives ( $\epsilon_{\alpha\beta}$ ) of the energy, see Eq. 2.24, where  $\Omega$  denotes the cell volume.

$$\sigma_{\alpha\beta} = \frac{1}{\Omega} \frac{\partial}{\partial \epsilon_{\alpha\beta}} (T_s + E_H + E_{xc} + V_{ext} + V_{nn}) \quad (2.24)$$

Using the Hellmann-Feynman theorem, more explicit equations for the stress tensor can be derived [56, 57, 58].

Structural relaxations can be performed with the forces and stresses defined above informing the optimization algorithm of the shape of the energy landscape. Different optimization algorithms can be used for structural relaxations, such as Newton's method,

conjugate gradient, Broyden's method [59, 60] and more recent methods such as the Fast Inertial Relaxation Engine (FIRE)-method [61]. Lagrange-multipliers can be included to incorporate geometric constraints into the optimization process, such as relaxations of ions along a single Cartesian direction.

### 2.1.8 Density Functional Perturbation Theory

Many physical properties are related to the derivatives of the total energy with respect to some perturbation. Examples include mechanical, dielectric and vibrational (phonon) properties, with corresponding perturbations being strain, electric field and atomic displacements. The Hellmann-Feynman theorem discussed above furnishes first-order derivatives such as atomic forces arising from atomic displacements, and stresses arising from imposed strains. Additionally, the Berry-phase approach reviewed in the next section allows the calculation of the electric polarization, which is the linear response of the crystal to an applied electric field.

Second order derivatives of the total energy provide generalized susceptibilities, with examples being the force constant matrix (second order derivative of the energy with respect to atomic displacements), and the dielectric constant (related to the linear relation between polarization and applied electric field). In this way, for example phonon-spectra and elastic constants can be calculated, which is sometimes referred to as the frozen-phonon approach [62, 63, 64]. An example of the use of such an approach in the calculation of elastic constant tensors will be given in Chapters 3, 6 and 7, where the details of the implementation of the approach will also be discussed. In some applications of such finite-difference approaches an issue arises, namely that the calculations can be difficult to converge numerically and thus require significant computational time in some cases.

An alternative way to calculate higher-order derivatives of the total energy is to solve the Sternheimer equation, which is obtained by expanding the Kohn-Sham equations to first order [65]. Yet another approach, employed in this work to compute piezoelectric coefficients, is to employ perturbation theory. This is commonly referred to as Density Functional Perturbation Theory (DFPT) [66] within a DFT-context. Efficient and numerically accurate schemes have been proposed to calculate the derivatives based on DFPT in the literature [67, 68, 69, 70, 71].

Consider again a perturbation  $\lambda$  and expand the total energy  $E$  in terms of  $\lambda$  around the unperturbed state as in Eq. 2.25. In Eq. 2.25 the parameter  $\lambda$  can be thought of as a vector with entries  $\lambda = (\mathbf{R}, \eta, \mathcal{E})$ .

$$E(\lambda) = E(0) + \sum_i \left. \frac{\partial E}{\partial \lambda_i} \right|_0 \lambda_i + \frac{1}{2} \sum_{i,j} \left. \frac{\partial^2 E}{\partial \lambda_i \partial \lambda_j} \right|_0 \lambda_i \lambda_j + \dots \quad (2.25)$$



Table 2.1: Physical quantities that can be calculated from DFPT by taking first and second order derivatives with respect to atomic positions  $\mathbf{R}$ , homogeneous strains  $\eta$  and electric fields  $\mathcal{E}$ .

| $\lambda$     | 1 <sup>st</sup> order | 2 <sup>nd</sup> order |          |                   |
|---------------|-----------------------|-----------------------|----------|-------------------|
|               |                       | $\mathbf{R}$          | $\eta$   | $\mathcal{E}$     |
| $\mathbf{R}$  | $\mathbf{F}$          | $\mathcal{C}$         | $\gamma$ | $Z^*$             |
| $\eta$        | $\sigma$              | $\gamma$              | $c^0$    | $e^0$             |
| $\mathcal{E}$ | $\mathbf{P}$          | $Z^*$                 | $e^0$    | $\epsilon^\infty$ |

Now consider Eq. 2.25 up to second order and 3 types of perturbations, i) atomic displacements  $\mathbf{R}$ , ii) a homogeneous strain  $\eta$  and iii) a homogeneous electric field  $\mathcal{E}$ . Table 2.1 reports the physical quantities that can be extracted from DFPT when such perturbations are imposed on a material. The derivatives of first order with respect to (w.r.t.) the atomic displacements  $\mathbf{R}$  allow for the calculation of the forces  $\mathbf{F}$ , the first order derivatives w.r.t. strain  $\eta$  yield the stress  $\sigma$  and finally the the first order derivatives w.r.t.  $\mathcal{E}$  result in the induced polarization  $\mathbf{P}$ . The second order derivatives result in a total of 6 independent quantities. Referring to Table 2.1, these are the interatomic force constants  $\mathcal{C}$ , the clamped-ion elastic constants  $c^0$ , the internal strain coupling constants  $\gamma$ , the Born effective charges  $Z^*$ , the clamped-ion piezoelectric constants  $e^0$  and finally the optical dielectric tensor  $\epsilon^\infty$ . These quantities can be used to calculate other properties such as phonon spectra, the elastic tensor, the piezoelectric tensor and the static dielectric tensor.

### 2.1.9 Polarization and Berry Phases

In periodic systems, absolute polarization is ill-defined and only changes in polarization between states can be defined precisely [72]. Experimentally, the polarization is determined by extracting differences in polarization. By applying an electric field,  $\mathbf{P}$  can be reversed to the opposite direction  $-\mathbf{P}$  and by systematically varying the electric field  $\mathcal{E}$ , the hysteresis loop of  $\mathbf{P}$  versus  $\mathcal{E}$  can be mapped out. In practice this is done by measuring the macroscopic current  $\mathbf{j} = \mathbf{j}(t)$ , as a function of time,  $t$  during a period of  $\Delta t$ . The change in polarization can then be obtained from Eq. 2.26.

$$\Delta\mathbf{P} = \int_0^{\Delta t} \mathbf{j}(t)dt = \mathbf{P}(\Delta t) - \mathbf{P}(0) \quad (2.26)$$

For periodic solids, the total change in polarization  $\Delta\mathbf{P}$  is decomposed into an electronic and an ionic contribution as in Eq. 2.27. The justification for doing so relies on the Born-Oppenheimer approximation.

$$\Delta\mathbf{P} = \Delta\mathbf{P}_{ion} + \Delta\mathbf{P}_{el} \quad (2.27)$$

Further, if the initial state is chosen to have  $\mathbf{P} = \mathbf{0}$ , Eq. 2.27 reduces to Eq. 2.28, in which  $\mathbf{P}$  represents the total polarization of the unit cell in the final state.

$$\Delta\mathbf{P} = \mathbf{P} = \mathbf{P}_{ion} + \mathbf{P}_{el} \quad (2.28)$$

Eq. 2.29 gives the expression for the ionic contribution to the total polarization, where  $e$  denotes the elementary charge,  $\Omega$  denotes the cell volume,  $Z_n^*$  is the charge of ion  $n$  and  $\mathbf{R}_n$  is the position of ion  $n$ .

$$\mathbf{P}_{ion} = \frac{e}{\Omega} \sum_n Z_n^* \mathbf{R}_n \quad (2.29)$$

Eq. 2.30 is the Berry phase-expression for the electronic contribution to the total polarization [72].

$$\mathbf{P}_{el} = -\frac{2ie}{(2\pi)^3} \sum_{n=1}^m \int_{BZ} \langle u_{n\mathbf{k}} | \nabla_{\mathbf{k}} | u_{n\mathbf{k}} \rangle d\mathbf{k} \quad (2.30)$$

The starting point for its derivation is to express the electronic contribution to the change in polarization as a function of a finite adiabatic change in the Kohn-Sham Hamiltonian of the crystalline solid [73]. The change is parameterized by a variable  $\lambda$  that varies along the path from 0 to 1. It can be shown that the change of polarization can be calculated without considering conduction-band states explicitly and that it is path-independent and thus depends only on the end points [72]. It can be shown that Eq. 2.30 has a clear physical interpretation: the change in polarization of a solid, induced by an adiabatic change in the Hamiltonian, is proportional to the displacement of the charge centers of the Wannier functions corresponding to the valence bands [72, 74].

In Eq. 2.30, the summation is performed over the  $m$  occupied electronic bands and the integral is carried out over the full Brillouin Zone (BZ). The function  $u_{n\mathbf{k}}$  has the same periodicity as the underlying crystal lattice and is related to the Bloch wave function  $\psi_{n\mathbf{k}}(\mathbf{r})$ , i.e.  $\psi_{n\mathbf{k}}(\mathbf{r}) = e^{i\mathbf{k}\cdot\mathbf{r}} u_{n\mathbf{k}}(\mathbf{r})$ . Eq. 2.30 holds only for systems that are insulating everywhere along the integration path and therefore would break down for e.g. metals.

From the quantities shown in Table 2.1, the piezoelectric constants are of primary interest to the work presented in this dissertation. The clamped-ion piezoelectric tensor  $e^0$  (evaluated at fixed ionic positions  $\mathbf{R}$ ), can be formally defined as in Eq. 2.31, where  $\alpha$  and  $j$  denote Cartesian directions [72].

$$e_{\alpha j}^0 = -\left( \frac{\partial^2 E}{\partial \mathcal{E}_\alpha \partial \eta_j} \right)_{\mathbf{R}} \quad (2.31)$$

In this work, the relaxed-ion piezoelectric tensors are calculated, as defined in Eq. 2.32.

$$e_{\alpha j} = \left( \frac{\partial P_{\alpha}}{\partial \eta_j} \right)_{\mathcal{E}} = - \left( \frac{\partial \sigma_j}{\partial \mathcal{E}_{\alpha}} \right)_{\eta} \quad (2.32)$$

The precise definition of  $\mathbf{P}$  and  $\mathcal{E}$  in Eq. 2.32 is subtle, since these are the reduced polarization and electric field, which are slightly different from what has been used earlier in this section. These reduced quantities can be related to the original electric field and polarization by the strain matrix. Details can be found in Refs. [72, 75].

## 2.2 Disorder in solids

Crystalline solids with a perfectly regular arrangement of atoms do not exist in nature, and disorder is introduced in various ways, such as by point, line, planar and volumetric defects. In this section another type of disorder is considered in relation to the occupation of different atomic species over the sites of the crystal lattice. This compositional disorder can be on the sites of a given crystal structure, leading to what is referred to as substitutional solid solutions, or over the interstitial sites of a crystalline structure, leading to interstitial alloys, or both. The alloys considered in this work tend to be composed of atoms with similar sizes and electronegativity, hence according to the Hume-Rothery rules [6], substitutional solid solutions are more likely to occur than interstitial solid solutions. Disordered substitutional alloys tend to show higher stability ranges at high temperatures where entropic terms favor compositional disorder, but can sometimes be frozen into a metastable state at lower temperatures by for example quenching. In nature, many solids are disordered rather than ordered and this can have profound influences on their mechanical behavior. Therefore, it is of great interest to be able to model substitutionally disordered alloys with modern electronic structures calculations based on DFT.

Modeling perfectly ordered, periodic structures is relatively straightforward in DFT because of translational symmetry and Bloch's theorem. However, complications arise when considering random solid solutions. The principal problem is that compositional disorder is characterized by a distribution of local atomic configurations that can only be exactly sampled in the limit reached of infinitely large system sizes. Modern DFT calculations are limited to system sizes of only about 1,000 atoms and therefore, approximations are required to model random alloys in relatively small, periodic unit cells. Some of the common approaches are as follows.

1. One class of approaches uses a single-site approximation, in which the random alloy is modeled as an ordered structure of identical, effective atoms. Within this class of approaches, commonly used methods are the coherent potential approximation (CPA) [76] and the virtual crystal approximation (VCA) [77, 78]. The principle of the CPA is to construct effective atoms such that the average electron scattering

off the alloy constituents should equal zero [79]. In the VCA, instead an effective medium is created by averaging the potentials of the individual species present in the alloy by their concentration (see below for more detail). Effective-medium theories such as these have a number of serious drawbacks. First, local relaxations due to atomic size mismatches are not accounted for [80]. This can be a problem especially for atoms with very different sizes. Second, approximations have to be made in the CPA formalism to incorporate charge transfer between atoms due to differences in electronegativity since all atoms are identical in the effective medium. These approximations [81, 82, 83] might or might not be appropriate depending on the details of the system under consideration. Within the VCA, we are unaware of methods of incorporating charge transfer at all [84].

2. A second approach is a cluster expansion (CE) [85, 86]. In a CE, interatomic interaction parameters are obtained from fitting the energy of a number of different atomic (usually ordered) configurations on a parent lattice to an Ising model. In theory, a well-converged CE is able to predict the energy of any configuration of atoms on a given parent lattice. Hence, it can be used to approximate energetics of random and short-range-ordered solid solutions and an advantage is that much larger system sizes can be considered than in DFT.
3. The most direct approach to modeling random alloys is through the use of a supercell method, where (for a binary alloy) each lattice site is decorated with either an A or B atom. The problem with this approach is that either large supercells are required to reproduce the statistics of the local distributions of atoms in a random alloy or averaging over many distinct configurations has to be performed, making it computationally prohibitive. However, by distributing the atoms on the parent lattice in a particular fashion, it is possible to create a proper representation of the random alloy in a small supercell. The method of special quasirandom structures (SQS) is based on this premise and is reviewed below.

### 2.2.1 Special Quasirandom Structures

The idea of the SQS approach [87, 88] is to mimic random alloys as closely as possible in small periodic unit cells by distributing the atoms on the lattice sites in such a way that locally around each atom (within a chosen cutoff) the average occupation of the neighbors, as measured by compositional correlation functions, are as close as possible to that of a random alloy at the same overall composition. In particular for systems in which electronic and elastic interactions are relatively short-ranged, this approach is justified, however it can be problematic when dealing with systems where long-range contributions to the interatomic interactions are important.

Mathematically, a given atomic configuration can be described in terms of its correlation functions [89]. In lattice algebra, a spin-value  $\sigma = \pm 1$  is assigned to each lattice site, depending on whether the lattice site is decorated with an A or B-atom. Each lattice site is also characterized by several geometric figures, such as point, pair, triplet clusters etc. Let each geometric figure have  $k$  vertices ( $k = 1$  for points,  $k = 2$  for pairs etc.) and let those figures have a maximum length  $m$ , where  $m = 1, 2, 3, \dots$  denotes the first, second and third-nearest neighbor shells. The geometric figures are then indicated by  $f(k, m)$ . The correlation functions are denoted by  $\bar{\Pi}_{k,m}$  and can be calculated by taking the products of the spin variables for the geometric figure  $k$  within a distance  $m$ , and averaging over the sites in the lattice. For a binary random alloy at atomic fraction  $x$  of  $\sigma = 1$  species, the correlation functions are given in Eq. 2.33.

$$\bar{\Pi}_{k,m} = \bar{\Pi}_{k,m}^R = (2x - 1)^k \quad (2.33)$$

The optimum SQS satisfies the relation in Eq. 2.34 as closely as possible.

$$\bar{\Pi}_{k,m}^{SQS} \approx \bar{\Pi}_{k,m}^R \quad (2.34)$$

Eq. 2.34 gives rise to an optimization problem of how to distribute  $N_A$  A-atoms and  $N_B$  B-atoms over  $N = N_A + N_B$  lattice sites in such a way that Eq. 2.34 is satisfied as closely as possible. In the optimization process, choices are required where to truncate the number of geometric figures to include (e.g. include up to triplets) and at what length to truncate the figures (e.g. include up to second nearest-neighbors only). In principle, these parameters are system dependent and no general rules exist what are appropriate choices. Ideally, convergence testing of the physical quantity of interest is performed with respect to these parameters so that a well-informed choice can be made. Various algorithms are available to find the optimum SQS such as exhaustive enumeration [90, 91, 92], simulated annealing and genetic algorithms (GA's) [93]. Traditionally, SQS have been applied for the calculation of bulk properties such as formation energies [94, 95], lattice constants, elastic constants [96, 97] and electronic structure [98, 99]. In this work, SQS are applied also to planar defects, for which several adaptations are required as described in subsequent chapters.

### 2.2.2 Virtual Crystal Approximation

VCA averages different non-local ionic pseudopotentials according to their concentration to yield a single effective ion potential. This method allows for performing DFT calculations on substitutionally disordered systems at the same computational cost as for ordered systems. Any possible short range order is ignored in VCA calculations and each lattice site is decorated with a virtual atom with interpolated properties of the actual species in the alloy. Fine details related to local distortions and relaxations in atomic environments cannot be captured with VCA in general, as atomic size mismatch effects are not

included. A practical advantage of VCA is that several efficient schemes exist to generate pseudopotentials for a given desired alloy concentration. One such scheme that is employed in this work is the Troullier-Martins method for generating norm-conserving pseudopotentials (NCPP's) [51, 100, 101]. NCPP's for alloys are generated using the fhi98PP code [101], by including (non-integer) numbers of  $s$ ,  $p$  and  $d$ -electrons in a way that is representative of the alloy concentration and the species present. In the generation of the pseudopotentials, the number of core and valence states has to be specified, together with the type of exchange-correlation, core cutoff radius and a number of other parameters. Details on the formalism can be found in Ref. [101].

Part II

Results and Discussion

## Chapter 3

# Rhenium and its Alloys: Structure, Elasticity and Ductility

### 3.1 Foreword

In this chapter, the structural properties, elastic properties and intrinsic ductility of Re and its alloys are studied. This study is part of a combined computational and experimental rhenium replacement-effort, in which the goal is to identify new alloys with similar properties as elemental Re, but at a lower material cost. Rhenium's combination of high ductility, high strength and good high-temperature properties is rather unique. The room-temperature ductility in particular is of interest in this work, since it governs how easily the material can be plastically deformed and made into components without fracturing.

Re is among the most expensive refractory metals with prices recently varying from \$ 4 to over \$ 10 per gram as shown in Fig. 3.1 [102]. Further, the worldwide reserve of Re is limited and it is mined in only 20 different places [103], making it a strategically important metal. Due to the limited supply of Re to the markets, its prices also tend to be susceptible to large increases, which is what happened around 2008, according to Fig. 3.1. For these reasons, cost-effective rhenium replacement strategies are of clear interest.

There are several metrics to describe the intrinsic ductility of metals and solid solution-alloys, which are reviewed in the following section. In the literature, several studies have been presented employing intrinsic ductility parameters to investigate the effect of alloying on intrinsic ductility. A wide range of materials has been studied such as magnesium-alloys [104, 105, 106], NiAl-Fe and NiAl-Mn-alloys [107], Mo-alloys [108], W-Re alloys [109] and a range of other transition metal-alloys [110, 111]. Although the 'Re-effect', which refers to creating alloys with small amounts of Re, has been studied quite extensively



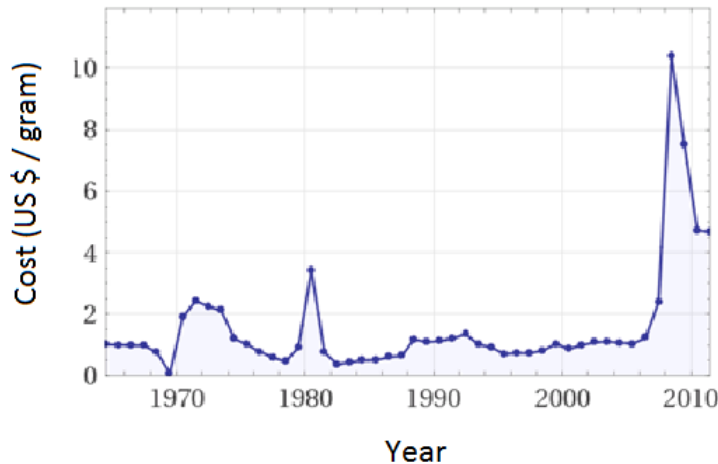


Figure 3.1: The cost of elemental Re in US \$ per gram, with time.

in the literature, little or no attention has been paid to Re-rich alloys, which are the focus of this chapter.

In this chapter, a systematic investigation of the effect of alloying Re with various solutes is performed. Re-based solid solutions are considered and defects are not taken into account initially. It is assumed that all solid solutions are HCP-based, and are formed for example as schematically indicated in Fig. 3.2, with solutionizing at high temperature in the single HCP phase region, followed by quenching upon which a (metastable) HCP solid solution is obtained. We focus in this chapter on alloying Re with transition metal (TM) solutes, as it is expected that combinations of these elements chosen to maintain a  $d$ -band filling close to that characteristic of Re could be effective in retaining high melting temperatures, due to the well-known maximum in the cohesive energy that occurs at approximately half  $d$ -band filling [112, 113, 114]. We thus consider HCP Re- $X$  alloys, with all possible  $3d$ ,  $4d$  and  $5d$  solute elements  $X$ , and calculate by DFT three classes of properties: dilute heats of mixing, single-crystal elastic constants, and structural properties including atomic volume and axial  $c/a$  ratio. Since one of the main attractive features of Re is its low-temperature ductility, we use these DFT results also to study trends in the effects of TM solutes on properties that are expected to correlate with this property. To this end, intrinsic ductility parameters are employed, which are discussed in subsequent sections.

The outline of the rest of this chapter is as follows. First, several intrinsic ductility parameters are reviewed that will be used extensively in the remainder of this work. The computational methodology is discussed next, with particular attention being paid to DFT-settings and the calculations of elastic constants and solute effects on Re-based

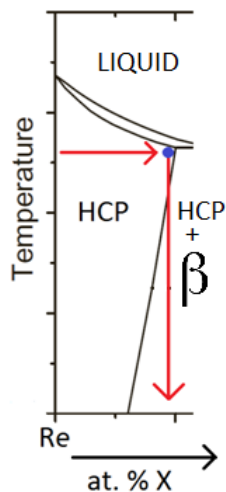


Figure 3.2: Schematic of the alloying strategy for Re replacement in this chapter.

alloys. Results pertaining to structural, elastic and energetic properties of Re-based alloys are presented next, followed by a discussion and interpretation of the results.

Part of the results presented in this chapter, including the figures and tables, were published by Maarten de Jong, David Olmsted, Axel van de Walle and Mark Asta in Physical Review B, 86(22):224101, 2012 [115]. The material is reproduced here with permission of the co-authors and publishers.

## 3.2 Review of Intrinsic Ductility

### 3.2.1 Pugh's criterion

Several methods to model ductility from first principles density-functional-theory (DFT) calculations have been proposed in the literature [116, 117, 118, 17, 119]. In this chapter, we will confine ourselves to a simple ductility parameter  $D$  to perform the screening which is based solely on linear-elasticity, namely the ratio of the single crystal bulk modulus  $K$  to the Voigt-average of the single crystal shear modulus,  $G$ . Hence, we define the ductility parameter as the ratio  $D = K/G$  [116], also known as Pugh's parameter. In HCP metals, this ratio is known to correlate well with relative ductility [17]. A higher  $K/G$ -ratio generally indicates enhanced ductility. This can be understood by realizing that microcrack initiation and propagation requires bond breaking, which becomes more difficult for high values of the bulk modulus,  $K$ . On the other hand, deformation mechanisms that give rise to a ductile response, such as twinning and dislocation movement, are more

prevalent in materials with comparatively low shear moduli  $G$ .

A second property based on elastic constants that can be expected to affect ductility in polycrystalline samples is the elastic anisotropy. Specifically, for systems with highly anisotropic elastic constants, applied loads can lead to stress concentrations at grain boundaries and triple junctions that can contribute to brittle failure [120, 121]. From this standpoint, it is expected that a lower degree of elastic anisotropy should contribute to an enhancement in the ductility of polycrystalline materials. We thus consider the effect of solute additions on elastic anisotropy in Re-based TM alloys, using as a measure of the crystalline two anisotropy parameters introduced recently [122], measuring the anisotropy in the Young's and shear modulus, respectively.

### 3.2.2 Yoo's criterion

Ductility parameters exist that are not based on linear elasticity, but rather take into account dislocation slip on basal and prismatic planes and twinning, which are known to constitute important deformation mechanisms in Re and HCP metals in general [123, 124, 125, 126]. In these models, the energetic competition between the creation of fresh surface (brittle behavior) versus the formation of twins or stacking faults (ductile behavior) is considered [117, 118, 17, 119]. Relative ductility is considered by examining the energetic trade-off between cracking and twinning or the emission of dislocations. Depending on which plastic deformation mechanism is active in a given material (e.g. dislocation glide or twinning), different ductility parameters are proposed. Using a Peierls-analysis, Rice and co-workers [127, 128, 129] proposed a ductility parameter  $D = \gamma_{us}/\gamma_s$ , where  $\gamma_{us}$  represents the unstable stacking fault energy and  $\gamma_s$  represents the surface energy. This ductility parameter aims to capture the ease of dislocation glide versus cracking and is applicable primarily in materials where dislocations are the primary carrier of plasticity. On the other hand, for materials in which twinning is the primary deformation mechanism, Yoo proposed a ductility parameter  $D = \gamma_t/\gamma_s$ , where  $\gamma_t$  denotes the twin boundary energy [17]. The ductility parameter by Yoo is used in this work since twinning is a prevalent deformation mode in Re and in HCP-materials in general. This class of ductility parameters will be considered in Chapter 4.

### 3.2.3 Ideal Strength-Based

The third intrinsic ductility parameter is based on the ideal of ideal strength and elastic instabilities of the perfect crystal. At an atomistic level, the nucleation of a dislocation requires the resolved shear stress on the slip plane to be close to the ideal shear strength of the material. On the other hand the nucleation of a crack requires the local tensile strength perpendicular to the cleavage plane to be close in magnitude to the ideal tensile strength [108]. When an ideal material is loaded in tension perpendicular to the

cleavage plane, it does not necessarily fail in tension in that direction. Instead, the material can become unstable to shear before tensile failure. In that case, the nucleation of dislocations might be expected to occur before the nucleation of cracks and the materials is considered to be intrinsically ductile [130, 131].

In the literature, DFT calculations have been reported that show that W and Mo fail in tension whereas V and Nb fail in shear when pulled along the  $\langle 001 \rangle$  directions of the bcc structures for these materials [108, 132]. These results correlate with experimental observations showing that W and Mo are brittle metals whereas V and Nb are relatively ductile. These observations lend support to the ideal strength-view on intrinsic ductility. Ideal-strength calculations have been used extensively in the literature to study cubic materials [133, 134, 135], however not much work has been performed for HCP metals and alloys, in particular in the context of intrinsic ductility. In Chapter 6, ideal-strength calculations are used to study trends in intrinsic ductility of HCP metals as well as the effect of alloying on the ideal deformation behavior.

### 3.3 Methodology

#### 3.3.1 DFT Calculations

All of the DFT results presented in this work were performed using the projector augmented wave (PAW) method [52, 53], as implemented in the Vienna Ab initio Simulation Package (VASP) [136, 137]. In these calculations use was made of the Perdew-Zunger parametrization of the Ceperly-Alder [138, 34] exchange-correlation energy within the local density approximation (LDA-CA).

An energy cutoff for the plane wave basis set of 450 eV was used. Brillouin zone integrations were performed using Monkhorst-Pack  $k$ -point sampling [139]; in all the total energy calculations, the density of  $k$ -points is chosen such that the number of  $k$ -points in the first Brillouin zone times the number of atoms in the cell was approximately 15,000. Occupation of the electronic states was performed using the Methfessel-Paxton scheme [140], with a smearing width of 0.1 eV. For the structural optimizations, internal coordinates were relaxed until the atomic forces converged to within 0.001 eV/Å. The equilibrium lattice parameters were computed using a conjugate-gradient minimization algorithm, employing the calculated stress tensors. In all calculations, the residual stresses, after the full relaxation, did not exceed 0.05 kBar (5 MPa).

The PAW potential used for Re corresponds to the electron configuration  $5d^56s^2$ , with seven electrons treated explicitly as valence. For all solutes, PAW-potentials corresponding to the nominal valence electrons were employed. For Re and the alloy supercells (see below) the results presented, were obtained using non-magnetic calculations. For so-

lute species Fe, Co, Ni, Cr and Mn spin-polarization was considered although non-magnetic states were obtained upon structural relaxation. In calculations of the dilute heats of solution, the reference energies for elemental Cr, Mn, Fe, Co or Ni were also performed employing spin-polarized calculations; for Fe, Co and Ni a ferromagnetic ground state was obtained, while for Cr and Mn, the relaxed structure converged to non-magnetic solutions.

### 3.3.2 Elastic Constant Calculations

The calculation of the elastic constants was performed using as a starting point the relaxed structures obtained from the calculations described in the previous sub-section. For each such structure 24 unique deformation mappings are constructed, corresponding to six independent deformation modes. In the first set,  $\varepsilon_{11}$ ,  $\varepsilon_{22}$  and  $\varepsilon_{33}$  corresponds to the uniaxial deformations whereas the second,  $\varepsilon_{12}$ ,  $\varepsilon_{23}$ ,  $\varepsilon_{13}$  corresponds to the simple shear deformations. For calculating the elastic constants, four values for the strain ( $-\varepsilon_0$ ,  $-\frac{1}{2}\varepsilon_0$ ,  $+\frac{1}{2}\varepsilon_0$ ,  $+\varepsilon_0$ ) were applied for each of the six deformation modes. For uniaxial deformation, we used  $\varepsilon_0 = 0.01$  and for simple shear  $\varepsilon_0 = 0.004$ . Each of the deformations is characterized by a deformation gradient tensor  $\mathbf{F}$ . The Green-Lagrange strain tensor  $\mathbf{E}$  (which reduces to the linear strain tensor for small strains) is calculated according to Eq. 3.1.

$$\mathbf{E} = \frac{1}{2} (\mathbf{F}^T \mathbf{F} - \mathbf{I}) \quad (3.1)$$

The components of the Cartesian stress tensor are calculated from first principles, while allowing for ionic relaxations. Subsequently, all components of the elastic tensor can be determined by a least squares-fit of the calculated stresses to the applied Green-Lagrange strain. This means every elastic constant is fit to a total of five points, including the fully relaxed (zero stress, zero strain) configuration.

Several tests were performed to estimate the numerical precision of the calculated elastic constants. In the first set of tests we considered the convergence with respect to  $k$ -points and plane wave energy-cutoff, giving an estimated precision of about 9.5 GPa for all elastic moduli presented below. Further, the fitting procedure for the elastic constants was examined to test the assumption of linear stress-strain relations. Specifically, we compared the results obtained for the range of deformations given above to values obtained by fitting to a more limited range of strains:  $(-\varepsilon_0, 0, +\varepsilon_0)$ . It was found that the consideration of this more limited range of strains led to very similar results for the elastic constants, differing by less than 1.5 GPa, compared to the values obtained from the expanded range of strains given above. A final check of the accuracy of the elastic constants was performed by comparing the symmetry of the calculated elastic tensor to the theoretical symmetry, as dictated by the hcp structure. To this end, the calculated elastic tensor is projected onto the closest fourth-order elastic tensor exhibiting hcp symmetry. This method [141, 142, 143] effectively minimizes the Euclidean distance between the calculated elastic tensor and the tensor on which the calculated elastic tensor is projected.

For the first principles-parameters used in this study, we found that all components of the calculated elastic tensor were converged to within 2.6 GPa of the closest tensor exhibiting the underlying hcp symmetry.

For the calculation of the ductility parameter  $K/G$  the bulk modulus  $K$  is determined from the calculated single-crystal elastic constants through the relation [144]:

$$K = \frac{2(C_{11} + C_{12}) + 4C_{13} + C_{33}}{9}. \quad (3.2)$$

The Voigt average of the shear modulus  $G$  is calculated from the single-crystal elastic constants using the following expression [144]:

$$G = \frac{(C_{11} + C_{33} - 2C_{13} - C_{66})/3 + 2C_{44} + 2C_{66}}{5} \quad (3.3)$$

From the convergence tests described above, the numerical precision of the calculated values of  $K/G$  is estimated to be within about 2% of the values given below.

To investigate the degree of elastic anisotropy we make use of two parameters,  $f_E$  and  $f_G$ , introduced in Ref. [145]. These parameters measure respectively the anisotropy of the Young's modulus and shear modulus, and are defined in terms of the elastic compliances ( $S_{ij}$ ), as follows:

$$f_E = S_{11}/S_{33} \quad (3.4)$$

$$f_G = (S_{44} + 2S_{11} - 2S_{12})/2S_{44} \quad (3.5)$$

Values of  $f_E$  and  $f_G$  equal to one correspond to elastically isotropic solids, while deviations from unity provide a measure of elastic anisotropy.

### 3.3.3 Supercell Models for Alloys

To study the effects of alloying Re with  $3d$ ,  $4d$  and  $5d$  TM solutes, we employ a  $2 \times 2 \times 2$  HCP supercell containing 16 total atoms. A single Re atom is substituted by a TM atom  $X$ , yielding composition  $\text{Re}_{15}\text{X}_1$ . For each such supercell, structural relaxations were performed, and the results used to compute three quantities: the solute expansion coefficients  $\eta_a$  and  $\eta_c$ , and the heat of solution  $\Delta H_{\text{sol}}$ . These latter quantity is computed as follows:

$$\Delta H_{\text{sol}} = E(\text{Re}_{15}\text{X}) - 15E(\text{Re}) - E(\text{X}) \quad (3.6)$$

where  $E(\text{Re}_{15}\text{X})$  is the energy of the  $\text{Re}_{15}\text{X}$  supercell, while  $E(\text{Re})$  and  $E(\text{X})$  denote the energies per atom of pure Re and  $X$  in their relaxed equilibrium crystal structures, respectively. The solute expansion coefficients are computed as:

$$\eta_a \equiv \partial \ln(a)/\partial x \approx 16 [a(\text{Re}_{15}\text{X}) - a(\text{Re})] / a(\text{Re}) \quad (3.7)$$

$$\eta_c \equiv \partial \ln(c)/\partial x \approx 16 [c(\text{Re}_{15}\text{X}) - c(\text{Re})] / c(\text{Re}) \quad (3.8)$$

where  $x$  denotes the mole fraction of the solute,  $a(\text{Re}_{15}\text{X})$  and  $c(\text{Re}_{15}\text{X})$  denote the lattice parameters derived from the relaxed 16-atom supercell, and  $a(\text{Re})$  and  $c(\text{Re})$  correspond to the lattice parameters for pure Re. The relaxed supercells are also used as the starting point for calculations of the single-crystal elastic constants, following the procedure described in the previous sub-section.

## 3.4 Results

In this section we present the results of calculated structural, energetic and elastic properties for pure Re and Re-X transition-metal alloys and compare to previously published computational and experimental results. Each of the calculated properties for the alloys considered in this work is shown to display clear trends with the number of  $d$  electrons in the TM solutes. These trends are discussed in the context of canonical  $d$ -band theory in the next section.

### 3.4.1 Structural and Elastic Properties of Pure Rhenium

In Table 3.1 the values of the structural parameters and elastic moduli computed in the present work for elemental Re are compared to results from previous computational studies and experimental measurements. Considering first the comparison between our results and experiments, we see that the calculated  $a$  and  $c$  lattice constants are underestimated by approximately 0.7%, while the elastic moduli are overestimated by approximately 8%, except for  $C_{13}$  which shows a larger disagreement with experiments of about 20%. This level of agreement is viewed to be reasonable given that the present calculations made use of the LDA, which generally shows a tendency to overbind. We note, however, that the only other previous calculation that made use of the LDA-CA exchange-correlation potential [146] shows slightly better agreement with experiment for  $a$  and  $c$  lattice parameters, while the values of  $C_{11}$ ,  $C_{33}$  and  $C_{44}$  are considerably larger than those obtained in the current work and all other previous calculations listed in Table 3.1.

By contrast, the two other sets of LDA results [147, 148] listed in Table 3.1 feature elastic moduli which are on average 6 and 16% smaller than the values calculated in the present work, and closer to experimental measurements. The differences with the present results may be due to the different parameterizations of the LDA used in the previous LDA calculations: the work in Ref. [147] and [148] made use of the Vosko, Wilk and Nusair (VWN) [31] and Hedin-Lundqvist (HL) [149] parametrizations of LDA, respectively. The calculated results listed in Table 3.1 [147, 148] obtained with the generalized-gradient approximation of Perdew *et al.* [150] (GGA-PBE) show the expected trend featuring larger lattice parameters and smaller elastic moduli, relative to the present LDA-CA results.

Overall, the best level of agreement between experiment and theory appears to be obtained from the GGA-PBE results of Ref. [148]. In what follows we will focus on the changes in structural and elastic properties associated with the addition of TM solutes to hcp Re, and the trends which these changes display as a function of bandfilling. For this purpose, the slightly lower accuracy of the LDA-CA exchange-correlation is not expected to affect the main conclusions of the work. Moreover, since much of this work involves investigating dimensionless alloy parameters such as the ductility parameter  $K/G$ , it is expected that systematic biases between GGA and LDA will not affect the overall results strongly.



Table 3.1: Structural and elastic properties of hcp Re, based on the computational and experimental (Exp.) methods listed in the first column. The units for the reported values of lattice constants ( $a$  and  $c$ ), atomic volume ( $\Omega$ ), and elastic moduli ( $C_{ij}$ ) are Å, Å<sup>3</sup>, and GPa, respectively. For the lattice parameters and atomic volume, experimental values extrapolated to zero temperature, using reported thermal expansion coefficients, are given in parentheses.

| Method                   | $a$     | $c$     | $c/a$ | $\Omega$ | $C_{11}$ | $C_{33}$ | $C_{12}$ | $C_{13}$ | $C_{44}$ | $K/G$ | $f_E$ | $f_G$ |
|--------------------------|---------|---------|-------|----------|----------|----------|----------|----------|----------|-------|-------|-------|
| NCPP, GGA-PBE [147, 49]  | 2.762   | 4.442   | 1.608 | 14.67    | 607      | 705      | 307      | 209      | 164      | 2.14  | 1.40  | 1.05  |
| NCPP, LDA-VWN [147]      | 2.756   | 4.437   | 1.61  | 14.58    | 623      | 731      | 327      | 218      | 170      | 2.18  | 1.45  | 1.07  |
| FLMTO, LDA-CA [146, 151] | 2.748   | 4.474   | 1.628 | 14.62    | 837      | 895      | 293      | 217      | 223      | 1.68  | 1.14  | 0.91  |
| FLAPW, LDA-HL [148, 152] | 2.750   | 4.442   | 1.615 | 14.54    | 605      | 650      | 235      | 195      | 175      | 1.83  | 1.14  | 0.97  |
| FLAPW, GGA-PBE [148]     | 2.794   | 4.513   | 1.615 | 15.25    | 640      | 695      | 280      | 220      | 170      | 2.02  | 1.20  | 0.97  |
| PAW, LDA-CA (This work)  | 2.741   | 4.422   | 1.613 | 14.39    | 672      | 740      | 309      | 252      | 176      | 2.16  | 1.18  | 0.98  |
| Exp. (X-ray) [153]       | 2.762   | 4.455   | 1.613 | 14.71    | ×        | ×        | ×        | ×        | ×        | ×     | ×     | ×     |
|                          | (2.756) | (4.448) | 1.613 | (14.63)  | ×        | ×        | ×        | ×        | ×        | ×     | ×     | ×     |
| Exp. (X-ray) [154]       | 2.761   | 4.456   | 1.614 | 14.70    | ×        | ×        | ×        | ×        | ×        | ×     | ×     | ×     |
|                          | (2.755) | (4.449) | 1.614 | (14.63)  | ×        | ×        | ×        | ×        | ×        | ×     | ×     | ×     |
| Exp. (X-ray) [155]       | ×       | ×       | ×     | ×        | 619      | 687      | 278      | 204      | 162      | 2.02  | 1.25  | 0.98  |
| Exp. (Ultrasound) [156]  | ×       | ×       | ×     | ×        | 616      | 683      | 273      | 206      | 161      | 2.02  | 1.24  | 0.97  |

### 3.4.2 Structural properties of Re-based transition metal alloys

Table 3.2 lists the calculated values of the solute expansion coefficients ( $\eta_a = \partial \ln(a)/\partial x$  and  $\eta_c = \partial \ln(c)/\partial x$ ) for each of the  $3d$ ,  $4d$  and  $5d$  solutes  $X$  considered. Trends in associated structural properties are plotted as a function of the number of  $d$  electrons for the solute species in Figs. 3.3 and 3.4.

Figure 3.3 plots the volume expansion coefficient  $\eta_V = \partial \ln(V)/\partial x = 2\eta_a + \eta_c$  as a function solute  $d$ -band filling. A nearly parabolic trend is observed for each of the  $3d$ ,  $4d$  and  $5d$  series, with minima corresponding to the Co/Rh/Ir column. All of the  $3d$  solutes except Sc and Ti lead to a decrease in molar volume, with the most negative values corresponding to Co. The values for the  $4d$  and  $5d$  elements are comparable; most of these solutes show positive values of  $\eta_V$ , with Tc, Ru/Os, Rh/Ir, Pd/Pt giving weakly negative values.

Figure 3.4 plots the axial  $c/a$  ratio of the 16-atom  $\text{Re}_{15}\text{X}$  cells as a function of the solute  $d$ -band filling. In this case a general trend is observed for a decreasing value of  $c/a$  going from the left to the right in the  $d$ -band series. The trend is nearly monotonic, with some exceptions at the ends of the series on either side (La, Cd and Hg). It is noteworthy that pure Re has a value of  $c/a \approx 1.61$  which is roughly one percent lower the ideal value of  $\sqrt{8/3} \approx 1.63$  corresponding to optimal close packing. Solutes to the left of Re in the periodic table are seen to increase  $c/a$ , making it closer to ideal, while those to the right of Re lower  $c/a$ .

Experimental data on the structural parameters of Re-based alloys is scarce and the effects of alloying with different solutes is not well-established. However, for the binary systems Re-W, Re-Ir and Re-Pt, our results regarding the trends in the structural parameters are consistent with the those identified in some early experimental efforts [157]. In Ref. [157], the lattice parameters,  $c/a$ -ratio and atomic volume of Re-based alloys were experimentally determined. Solute elements W, Ir and Pt were added in concentrations between 5 and 40 at.% while maintaining the hcp phase. Consistent with the current work, Ir and Pt were found to decrease the  $c/a$ -ratio whereas W leads to an increase. The trends in the variation of volume with bandfilling, as found in Ref. [157] are confirmed in the present work as well. Alloying with W is found to lead to a positive lattice expansion coefficient in elemental Re, whereas both Ir and Pt show negative lattice expansion coefficients. Pt is known experimentally [157] to exhibit positive volume expansion coefficients when added to Re in concentrations exceeding about 40 at.%. These observations cannot be compared to results from the present work in which much lower solute concentrations have been studied.

Table 3.2: Calculated solute lattice expansion coefficients  $\eta_a$  and  $\eta_c$  and heat of solution  $\Delta H_{\text{sol}}$  (kJ / mol solute) of solutes in rhenium in the dilute limit for full structural relaxations.

|           |                         |       |        |        |        |        |        |        |        |        |        |
|-----------|-------------------------|-------|--------|--------|--------|--------|--------|--------|--------|--------|--------|
| <i>3d</i> |                         | Sc    | Ti     | V      | Cr     | Mn     | Fe     | Co     | Ni     | Cu     | Zn     |
|           | $\eta_a$                | 0.047 | -0.013 | -0.050 | -0.071 | -0.081 | -0.084 | -0.086 | -0.071 | -0.038 | -0.001 |
|           | $\eta_c$                | 0.186 | 0.098  | 0.011  | -0.047 | -0.089 | -0.114 | -0.118 | -0.123 | -0.119 | -0.089 |
|           | $\Delta H_{\text{sol}}$ | 100.7 | 17.6   | 37.4   | 64.9   | 28.6   | 3.9    | -5.2   | 2.57   | 87.6   | 93.1   |
| <i>4d</i> |                         | Y     | Zr     | Nb     | Mo     | Tc     | Ru     | Rh     | Pd     | Ag     | Cd     |
|           | $\eta_a$                | 0.117 | 0.073  | 0.024  | 0.004  | -0.010 | -0.011 | -0.012 | 0.005  | 0.044  | 0.078  |
|           | $\eta_c$                | 0.373 | 0.277  | 0.164  | 0.062  | -0.018 | -0.063 | -0.068 | -0.058 | -0.036 | 0.0236 |
|           | $\Delta H_{\text{sol}}$ | 268.2 | 99.7   | 53.1   | 46.3   | -1.8   | -25.4  | -58.3  | -3.0   | 167.2  | 206.5  |
| <i>5d</i> |                         | La    | Hf     | Ta     | W      | Re     | Os     | Ir     | Pt     | Au     | Hg     |
|           | $\eta_a$                | 0.184 | 0.052  | 0.020  | 0.001  | 0      | 0.001  | 0.005  | 0.020  | 0.055  | 0.092  |
|           | $\eta_c$                | 0.348 | 0.249  | 0.170  | 0.078  | 0      | -0.048 | -0.067 | -0.057 | -0.036 | 0.032  |
|           | $\Delta H_{\text{sol}}$ | 403.9 | 54.2   | 35.2   | 47.2   | 0      | -27.3  | -85.5  | -72.2  | 82.7   | 212.6  |

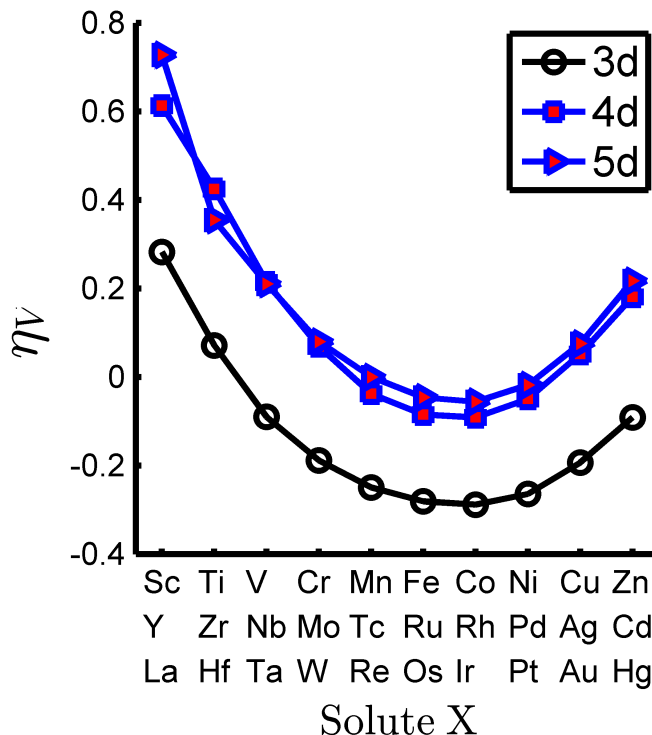


Figure 3.3: Volume solute expansion coefficient as a function of  $3d$ ,  $4d$  or  $5d$  solute element for alloy composition  $\text{Re}_{15}\text{X}_1$ .

### 3.4.3 Energetics of Re-based transition metal alloys

The energetics of alloying is examined through consideration of the dilute heat of solution  $\Delta H_{sol}$  defined in Eq. 3.6. Results for this property are listed in Table 3.2 and plotted in Fig. 3.5. The heats of solution for the  $3d$ ,  $4d$  and  $5d$  elements with 3 or 4  $d$  electrons (V, Nb, Ta, Cr, W, Mo) are weakly positive, while elements further to the left in the periodic table feature increasingly positive values. The  $4d$  and  $5d$  elements having 5,6 or 7  $d$  electrons (Ru, Os, Rh, Ir, Pd, Pt), all yield negative heats of solution, whereas the corresponding  $3d$  elements (Fe, Co, Ni) show weakly positive values. Moving further to the right in the periodic table, to elements with 8, 9 or 10  $d$  electrons, we observe again strongly positive heats of solution for all of the  $3d$ ,  $4d$  and  $5d$  solutes.

Experimental data on the thermodynamics of Re-rich alloys is relatively scarce. However, the present results can be compared to recent related computational studies [158, 159], as well as free-energy models derived from phase-diagram assessments performed within the framework of the Calculation of Phase Diagrams (CALPHAD) formalism [24].

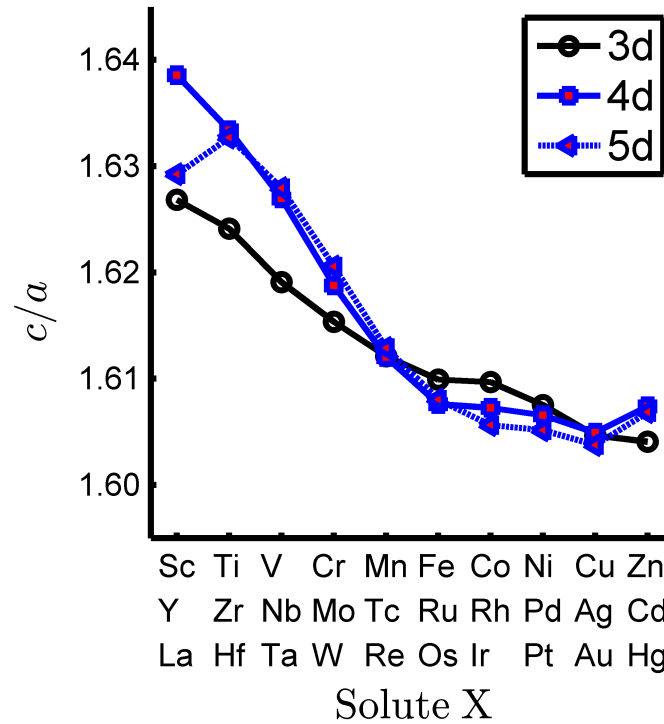


Figure 3.4: Variation in  $c/a$  as a function of 3d, 4d or 5d solute element for alloy composition  $\text{Re}_{15}\text{X}_1$ .

To enable these comparisons, it is useful to consider the dilute heat of mixing  $\Delta H_{mix}$  which is defined analogously to Eq. 3.6 but with the  $E(X)$  defined as the energy of element  $X$  in the hcp structure (rather than its lowest-energy structure if different than hcp). A negative value of  $\Delta H_{mix}$  is indicative of an ordering tendency, such that the lowest-energy atomic configurations on the hcp parent structure would be expected to be ordered compounds. In the computational work reported in Refs. [158, 159], Re-rich  $\text{D0}_{19}$ -prototype groundstate structures were identified with compositions  $\text{Re}_3\text{Pd}$ ,  $\text{Re}_3\text{Pt}$ ,  $\text{Re}_3\text{Rh}$ ,  $\text{Re}_3\text{Ir}$ ,  $\text{Re}_3\text{Co}$ . This is consistent with the results found in this work, in which these systems were found to have large negative heats of mixing. Another hcp-based superstructure, B19, is identified as a ground in the Re-Os system, for which we also find a negative heat of mixing.

Published CALPHAD models for the Re-W and Re-Ta system [24] feature negative excess Gibbs energies for both the Re-Ta and Re-W HCP phases. The mixing energy computed in the present work for Re-W with composition  $\text{Re}_{15}\text{W}_1$  is -2.86 kJ/mol, which compares reasonably well to the value of -7.986 kJ/mol from the assessment in Ref. [24]. For Re-Ta, however, the published free energy model predicts a mixing energy of -31.286

kJ/mol for  $\text{Re}_{15}\text{Ta}_1$  composition, which is in sharp contrast to the present calculated value of +4.85 kJ/mol.

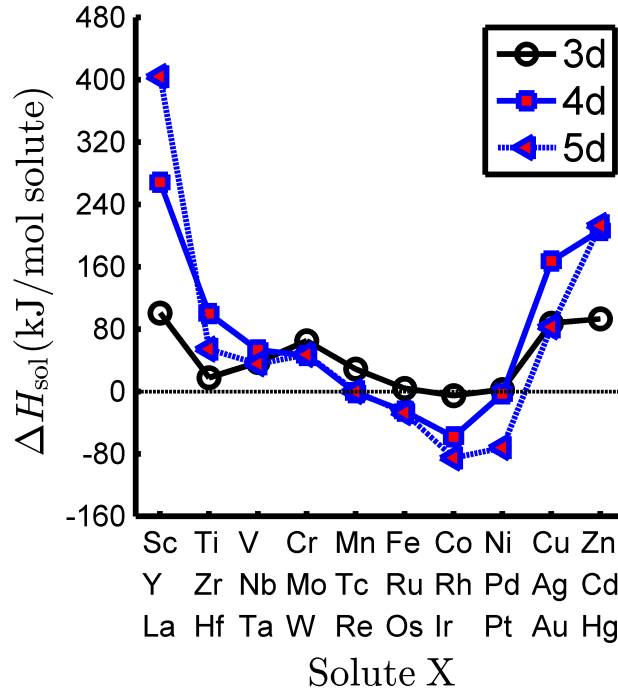


Figure 3.5: Heat of solution as a function of  $3d$ ,  $4d$  or  $5d$  solute element for alloy composition  $\text{Re}_{15}\text{X}_1$ .

### 3.4.4 Elastic properties of Re-based transition-metal alloys

Figure 3.6 plots the calculated values of  $K$ ,  $G$  and the intrinsic ductility parameter  $D = K/G$  for Re-X TM alloys as a function of the number of  $d$  electrons for the solutes (X). Both  $K$  and  $G$  are shown to display concave and roughly parabolic trends, with maximum values occurring in the Fe/Ru/Os column for  $K$  and in the Co/Rh/Ir column for  $G$ . The  $K/G$ -ratio displays a convex and roughly parabolic dependence on solute  $d$  electron count, with a minimum in the Co/Rh/Ir column. Since higher values of  $K/G$  correlate with higher intrinsic ductility, the results in Fig. 3.6(c) suggest that the addition of solutes to the left or right of Re in the periodic table should increase and decrease the intrinsic ductility, respectively. It is interesting to note that this trend is qualitatively similar to that displayed by the axial  $c/a$  ratio in Fig. 3.4. All independent symmetrized elastic constants of the Re-X TM alloys studied in this work are also included numerically in Table 3.3.

Table 3.3: Independent elastic constants of hcp  $\text{Re}_{15}\text{X}_1$  alloys. The unit of the reported values is GPa.

|    | X  | $C_{11}$ | $C_{33}$ | $C_{12}$ | $C_{13}$ | $C_{44}$ |
|----|----|----------|----------|----------|----------|----------|
|    | Sc | 514.9    | 513.6    | 329.0    | 249.6    | 100.8    |
|    | Ti | 588.6    | 601.3    | 311.4    | 254.8    | 120.5    |
|    | V  | 627.9    | 650.0    | 305.5    | 261.8    | 138.6    |
|    | Cr | 644.2    | 692.9    | 304.4    | 258.8    | 155.3    |
| 3d | Mn | 656.2    | 717.4    | 307.2    | 248.0    | 168.0    |
|    | Fe | 648.6    | 703.2    | 300.9    | 257.2    | 178.8    |
|    | Co | 653.8    | 716.6    | 305.4    | 247.6    | 183.0    |
|    | Ni | 643.9    | 724.7    | 310.2    | 241.8    | 181.9    |
|    | Cu | 614.5    | 700.6    | 312.0    | 252.2    | 169.3    |
|    | Y  | 506.8    | 425.1    | 304.1    | 232.5    | 97.4     |
|    | Zr | 554.9    | 524.7    | 311.2    | 243.1    | 116.2    |
|    | Nb | 611.7    | 620.3    | 306.1    | 252.9    | 138.3    |
|    | Mo | 650.4    | 688.0    | 303.5    | 253.3    | 159.6    |
| 4d | Tc | 667.9    | 731.9    | 306.1    | 249.6    | 176.7    |
|    | Ru | 665.9    | 723.5    | 300.5    | 257.3    | 187.4    |
|    | Rh | 662.7    | 719.4    | 293.7    | 259.5    | 193.8    |
|    | Pd | 649.4    | 732.6    | 299.9    | 246.1    | 188.2    |
|    | Ag | 612.1    | 692.2    | 298.8    | 249.1    | 174.1    |
|    | La | 502.6    | 323.1    | 269.9    | 228.5    | 106.7    |
|    | Hf | 560.4    | 544.0    | 315.4    | 247.5    | 116.4    |
|    | Ta | 614.3    | 616.6    | 308.4    | 254.8    | 137.5    |
|    | W  | 655.1    | 697.9    | 309.1    | 253.4    | 159.6    |
| 5d | Re | 671.8    | 739.6    | 309.4    | 253.5    | 176.0    |
|    | Os | 683.0    | 739.3    | 305.3    | 256.1    | 191.7    |
|    | Ir | 680.0    | 730.2    | 288.2    | 266.8    | 204.3    |
|    | Pt | 670.2    | 750.9    | 300.6    | 247.8    | 198.6    |
|    | Au | 631.3    | 713.1    | 303.1    | 251.0    | 186.7    |

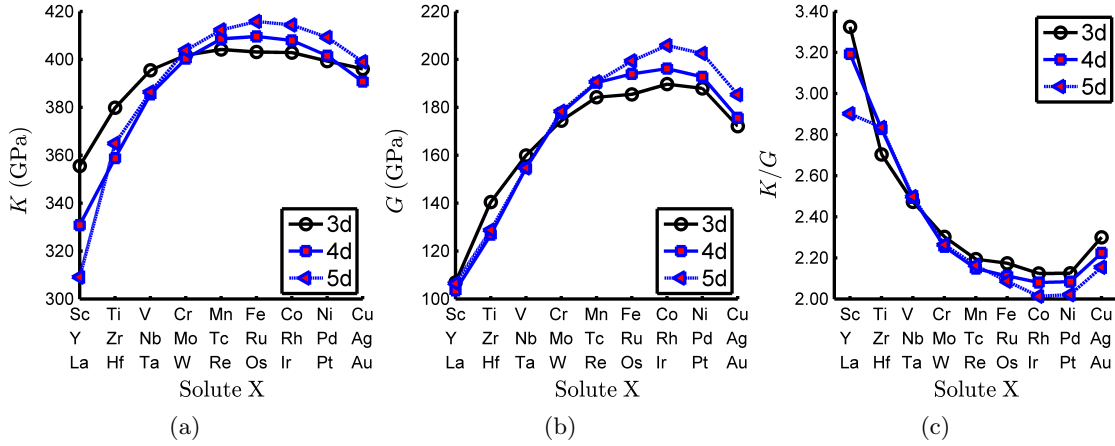


Figure 3.6: Variation of (a)  $K$ , (b)  $G$  and (c)  $K/G$  as a function of  $3d$ ,  $4d$  or  $5d$  solute element for alloy composition  $\text{Re}_{15}\text{X}_1$ .

Trends in the elastic anisotropy are shown in Fig. 3.7, which plots one minus the anisotropy parameters  $f_E$  and  $f_G$  for the Young's modulus and shear modulus, respectively, as defined in Eq. 3.4 and 3.5. An isotropic material corresponds to  $f_E$  and  $f_G$  values of one, so that deviations of  $1 - f_G$  and  $1 - f_E$  in Fig. 3.7 measure the degree of elastic anisotropy. Alloying of Re with neighboring elements to the left and right of the periodic table are seen to decrease slightly the degree of anisotropy in the Young's modulus. Alloying with elements at the end of the TM series increase the anisotropy in  $f_E$ , while the elements Sc, Y and La, on the left of the TM series, show a considerable scatter in  $f_E$ . The effects of alloying on  $f_G$  are seen to be weaker overall, relative to  $f_E$ . The anisotropy in the shear modulus is seen to be lowest for pure Re, and alloys with its isoelectronic solute elements; alloying with elements to the right or left are seen to weakly increase the magnitude of the deviation of  $f_G$  from unity.

### 3.5 Discussion

The DFT-calculated properties for  $\text{Re}_{15}\text{X}$  alloys presented in the previous section are shown to display pronounced trends with the number of  $d$  electrons in the TM solute atoms  $X$ . In this section we examine these trends further within the framework of canonical  $d$ -band theory.

We consider first the variation in atomic volume, which is shown to display a parabolic-like variation with band filling in Fig. 3.3 for each of the  $3d$ ,  $4d$  and  $5d$  periods.



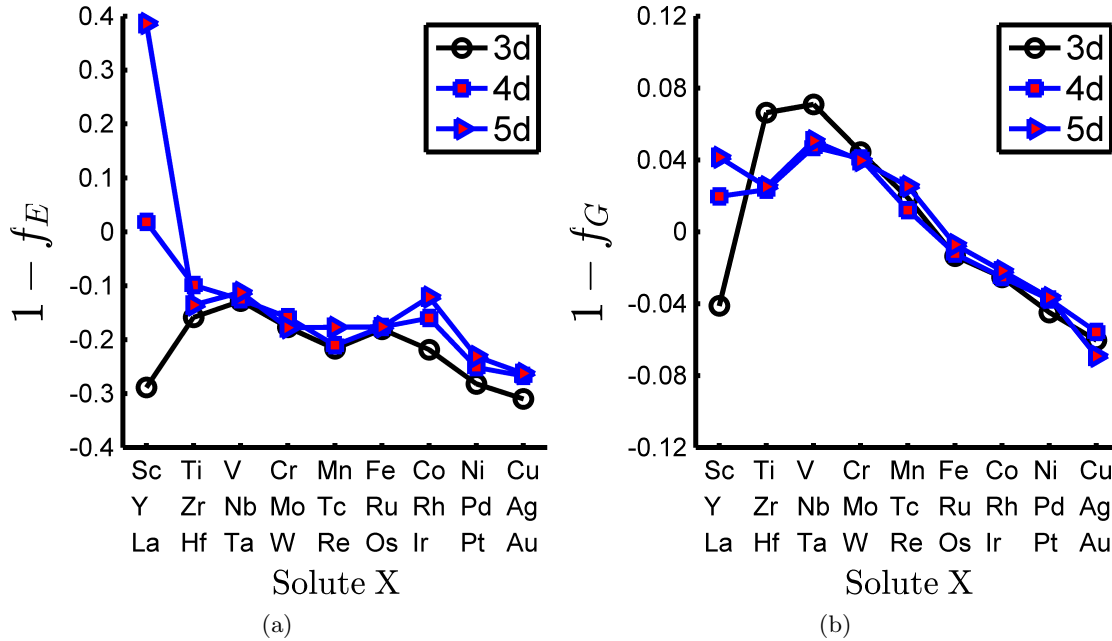


Figure 3.7: Variation of the elastic anisotropy parameters  $f_E$  (a) and  $f_G$  (b) as a function of  $3d$ ,  $4d$  or  $5d$  solute element for alloy composition  $\text{Re}_{15}\text{X}_1$ .

This can be explained readily from the well-known trends in the atomic volumes in the elemental transition metals in their respective equilibrium structures, which vary approximately parabolically with band filling [160, 161, 162]. Given that the alloys considered in the present work are substitutional and dilute in nature, Vegard's law (i.e., atomic volume of an alloy varying linearly with concentration) is expected to be a reasonable assumption, such that alloying with solutes with sizes increasingly larger (smaller) than Re should lead to increasingly larger increases (decreases) in atomic volume of the alloy.

We consider next the calculated trend in the axial  $c/a$ -ratio, which is shown in Fig. 3.4 to decrease almost monotonically with the number of  $d$  electrons for the solute atoms. In tight-binding, canonical  $d$ -band models of the electronic structure of hcp transition metals [163, 164, 165, 166] the bond order between neighbors within and out of the basal plane is decomposed into  $dd\sigma$ ,  $dd\pi$  and  $dd\delta$  two-center hopping-integral contributions. Bonding contributions between neighbors in the basal plane and out of the basal plane are denoted by  $\sigma_1, \pi_1, \delta_1$  and  $\sigma_2, \pi_2, \delta_2$ , respectively. Starting at half band filling, the  $\sigma_1$  and  $\sigma_2$  bonding weakens with a decrease in the number of  $d$  electrons, whereas the in-plane bonding  $\pi_1$  is enhanced while the  $\pi_2$  bonding levels off (the  $\delta$  bonding is relatively insignif-

icant) [163]. This implies that the bonding in the basal plane gets reinforced with respect to the bonding out of the basal plane with decreasing band filling, which is qualitatively consistent with our finding that the  $c/a$  ratio of Re increases when alloyed with TM solutes to the left in the periodic table. Additionally, the  $\pi_1$  and  $\pi_2$  bond orders cross at almost exactly the band filling of Re. Consequently, as the band filling is increased, starting from this crossover point, the  $\pi_2$  bonding starts dominating over  $\pi_1$ , which is expected to lead to the contraction of the  $c$ -direction relative to the in-plane lattice spacing ( $a$ ). This is consistent with the present results which show a decrease in  $c/a$  ratio when Re is alloyed with solutes to the right in the periodic table.

Trends in the elastic constants of the pure transition metals in their equilibrium structures with band filling have been fairly well established [167]. Bulk moduli  $K$  of the  $3d$ ,  $4d$  and  $5d$  transition metals have been predicted using canonical  $d$ -band theory by Pettifor and these trends have been confirmed by other authors, e.g. Rose and Shore [168]. In transition metals, the general trend is for the bulk modulus to reach a maximum at approximately the Re or Os column of the periodic table. More specifically, for the  $5d$  elements, the maximum bulk modulus seems to occur at band filling slightly higher than Re. Near the maximum, the behavior of the bulk modulus with band filling is approximately parabolic. On the other hand, both the Voigt-average  $G$  and the Reuss-average of the shear modulus of the elemental transition metals are known to exhibit different behavior with band filling [169]. Specifically, for the elemental  $5d$  transition metals, it is known that  $G$  increases almost linearly, varying by about 40 % with increasing band filling from W to Re to Os and finally to Ir. Since  $K$  levels out in the W-Re-Os band filling regime, whereas  $G$  monotonically increases, these observations are consistent with the present work showing that  $K/G$  decreases (increases) when alloying Re with solute atoms to the right (left) in the periodic table.

The variation of the bulk modulus and the Voigt average of the shear modulus of  $\text{Re}_{15}\text{X}_1$  alloys with band filling is shown in Figs. 3.6(a) and 3.6(b), respectively. These quantities approximately follow the same trend as those of the pure transition metals with band filling: approximately parabolic behavior with a maximum at higher band filling than Re. Interestingly, the higher ductility parameter from Re-based alloys with lower band filling than Re is not caused by an increase of  $K$  and a decrease of  $G$ , as one might expect but merely by a relatively lower decrease in  $G$  compared to  $K$  for lower band filling than Re. For example, the Re-based Re-La alloy has a value for  $K$  which is about 25 % lower than for Re, whereas  $G$  decreases by nearly 50 %, yielding an increase of the ductility parameter.

Canonical  $d$ -band theory can be used to outline the trends in the energetics of Re-based alloys as follows. Within this framework, the enthalpy of formation of a transition metal alloy from the pure elements can be decomposed in 4 physically distinct parts [112]: i) a contribution from the transfer of electrons to equalize the Fermi-level which is always

negative, ii) a contribution that stems from the difference in DOS-bandwidth of the pure elements, which can be either positive or negative, iii) a contribution that comes from the change of shape of the DOS when alloying, and iv) a contribution that comes from Coulomb energy due to charge transfer. In the simplest model, only the first 2 contributions are taken into account. Continuing along these lines, the heat of formation for a binary transition metal alloy  $A_xB_{1-x}$  can be expressed [170] as in Eq. 3.9.

$$E_{\text{form}} = -\frac{Z_d(1 - Z_d/10)}{2}W_d + x\frac{Z_{dA}(1 - Z_{dA}/10)}{2}W_{dA} + (1 - x)\frac{Z_{dB}(1 - Z_{dB}/10)}{2}W_{dB} \quad (3.9)$$

The DOS-bandwidth of the alloy  $A_xB_{1-x}$  is denoted by  $W_d$ , whereas the DOS-bandwidths for the pure elements A and B are given by  $W_{dA}$  and  $W_{dB}$ , respectively. The number of electrons in the  $d$ -band for the alloy and elements A and B is given by  $Z_d$ ,  $Z_{dA}$  and  $Z_{dB}$ , respectively.

The parameters appearing in Eq. 3.9 can be computed from DFT calculations. However, for the purposes of the present qualitative analysis we use the published muffin-tin-orbital values for transition metals [170] to compare with the trends shown in Fig. 3.5. Using the theory outlined above based on canonical  $d$ -band theory, we have obtained the heat of solution for various Re-based  $5d$  transition metal alloys shown in Fig. 3.8. Comparing the DFT-calculated heat of solution from Fig. 3.5 to the quantities computed from canonical  $d$ -band theory in Fig. 3.8, it is seen that the trends in the heat of solution are predicted correctly. The sign is not predicted consistently with DFT in all cases, although the trends with the deep minimum to the right of Re and the higher values to the left are present. The actual values of the heat of solution are off by factors of between 2 and 5 which is not unreasonable considering the approximations inherent in the model.

### 3.6 Summary and Conclusions

In summary, the present work has involved a computational study of the structural, energetic and elastic properties of hcp rhenium-based transition-metal alloys. Trends in the atomic volume, axial  $c/a$  ratio, elastic constants and formation energies of  $\text{Re}_{15}\text{X}$  alloys are investigated for all  $3d$ ,  $4d$  and  $5d$  solute species X. Each of the calculated properties show clear trends with band filling that are well described by the  $d$  band theory of transition-metal bonding.

The practical interest in Re-based materials is associated with the combination of their high melting points and good low-temperature ductility. Thus, in the context of

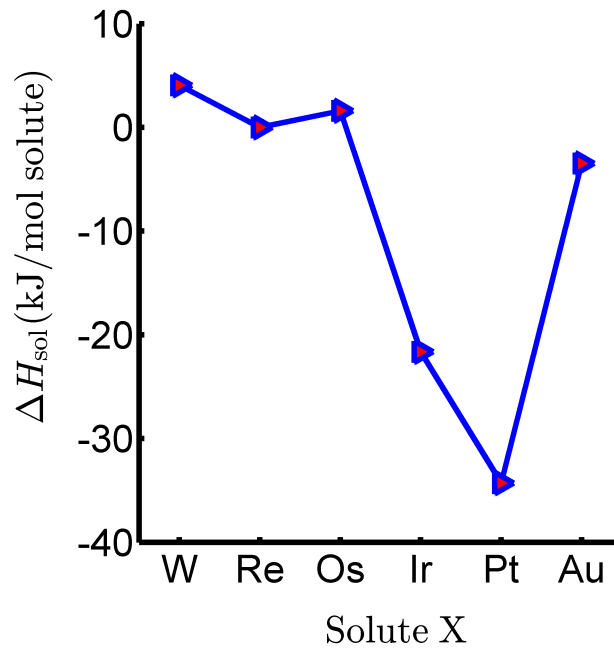


Figure 3.8: Canonical  $d$ -band heat of solution as a function of various  $5d$  solute elements for alloy composition  $\text{Re}_{15}\text{X}_1$ .

the design of lower-cost Re-based alloys the key findings of this work relate to the effects of solute additions on the elastic anisotropy and the intrinsic ductility parameter  $K/G$ . It is found that alloying Re with elements to the left in the periodic table increases  $K/G$ , and is thus expected to enhance the intrinsic ductility. The trend in  $K/G$  correlates with an increase in the axial  $c/a$  ratio, towards values closer to ideal close packing, when alloying with solutes that decrease the average band filling. The effect of alloying on the elastic anisotropy is examined by considering two parameters that measure the anisotropy of the Young's modulus and shear modulus. As described in the first section of the chapter, it is expected generally that an increase in the elastic anisotropy could contribute to brittle behavior in polycrystalline samples. In the present calculations alloying with solute additions near Re in the periodic table is found to weakly decrease (increase) the anisotropy in Young's modulus (shear modulus).

## Chapter 4

# Twinning Energetics in HCP Transition Metals and Alloys

In this chapter, the twinning energetics of elemental HCP metals and alloys are discussed in detail. Particular attention is focused on a twin energy anomaly for Re and Tc discovered in this work, and the interesting connection between twin boundary energy, twin boundary structure, electronic structure and  $d$ -band filling. Based on the insights obtained in this work, some avenues towards replacement of rhenium are discussed as well in this chapter.

### 4.1 Foreword

Twinning is a common deformation mechanism in materials where the number of active dislocation slip systems is limited [171, 172, 17, 173, 119]. In such materials, understanding of the mechanisms underlying twin boundary (TB) formation can thus be essential for optimizing mechanical properties [174, 175, 176, 177]. Theories of the crystallography of twinning and its relation to bulk deformation are well developed, and the mechanisms of twin nucleation and growth have been investigated in many technologically important systems [172]. However, the degree to which deformation twinning can be significantly influenced through variations in composition for materials design has been investigated in only a limited number of systems (e.g. [178, 179, 180, 181]).

In this chapter we report results of a study of the properties of commonly observed deformation twins in hexagonal close packed-structured transition metals, a class of materials that finds use in diverse applications including aerospace alloys, cladding for nuclear fuel, and magnetic recording. Through the use of density-functional-theory calculations, we demonstrate anomalously low TB energies ( $\gamma_t$ ) for the group VII transition metals, Re and Tc. This finding correlates with the unique mechanical properties of HCP-

structured Re, which displays pronounced deformation twinning [125, 123, 182, 183], and a unique combination of high temperature strength and low-temperature ductility [25] that have made it of interest for structural applications in extreme environments [184, 25]. To investigate the electronic origins of this anomalous twinning behavior, we introduce a new method for computing the composition dependence of  $\gamma_t$  in alloys. Results derived with this approach demonstrate that TB energies in Re can be decreased even further through alloying with elements that lower the average number of  $d$  electrons per atom relative to pure Re. These predictions are consistent with experimental characterization studies undertaken in this work, demonstrating pronounced differences in deformation microstructures in Re versus Re-10 at. % W alloys. The anomalous TB energetics in the group VII metals are correlated with the presence of structural units near the TB plane that are similar to the Frank-Kasper polyhedra characterizing the tetrahedrally-close-packed (TCP) transition-metal intermetallic compounds that are stable near half  $d$ -band filling [185, 186, 187, 188, 189]. Through an analysis of the electronic structure, a link between the theory of bulk structural stability and TB energies is established, which may be useful in controlling the energetics underlying twin formation in the design of transition metal alloys with targeted mechanical properties.

The rest of this chapter is organized as follows. First, the general nomenclature regarding the crystallography of deformation twinning in HCP-metals and alloys is discussed. Also, the crystallography of the deformation twins considered in this work is discussed in detail. Subsequently, the energetics of twinning in elemental HCP-metals is discussed, including both computational and experimental methodologies. Particular attention is paid to the twin energy-anomaly that was discovered in this work. The effect of alloying and  $d$ -band filling on the twin energies is discussed next, followed by a theoretical justification of the twin energy anomaly and the trends with  $d$ -band filling. Finally, some possible avenues towards rhenium-replacement are discussed, followed by the conclusions and summary.

Part of the results presented in this chapter, including the figures and tables, were published by Maarten de Jong, Josh Kacher, Marcel Sluiter, Liang Qi, David Olmsted, Axel van de Walle, John Morris Jr., Andrew Minor and Mark Asta in Physical Review Letters, 115(6):065501, 2015 [190]. The material is reproduced here with permission of the co-authors and publishers. All of the computational results were led by Maarten de Jong under the supervision of Mark Asta and Marcel Sluiter. Josh Kacher led the experimental studies under the supervision of Andrew Minor, and is responsible for all of the experimental results and methods presented in this chapter.

## 4.2 Crystallography of Twinning

The parent and product phases of any mechanically twinned crystal remain in contact during the process of twinning along the twin plane. The process can therefore be described in terms of an invariant plane strain. Further, volume conservation dictates that in fact, twinning is a simple-shear deformation. The geometry of a mechanically formed twin is commonly described in terms of the strain parameters associated with the simple-shear process. This is shown schematically in Fig. 4.1.

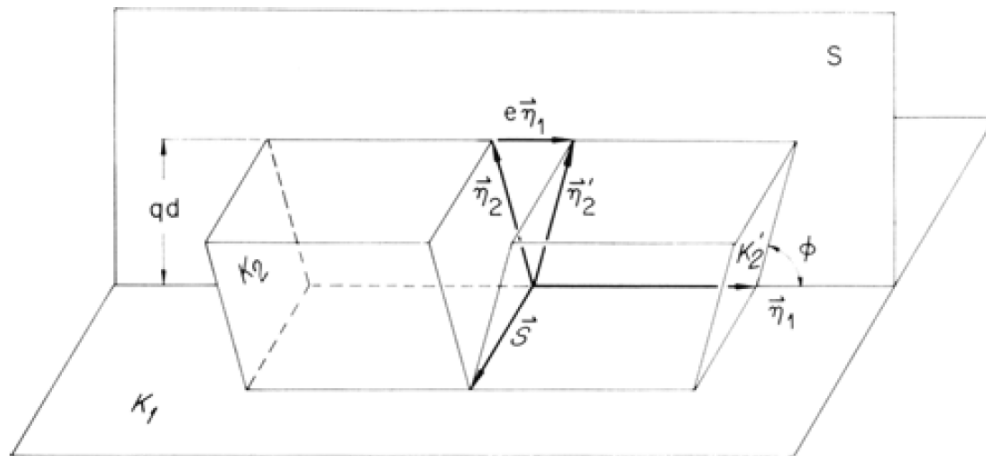


Figure 4.1: An illustration of twinning elements.

In Fig. 4.1, consider the unit cell spanned by the vectors  $\vec{S}$ ,  $\vec{\eta}_1$  and  $\vec{\eta}_2$ . A simple shear is now applied that transforms it into the twinned cell defined by  $\vec{S}'$ ,  $\vec{\eta}_1'$  and  $\vec{\eta}_2'$ . In Fig. 4.1,  $K_1$  denotes the twin plane, also called the composition plane. It is undistorted and unrotated during the process of twinning. The plane  $K_2$  is the second undistorted plane. It is rotated during mechanical twinning as indicated. The direction of the twinning shear is parallel to  $\vec{\eta}_1$ . The magnitude of the twinning shear is commonly denoted by  $e$  and can be expressed as a function of the axial ratio  $\gamma$  of the HCP-material,  $\gamma = c/a$ . The planes  $K_1$  and  $K_2$ , together with the directions  $\vec{\eta}_1$  and  $\vec{\eta}_2$  are collectively referred to as the twinning elements. Based on this description of the crystallography of twinning, 2 different types of twins are commonly distinguished. For type-I twins, both  $K_1$  and  $\eta_2$  have rational Miller-Bravais indices [172]. For this type of twin, the deformation process during twinning can be considered as simply a reflection of the structure in the  $K_1$  plane or alternatively, a rotation around the normal vector to  $K_1$ . For type-II twins on the other hand,  $K_2$  and  $\eta_1$  have rational indices. In that case, the twinning process can be thought of

as a rotation around  $\eta_1$  or a reflection in the plane normal to  $\eta_1$ . For crystal systems with high symmetry, the rotation and reflection operations are often equivalent. In that case, all indices for  $K_1$ ,  $K_2$ ,  $\eta_1$  and  $\eta_2$  are rational and this leads to degenerate or compound twins.

In HCP-metals, twinning is generally more complicated than in e.g. cubic metals, due to the fact that there is an additional atom in the basis. As a result, not all lattice points are necessarily sheared into their correct positions to restore the parent lattice. This induces a shuffling of a subset of atoms in the shear part of the material, restoring the original lattice and thereby lowering the energy of the crystal. This phenomenon is not observed in cubic metals and makes twinning in HCP-metals an inherently more complicated process. All twins considered in this work have rational indices for  $K_1$ ,  $K_2$ ,  $\eta_1$  and  $\eta_2$  and are therefore compound twins.

In the computational work, 5 commonly observed [172, 191, 192] TBs in hcp metals and alloys have been studied. Their twinning elements  $K_1$ ,  $K_2$ ,  $\eta_1$  and  $\eta_2$  are listed in Table 4.1. See Fig. 4.2 for a visualization of these 5 TBs.

Table 4.1: Twinning elements of the 5 twin boundaries studied in this work.

| $K_1$            | $K_2$                  | $\eta_1$                                       | $\eta_2$                                 |
|------------------|------------------------|--|--|
| $\{10\bar{1}1\}$ | $\{10\bar{1}\bar{3}\}$ | $\langle 10\bar{1}\bar{2} \rangle$             | $\langle 30\bar{3}\bar{2} \rangle$       |
| $\{10\bar{1}2\}$ | $\{10\bar{1}\bar{2}\}$ | $\pm \langle 10\bar{1}\bar{1} \rangle$         | $\pm \langle 10\bar{1}\bar{1} \rangle$   |
| $\{11\bar{2}1\}$ | $\{0001\}$             | $\frac{1}{3} \langle \bar{1}\bar{1}26 \rangle$ | $\frac{1}{3} \langle 1120 \rangle$       |
| $\{11\bar{2}2\}$ | $\{11\bar{2}\bar{4}\}$ | $\frac{1}{3} \langle 11\bar{2}\bar{3} \rangle$ | $\frac{1}{3} \langle 22\bar{4}3 \rangle$ |
| $\{10\bar{1}3\}$ | $\{\bar{1}011\}$       | $\langle \bar{3}032 \rangle$                   | $\langle 10\bar{1}2 \rangle$             |

### 4.3 Twinning and Twinning Energetics in Elemental HCP Transition Metals

In this section, a systematic study of twinning energetics in elemental HCP metals is presented.

#### 4.3.1 Computational Methodology

With the exception of the Virtual Crystal Approximation (VCA) and Coherent Potential Approximation (CPA) results, all calculations were performed using the Vienna Ab Initio Simulation Package (VASP) [136, 137]. The VASP calculations made use of the Local Density Approximation (LDA), employing the Ceperley-Alder (CA) exchange-correlation functional [138], based on the Perdew-Zunger parametrization [34]. All of these



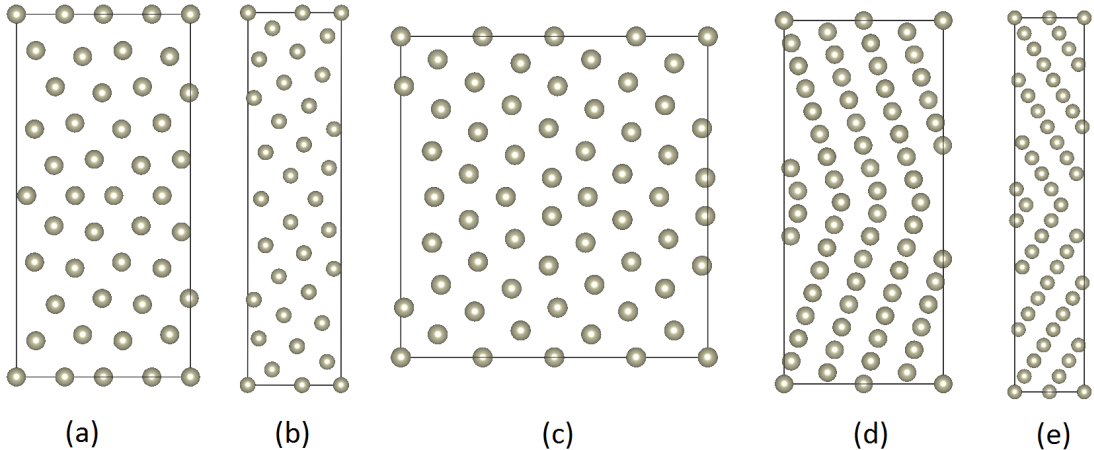


Figure 4.2: Projection-view of 5 twin boundaries considered in this work: (a)  $K_1 = \{10\bar{1}1\}$  (projection along  $[1\bar{2}10]$ ), (b)  $K_1 = \{10\bar{1}2\}$  (projection along  $[1\bar{2}10]$ ), (c)  $K_1 = \{10\bar{1}3\}$  (projection along  $[1\bar{2}10]$ ), (d)  $K_1 = \{11\bar{2}1\}$  (projection along  $[1\bar{1}00]$ ), (e)  $K_1 = \{11\bar{2}2\}$  (projection along  $[1\bar{1}00]$ ).

calculations made use of the projector augmented wave (PAW) method [52, 53]. An energy cutoff for the plane waves of 600 eV was used, and smearing of the electronic occupancies was performed using the Methfessel-Paxton scheme [140], with a broadening of 0.1 eV. Integrations in the Brillouin zone were carried out using Monkhorst-Pack  $k$ -point sampling [139] with a density chosen such that the number of  $k$ -points in the first Brillouin zone times the number of atoms in the cell equals approximately 20,000. The PAW potentials for Re included 7 valence electrons, corresponding to a configuration  $5d^56s^2$ . For the elements Ta, W, Os, Ir, the related valence electron configurations are of the form  $5d^x6s^2$  where  $x = 3, 4, 6, 7$ , respectively.

For the purpose of investigating the origins of alloying effects on calculated TB energies, we also employed calculations based on the VCA and CPA methods. The VCA calculations were performed using the Quantum Espresso software [193], employing norm-conserving Troullier-Martin pseudopotentials [51, 109]. Use was made of the local density approximation, based on the Perdew-Wang 91 exchange-correlation functional [36]. The pseudopotentials were generated using the fhi98PP code with intermediate nuclear charges [101]. The VCA pseudopotentials were generated for Re-Ta, Re-W, Re-Os and Re-Ir alloys, with electron per atom ratios corresponding to solute concentrations of 4.9 and 9.8 at.% solute. KKR-CPA calculations were performed with the Munich SPR-KKR package, version 6.3 [194], kindly provided by Prof. H. Ebert. The most important settings were: LDA exchange correlation functional of Vosko et al. [31], Atomic Sphere Approximation (ASA) with identical sphere sizes for all elements, valence electrons described up to  $l = 3$ , and

484 special  $k$ -points in the irreducible Brillouin zone, structurally relaxed atomic positions and cell parameters were taken from VASP calculations on pure Re.

For the pure elements, the twin boundary (TB) energies were calculated by employing supercells ranging from 32 to 64 atoms, depending on the type of TB. Tests with varying supercell size established that these cells lead to calculated values for the TB energy converged to within approximately 5 mJ/ m<sup>2</sup>. A comparable level of convergence was established relative to the choices of plane-wave cutoff and k-point sampling. The Special Quasirandom Structure (SQS) [87, 88] approach was applied to the calculation of the  $\{11\bar{2}1\}$  TB energy, and in this case, a 128-atom supercell was used, as described below. The TB energy was computed by averaging over ten 128-atom SQS cells, in order to derive an estimate of the TB energy for a randomly substitutionally disordered alloy with a statistical uncertainty within 10 mJ/ m<sup>2</sup>.

### 4.3.2 Experimental Methodology and Results

99.99 % pure Re and Re-10 at. % W samples were obtained from Rhenium Alloys Inc. in the form of 3 mm diameter rods. Prior to delivery, the samples, originally in powder form, were pressed, pre-sintered, swaged, heat treated at 1600 °C for 10 minutes, and finally ground to the finish size. As-received samples were prepared from this material. Samples used for mechanical testing were cut from the original rods using electrical discharge machining (EDM) and annealed for 20 hr in a 50 % H - 50 % Ar atmosphere at 1100 °C.

Electron back-scattered diffraction (EBSD) scans were collected from four different samples: two pure Re samples strained in compression to values of 0.043 and 0.068 and two Re-10 at. % W samples strained at room temperature to values of 0.025 and 0.055. EDAX-TSL Orientation Imaging Microscopy (OIM) software [195] was used for data collection and analysis. Scans were collected from each sample from  $70 \times 70 \mu\text{m}$  regions using an accelerating voltage of 20 keV and at a step size of 100 nm. The polycrystals were found to be weakly textured with most grains oriented with the c-axis perpendicular to the compression axis, though c-axis-oriented grains were also present in the scan, see Fig. 4.3 for the inverse pole figure map and pole figure. Twin boundaries were automatically detected in the software using the criteria for  $\{11\bar{2}1\}$ -type twins of a  $34.8^\circ$  rotation about the  $[1\bar{1}00]$  axis. Criteria for  $\{10\bar{1}2\}$ -,  $\{11\bar{2}2\}$ -, and  $\{10\bar{1}1\}$ -type twins were also included but none were detected in the scan. The twin width was measured manually in each grain to calculate the average twin width for the two different materials.

As-received samples were prepared for Transmission Electron Microscopy (TEM) characterization by first sectioning them from a rod into 3 mm diameter disks with a thickness of approximately 100  $\mu\text{m}$  using electron discharge machining. These samples

were expected to have heavy levels of deformation as material synthesis involved powder consolidation and swaging. Thinning to electron transparency was achieved by jet-polishing using an ethanol-butoxyethanol-perchloric electrolyte. TEM characterization was done using a JEOL 3010 operated at 300 keV. Figure 4.4 shows TEM images for pure hcp Re and a Re-10 at.% W alloy.

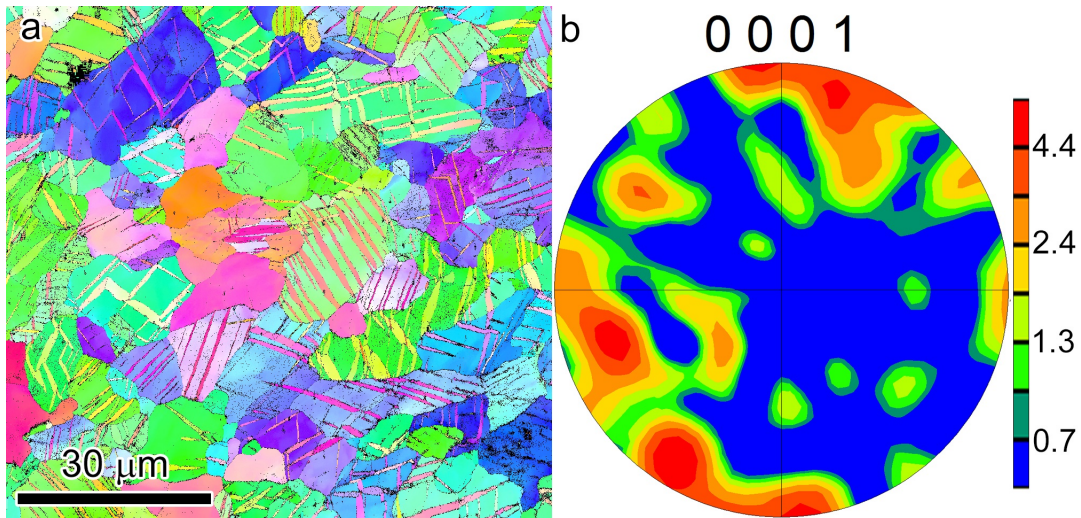


Figure 4.3: a) Inverse pole figure map of the deformed Re showing extensive twinning behavior. All twins present in the scan are  $\{11\bar{2}1\}$  - type. b) (0001) - Pole figure constructed from the data shown in (a) showing that the microstructure is weakly textured orthogonal to the (0001)-orientation. The legend is in terms of times random.

### 4.3.3 Results

In Fig. 4.5, results of DFT calculations of  $\gamma_t$  are plotted for two commonly observed twins in HCP transition metals, which we will refer to by the twinning plane:  $\{11\bar{2}1\}$  and  $\{10\bar{1}1\}$ . The calculations have been performed within the framework of the local density approximation to DFT [138, 34], using the Vienna ab-initio simulation package [196, 197, 198]. The  $\gamma_t$  results in Fig. 4.5 are plotted as a function  $G\Omega^{1/3}$ , where  $G$  is the Voigt-Reuss-Hill averaged isotropic shear modulus [199]) and  $\Omega$  is the atomic volume. With the notable exception of the group VII metals (Tc and Re), the results in Fig. 4.5 show (i) an overall trend towards increasing values of  $\gamma_t$  with the magnitude of  $G\Omega^{1/3}$ , and (ii) lower energetics for  $\{10\bar{1}1\}$  relative to  $\{11\bar{2}1\}$  TBs. The first observation is consistent with similar correlations reported previously for grain and twin boundaries in metals [200, 201], and is found to hold for TBs in other HCP metals based on the calculated values given in

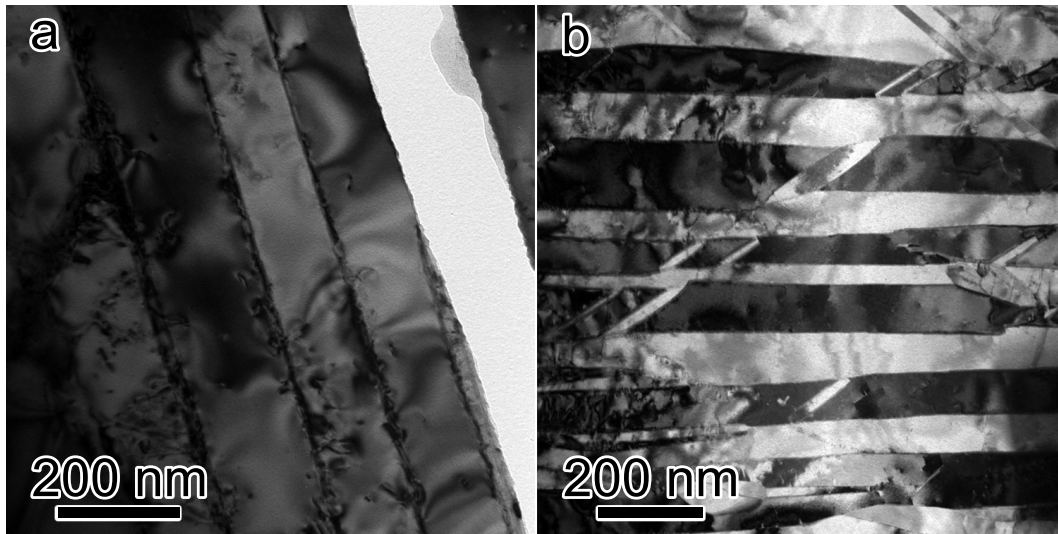


Figure 4.4: Bright-field TEM images showing twin deformation in a) pure Re and b) Re-10 at. % W.

Table 4.2.

The results in Fig. 4.5 and Table 4.2 for the group VII elements Tc and Re stand out in two ways. First, the magnitudes of  $\gamma_t$  are lower than expected based on the dashed trend lines fit to all the other transition metals. This is particularly true for the  $\{11\bar{2}1\}$  TB, for which  $\gamma_t$  for Tc and Re is more than a factor of five lower than that for Ru or Os, the neighboring elements in the periodic table. Second, Tc and Re are the only elements in the transition-metal series for which the  $\{11\bar{2}1\}$  TB has a lower calculated energy than the  $\{10\bar{1}1\}$  TB. Interestingly, the second of these two results is qualitatively consistent with experimental observations in deformed Re samples, which show a predominance of  $\{11\bar{2}1\}$  twins [183, 123, 125]. An example is given in Fig. 4.6, which shows electron back scattered diffraction images for Re and Re-10 at. % W alloys deformed in compression at room temperature to strains of 6.8 % and 7.8 %, respectively. A detailed investigation of the dominant twin type was undertaken for these deformed polycrystalline samples. Out of 1,040 twins investigated in pure Re all but 5 were found to be  $\{11\bar{2}1\}$  type (the other five were of  $\{10\bar{1}2\}$  type), and similarly 68 twins were analyzed in the Re-10 at. % W sample, all of which were of  $\{11\bar{2}1\}$  type.

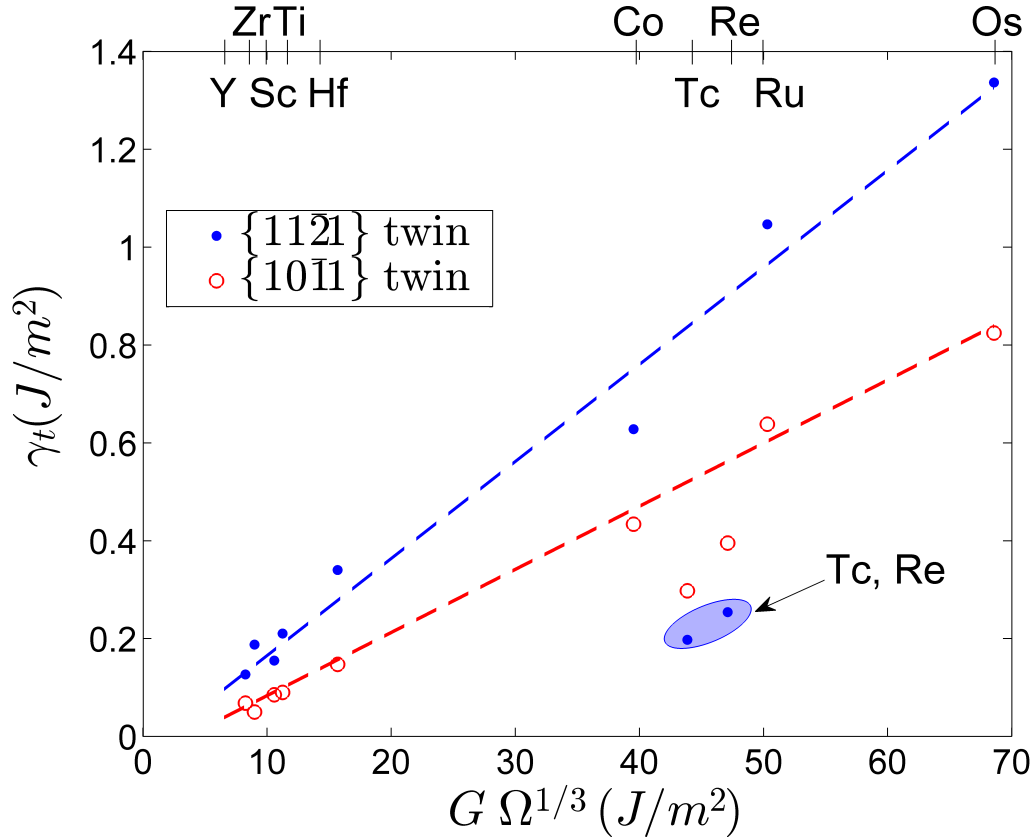


Figure 4.5: Calculated  $\{10\bar{1}1\}$  and  $\{11\bar{2}1\}$  twin boundary energies versus calculated values of the  $G\Omega^{1/3}$ , where  $G$  and  $\Omega$  are shear modulus and atomic volume, respectively. Dashed lines are least-squares fits excluding the data for Re and Tc.

#### 4.4 Twinning Energetics: Effect of Alloying and $d$ -band Filling

To further investigate the anomalous twinning behavior in the group VII transition metals, we focus on Re and examine the effect on  $\gamma_t$  resulting from alloying with neighboring elements in the periodic table. For this purpose we have developed a methodology for computing the energies of planar defects in substitutional alloys based on the special quasirandom structure (SQS) formalism. In the SQS approach a structure with a number of atoms small enough to be considered in DFT calculations is constructed with an atomic configuration for which the correlation functions for the near-neighbor shells mimics as closely as possible those for a random substitutional alloy [87, 88, 202]. In the

Table 4.2: Calculated twin boundary energies for selected HCP metals ( $mJ/m^2$ ), twin boundary with the lowest energy and  $G\Omega^{1/3}$  ( $J/m^2$ ) in  $mJ/m^2$ , where  $G$  is the Voigt-Reuss-Hill averaged shear modulus, and  $\Omega$  is the atomic volume. For each metal, an asterisk denotes the twin boundary with the lowest energy.

|    | Twin Boundary    |                  |                  |                  |                  | $G\Omega^{1/3}$ ( $J/m^2$ ) |
|----|------------------|------------------|------------------|------------------|------------------|-----------------------------|
|    | $\{10\bar{1}1\}$ | $\{10\bar{1}2\}$ | $\{10\bar{1}3\}$ | $\{11\bar{2}1\}$ | $\{11\bar{2}2\}$ |                             |
| Y  | 41*              | 117              | 171              | 117              | 231              | 8.3                         |
| Zr | 53*              | 221              | 302              | 209              | 373              | 9.0                         |
| Sc | 85*              | 166              | 274              | 122              | 296              | 10.6                        |
| Ti | 103*             | 320              | 409              | 253              | 446              | 11.3                        |
| Hf | 147*             | 395              | 399              | 339              | 473              | 15.7                        |
| Co | 433*             | 666              | 555              | 507              | 710              | 39.5                        |
| Tc | 297              | 497              | 506              | 191*             | 506              | 43.9                        |
| Re | 395              | 707              | 613              | 248*             | 643              | 47.1                        |
| Ru | 637*             | 1055             | 869              | 1064             | 872              | 50.3                        |
| Os | 824*             | 1359             | 1040             | 1348             | 1002             | 68.6                        |

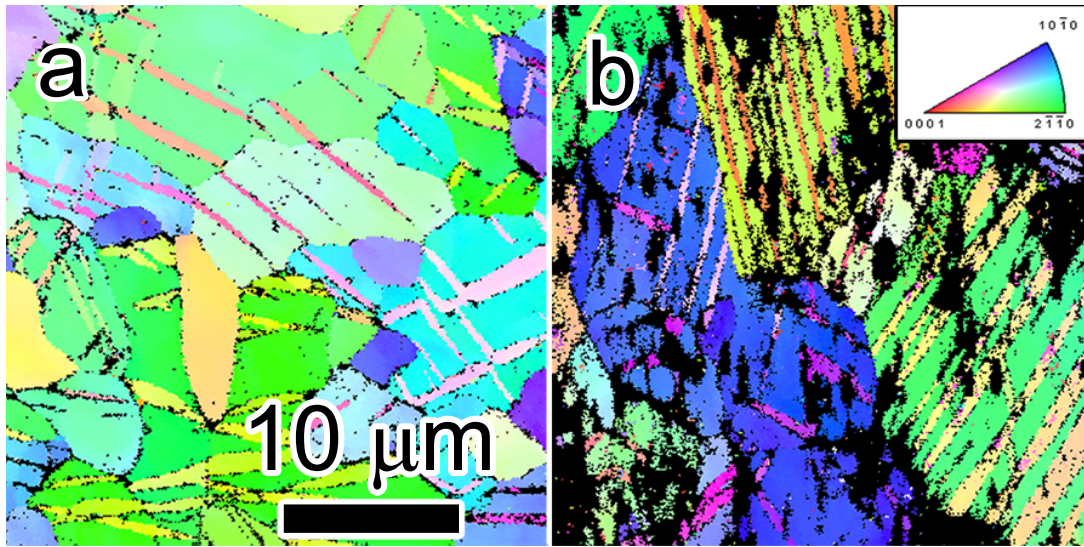


Figure 4.6: Electron back-scattered diffraction scans of a) pure Re deformed 6.8 % and b) a Re-10 at. % W alloy deformed 7.8 %. The colors represent crystallographic orientation as described by the legend top right. Black areas represent regions that were unable to be indexed due to surface pitting.

present generalization of the approach we generate SQS which, in addition, give correlation functions close to random values within the local vicinity of a plane where cleavage



or shearing/shuffling operations are imposed to create a surface or TB, respectively. The accuracy of the scheme developed in this work has been assessed for model alloys described by classical potential models, as will be discussed in the next chapter.

In the top panel of Fig. 4.7 we plot the variation of the DFT-calculated  $\{11\bar{2}1\}$   $\gamma_t$  for  $\text{Re}_{0.912}\text{X}_{0.098}$  alloys, as a function of the solute species  $X$ . In the middle panel we also plot, for comparison, calculated basal-plane ( $\{0001\}$ ) surface energies ( $\gamma_s$ ) for the same alloys. The lower panel plots the value of an intrinsic ductility parameter  $D = \gamma_s/\gamma_t$ , which has been proposed for HCP metals where cleavage occurs on the basal plane, and where deformation twinning is the primary mechanism for plasticity under tensile loading parallel to the  $c$  axis [173, 17]. It can be seen that  $\gamma_t$  calculated for  $\{11\bar{2}1\}$  TBs display a pronounced dependence on solute species: alloying with elements to the left (right) of Re is seen to give rise to a significant decrease (increase) in  $\gamma_t$ . Calculated  $\gamma_t$  values decrease by approximately 50 % when Re is alloyed with 9.8 at. % W or Ta, and increases by approximately the same magnitude with a comparable amount of alloying with Os or Ir. The  $\{10\bar{1}1\}$  TB energy on the other hand shows an order of magnitude smaller variation for the same compositions, see Fig. 4.8. The dependence of  $\gamma_t$  on band filling was further analyzed by computing TB energies for both  $\{11\bar{2}1\}$  and  $\{10\bar{1}1\}$  twin orientations, for all  $5d$  transition metals, including those not stable in the HCP structure. The results are plotted in Fig. 4.9 and show that both twins display maximum values of  $\gamma_t$  for Os. The values of  $\gamma_t$  decrease with decreasing band filling, reaching minimum (negative) values for W (Ta) for the  $\{11\bar{2}1\}$  ( $\{10\bar{1}1\}$ ) twin before increasing again (to positive values) as the band filling reaches Hf. As was found in the consideration of alloying effects, the results in Fig. 4.9 show that the  $\{11\bar{2}1\}$  twin displays a much larger (approximately four times) variation in TB energy relative to  $\{10\bar{1}1\}$  across the  $5d$  transition metal series. Similarly, the surface energy is seen to show relatively small variations with solute addition, and, as a consequence, alloying with elements to the left (right) is predicted to lead to a sharp increase (decrease) in the intrinsic ductility parameter  $D$ .

The computational prediction that alloying with W leads to a pronounced decrease in  $\gamma_t$  for the  $\{11\bar{2}1\}$  TB is supported by a comparison of the deformation microstructures for Re and Re-10 at.% W alloys shown in Fig. 4.6. Specifically, the spacing ( $\lambda$ ) between TBs in the twin variants for the Re-W alloy is considerably smaller than for pure Re. Generally, it is expected that a decrease in  $\gamma_t$  leads to a decreased value of  $\lambda$  [203] when all other conditions are roughly equal. This was verified by measuring twin thickness in approximately 50 grains from each material. Twins in the deformed Re and alloys samples were found to have an average thickness of 720 nm and 440 nm, respectively.

To probe the origin of the effect of alloying on  $\gamma_t$  for the  $\{11\bar{2}1\}$  TB in Re, additional DFT calculations were performed based on the virtual crystal (VCA) and coherent potential (CPA) approximations. In these calculations the individual Re and solute atoms

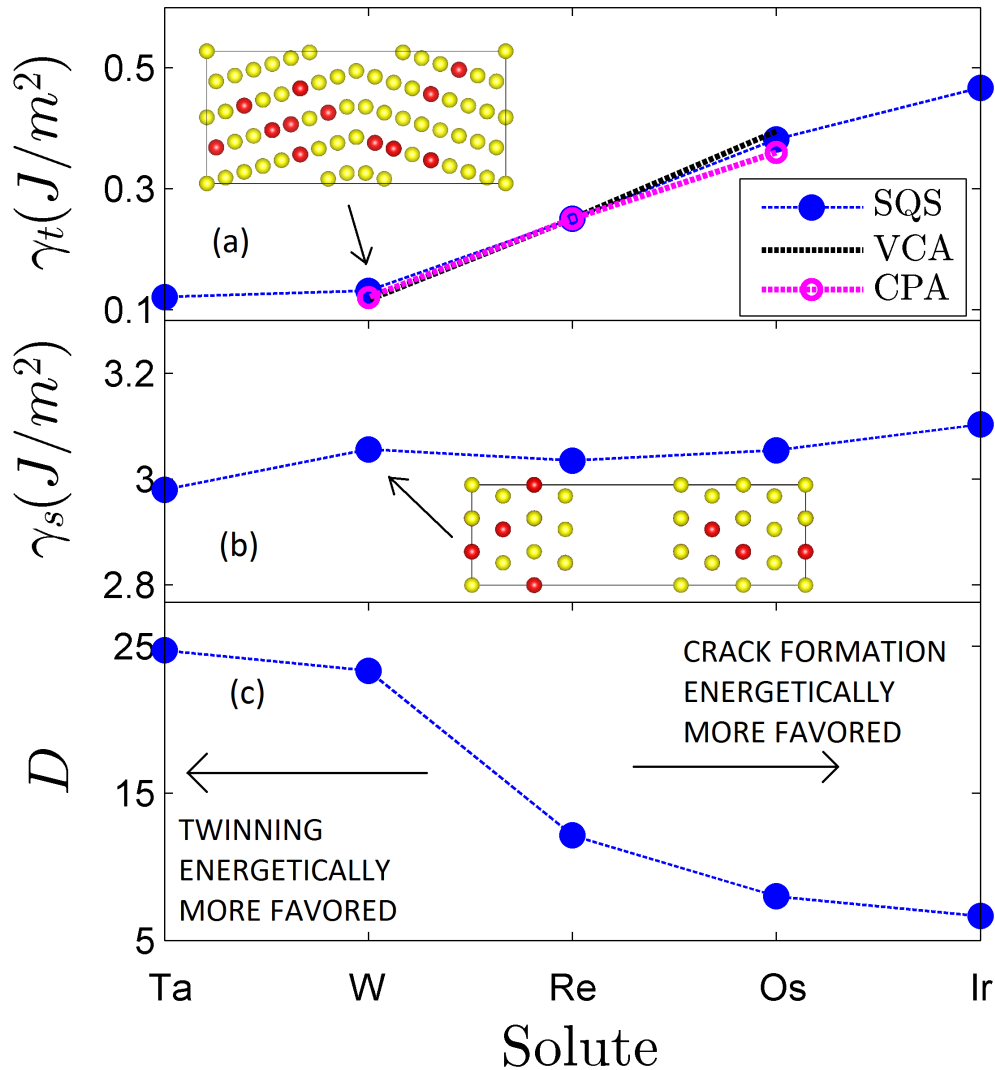


Figure 4.7: For Re-9.8 at. % X alloys, variations as a function of solute X, for (a) the  $\{11\bar{2}1\}$  TB energy as calculated from SQS, VCA and KKR-CPA, (b)  $\{0001\}$  surface energy calculated from SQS and (c) ductility parameter,  $D = \gamma_s/\gamma_t$ .

are replaced by single effective atoms with a concentration-weighted number of valence electrons or scattering properties, but without accounting for displacement effects associated with atomic size mismatch. The calculations thus allow investigation of the relative importance of electronic versus size effects underlying the concentration dependence of  $\gamma_t$ . In Fig. 4.7 (a) the slope of the  $\{11\bar{2}1\}$  TB energy is well reproduced (to within approxi-



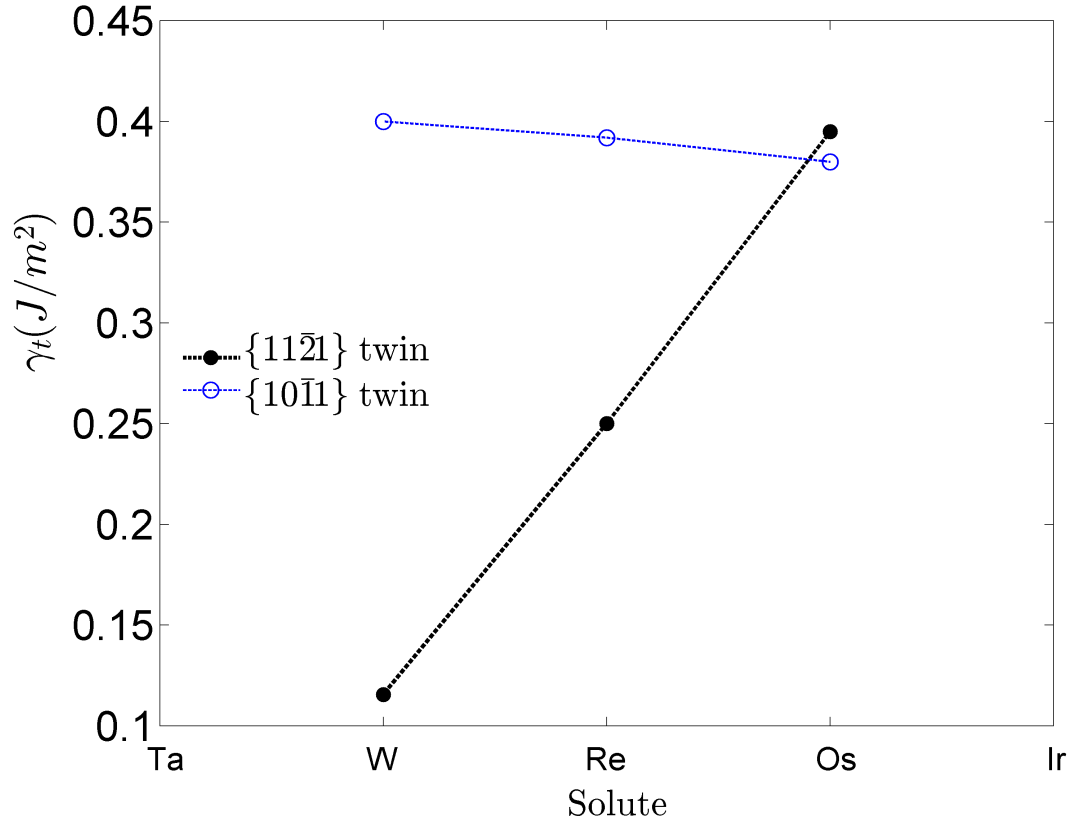


Figure 4.8: The energy of the  $\{11\bar{2}1\}$  and  $\{10\bar{1}1\}$  twin boundary in pure Re and Re-X alloys as a function of band filling, as calculated from the VCA. The composition of the alloys is Re- 10 at. % W and Re- 10 at. % Os.

mately 5 %) by both VCA and KKR-CPA calculations, suggesting a direct link with the band energy.

This finding is consistent with a comparison of the calculated electronic density of states (DOS) for bulk HCP Re, and supercells of Re containing  $\{11\bar{2}1\}$  and  $\{10\bar{1}1\}$  twins. Plotted in Fig. 4.10 is a comparison of the calculated electronic density of states (DOS) for bulk HCP Re, and supercells of Re containing  $\{11\bar{2}1\}$  and  $\{10\bar{1}1\}$  twins. The DOS show a shallower slope at the Fermi level for the supercell with the  $\{11\bar{2}1\}$  twin than it does for the bulk structure. As a consequence, the band energy for this twin decreases (increases) with a shift in the Fermi energy to lower (higher) band fillings. Further, a comparison of the DOS of the  $\{11\bar{2}1\}$  and  $\{10\bar{1}1\}$  shows that the former attains more

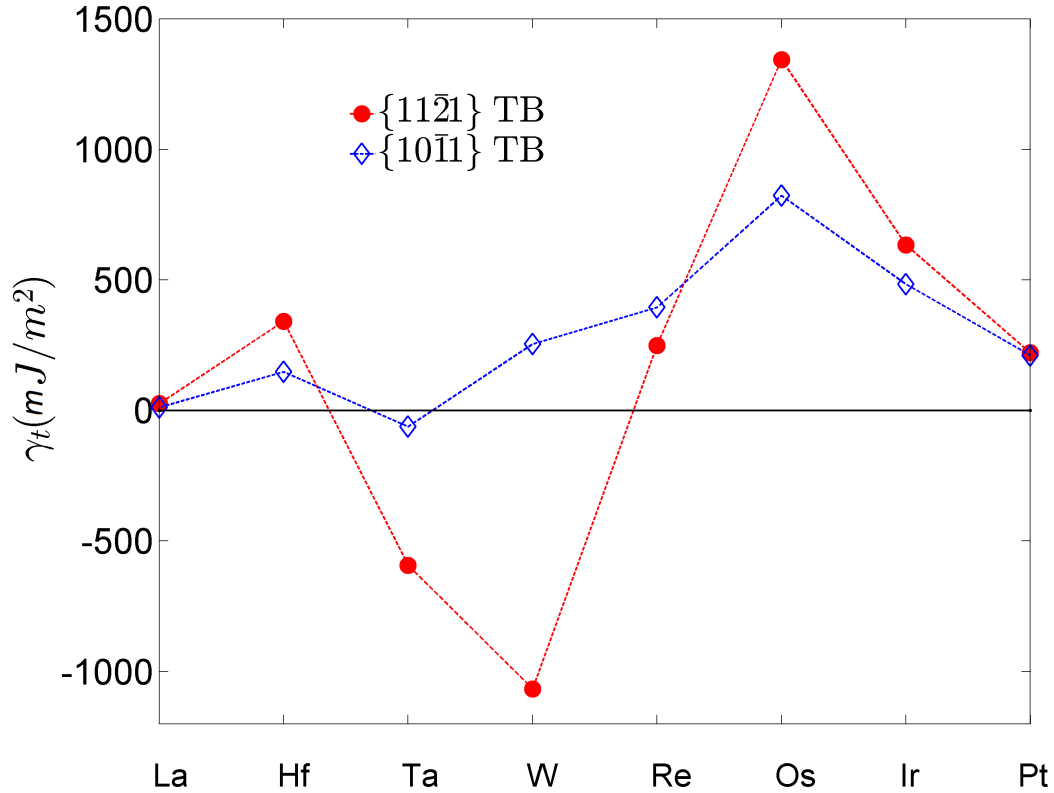


Figure 4.9: Calculated energies for  $\{11\bar{2}1\}$  and  $\{10\bar{1}1\}$  TBs for all  $5d$  transition metals, including those stable in bcc and hcp crystal structures.

states at lower energies, whereas the latter has a higher DOS at higher energies just below the Fermi level, as indicated by the arrows in the inset of Fig. 4.10. This contributes to the lower energy of the  $\{11\bar{2}1\}$  TB relative to the  $\{10\bar{1}1\}$  TB. To the right of the Fermi level, the DOS of the  $\{11\bar{2}1\}$  TB attains higher values than that of the  $\{10\bar{1}1\}$  TB, with the HCP DOS lying approximately in between. This is consistent with our findings that as band filling is increased, the  $\{11\bar{2}1\}$  TB gradually loses stability with respect to the  $\{10\bar{1}1\}$  TB. Although the calculated TB energy is clearly influenced by contributions to the total energy beyond just the band energy, the results in Fig. 4.10 are consistent with the trends for the concentration dependence of the calculated values of  $\gamma_t$ . In summary, the calculated DOS show that within a rigid-band model a reduction in band filling leads to (i) a lowering of the band energy contribution to  $\gamma_t$  for the  $\{11\bar{2}1\}$  twin, and (ii) a lowering of the band energy for this twin relative to that for  $\{10\bar{1}1\}$ ; both findings are qualitatively consistent

with the results for alloying effects on  $\gamma_t$  in Re presented above.

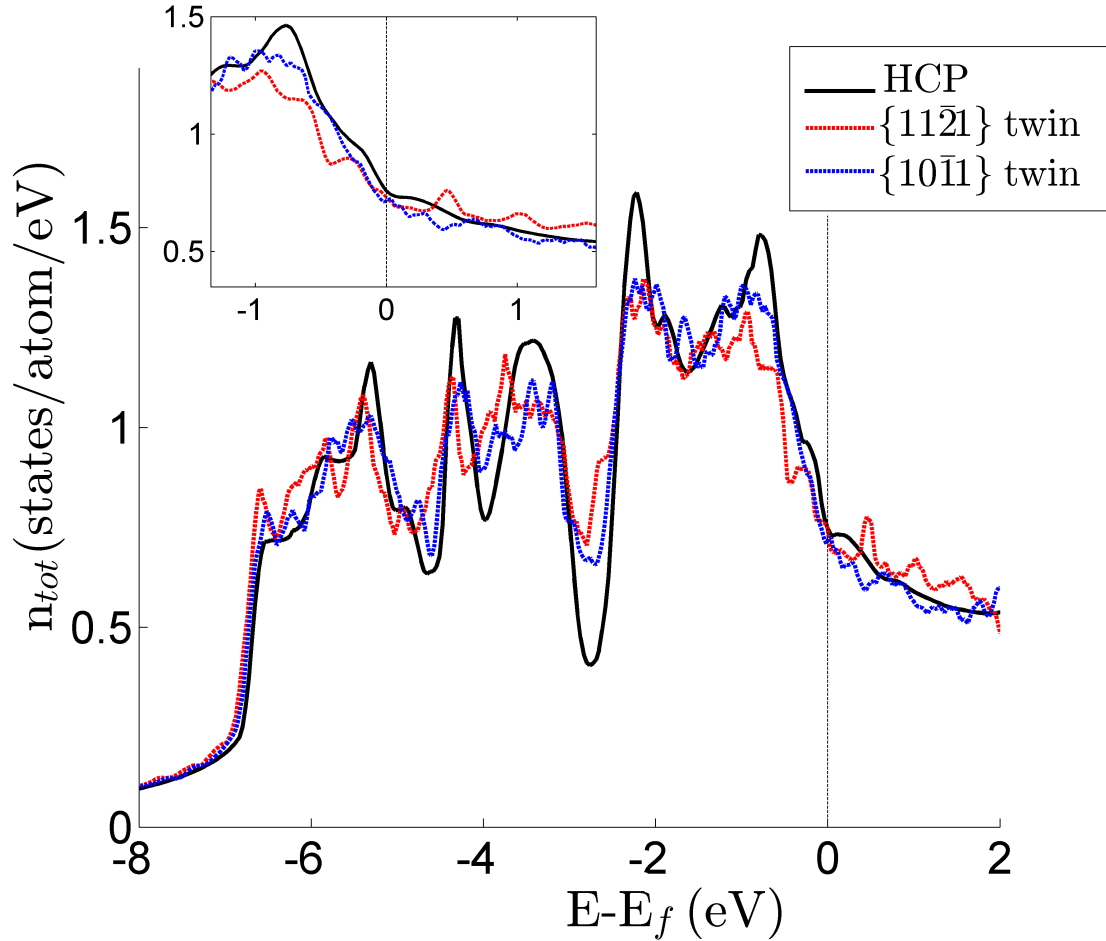


Figure 4.10: Electronic DOS for the  $\{11\bar{2}1\}$  and  $\{10\bar{1}1\}$  TB and HCP Re. The inset shows that the DOS of the  $\{11\bar{2}1\}$  TB is lower than the  $\{10\bar{1}1\}$  TB DOS just left of the Fermi-level, with the opposite behavior to the right of the Fermi-level.

## 4.5 Origin of the Twin Energy Anomaly

Additional insights into the origin of the effect of band filling on  $\gamma_t$  for the  $\{11\bar{2}1\}$  twin can be obtained by examining the local atomic structure in the TB plane. As indicated in Fig. 4.11 the nearest-neighbor coordination polyhedron for atoms in the  $\{11\bar{2}1\}$  TB plane takes the shape of a distorted icosahedron (pentagonal bipyramidal prism). This polyhedron increases the number of triangular faces by 2 and reduces the number of square

faces by one as compared to the anti-cubooctahedron polyhedron characteristic of the bulk HCP structure. In contrast, atoms in the  $\{10\bar{1}1\}$  TB plane have two distinctly coordinated sites: a 13 coordinated site with 2 additional triangular faces, and an 11 coordinated site with 2 less triangular faces than the anti-cubooctahedron shell of HCP. Therefore, for the  $\{10\bar{1}1\}$  TB the total number of triangular and square faces averaged over the coordination polyhedra of the two interface sites are the same as in bulk HCP. An increase in the fraction triangular faces in the coordination polyhedra of the  $\{11\bar{2}1\}$  TB makes the interface atomic structure similar to tetrahedrally close packed (TCP) structures, such as the well-known  $\sigma$ ,  $\chi$  and  $A15$  Frank-Kasper structures, where coordination polyhedra have exclusively triangular faces. The TCP phases occur in transition metals and their alloys at characteristic valence electron/atom (e/a) ratios intermediate between Re and W [185].

A connection between these geometrical considerations, and the effects of band filling on  $\gamma_t$  for  $\{11\bar{2}1\}$  twins in Re can be made through consideration of a moments analysis of the DOS [204, 205]. Previous work has demonstrated that for transition metals near half  $d$ -band filling, the relative stability of structures with similar second moments (i.e., with similar bond lengths and coordination numbers) can be understood based on the fourth moment of the DOS. It has been shown that near half  $d$ -band fillings, the nearest neighbor square clusters found in the HCP structure are penalized energetically relative to tetrahedral configurations (as found in TCP phases, and reflected by triangular faces on the coordination polyhedron), due to their contribution to the fourth moment [206, 207, 208]. This is consistent with our finding that the  $\{11\bar{2}1\}$  twin shows an anomalous energetic stabilization with band fillings near to and slightly lower than Re: the atoms on and near the twin plane exhibit environments built from tetrahedra and distorted squares, instead of the planar nearest-neighbor square clusters found in the bulk HCP structure.

This model is supported by calculations of the moments of the local DOS (LDOS) for atoms as a function of distance from the TB. The  $n$ -th moment of the LDOS ( $d_i$ ) for atom  $i$  is defined as  $\mu_i^{(n)} = \int_{-\infty}^{\infty} (E - \varepsilon_i)^n d_i(E) dE$ , where  $\varepsilon_i$  is the center of gravity [209]. A ‘‘bimodality’’ parameter can be defined as  $s = \{\mu^{(4)}\mu^{(2)} - (\mu^{(2)})^3 - (\mu^{(3)})^2\}/(\mu^{(2)})^3$  [209], such that a completely bimodal LDOS corresponds to  $s = 0$ , while for  $s < 1$  ( $s > 1$ ) the LDOS is said to exhibit bimodal (unimodal) behavior. As shown in Fig. 4.11 (d), for the atoms near the  $\{11\bar{2}1\}$  twin plane,  $s < 1$  whereas far away from the twin  $s > 1$ . Hence, atoms on the twin plane exhibit a more bimodal LDOS than those in the HCP environment. Thus the low values of  $\gamma_t$  for the  $\{11\bar{2}1\}$  TB can be understood by analogy with earlier work [188] showing that large stabilizing contributions to the atomic geometries of TCP structures, which are similar to those found in the twin plane, arise from hopping paths that produce a more bimodal DOS, with an associated enhanced energetic stabilization, near half  $d$ -band filling.

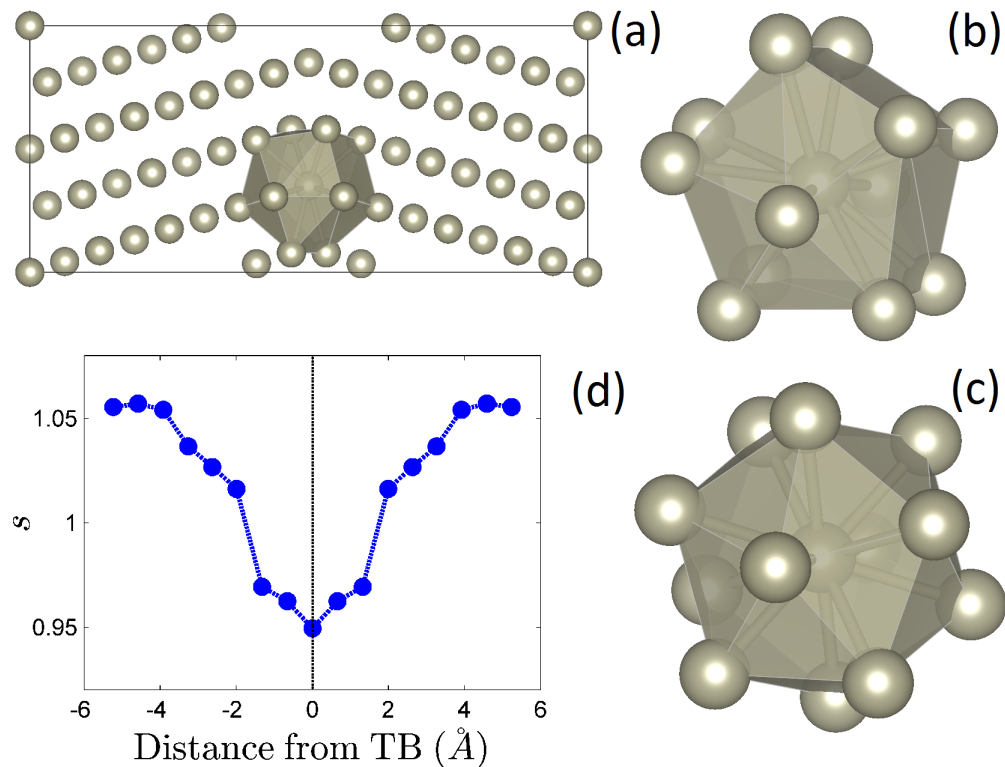


Figure 4.11: (a) The  $\{11\bar{2}1\}$  TB, viewed in projection along an  $[1\bar{1}00]$  direction, highlighting a distorted icosahedron on the TB plane, (b) detailed view of the distorted icosahedron as found in the  $\{11\bar{2}1\}$  TB, (c) an undistorted Z12 icosahedron, and (d) the calculated bimodality parameter  $s$  as a function of distance relative to the TB plane.

## 4.6 Rhenium Replacement Scenarios

The work in previous sections has identified an anomalously low  $\{11\bar{2}1\}$  twin energy for  $d$ -band fillings near that of Re. It is believed that the high ductility and the propensity of Re to deform by virtue of  $\{11\bar{2}1\}$  twins, is closely related to the anomalously low energy of this particular twin. Furthermore, it has been shown that the  $\{11\bar{2}1\}$  twin energy of Re can be lowered even further by reducing the  $d$ -band filling, thereby stabilizing the characteristic icosahedral atomic features that are found in the  $\{11\bar{2}1\}$  twin. This observation can be exploited to suggest new alloys, free of Re and at lower overall cost, that exhibit similar twin boundary energetics, and presumably also a high level of intrinsic ductility. The idea pursued in this section is to consider transition metals at lower  $d$ -band filling (left of Re in the periodic table) and at higher  $d$ -band filling (right of Re in the periodic table) and create alloys such that the  $d$ -band filling coincides approximately with

that of pure Re or slightly lower values, near where the twin energy anomaly occurs.

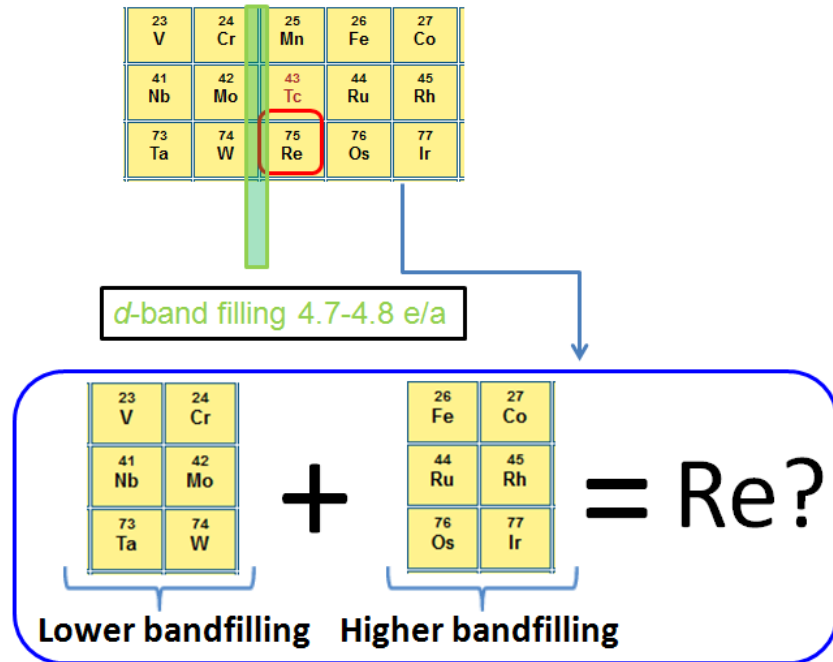


Figure 4.12: A depiction of rhenium replacement strategies pursued in this section: create alloys

This premise is shown schematically in Fig. 4.12. Some possible combinations of elements that would yield alloys with  $d$ -band fillings near Re are for example equi-atomic concentrations of Os and W or Ru and Mo. However, not all alloy-compositions are feasible candidates for a replacement of rhenium. Recall that the goal of rhenium replacement is cost saving. The elements osmium (Os) and iridium (Ir) therefore do not seem good starting point for replacement candidates since both are not only significantly more expensive than Re but also very brittle. The same is true for rhodium (Rh). The element ruthenium (Ru) seems like a better starting point: even though it is costly, it is less expensive than Re. Second, Ru has the same crystal structure as Re, so that potentially the same twinning mechanisms can be activated.

Elemental Ru however is very brittle and hence, alloying is required to create ductile Ru-based alloys with  $d$ -band fillings near those of the twin energy anomaly. To this end, alloying Ru with transition metals to the left of Re in the periodic table is required. Elements such as vanadium (V) and chromium (Cr) satisfy this requirement, but

Table 4.3:  $\{11\bar{2}1\}$  twin boundary energies, calculated for several Ru-bases substitutionally disordered alloys.

| System                                | $d$ -band filling | $\gamma_t$ ( $\{11\bar{2}1\}$ TB, mJ/m <sup>2</sup> ) |
|---------------------------------------|-------------------|---|
| Pure Re                               | 5.00              | 248   |
| Ru-Mo (37.5 at.% Mo)                  | 5.25              | 470   |
| Ru-Ta (37.5 at.% Ta)                  | 4.875             | 261   |
| Ru-W-Re (25 at.% W, 25 at.% Re)       | 5.25              | 478   |
| Ru-Ta-Re (37.5 at.% Ta, 15.6 at.% Re) | 4.72              | 165   |

are not considered further as alloying elements to Ru due to their relatively low melting temperatures relative to Re, rendering them less useful for high-temperature applications. In this section, W, Ta, Mo and Re are considered as alloying elements to Ru since i) these lower the overall  $d$ -band filling towards regions where high intrinsic ductility is expected and ii) their high melting temperatures make them suitable replacement candidates for Re.

Table 4.3 shows the compositions of the Ru-based alloys considered in this work, the calculated  $\{11\bar{2}1\}$  twin boundary energy and their average  $d$ -band filling. These alloy compositions were chosen based on  $d$ -band fillings that are near those of pure Re, while stabilizing the HCP-phase. The reference values for elemental Re are also indicated. These calculations were performed on SQS-cells, accounting for the full effect of atomic size mismatch, elastic relaxations and charge transfer. Table 4.3 clearly shows the strong connection between  $d$ -band filling and twin energy: the Ru-Ta and Ru-Ta-Re alloys at the same  $d$ -band filling exhibit twin energies within 2 %, even though the compositions are very different. Further, alloys with  $d$ -band fillings higher than Re (Ru-Mo and Ru-W-Re) exhibit twin energies that are approximately 90 % larger than for elemental Re. The Ru-Ta alloy, which has a  $d$ -band filling very similar to Re, is within 5 % of the twin boundary energy of Re. Interestingly, as  $d$ -band fillings are lowered significantly below Re, as in the Ru-Ta-Re alloy in Table 4.3, the twin energy drops rapidly, which is consistent with the calculations based on the VCA, as presented in Fig. 4.8. Due to the low twin energy of alloys such as Ru-Ta-Re, the intrinsic ductility is expected to be higher than for pure Re, although surface energy-calculations would have to be carried out to confirm the expected increase in Yoo's ductility parameter.

The results presented in Table 4.3 indicate that Re-substitute alloys with a high intrinsic ductility can be created by tuning the  $d$ -band filling to coincide with or below Re, near the twin energy anomaly. The most promising alloy in Table 4.3 in terms of twin energy is Ru-Ta-Re, although lowering band filling further may lead to even higher intrinsic ductility.

## 4.7 Conclusions and Summary

In summary, we have undertaken DFT calculations demonstrating anomalously low energies for  $\{11\bar{2}1\}$  TBs in the group VII transition metals. Additionally, we have shown for Re that the energy of this TB can be significantly lowered further by alloying with elements that decrease the filling of the  $d$  band relative to pure Re. The theoretical results are consistent with experimental observations of pronounced twinning in the deformation microstructures of Re and Re-W alloys, as  $\gamma_t$  is an important factor affecting twin nucleation (e.g. [210, 211]). Based on an analysis of the electronic and atomic structures of Re  $\{11\bar{2}1\}$  and  $\{10\bar{1}1\}$  TBs it is argued that the anomalously low energies of  $\{11\bar{2}1\}$  twins originate from the presence of structural units at the interface which are stabilized for  $d$  band fillings intermediate between those characteristic of group VI and VII transition metals. The results thus suggest a strategy for the selection of alloying species that may be utilized to control twin activity in the design of transition metals with optimized mechanical properties. In particular, the results suggest strategies for designing alloys that mimic the unique properties of Re by choosing combinations of alloying elements that lead to similar overall band fillings.

More generally, the results demonstrate a link between electronic structure and interfacial stability that may be effective in controlling interface-related properties of transition-metal alloys more generally. Specifically, the tuning of  $d$  band filling to stabilize specific atomic configurations may represent an effective strategy in stabilizing grain and twin boundaries that feature a high fraction of such structural units. Thus, classical theories of bulk phase stability in transition metals can provide guidelines for “interfacial engineering” of transition-metal alloys with properties controlled by their interfaces.



## Chapter 5

# Calculations of Planar Defect Energies in Substitutional Alloys Using Special-Quasirandom-Structures

### 5.1 Foreword

Dislocation slip and deformation twinning are the most commonly observed mechanisms for plastic deformation in metals and alloys. Which of these mechanisms dominates for a given material and loading condition is generally governed by the ease of nucleation of the relevant defects, and their growth and propagation. These processes are in turn strongly influenced by the energetics of planar defects, such as generalized stacking faults and twin boundaries. The competition between plastic deformation and fracture, underlying the intrinsic ductility of a material, is thus commonly investigated through the consideration of the relative values of the energies for relevant planar faults and the free surfaces formed by crack propagation [212, 213, 214, 215].

For example, in the theory of Thomson and Rice [213, 216], larger values of the ratio of the surface energy ( $\gamma_s$ ) to the unstable stacking fault energy ( $\gamma_{\text{USF}}$ ) are an indicator of increasingly ductile behavior, as  $\gamma_{\text{USF}}$  corresponds to the barrier for dislocation slip at the crack tip, while  $\gamma_s$  measures the increase in surface energy due to crack growth. This theory has been used in the literature to study the ductility in metals from first principles (e.g. [127, 217]). Similarly, for hcp metals larger values of the ratio  $\gamma_s/\gamma_t$  between surface and twin-boundary ( $\gamma_t$ ) energies have been shown to correlate with higher ductility under conditions where twinning at the crack tip is the relevant mechanism for plastic deformation [17]. For body centered cubic (bcc) and face centered cubic (fcc) materials, similar

measures of twinnability have been developed and employed, which are based on (unstable) stacking fault energies and unstable twin energies [118, 217, 218, 219, 220].

In applications of computational modeling to guide alloy design, methods for calculating the effect of composition on the planar fault energies defined above are useful to understand whether the introduction of specific solute species will tend to increase or decrease the ductility and strength of a given material. However, the calculation of planar defect energies in alloys is considerably more difficult than for elemental metals or ordered intermetallic compounds, due to the presence of configurational substitutional disorder, leading to a lack of translational periodicity. At present, two main approaches have been introduced for computing the composition dependence of planar defect energies in alloy solid solutions from first-principles.

In the first, stacking fault energies in alloys have been computed within the axial next-nearest-neighbor Ising (ANNNI) lattice-model formalism [221, 105, 222, 223, 224, 225, 226, 227, 228, 229, 230, 106, 231, 232]. In this approach, the energies of fcc, hcp and double-hcp structures are computed to derive pairwise interactions that parametrize the change in energy associated with different stacking sequences of close-packed planes. Once derived from bulk energy calculations, these interactions are used to predict the excess energy of an isolated stacking fault. This method has been used for alloys, in which case the special-quasirandom-structure (SQS) approach [87, 88, 93] has been used to model the energetics of compositionally disordered fcc, hcp and double hcp structures [87, 88, 93, 233, 234]. While this approach provides a powerful framework for computing the composition dependence of stable stacking fault energies, it is not possible to apply the method to calculations of unstable stacking fault energies, defined as the energy maximum in the generalized-stacking-fault (GSF) surface. Further, it is not apparent how to generalize the approach in the consideration of the energies of surfaces, or the large variety of twin boundaries observed in the deformation of hcp metals.

Another approach that has been employed to compute stacking-fault and surface energies in alloys is based on the use of the coherent potential approximation (CPA) [194, 235, 236]. In applications of the CPA to the calculation of energies of bulk alloys, a disordered substitutional arrangement of atoms over the sites of a parent lattice is modeled using a single effective atomic species defined to have the average electron-scattering properties of the alloy. This procedure restores the translational symmetry of the underlying parent lattice, facilitating direct DFT calculations of bulk alloy energetics. The CPA approach has been generalized to consider layered structures, to enable calculations of stable stacking fault and surface energies [237, 238, 239, 240, 194, 241, 242, 243, 244, 245]. At present, however, the implementations of the approach do not allow for the accurate treatment of atomic displacements and the generalization of the method to the study of unstable stacking faults and general low-symmetry twin boundaries, for which significant

atomic shuffles may arise, has not been demonstrated to the best of our knowledge.

In the present chapter we describe a general approach for calculating the energies of planar defects in substitutional alloys, based on a generalization of the SQS method [87, 88] developed to compute the electronic structure and energetics of bulk substitutional alloys. The approach was demonstrated recently in applications to the calculation of twin-boundary and surface energies in hcp Re-based alloys [246]. In this chapter we describe a refinement of the approach, employing planar averaging, and provide details of the SQS structures used in the method. Further, we demonstrate the application of this approach also in the study of unstable stacking fault and surface energies. We present a test of the accuracy of the approach, through comparisons with large-supercell benchmark results derived employing a classical embedded-atom-method (EAM) interatomic potential model for Ti-Al alloys [247]. Finally, an application of the SQS-based method in DFT calculations of the dependence of twin boundary energies on Al content in Ti-Al hcp alloys is demonstrated.

Part of the results presented in this chapter, including the figures and tables, have been submitted as a regular article to Physical Review B, titled “Calculations of Planar Defect Energies in Substitutional Alloys Using Special-Quasirandom-Structures”, with authors Maarten de Jong, Liang Qi, David Olmstes, Axel van de Walle and Mark Asta.

## 5.2 Methodology

In this section we describe details associated with the calculation of planar defect energies in alloys, employing supercell models in conjunction with the SQS approach for configurational averaging. The focus is on hcp alloys, considering three types of planar defects that are relevant to their mechanical properties: twin boundaries, unstable stacking faults and free surfaces. Specifically, we consider the  $\{11\bar{2}1\}$  twin boundary, which is observed in the deformation microstructures of many hcp metals and alloys such as Ti, Re, Mg and Be [17, 126, 248, 119]. Further we consider calculations of the generalized stacking fault (GSF) surface corresponding the common  $\{1\bar{1}00\}$   $\langle 11\bar{2}0 \rangle$  slip system in hcp metals. Finally, the energies of  $\{1\bar{1}00\}$  free surfaces are considered. We begin by describing the supercells and planar averaging employed for the modeling of these planar defects and the calculation of their energies. A discussion of the generation of the SQS models is then presented, followed by the computational details for the present studies.

## 5.2.1 Supercell Geometries

### Twin Boundaries

The  $\{11\bar{2}1\}$  twin boundary in the hcp structure can be described by 4 twinning elements  $K_1 = (11\bar{2}1)$ ,  $K_2 = (0001)$ ,  $\eta_1 = [\bar{1}\bar{1}26]$  and  $\eta_2 = [11\bar{2}0]$ . [249, 250] These twinning elements denote the twinning plane, conjugate twinning plane, twinning direction and conjugate twinning direction, respectively. The amount of twinning shear for this twin is  $S = \gamma^{-1}$ , where  $\gamma = c/a$ , i.e. the axial ratio of the  $c$  and  $a$  lattice parameters. Since hcp metals have 2 atoms in the motif corresponding to a hexagonal Bravais lattice-point, in general twins cannot be formed by the application of a homogeneous twinning shear alone, and additional atomic shuffles are required [249, 172]. For the  $\{11\bar{2}1\}$  twin boundary, the required atomic shuffles on both sides of the twin boundary plane are given by the vector  $\tau = \pm 0.5 [1\bar{1}00]$  [172].

In this work, the  $\{11\bar{2}1\}$  twin boundary is constructed directly from an appropriate bulk cell as follows. First, as illustrated in Fig. 5.1 (a) the bulk cell is constructed with lattice vectors parallel to  $\mathbf{a} = [10\bar{1}2]$ ,  $\mathbf{b} = [10\bar{1}0]$  and  $\mathbf{c} = [\bar{1}100]$ . The dimension along  $\mathbf{b}$  is 8 times the conventional bulk hcp lattice constant  $a$ . This dimension is chosen such that the bulk cell can be employed to build twin boundary geometries, with sufficient spacing between the twin and its periodic images to minimize spurious interactions. The required bulk cell size is established by convergence studies, which show for the systems considered in this work that beyond 6 planes from the twin boundary, the solute formation energies are essentially converged to the bulk value. This leads to a bulk cell consisting of 64 atoms. The distance separating the two twins in the periodic cell that is required to achieve converged interfacial energies is expected to be system dependent, such that the dimensions of the cells employed in this work may not transfer directly to other alloy compositions. For each system, convergence testing should be undertaken.

In the second step, the twin boundary cell is formed by i) applying a twinning shear  $S$  to all atoms located on one side of the twin plane in the middle of the supercell (i.e., half way along the periodic length along the  $\mathbf{b}$  direction), followed by ii) an atomic shuffle on one side of the twin plane, as described above. This results in a twinned cell with a twin plane in the middle and another on the edge of the cell, as illustrated in Fig. 5.1 (b). Note that there exists a direct mapping between atoms in the bulk and twinned cell, which is important for the application of the SQS approach. Further note that several possible independent locations exist in the bulk cell where the twin plane can be inserted. In Fig. 5.1, the twin is placed in the center of the cell, but this location is arbitrary and for studying planar defects in alloys, we have found improved accuracy when results are averaged over all possible locations of the planar interface, as described below.

For calculations of the twin boundary energy, the initial and final geometries

shown schematically in Figs. 5.1 (a) and (b), respectively, are calculated and  $\gamma_t$  is extracted from the energy difference divided by the twin boundary surface area, taking into account the presence of two twin boundaries per periodic supercell. In the energy calculations for the twinned supercells ionic relaxations are performed, and the dimension perpendicular to the twin plane is relaxed, while holding the periodic distances in the twin plane (i.e., along **a** and **c**) fixed at the values dictated by the bulk hcp supercell.

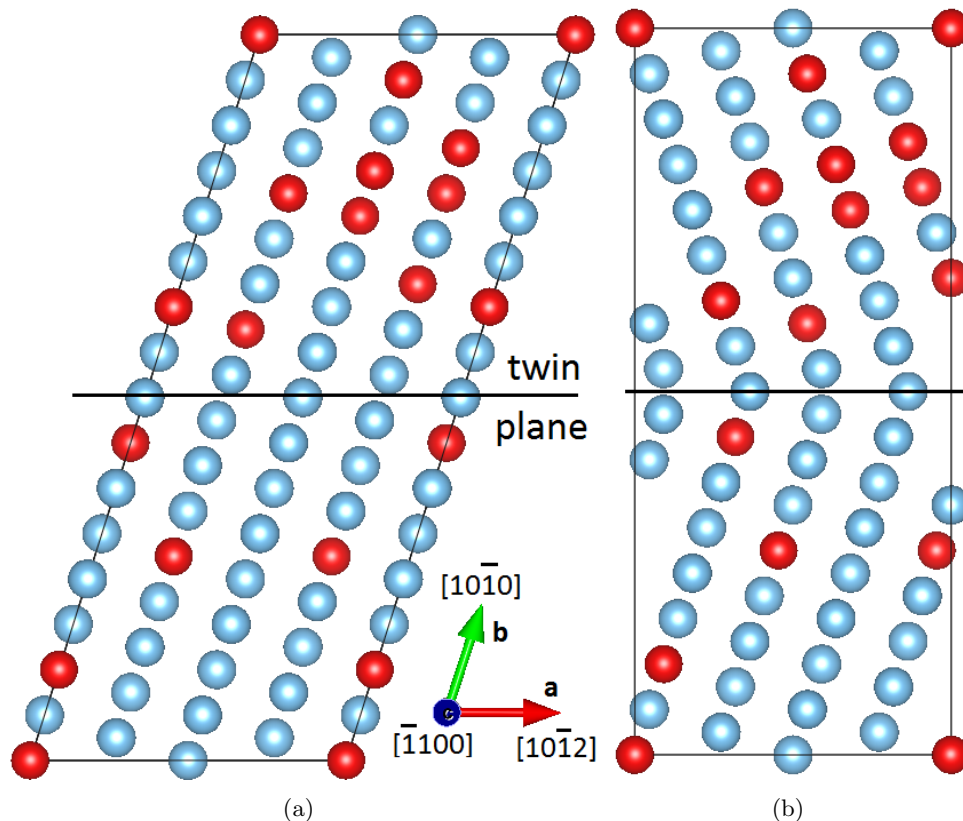


Figure 5.1: Example supercell geometry for (a) a bulk alloy with an appropriate orientation for defect calculations and (b) a  $\{11\bar{2}1\}$  twin boundary cell, formed from the bulk after an appropriate combination of shear and shuffle. This figure shows a projection along the  $[\bar{1}100]$ -direction. The twin-plane is inserted in the center of the bulk cell and is also indicated.

## Unstable Stacking Faults and Surfaces

Supercells for the calculation of the  $\{1\bar{1}00\}$   $\langle 11\bar{2}0 \rangle$  GSF energy, and the  $\{1\bar{1}00\}$  surface energy are constructed by choosing lattice vectors in the directions  $\mathbf{a} = [11\bar{2}0]$ ,  $\mathbf{b} = [0001]$  and  $\mathbf{c} = [1\bar{1}00]$ , as illustrated in Fig. 5.2 (a). As above, the cells contain atomic configurations derived from the SQS algorithm described in the next section. When performing calculations of the GSF and surface energies, two planes are picked which will be (i) rigidly shifted along the  $\mathbf{a} = [11\bar{2}0]$  direction in order to create a stacking fault, or (ii) separated by a vacuum layer in order to create two free surfaces. All possible choices for these neighboring planes are considered and the planar energies are derived by averaging results over these different sets of planes.

Considering first the calculation of the GSF energy, the bulk supercell is set up initially to be periodic along all three directions. The size of the original bulk supercell is three times the bulk hcp lattice constant ( $a$ ) along  $\mathbf{a}$ , two times the bulk hcp lattice parameter ( $c$ ) along  $\mathbf{b}$ , and there are 6 layers of prismatic planes (for each plane there are two sub-layers) along  $\mathbf{c}$ , resulting in a total number of 72 atoms. To calculate the GSF energy and  $\gamma_{\text{USF}}$  in particular, all atoms in the half supercell below a given  $(1\bar{1}00)$  plane in the middle of the supercell are rigidly shifted along the  $[11\bar{2}0]$  direction with the slip distances set as 0, 0.35, 0.45, 0.5 and 0.6  $a$ , respectively. These shifts are accommodated by distorting the unit cell to have an angle different from 90 degrees between the  $\mathbf{a}$  and  $\mathbf{c}$  directions, so there is only one stack fault interface in this periodic supercell, as illustrated in Fig. 5.2 (b). For each slip vector, all the atoms in the supercells are relaxed along the  $\mathbf{c}$  direction but fixed along the  $\mathbf{a}$  and  $\mathbf{b}$  directions. The supercell size along the  $\mathbf{c} = [1\bar{1}00]$  direction is also relaxed to remove the normal stress perpendicular to the  $(1\bar{1}00)$  plane. The GSF energy surface is plotted based on the energy increase at these slip distances relative to the undeformed structure, and  $\gamma_{\text{USF}}$  is derived by interpolating the maximum point on the GSF curve.

To compute the  $\{1\bar{1}00\}$  surface energy  $\gamma_{\text{s}}$ , we start by calculating the energy of the bulk supercell illustrated in Fig. 5.2 (a). This reference energy is computed with periodic boundaries in all three directions, the same as the reference supercells for GSF calculations. The energy of this periodic bulk supercell reference energy is then compared to the energy obtained for the supercell illustrated in Fig. 5.2 (c), where a vacuum layer of 15 Å is introduced in the middle of the relaxed supercell, giving rise to two  $\{1\bar{1}00\}$  surface planes. From the energy difference of these two supercells, divided by twice the cross-sectional area parallel to the surface planes, the value of  $\gamma_{\text{s}}$  is derived. In the calculations of the energies of the bulk and surface supercells the positions of all atoms are relaxed.

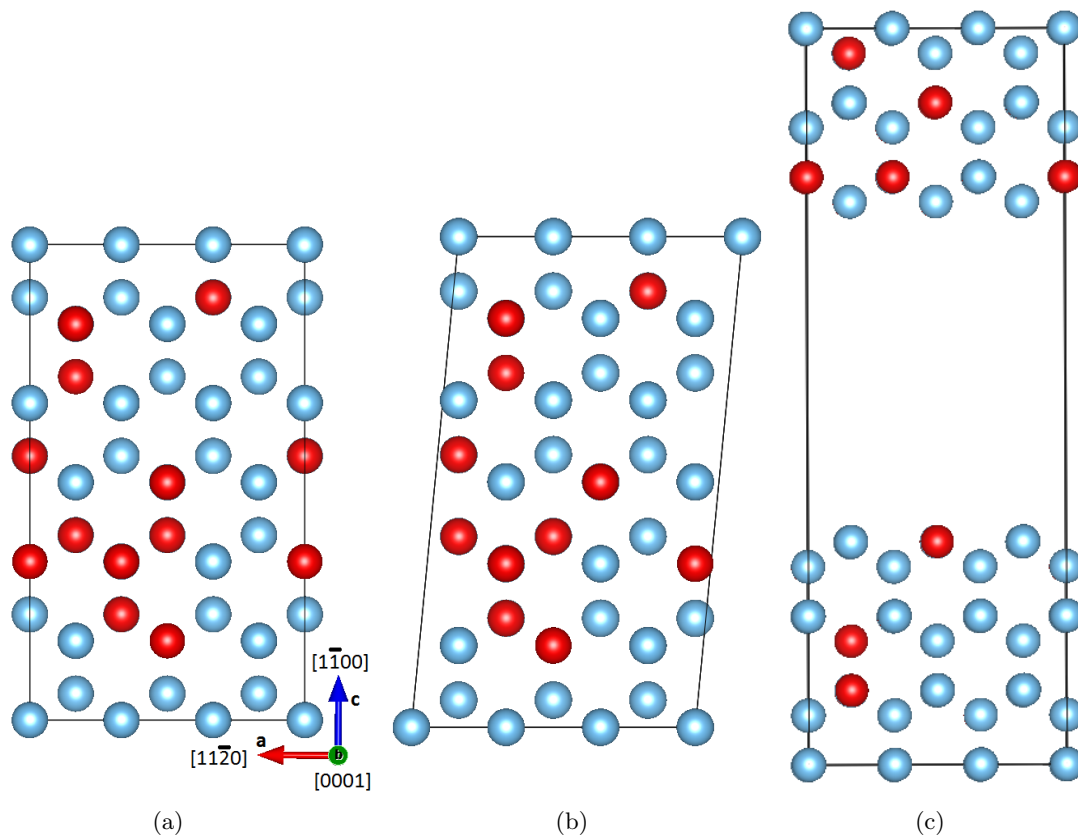


Figure 5.2: Supercell geometry for (a) a bulk cell with an appropriate orientation for defect calculations (b) calculation of the generalized stacking-fault energy and (c) calculation of free-surface energies. These figures show a projection along the  $[0001]$ -direction.

### 5.2.2 SQS Generation

The SQS structures were developed for each of the bulk supercells defined in the previous subsection at different compositions starting at approximately 3 at.% solute, up to a maximum concentration of 25 at.% solute, with increments of approximately 3 at.%. A genetic algorithm (GA) was used for optimizing the SQS configuration, as described below. GA's have been employed in the materials-science community in the study of different topics such as crystal-structure prediction [251, 252, 253] and in the construction of cluster expansions [254, 255].

We consider one of the bulk hcp supercells above, containing a total of  $N$  atomic sites. A binary alloy configuration for a given cell shape can be represented by a chro-

mosome of length  $N$  of the form [01101001...], where each location  $i$  in the chromosome uniquely corresponds to an atomic position in the bulk cell, and each can take a value of either 0 or 1, indicating that the position  $i$  is occupied by either an A-type or B-type atom, respectively. The objective function to be minimized is the euclidian difference norm between the vector describing the atomic correlation functions of a random solid solution,  $\mathbf{x}^{random}$  and the vector describing the correlation functions of the finite-sized supercell  $\mathbf{x}^{scell}$ . The fitness of any given configuration is inversely proportional to this euclidian difference norm  $\|\mathbf{x}^{random} - \mathbf{x}^{scell}\|$ . In this work, 6 atomic correlation functions are considered for pairs, and 3 for triplets. The atomic correlation functions for both the random alloys and the trial configurations are calculated using the alloy theoretic automated toolkit (ATAT) [256, 257] and fed to the GA during the iterative optimization process. In defining the fitness function, we explored different weighing factors for the different pair and triplet clusters, e.g., giving higher weight in the difference norm to shorter pairs and/or to clusters with higher multiplicities. Several different sets of weights were explored and even though different SQS were obtained for each, we found minimal influence on the resulting planar defect energies.

The optimization procedure is initiated by generating an initial population of 800 randomly generated configurations at a given composition. The selection method used is roulette wheel selection, in which selection probability for mating is proportional to the fitness score. Crossover cannot be performed using standard schemes such as 1 or 2-point crossover, since these will change alloy composition during the optimization. Instead, crossover is performed using the edge crossover algorithm [258], which ensures the composition of the configurations remains constant, i.e., the number of 0's and 1's remains unchanged during the optimization process. Further, a 0.5 % probability of mutation is allowed and the algorithm is run for 1000 generations. In practice, we found that after only about 100 generations the resulting SQS had converged to the optimum near-random atomic correlation functions.

For an optimized bulk SQS such as shown in Fig. 5.3, there are several choices where the twin planes can be inserted into the cell. Fig. 5.3 shows 8 possible locations of the TB plane within the 64-atom SQS. A single SQS cell contains (after the deformation process shown in Fig. 5.1 (a) and (b)) both a twin boundary at the center (location 5 in Fig. 5.3) as well as another at the periodic boundary at location 1. Hence, all possible twin planes can be considered with a single bulk SQS configuration, that is deformed according to 4 independent shear modes. The local atomic environment and solute-concentration vary along the  $b$ -direction and hence, the TB energy will vary depending on the location of the twin plane in the supercell. As discussed above, planar defect energies are calculated by inserting the TB into different locations in a single SQS and taking a configurational average over those individual configurations. Similarly, for the GSF and surfaces, there are six independent choices for the location of the surfaces and planar defect energies are



computed by averaging over each.

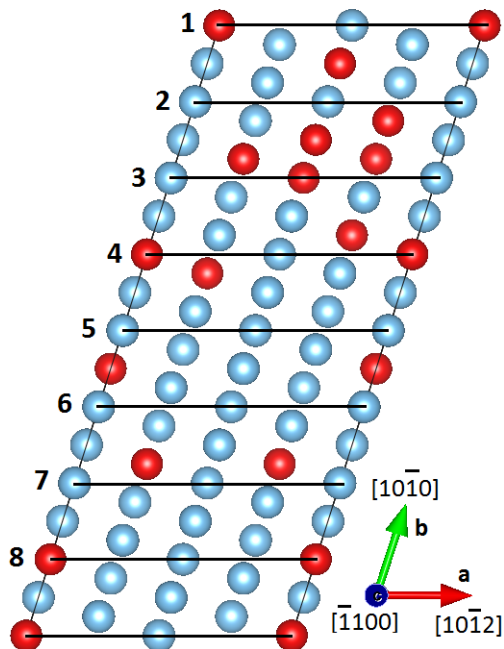


Figure 5.3: Illustration of an SQS and configurational averaging-procedure used to compute the  $\{11\bar{2}1\}$  TB energy. For the TB-calculations, a configurational average over 8 configurations within a single SQS-cell is employed. This figure shows a projection along the  $[1\bar{1}00]$ -direction.

### 5.2.3 Computational Methods

#### Embedded-Atom-Method Calculations

The purpose of the computations based on classical embedded-atom-method (EAM) potentials performed in this work is to enable a comparison of planar defect energies obtained from the relatively small SQS supercells, with benchmark results obtained by direct configurational averaging over much larger supercells having a size that ensures minimal effects of periodic boundary conditions and accurate configurational averaging. These large cells are beyond the size that can be modeled directly by DFT, but their energies can be readily calculated using EAM potentials. Specifically, due to the small computational cost of performing EAM energy calculations, we consider as our benchmark results obtained from supercell models containing up to a million (1M) atoms in total, with the configuration of A and B atoms generated randomly for a given fixed overall alloy composition.

These very large 1M cells are assumed to provide adequate configurational averaging to yield converged planar-defect energies for random solid solutions. As in the small SQS models, the planar defect energy is computed by subtracting the energy of the bulk cell from the energy of the corresponding cell containing the desired twin, surface or unstable stacking-fault defect. A reliable estimate of the planar defect energy in the random alloy can be obtained by averaging over a few of these large supercells. This procedure can be repeated for different solute compositions such that the concentration dependence of the defect energies for a random substitutional alloy can be computed. The results computed as such form a benchmark for the defect energies in disordered substitutional alloys, and the aim is to assess the accuracy of the SQS models in reproducing these values. In all of the EAM calculations we consider the defect energies for hcp-based Ti-Al alloys, modeled with the potential of Zope and Mishin [247].

## Density Functional Theory Calculations

In addition to the EAM modeling described in the previous section, we also demonstrate the application of the SQS methodology in DFT-based computations of the concentration dependence of  $\{11\bar{2}1\}$  twin boundaries in hcp-based Ti-Al alloys. These DFT calculations were performed using the Vienna Ab Initio Simulation Package (VASP) [136, 137]. The VASP calculations made use of the generalized-gradient-approximation exchange-correlation energy due to Perdew-Burke-Ernzerhof generalized gradient functional (PBE-GGA) [150]. All calculations made use of the projector augmented wave (PAW) formalism [52, 53], in which the potentials for Ti (Al) treat  $4s$  and  $3d$ -states ( $3s$  and  $3p$  states) as valence. An energy cutoff for the plane waves of 600 eV was used, and smearing of the electronic occupancies was performed using the Methfessel-Paxton scheme [140], with a broadening of 0.05 eV. Integrations in the Brillouin zone were carried out using Monkhorst-Pack  $k$ -point sampling [139] with a density chosen such that the number of  $k$ -points in the first Brillouin zone times the number of atoms in the cell equals approximately 25,000.

## 5.3 Results and Discussion

### 5.3.1 Embedded Atom Method Results

#### Twin Boundary Energies

In Fig. 5.4, the variation of the  $\{11\bar{2}1\}$  twin boundary energy is plotted as a function of the atomic concentration of Al. The (red) open circle symbols are the benchmark results, labeled “Random-1M,” obtained from a supercell containing approximately a million atoms, with randomly generated atomic configurations. The results labeled “SQS-64” were obtained by averaging over the different possible positions of the twin planes in SQS 64-atom supercells, generated as described in the previous section, and are plotted with

(blue) filled squares. The error bars for the SQS results denote one standard deviation in the values obtained for the different choices of the TB plane position, and provide a measure of the width of the distribution in the individual planar defect energies.

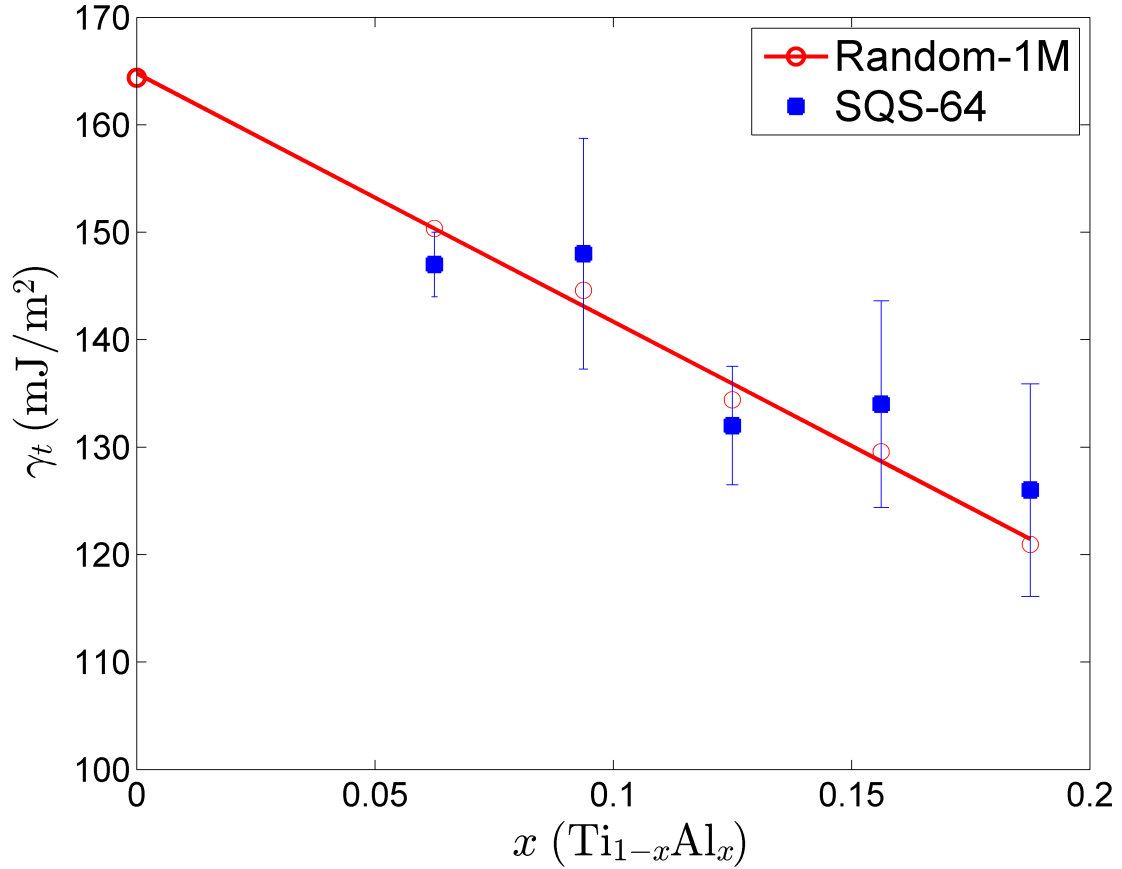


Figure 5.4:  $\{11\bar{2}1\}$  twin boundary energies ( $\gamma_t$ ) in  $\text{Ti}_{1-x}\text{Al}_x$  alloys calculated using EAM potentials with two different supercell models: the benchmark Random-1M supercell, and the SQS-64 supercell. For the 64-atom SQS supercell, the results are an average over 8 planes in one SQS, and the error bars are standard deviations. The line through the benchmark Random-1M results is a guide to the eye.

It can be seen from Fig. 5.4 that the SQS and benchmark results at each composition agree to within approximately 10 %. To further quantify the degree of agreement between the SQS and benchmark results, we consider the composition dependence of the twin-boundary energies, as characterized by a dimensionless parameter, defined as  $\eta_\gamma = (\partial\gamma/\partial x)/\gamma_0$ , where  $\gamma$  represents the planar defect energy corresponding to the atomic

Table 5.1: Concentration dependence of planar defect energies in hcp  $\text{Ti}_{1-x}\text{Al}_x$  solid solutions,  $\eta_\gamma = (\partial\gamma/\partial x)/\gamma_0$ , as calculated with EAM interatomic potentials, using benchmark Random-1M and SQS-72/64 supercell models. For the twin boundary, 64-atom SQS supercells are employed, and for the surface and stacking fault energies, 72-atom SQS supercells are employed. The Al atomic fraction is denoted by  $x$  for the  $\{1\bar{1}00\}$  surface.

| Planar defect                                     |                   | EAM (Random-1M) | EAM (SQS) |
|---|-------------------|-----------------|-----------|
| $\{11\bar{2}1\}$ Twin                             |                   | -1.56           | -1.43     |
| $\{1\bar{1}00\}$ $\langle 11\bar{2}0 \rangle$ USF |                   | 0.57            | 0.55      |
| $\{1\bar{1}00\}$ Surface                          | $x \approx 0.08$  | -0.12           | -0.10     |
| $\{1\bar{1}00\}$ Surface                          | $x \approx 0.195$ | -0.19           | -0.22     |

fraction of Al in the  $\text{Ti}_{1-x}\text{Al}_x$  binary alloy, and  $\gamma_0$  is the defect energy for the pure-Ti reference state. The results obtained for  $\eta_\gamma$ , from a linear least squares fit (forced through the pure-Ti value) to the data sets in Fig. 5.4 are listed in Table 5.1. The SQS-64 supercells yield a value for  $\eta_\gamma$  that is about 10 % larger in magnitude than the corresponding value for the random-1M cells. Overall, the results in this section suggest that for atomic fractions of solute up to approximately  $x = 0.25$ , estimates of the twin boundary energy at each composition converged to within about 10 % (10 mJ/m<sup>2</sup>) can be derived by averaging results for 8 planes of a single 64-atom SQS-supercell configuration.

### Unstable Stacking-Fault Energies

In Fig. 5.5 the unstable stacking-fault energy  $\gamma_{\text{USF}}$  results are plotted as a function of solute concentration, based on calculations employing the 72-atom SQS supercells illustrated in Fig. 5.2 (a)-(b), and benchmark Random-1M supercells. As in the previous section, the error bars on the SQS results were obtained from the standard deviation in the six values corresponding to different choices for the prismatic plane defects.

A roughly linear variation of  $\gamma_{\text{USF}}$  with Al concentration is obtained for the benchmark Random-1M supercells, up to the concentration of  $x = 0.25$  considered in the calculations. Compared to these benchmark values, those obtained with the smaller 72-atom SQS supercell show significantly more scatter. However, for all compositions the SQS-72 supercells produce values for  $\gamma_{\text{USF}}$  that agree to within approximately 10 mJ/m<sup>2</sup> ( $\approx 2.5$  %) with the benchmark values. The concentration dependence of  $\gamma_{\text{USF}}$  is slightly underestimated relative to the benchmark results, by 5.3 %, with the SQS-72 supercells, as shown in Table 5.1.

### Surface Energies

In Fig. 5.6 results for the calculated  $\{1\bar{1}00\}$  surface energy ( $\gamma_s$ ) are plotted as a function of Al concentration. As in Fig. 5.5 results are plotted for the benchmark su-

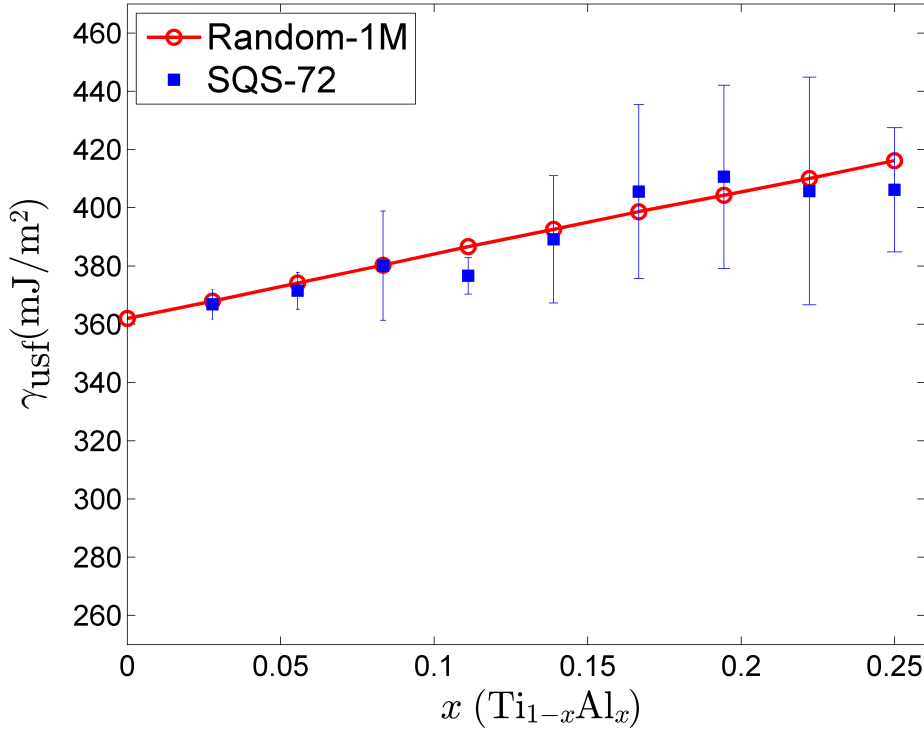


Figure 5.5: Unstable stacking fault energies in  $\text{Ti}_{1-x}\text{Al}_x$  alloys calculated using EAM potentials with two different supercell models: the benchmark Random-1M supercell, and the SQS-72 supercell. For the 72-atom SQS supercell, the results are an average over 6 planes in one SQS, and the error bars are standard deviations. The line through the benchmark Random-1M results is a guide to the eye.

percells, and for the 72-atom SQS supercells. The average values and error bars for the SQS cells have again been obtained from an average over 6 planes. The averaged values obtained from the SQS-72 supercells show agreement with the benchmark results to within  $10 \text{ mJ/m}^2$ , or less than 1 % of the magnitude of  $\gamma_s$ .

To compare the predictions of the 72-atom supercells for the concentration dependence of  $\gamma_s$ , we fit each data set in Fig. 5.6 with a parabola, to account for the non-linear behavior that can clearly be observed in the figure. The composition dependence, as characterized by the  $\eta_\gamma$  parameter, is evaluated for two compositions and the Random-1M and SQS-72 values are compared in Table 5.1. The agreement is seen to be at the level of 15-17 % at the two different compositions listed.

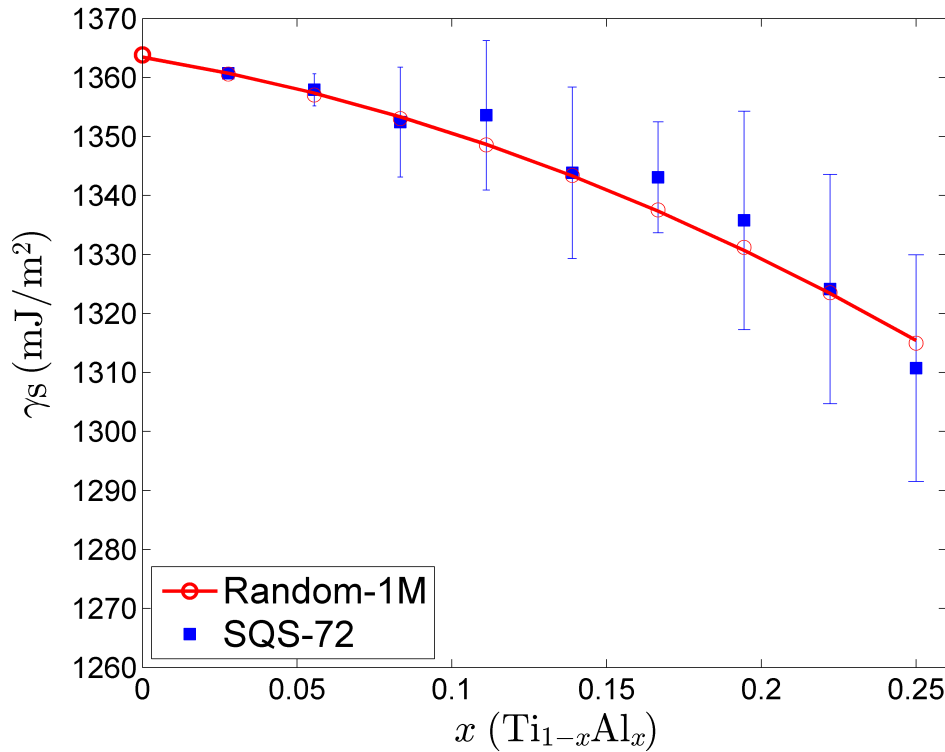


Figure 5.6:  $\{1\bar{1}00\}$  surface energies in  $\text{Ti}_{1-x}\text{Al}_x$  alloys calculated using EAM potentials with two different supercell models: the benchmark Random-1M supercell, and the SQS-72 supercell. For the 72-atom SQS supercell, the results are an average over 6 planes in one SQS, and the error bars are standard deviations. The line through the benchmark Random-1M results is a guide to the eye.

### SQS Versus Random Supercells

It is interesting to consider whether the SQS configurations used in the comparisons above lead to improved agreement with benchmark results, relative to values derived from supercells with the same size, but with the atomic configurations generated randomly rather than by the SQS algorithm. In other words, it is of interest to consider whether the extra work that is required to generate the SQS configurations for a given defect supercell leads to a significant increase in accuracy. To test this, we have undertaken a statistical analysis comparing the performance of random and SQS supercell configurations against the benchmark values. Results of such tests are reported in this section for the specific case of the twin-boundary planar defects, but similar conclusions were reached for the GSF and surface defects.

We begin by generating a large number of randomly occupied structures and rank these according to a performance metric that measures how close the pair and triplet correlation functions are to the values for a random alloy with the same composition. For the dilute compositions, an exhaustive enumeration [90, 91, 92] is performed of *all* symmetrically inequivalent atomic configurations at a fixed composition. For the more concentrated alloys, exhaustive enumeration is beyond reach and we instead generate a million symmetry inequivalent structures. These configurations are then ranked from #1, indicating the best agreement with random correlation functions, in ascending order towards the worst. For all the configurations generated, the  $\{11\bar{2}1\}$  twin boundary energy is calculated by planar averaging and it is examined how well the resulting defect energies approximate the benchmark Random-1M results. In this section, Ti-Al alloys with a solute concentration of 12.5 at. % Al are considered, but similar conclusions hold for different compositions.

In total, a million symmetry-inequivalent alloys are generated at a composition of  $\text{Ti}_{56}\text{Al}_8$  and for each, the atomic correlation functions (6 pairs, 3 triplets) are calculated. These are referred to as  $\text{corr}^{\text{SQS}}$ . The million structures are then ranked according to the metric  $\|\text{corr}^{\text{SQS}} - \text{corr}^{\text{Random}}\|$ . Smaller values for  $\|\text{corr}^{\text{SQS}} - \text{corr}^{\text{Random}}\|$  indicate a configuration that is a better approximation of the true random alloy. Figure 5.7 shows the distribution of this metric over the million structures, together with a  $\beta$ -distribution that is fit through the data. The mean of the distribution is approximately 0.26, the best SQS structures exhibit qualities  $\|\text{corr}^{\text{SQS}} - \text{corr}^{\text{Random}}\| \approx 0.10$  and for the worst configurations  $\|\text{corr}^{\text{SQS}} - \text{corr}^{\text{Random}}\| \approx 0.65$ .

It is now addressed how well the structures used to generate Fig. 5.7 perform in their prediction of  $\{11\bar{2}1\}$  twin boundary energies, compared with the Random-1M benchmark results. To this end, the million structures are split-up in 1,000 bins of 1,000 structures, where the first bin represents the 1,000 best configurations (corresponding to  $\|\text{corr}^{\text{SQS}} - \text{corr}^{\text{Random}}\| \approx 0.10$ ), the second bin represents the second best group of configurations, and so forth. The last bin corresponds to  $\|\text{corr}^{\text{SQS}} - \text{corr}^{\text{Random}}\| \approx 0.65$  and represents the bin containing the worst performing configurations. It is next examined for each of the bins how large the probability is that a structure picked at random from the bin yields a  $\{11\bar{2}1\}$  twin boundary energy that is within 10 % of the Random-1M benchmark value. The results are shown in Fig. 5.8, in which a second order polynomial is fit through the calculated probability data. The horizontal axis again represents the value of  $\|\text{corr}^{\text{SQS}} - \text{corr}^{\text{Random}}\|$ , as in Fig. 5.7. The vertical axis in Fig. 5.8 represents  $P\left(\left\|\frac{\gamma_t^{\text{SQS}} - \gamma_t^{\text{Random}}}{\gamma_t^{\text{SQS}}}\right\| < 0.1\right)$ , i.e., the probability that a configuration in the bin and the random-1M benchmark twin-boundary energies are within 10 %.

Figure 5.8 shows clearly that among the best SQS structures (i.e., amongst the configurations with the lowest values of  $\|\text{corr}^{\text{SQS}} - \text{corr}^{\text{Random}}\|$ ), there is a significantly

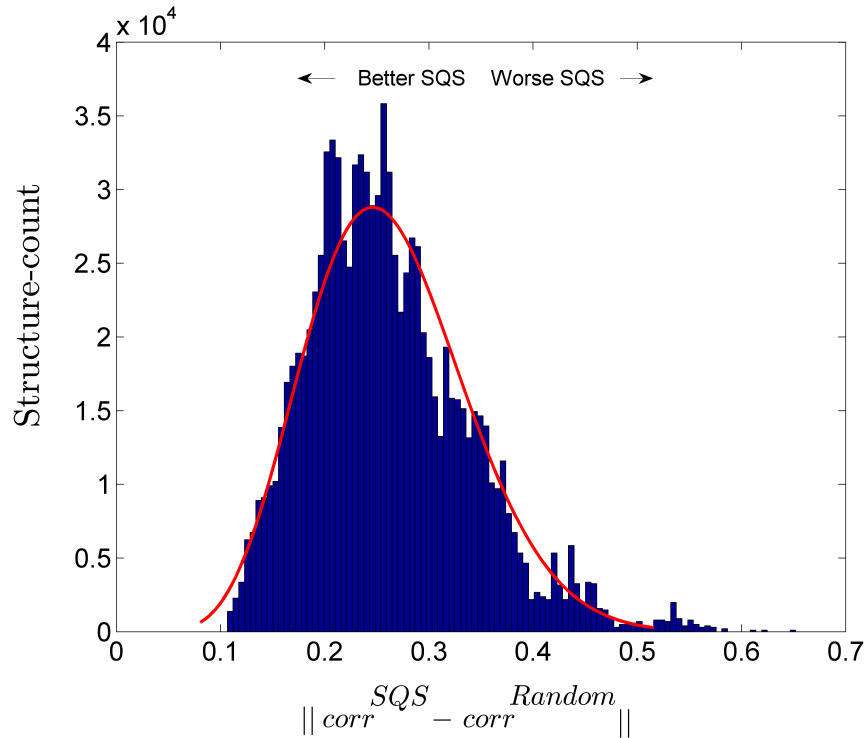


Figure 5.7: The distribution of  $\|corr^{SQS} - corr^{Random}\|$  over a million substitutional configurations for an hcp  $Ti_{56}Al_8$  bulk alloy. A  $\beta$ -distribution is fit to the data and plotted by the solid (red) line in the histogram.

higher probability of reproducing the Random-1M results for the  $\{11\bar{2}1\}$  twin boundary energy than among the poorly performing configurations. For example, in the bin containing the best configurations, approximately 80 % of the structures reproduce the Random-1M twin energies to within 10 %. On the other hand, in the bin containing the configurations with the highest values of  $\|corr^{SQS} - corr^{Random}\|$ , only 25 % of the structures reproduce the Random-1M twin energies to within 10 %. Structures that are located near the mean of the distribution reproduce the Random-1M energies to within 10 % in approximately 50 % of the cases. Hence, we conclude that a high-quality SQS structure is expected statistically to perform significantly better than structures generated by random occupations.

### 5.3.2 Density Functional Theory Results

As an illustration of the use of the SQS approach in combination with DFT-based total-energy calculations, we plot in Fig. 5.9 calculated results for the  $\{11\bar{2}1\}$  twin boundary as a function of Al concentration in  $Ti_{1-x}Al_x$  hcp-based solid solutions. The DFT



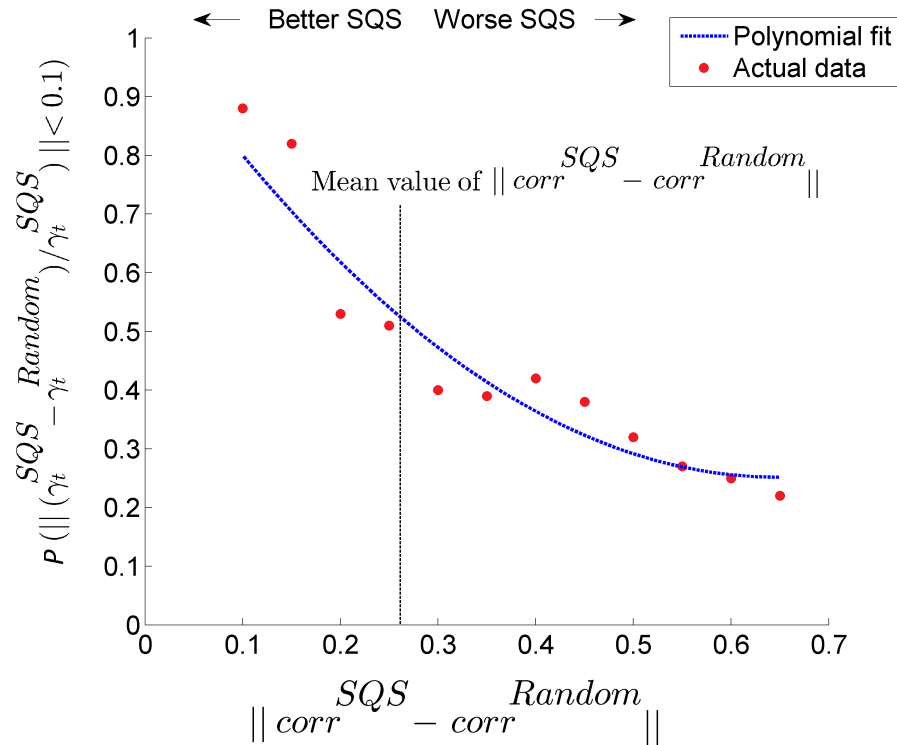


Figure 5.8: Probability of reproducing the Random-1M twin energies to within 10 % as a function of the metric  $\|corr^{SQS} - corr^{Random}\|$ . The curve indicates a second order polynomial, fit to the calculated data.

results were obtained with a 64-atom SQS supercell, averaging over the different choices for the TB plane position, as above. The average values and standard deviations obtained by DFT are plotted with filled circles, and the results are compared to those obtained from the EAM employing the same SQS approach, which are reproduced in the lower panel.

It is seen in Fig. 5.9 that the EAM underestimates the  $\{11\bar{2}1\}$  twin boundary energy significantly with respect to the DFT value for pure Ti. We further note that EAM and DFT predict different trends of twin energy versus Al concentration. Whereas EAM predicts a monotonic and almost linear decrease of the  $\{11\bar{2}1\}$  twin boundary energy with increasing Al content, the DFT calculations predict a much weaker concentration dependence.

It should be emphasized that the differences between EAM and DFT observed here are not a result of the SQS planar averaging, but a reflection of inaccuracies in the

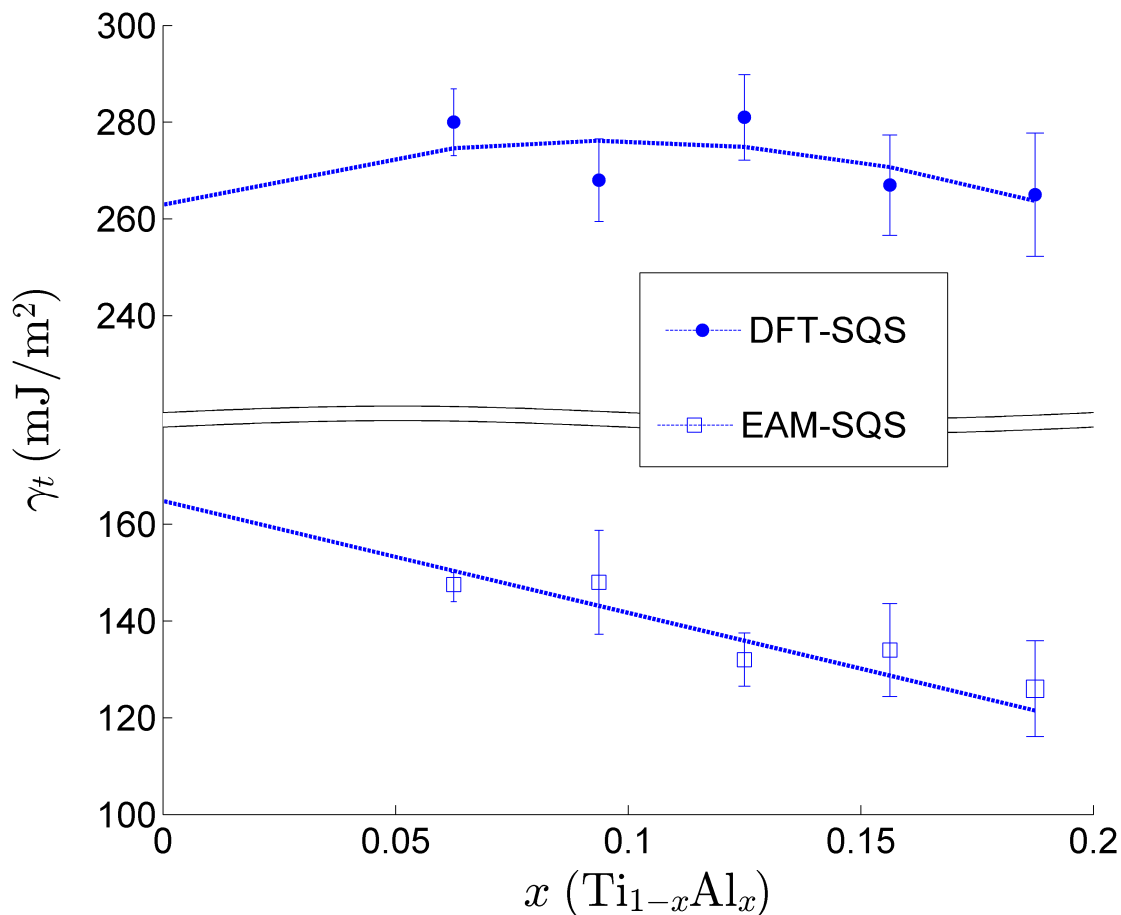


Figure 5.9:  $\{11\bar{2}1\}$  twin boundary energy  $\gamma_t$  in  $\text{Ti}_{1-x}\text{Al}_x$  alloys calculated with 64-atom SQS supercells by DFT and EAM. The results plotted are averaged over 8 planes per supercell, with error bars denoting standard deviations. The lines are guides to the eye.

classical potential model for twin boundary energies in Ti-Al alloys. This is apparent based on the discrepancies for the results for pure Ti. Additionally, we have used the 64-atom supercell models with one Al solute atom present to compute segregation energies to the  $\{11\bar{2}1\}$  twin boundary. It is found that the EAM potential predicts an energetic preference of an individual Al-atom to segregate to the twin plane and nearby planes, whereas DFT shows the opposite: the Al-atom prefers to reside in positions away from the twin. Since DFT and EAM yield contradictory results even in this dilute limit, the discrepancies in the results obtained for more concentrated alloys are not surprising. We note that discrepancies between EAM and DFT are not uncommon in cases such as these where the property of interest (namely twin boundary energetics) were not included in the fitting of the EAM

potential (e.g., [259]).

## 5.4 Summary and Conclusions

In the present work we have presented a method for computing the energetics of planar defects in random substitutional alloys employing an approach based on the use of the SQS formalism. It is shown using an EAM model for hcp-based Ti-Al alloys that averaging over results obtained for different planes in an SQS cell gives values for twin boundary, unstable stacking fault and surface energies that agree to within approximately 10 % with benchmark values obtained from direct configurational averaging using large supercells. The SQS-based supercells considered in this work are small enough such that their energies can be computed by DFT. This is demonstrated in DFT-based studies of the concentration dependence of  $\{11\bar{2}1\}$  twin-boundary energies in hcp-based Ti-Al alloys. We anticipate that the method presented in this work will be useful in future DFT-based efforts aimed at alloy design. By combining results obtained with this approach within continuum theories of mechanical behavior, the SQS-approach described here provides a framework for investigating the effects of specific solute additions on the slip and twinning properties of alloys for targeted applications.

## Chapter 6

# Ideal-Strength Calculations on Hexagonal Close Packed Metals and Alloys

### 6.1 Foreword

Under tensile loading the ideal strength of a solid is governed by mechanical instabilities corresponding to failure in tension or shear, indicative of intrinsic brittle or ductile behavior, respectively. First principles-calculations for hexagonal close packed (hcp) metals under tensile loading along the  $c$  axis reveal that Be, Mg, Ru, Os and Zn fail in tension, while Sc, Y, Ti, Zr, Hf, Tc and Re fail in shear. An analytical model is developed that predicts this behavior in terms of the second and third order elastic constants. For the transition metals, filling of the  $d$ -bands is shown to correlate with the type of instability realized, thus providing unique insights into the effect of alloying on the intrinsic mechanical behavior of hcp metals.

### 6.2 Introduction

For a given loading condition, the ideal strength of a crystalline solid forms an upper bound on the mechanical stress that the material can sustain prior to reaching a mechanical instability. The nature of the instability reached at this stress level can provide insights into the intrinsic failure mechanisms for a material. For example, under tensile loading crack initiation requires that the local normal stress perpendicular to the cleavage plane is equal to or larger than the ideal tensile strength [130, 131, 260, 261]. However, when a material yields under tensile loading, it is possible for it to fail through a shear instability [262, 263, 264, 132, 265]. The tensile versus shear nature of the mechanical instability realized under tensile loading is of considerable interest as an indicator of whether

a material will behave in an intrinsically brittle or ductile manner. For cubic metals, first-principles calculations of ideal strength under tensile loading have revealed shear instabilities for the ductile metals V and Nb, whereas more brittle materials such as W and Mo have been shown to fail in tension [263]. Similar studies in alloys [266, 267, 268, 269] have been undertaken recently, yielding insights into compositional effects. For example, it has been shown that BCC-based Mo-alloys can be made intrinsically more ductile by tuning the  $d$  band filling through alloying [263].

In this work we consider the deformation behavior of the HCP metals, a class of materials that find use in diverse technological applications, spanning biomedical to automotive and aerospace. These materials can possess attractive properties such as high strength-to-weight ratios, high stiffness and/or high melting temperatures. However applications of these materials is often limited by low ductility, associated with the limited number of active slip systems in the HCP structure. Substantial efforts have been devoted to optimizing the ductility of HCP metals and alloys, for example by alloying and through the control of microstructure. Despite this significant body of work, the fundamental ideal strengths of HCP-metals have been reported for only a few systems [270], and no attempts at using the results of such studies to derive insights into the intrinsic ductility of these materials, and how they may be altered through alloying, have been made to the best of our knowledge.

For the HCP metals Be, Mg, Sc, Y, Ti, Zr, Hf, Tc, Re, Ru, Os and Zn, we compute the ideal strength and associated mechanical instabilities under tensile loading along the crystallographic  $c$  axis, i.e., perpendicular to the basal plane. This is a particularly important loading condition for the consideration of the intrinsic ductility of HCP metals, as the basal plane is a typical cleavage plane in these materials [17], and slip of the dominant  $a$ -type dislocations does not provide a mechanism for plastic elongation along the  $c$  direction. Based on the ideal deformation behavior, each of the HCP metals is characterized as intrinsically brittle or ductile, i.e., as possessing elastic instabilities that are either tensile or shear in nature, respectively. We further study map out domains of  $d$ -band filling for HCP transition metals where ductile vs brittle behavior can be expected. Finally, we provide an analytical formalism which enables the ideal strength and the nature of the intrinsic instability under tensile loading along the  $c$  axis to be derived solely from a knowledge of the second and third-order elastic constants. The analytical model is shown to yield predictions in reasonable agreement with explicit density-functional-theory (DFT) calculations across all of HCP metals considered in this work, with reduced computational cost.

## 6.3 Methodology

### 6.3.1 Wallace formalism and elastic instabilities in HCP materials

The elastic stability of a solid under zero stress is governed by the eigenvalues of its elastic-constant tensor; specifically, all 6 eigenvalues of this tensor must be larger than zero for the solid to be elastically stable. For a solid under an applied stress, elastic stability is governed instead by the Wallace tensor, defined as follows:

$$B_{ijkl} = C'_{ijkl} + \frac{1}{2} (\sigma_{il}\delta_{jk} + \sigma_{jl}\delta_{ik} + \sigma_{ik}\delta_{jl} + \sigma_{jk}\delta_{il} - 2\sigma_{ij}\delta_{kl}) \quad (6.1)$$

where  $C'_{ijkl}$  represents the elastic constants in the deformed configuration [271, 272, 273],  $\sigma_{ij}$  denotes the applied stress acting on the solid, and  $\delta_{ij}$  is the Kronecker-delta. The eigenvalues of the symmetrized Wallace tensor govern the elastic stability of a solid under stress [274]. In the present context, the symmetrized Wallace tensor,  $B_{sym}$  is defined as  $B_{sym} = 1/2 (B + B^T)$  (with  $B$  given in Eq. 6.1), where the use of Voigt notation is implied so that both  $B$  and  $B_{sym}$  reduce to 6×6 matrices. In the remainder of this chapter, the Wallace-tensor  $B_{ijkl}$  refers to the symmetrized Wallace tensor.

For the special case of an HCP structured material loaded in tension along the  $c$  axis, i.e., with only the stress component  $\sigma_{33}$  being non-zero, the Wallace tensor takes the following form:

$$B_{ijkl} = \begin{bmatrix} C'_{11} & C'_{12} & C'_{13} + \frac{\sigma_{33}}{2} & 0 & 0 & 0 \\ C'_{12} & C'_{11} & C'_{13} + \frac{\sigma_{33}}{2} & 0 & 0 & 0 \\ C'_{13} + \frac{\sigma_{33}}{2} & C'_{13} + \frac{\sigma_{33}}{2} & C'_{33} - \sigma_{33} & 0 & 0 & 0 \\ 0 & 0 & 0 & C'_{44} - \frac{\sigma_{33}}{2} & 0 & 0 \\ 0 & 0 & 0 & 0 & C'_{44} - \frac{\sigma_{33}}{2} & 0 \\ 0 & 0 & 0 & 0 & 0 & \frac{C'_{11} - C'_{12}}{2} \end{bmatrix} \quad (6.2)$$

where the terms  $C'_{ij}$  are the elastic constants in the deformed configuration. The eigenvalues of Eq. 6.2 determine the elastic stability of an HCP material under uniaxial tension along the  $c$ -axis. In this case there are 5 distinct eigenvalues, 3 of which involve the stress  $\sigma_{33}$  explicitly. From the 5 distinct eigenvalues, 2 are associated with a shear mode:  $\lambda^{(1)} = C'_{44} - \frac{\sigma_{33}}{2}$  and  $\lambda^{(2)} = \frac{1}{2} (C'_{11} - C'_{12})$ . The other 3 eigenvalues ( $\lambda^{(3)}$ ,  $\lambda^{(4)}$  and  $\lambda^{(5)}$ ) relate to non-shear modes. In particular,  $\lambda^{(3)}$  represents a tensile failure in the basal plane and is given as:  $\lambda^{(3)} = (C'_{11} - C'_{12})$ . Finally,  $\lambda^{(4)}$  and  $\lambda^{(5)}$  occur as a pair of solutions to a quadratic equation, with  $\lambda^{(4)} < \lambda^{(5)}$ . From these 5 eigenvalues, only the eigenvectors corresponding to  $\lambda^{(4)}$  and  $\lambda^{(5)}$  have a non-zero component along the  $c$  axis and hence, correspond to tensile failure along the loading direction. Since  $\lambda^{(4)} < \lambda^{(5)}$ ,  $\lambda^{(4)}$  is the

relevant eigenvalue governing tensile failure. The 2 eigenvalues considered in the remainder of this work are  $\lambda_1 = \lambda^{(1)}$  and  $\lambda_2 = \lambda^{(4)}$ , see Eqs. 6.3 and 6.4. In principle,  $\lambda^{(2)}$  and  $\lambda^{(3)}$  have to be considered as well for the study of elastic instabilities. However these eigenvalues in fact increase along the deformation path for the materials and loading case studied in this chapter and do not attain a value of zero. Hence, these do not contribute to elastic instabilities in the present case and will not be considered further. This can be rationalized by considering the strain state of the materials and elastic constants of second and higher order (see below).

$$\lambda_1 = C'_{44} - \frac{\sigma_{33}}{2} \quad (6.3)$$

$$\lambda_2 = \frac{C'_{11} + C'_{12} + C'_{33} - \sigma_{33}}{2} - \frac{\sqrt{N}}{2}, \quad \text{where :}$$

$$N = C'^2_{11} + 2C'_{11}C'_{12} - 2C'_{11}C'_{33} + 2C'_{11}\sigma_{33} + \dots$$

$$C'^2_{12} - 2C'_{12}C'_{33} + 2C'_{12}\sigma_{33} + 8C'^2_{13} + 8C'_{13}\sigma_{33} + C'^2_{33} - 2C'_{33}\sigma_{33} + 3\sigma^2_{33} \quad (6.4)$$

With increasing tensile stress, if  $\lambda_1$  becomes negative before  $\lambda_2$ , the crystal fails in shear, with the opposite case corresponding to failure in tension.

The eigenvalues given in Eq. 6.3 and 6.4 contain the elastic constants of the crystal in its deformed state. These can be obtained in principle by calculating the elastic tensor from DFT as a function of applied stress. However, this is a computationally expensive procedure that does not lead to a clear physical understanding of the underlying physics underlying the elastic instabilities. Alternatively, the elastic constants in the deformed configuration,  $C'_{ij}$ , can also be approximated from the third order elastic constants (TOEC's) and the standard second order elastic constants at zero stress (SOEC's). The TOEC's dictate how the elastic constants  $C'_{ij}$  evolve as a function of the imposed strain. Let  $\xi = \eta_{33}$  represent the (imposed) tensile strain along the  $c$ -axis of an HCP-materials and let  $\eta = \eta_{11} = \eta_{22}$  be the resulting strain in the basal plane (usually contraction in accordance with a positive Poisson's ratio) corresponding to zero normal stress in these directions. For this strain state, the expressions for  $C'_{11}$ ,  $C'_{12}$ ,  $C'_{13}$ ,  $C'_{33}$  and  $C'_{44}$  are given as follows in Eqs. 6.5 [275, 276]:

$$C'_{11} = C_{11} + \eta(4C_{11} + 2C_{12} + C_{111} + C_{112}) + \xi(-C_{11} + 2C_{13} + C_{113}), \quad (6.5a)$$

$$C'_{12} = C_{12} + \eta(C_{111} + 2C_{112} - C_{222} + 2C_{12}) + \xi(-C_{12} + C_{123}), \quad (6.5b)$$

$$C'_{13} = C_{13} + \eta(C_{113} + C_{123}) + \xi(C_{13} + C_{133}), \quad (6.5c)$$

$$C'_{33} = C_{33} + \eta(4C_{13} - 2C_{33} + 2C_{133}) + \xi(5C_{33} + C_{333}), \quad (6.5d)$$

$$C'_{44} = C_{44} + \eta\left(\frac{1}{2}C_{11} + \frac{1}{2}C_{12} + C_{13} + C_{144} + C_{155}\right) + \xi\left(\frac{1}{2}C_{13} + \frac{1}{2}C_{33} + C_{44} + C_{344}\right) \quad (6.5e)$$

where the terms  $C_{ijk}$  denote the 10 independent TOEC's for the HCP-materials studied in this work [277, 278, 279, 280]. We now proceed by eliminating  $\eta$  from Eqs. 6.5 by expressing it in terms of  $\xi$ . As shown in Appendix A, from a third-order expansion of the energy versus strain, it can be derived that this value of  $\eta = \bar{\eta}$  for a given  $\xi$  can be obtained from the solution to the following equation:

$$\bar{\eta}^2(2C_{111} + 3C_{112} - C_{222}) + \bar{\eta}(C_{11} + 2C_{12} + 2C_{113}\xi + 2C_{123}\xi) + \xi^2C_{133} + 2\xi C_{13} = 0. \quad (6.6)$$

This resulting expression for  $\bar{\eta}(\xi)$  is lengthy and is not presented here. When this expression is substituted into Eqs. 6.5,  $\xi$  becomes the only remaining (control) variable. The resulting expressions for  $C'_{ij}$  can be substituted into Eqs. 6.3 and 6.4 to determine which eigenvalue becomes negative first under applied strain, and the associated stress which defines the ideal strength.

To obtain the final closed-form expressions, we express the stress  $\sigma_{33}$  in terms of the strain state, SOEC's and TOEC's, using the relations given in Appendix B. An equation can then be set up to determine the value of the strain  $\xi$ , at which a shear instability first occurs; starting from Eq. 6.3, we substitute the expression for  $C'_{44}$  from Eq. 6.5, with  $\xi$  is the control variable and  $\eta = \eta_1 = \eta_2 = \bar{\eta}$  the resulting contraction in the basal plane of the material, as given in Eq. 6.6, and  $\sigma_{33}$  specified from the expressions in Appendix II. Similarly, the strain  $\xi$  at which a tensile elastic instability occurs can be derived by considering the eigenvalue in Eq. 6.4 and substituting the expressions for  $C'_{ij}$  and  $\sigma_{33}$ . The smallest strain  $\xi$  at which an elastic instability (either shear or tensile) first occurs is indicated by  $\bar{\xi}$  hereafter.

### 6.3.2 Calculation of second and third-order elastic constants

The previous section has laid out a methodology to study elastic instabilities in HCP materials loaded in tension along the  $c$  axis, in terms of SOEC's and TOEC's. In this section, it is shown how these quantities can be calculated in a robust manner. By



applying a set of carefully constructed deformations to a cell, all 10 independent TOEC's can be extracted by fitting the stress components, as calculated from DFT, to the applied strains. The pertinent expressions used in this work are given as follows:

$$t_1(\eta_1) = \rho_0 \frac{\partial E}{\partial \eta_1} \Big|_{\eta_2=\eta_3=\eta_4=\eta_5=\eta_6=0} = \frac{C_{111}\eta_1^2}{2} + C_{11}\eta_1 \quad (6.7)$$

$$t_2(\eta_2) = \rho_0 \frac{\partial E}{\partial \eta_2} \Big|_{\eta_1=\eta_3=\eta_4=\eta_5=\eta_6=0} = \frac{C_{222}\eta_2^2}{2} + C_{11}\eta_2 \quad (6.8)$$

$$t_3(\eta_3) = \rho_0 \frac{\partial E}{\partial \eta_3} \Big|_{\eta_1=\eta_2=\eta_4=\eta_5=\eta_6=0} = \frac{C_{333}\eta_3^2}{2} + C_{33}\eta_3 \quad (6.9)$$

$$t_3(\eta_1) = \rho_0 \frac{\partial E}{\partial \eta_3} \Big|_{\eta_2=\eta_3=\eta_4=\eta_5=\eta_6=0} = \frac{C_{113}\eta_1^2}{2} + C_{13}\eta_1 \quad (6.10)$$

$$t_1(\eta_3) = \rho_0 \frac{\partial E}{\partial \eta_1} \Big|_{\eta_1=\eta_2=\eta_4=\eta_5=\eta_6=0} = \frac{C_{133}\eta_3^2}{2} + C_{13}\eta_3 \quad (6.11)$$

$$t_2(\eta_1) = \rho_0 \frac{\partial E}{\partial \eta_2} \Big|_{\eta_2=\eta_3=\eta_4=\eta_5=\eta_6=0} = \frac{C_{112}\eta_1^2}{2} + C_{12}\eta_1 \quad (6.12)$$

$$t_4(\eta_4) = \rho_0 \frac{\partial E}{\partial \eta_4} \Big|_{\eta_1=\eta_2=\eta_3=\eta_5=\eta_6=0} = C_{44}\eta_4 \quad (6.13)$$

$$t_3(\eta_3, \eta_5) = \rho_0 \frac{\partial E}{\partial \eta_3} \Big|_{\eta_1=\eta_2=\eta_4=\eta_6=0} = \frac{C_{333}\eta_3^2}{2} + C_{33}\eta_3 + \frac{C_{344}\eta_5^2}{2} \quad (6.14)$$

$$t_5(\eta_3, \eta_5) = \rho_0 \frac{\partial E}{\partial \eta_5} \Big|_{\eta_1=\eta_2=\eta_4=\eta_6=0} = C_{44}\eta_5 + C_{344}\eta_3\eta_5 \quad (6.15)$$

$$t_3(\eta_1, \eta_2) = \rho_0 \frac{\partial E}{\partial \eta_3} \Big|_{\eta_3=\eta_4=\eta_5=\eta_6=0} = \frac{C_{113}\eta_1^2}{2} + C_{123}\eta_1\eta_2 + C_{13}\eta_1 + \frac{C_{113}\eta_2^2}{2} + C_{13}\eta_2 \quad (6.16)$$

$$t_4(\eta_1, \eta_4) = \rho_0 \frac{\partial E}{\partial \eta_4} \Big|_{\eta_2=\eta_3=\eta_5=\eta_6=0} = C_{44}\eta_4 + C_{144}\eta_1\eta_4 \quad (6.17)$$

$$t_5(\eta_1, \eta_5) = \rho_0 \frac{\partial E}{\partial \eta_5} \Big|_{\eta_2=\eta_3=\eta_4=\eta_6=0} = C_{44}\eta_5 + C_{155}\eta_1\eta_5 \quad (6.18)$$

where the following Voigt-notation is employed: 11  $\mapsto$  1, 22  $\mapsto$  2, 33  $\mapsto$  3, 23  $\mapsto$  4, 13  $\mapsto$  5, 12  $\mapsto$  6. In Eqs. 6.7-6.18,  $t_i$  denotes components of the Lagrangian stress tensor, defined in terms of the true stress tensor components  $\sigma_i$  as given in Appendix B,  $\rho_0$  is the

mass density in the undeformed state, and  $E$  denotes the strain energy per unit mass [281].

In the applications of Eqs. 6.7-6.18 to determine the SOEC's and TOEC's, strains are applied varying from -6 % to + 20%, in steps of 0.5 %, and the resulting true stresses and Lagrangian stresses are computed from the true stress tensor obtained by DFT [281]. Note that this strain range is considerably larger than what is commonly used for the calculation of the SOEC's. The TOEC's give rise to a nonlinear stress-strain behavior and this effect only becomes apparent at relatively large strains (larger than approximately 10 % for the materials studied in this work), hence the extended strain range.

The set of Eqs. 6.7-6.18 give rise to an overdetermined system that is solved for the 5 independent SOEC's and 10 independent TOEC's. A pseudo-inverse is employed, calculated from a singular value decomposition. The values of the calculated TOEC's are found in this work to be rather sensitive to the precise strain range that is employed in the fitting, which has been observed also in the literature [282, 281, 283]. For the HCP systems studied in this work, the TOEC's converge to a plateau when approximately 11-16 % maximum strain is used in the fit. Using smaller or larger maximum strains than those corresponding to the plateau can lead to TOEC's differing by up to a factor 5 for the systems studied in this work. For maximum strains within the plateau-region, TOEC's are generally converged to within 25 % in this work. Consistent with other work in the literature, the location of this plateau dictates which precise strain range is used in the fitting [282, 283].

### 6.3.3 DFT-calculations

For the elemental metals all calculations were performed using the Vienna Ab Initio Simulation Package (VASP) [136, 137]. In these calculations use was made of the Perdew-Burke-Ernzerhof generalized gradient functional (PBE-GGA) [150], and the projector augmented wave (PAW) method [52, 53]. An energy cutoff for the plane waves of 700 eV was used, and smearing of the electronic occupancies was performed using the Methfessel-Paxton scheme [140], with a broadening of 0.05 eV. Integrations in the Brillouin zone were carried out using Monkhorst-Pack  $k$ -point sampling [139] with a density chosen such that the number of  $k$ -points in the first Brillouin zone times the number of atoms in the cell equals approximately 25,000. The employed PAW potentials for Sc, Ti, Y, Zr and Hf include  $s$  and  $p$  semi-core states as valence electrons. For the other elements, only the outermost  $s$  and  $d$ -states are used as valence. The maximum calculated tensile stress  $\sigma_{33}$  that occurs along the deformation path (similar to the ultimate tensile strength) is converged to within approximately 2% with these DFT settings.

For the purpose of investigating  $d$ -band filling effects on ideal deformation behavior, we also employed calculations based on the virtual crystal approximation (VCA). The

VCA calculations were performed using the Quantum Espresso software [193], employing norm-conserving Troullier-Martin pseudopotentials [51, 109]. Use was made of the generalized gradient approximation, based on the Perdew-Burke-Ernzerhof exchange-correlation functional [150]. The pseudopotentials were generated using the fhi98PP code with intermediate nuclear charges [101] to approximate a given alloy composition. The plane-wave cutoff, k-point sampling and broadening employed for these DFT calculations based on VCA are the same as those described earlier, employing PAW pseudopotentials. The maximum calculated tensile stress for these calculations is converged to within approximately 3%.

## 6.4 Results and Discussion

In this section, results for HCP Be, Mg, Sc, Y, Ti, Zr, Hf, Tc, Re, Ru, Os and Zn are presented. Lattice stabilities are calculated as a function of the strain  $\eta_{33}$  along the  $c$  axis, and the failure modes are determined. This results in a categorization of the HCP metals considered into two classes: those that fail in shear (intrinsically ductile) or in tension (intrinsically brittle) for this loading condition. Further, the effect of  $d$ -band filling is studied on the failure modes for the HCP transition metals, leading to guidelines for the compositions where their solid solutions are expected to be intrinsically brittle or ductile for tensile loading along  $c$ .

### 6.4.1 Elastic instabilities in HCP materials: A comparison of direct DFT and analytical model results

The Wallace-tensor (see Eq. 6.2) can be approximated from the above formalism by means of the SOEC's and TOEC's. However, it also can be calculated explicitly from DFT for each strain along the  $c$ -deformation path. This direct DFT approach is expensive since for every strain along the  $c$ -axis, a structural relaxation of the lattice vectors in the basal plane, and the atomic coordinates, must be performed to give zero shear stresses, zero normal stresses within the basal plane, and zero forces. Further, a calculation of the elastic constants in the deformed configuration,  $C'_{ijkl}$ , is required for each such relaxed strained configuration, which further increases the computational cost. Such a direct approach to calculating the Wallace tensor and lattice instabilities is in principle more accurate than the analytical formalism based on the SOEC's and TOEC's, since it does not require the evaluation of the TOEC's and hence mitigates some of its associated inaccuracies. In this section, we present results based on both methods to compare the accuracy of the approaches.

Results are shown in Table 6.1. The analytical model predicts the ideal failure mode (either shear or tensile failure) correctly for the 10 transition metals considered, as

well as Zn, Cd, Be and Mg. Further, the critical  $c$ -axis strain ( $\bar{\xi}$ ) at which an elastic instability first occurs is predicted to within an accuracy of approximately 4 %. The differences in  $\bar{\xi}$  calculated directly from DFT and from the analytical model can be attributed to two main factors. First, the calculation of TOEC's from DFT is prone to numerical errors, which will propagate through in the evaluation of  $\bar{\xi}$ . Second, in this work the strain energy is only expanded up to the third order in the strains. As strains increase, fourth-order terms would have to be included to increase numerical accuracy. Given the computational cost required to achieve numerically stable values of these higher-order elastic constants, the inclusion of these terms in the analytical models were not pursued in this work. We note that the discrepancies between the ideal strength predicted according to DFT and the analytical model are in reasonable agreement, with maximum errors comprising 50 %, in particular for the transition metals near half  $d$ -band filling. The possible explanation for this is again that for relatively large strains, higher-order elastic constants would have to be included in the model.

Table 6.1: Calculated SOEC's, TOEC's and ideal-failure characteristics for 12 HCP metals. Failure modes are characterized as either shear (S) or tension (T).

|                                  | Sc   | Y    | Ti    | Hf    | Zr    | Tc    | Re    | Ru    | Os    | Zn    | Mg    | Be    |
|----------------------------------|------|------|-------|-------|-------|-------|-------|-------|-------|-------|-------|-------|
| <b>SOEC's (GPa)</b>              |      |      |       |       |       |       |       |       |       |       |       |       |
| $C_{11}$                         | 100  | 77   | 174   | 182   | 145   | 489   | 618   | 554   | 733   | 166   | 59    | 306   |
| $C_{12}$                         | 37   | 25   | 81    | 72    | 64    | 225   | 275   | 181   | 227   | 36    | 29    | 32    |
| $C_{13}$                         | 29   | 27   | 75    | 69    | 66    | 192   | 224   | 176   | 225   | 35    | 20    | 15    |
| $C_{44}$                         | 29   | 25   | 43    | 52    | 25    | 171   | 159   | 175   | 248   | 30    | 17    | 165   |
| $C_{33}$                         | 71   | 61   | 183   | 20    | 161   | 534   | 677   | 613   | 801   | 71    | 67    | 406   |
| <b>TOEC's (GPa)</b>              |      |      |       |       |       |       |       |       |       |       |       |       |
| $C_{133}$                        | -117 | -143 | -273  | -214  | -146  | -1014 | -1557 | -1220 | -1408 | -21   | -1808 | -318  |
| $C_{333}$                        | -230 | -303 | -1078 | -1463 | -1173 | -4004 | -5715 | -5980 | -7955 | -797  | -4625 | -4347 |
| $C_{111}$                        | -734 | -529 | -1584 | -1567 | -1301 | -4771 | -6786 | -5758 | -7764 | -2179 | -5247 | -2407 |
| $C_{112}$                        | -83  | -24  | 10    | -120  | 103   | -526  | -1020 | -656  | -828  | -57   | -1531 | -81   |
| $C_{113}$                        | -50  | -58  | 169   | -22   | 169   | 6     | 107   | -621  | -604  | 31    | 432   | 59    |
| $C_{222}$                        | -691 | -475 | -1173 | -1354 | -961  | -4175 | -6103 | -5263 | -7146 | -2862 | -5043 | -1887 |
| $C_{123}$                        | -219 | -185 | -661  | -237  | -494  | -1768 | -712  | -275  | -332  | -498  | -1886 | -7    |
| $C_{144}$                        | -15  | 8    | 170   | -260  | 218   | -1100 | -451  | -417  | -562  | -227  | -964  | -332  |
| $C_{155}$                        | 37   | 58   | -34   | -154  | 49    | -126  | -519  | -566  | -801  | -351  | 8     | -88   |
| $C_{344}$                        | -135 | -128 | -246  | -460  | -162  | -1061 | -1281 | -930  | -1297 | -234  | -727  | -726  |
| <b>Failure characteristics</b>   |      |      |       |       |       |       |       |       |       |       |       |       |
| $\bar{\xi}$ (direct DFT)         | 0.22 | 0.20 | 0.19  | 0.14  | 0.19  | 0.18  | 0.19  | 0.15  | 0.15  | 0.12  | 0.22  | 0.17  |
| $\bar{\xi}$ (analytical)         | 0.30 | 0.26 | 0.24  | 0.20  | 0.15  | 0.19  | 0.24  | 0.18  | 0.19  | 0.13  | 0.24  | 0.16  |
| $\sigma_{id}$ (GPa) (direct DFT) | 13   | 9    | 15    | 12    | 11    | 44    | 54    | 48    | 62    | 5     | 6     | 24    |
| $\sigma_{id}$ (GPa) (analytical) | 11   | 8    | 13    | 10    | 8     | 36    | 44    | 33    | 42    | 3     | 5     | 20    |
| Failure mode                     | S    | S    | S     | S     | S     | S     | S     | T     | T     | T     | T     | T     |

In this work it is found that out of the 12 HCP metals studied, 5 fail in tension: Ru, Os, Zn, Mg and Be and are categorized as intrinsically brittle, whereas the other 7 HCP metals are intrinsically ductile. The results in Table 6.1 are qualitatively in agreement with experiments, in which the ductility of Be, Os, Zn and Ru was characterized as poor, meaning less than 15 % elongation in a tensile test. Further, the ductility of Zr, Ti and Hf was characterized as good (elongation greater than 40 %) and finally the ductility of Y, Mg and Re was characterized as fair, indicating maximum elongations in between 15 % and 40 % [17]. It should be noted however that ductility is ultimately dictated by strength and work hardening. The calculations in this work provide only a way of gauging intrinsic ductility, thereby not taking into consideration extrinsic effects that largely govern the ductility of real materials. Therefore, care has to be taken to make comparisons with experimental data.

#### 6.4.2 Elastic instabilities and $d$ -band filling

The results in the previous section indicate that group III (Sc, Y), IV (Ti, Zr) and VII (Tc, Re) HCP transition metals fail in shear whereas group VIII (Ru, Os) HCP transition metals fail in tension when loaded in tension along the  $c$  axis. The formalism developed in this chapter shows that second and third order elastic constants dictate the failure mode under this loading condition. Further, it is known that the  $d$ -band filling plays an important role in determining properties such as lattice constants, cohesive energies and elastic constants. Hence, it may be expected that the ideal strength behavior of the HCP transition metals may show systematic trends versus  $d$ -band filling. We explore this issue further in the present section, employing results obtained from VCA calculations.

The VCA is employed here to study the ideal strength behavior of alloys with  $d$ -band filling between groups i) III and IV, ii) VI and VII and iii) VII and VIII. By employing VCA-calculations, approximate ranges of  $d$ -band filling are mapped out in which shear versus tensile failure occurs. This leads to the map given in Fig. 6.1, of the periodic table showing band filling domains in which either intrinsically ductile (shear) or intrinsically brittle (tensile) failure are found to occur. We note that the group III and IV HCP transition metal alloys fail in shear, and the same holds true for all HCP alloys with  $d$ -band fillings in between. Further, group IV HCP metals can be alloyed with elements having  $d$  band fillings larger than those in group IV (e.g. Nb, Ta) and maintain intrinsically ductile behavior. However, there is a limit on how much  $d$ -band filling can be increased since i) the HCP-phase becomes energetically destabilized with respect to the BCC structure as the  $d$ -band filling moves towards group V, and ii) the HCP phase becomes mechanically unstable under zero stress as the  $d$ -band filling goes beyond a critical value. Fig. 6.1 suggests guidelines for the design of HCP transition metal alloys, by indicating approximate alloy compositional ranges that result in intrinsically ductile behavior, while maintaining mechanical stability at zero stress.

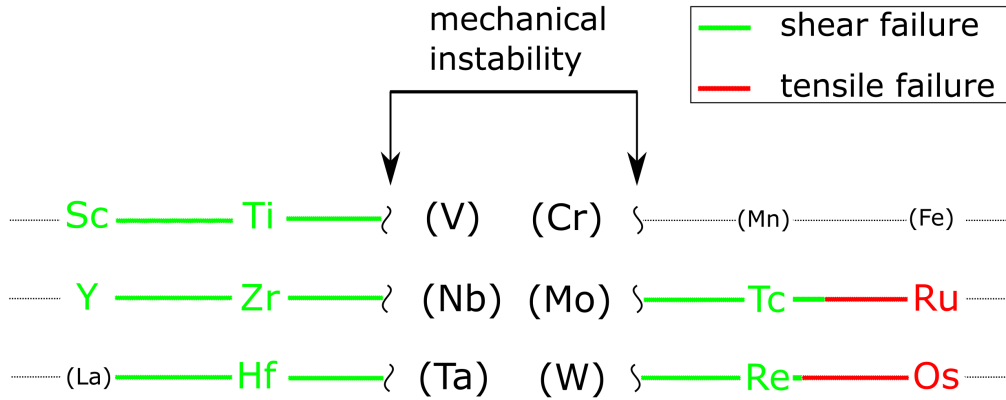


Figure 6.1: Ideal failure mode-diagram vs.  $d$ -band filling in HCP metals and alloys

Moving to the right of the periodic table, we note that the group VII HCP-metals Re and Tc fail in shear and are hence intrinsically ductile. The metal Re is of particular interesting, as it exhibits the highest shear modulus among all HCP metals that fail in shear, suggesting the interesting combination of high strength and ductility. Moving further to the right, we note the metals Ru and Os in group VIII, exhibiting the highest shear moduli among all HCP-metals and almost all other elements in the periodic table. These fail in tension when loaded along  $c$ , largely due to their very high shear moduli. Small perturbations in  $d$ -band filling towards lower values do not change the ideal deformation behavior and the intrinsically brittle failure mode is maintained all the way up to  $d$ -band fillings close to group VII.

The formalism based on SOEC's and TOEC's developed in this work can be used to understand the features of the elastic response underlying shear versus tensile failure. Consider first HCP materials with high shear moduli,  $C_{44}$ , such as Ru and Os. These materials are not likely to fail in shear, since the eigenvalue associated with shear failure (Eq. 6.3) is rather large and may not reach zero before the eigenvalue in Eq. 6.4. Hence, this observation explains from an ideal strength point of view why the HCP metals that are most stiff in shear, and thus expected to have high strength, tend to be brittle under  $c$ -axis loading. Strong materials with a high shear modulus  $C_{44}$  will only fail in shear and be accordingly intrinsically ductile according to Eq. 6.3 if  $\sigma_{33}$  is relatively large in magnitude, requiring that  $C_{33}$  is large. Further, the modulus  $C_{333}$  is negative for most materials, implying softening of  $C_{33}$  as the materials is strained along  $c$  by  $\xi$ . A small magnitude of  $C_{333}$  is also favorable for shear failure as it causes the magnitude of the stress  $\sigma_{33}$  decrease less rapidly as a function of  $\xi$ .

Metals and alloys near half  $d$ -band filling, such as Re and Tc, are intrinsically

ductile and fail in shear but are on the border of  $d$ -band filling regions where tensile failure occurs. Their shear failure is caused by an interplay of the SOEC's and TOEC's. First, the shear moduli  $C_{44}$  of Re and Tc are large but smaller than those for Os and Ru. The same is true for the moduli  $C_{33}$ , but the ratio  $C_{33}/C_{44}$  for group VII metals is larger than for group VIII: for Os  $C_{33}/C_{44} \approx 3.2$  whereas for Re  $C_{33}/C_{44} \approx 4.5$ . Second, for group VII metals, the magnitude of  $C_{333}$  is smaller than for group VIII, which also promotes shear failure over tensile failure. Third, the TOEC  $C_{344}$ , which is a negative quantity for most materials, is relatively large in magnitude for group VII metals, relative to those in group VIII. According to Eq. 6.5 (e), this implies that the shear modulus  $C_{44}$  decreases relatively rapidly with strain  $\xi$ , which according to Eq. 6.3, favors a shear instability over a tensile instability.

Finally, the high ductility HCP metals in group IV exhibit values of  $C_{33}/C_{44}$  between approximately 4 and 6 which is higher than for groups VII and VIII. The relatively low values for  $C_{44}$  causes the eigenvalue in Eq. 6.3 to attain negative values before the eigenvalue in Eq. 6.4, and consequently to fail in shear.

## 6.5 Summary and Conclusions

In this work, the ideal deformation behavior and elastic stabilities of 12 HCP metals under uniaxial stress along the  $c$ -axis are studied: Be, Mg, Sc, Y, Ti, Zr, Hf, Tc, Re, Ru, Os and Zn. It is found that out of these, 5 fail in tension along  $c$  (Be, Mg, Ru, Os and Zn) whereas the 7 others (Sc, Y, Ti, Zr, Hf, Tc and Re) fail in shear. This leads to a natural division of the HCP metals into 2 classes: those that are intrinsically ductile (i.e., fail in shear) or intrinsically brittle (i.e., fail in tension) under tensile loads along  $c$ . Using a formalism based on the expansion of the elastic energy to third order in strain, it is further shown that the critical strain and the deformation mode can be predicted from the relative magnitudes of these of the second and third order elastic constants. It is found that HCP metals exhibiting high moduli  $C_{44}$  tend to fail in tension rather than shear and hence, are intrinsically brittle. This occurs for transition metals and alloys in group VIII (Os, Ru). The HCP metals in groups III and IV are found to be intrinsically ductile under  $c$ -axis loading, primarily due to their low shear moduli  $C_{44}$ , which promotes shear failure. The group VII HCP metals (Re, Tc) are an interesting case that combine a high shear modulus with intrinsically ductile behavior. The physical reason for this behavior is the specific combination of SOEC's and TOEC's that this class of materials exhibits: a high  $C_{33}$ , but a relatively small magnitude of  $C_{333}$  and a large magnitude of  $C_{344}$ . Finally, the trends of the ideal deformation behavior with  $d$ -band filling are revealed, resulting in approximate  $d$ -electron counts per atom for which an alloy is expected to fail in a ductile or brittle mode.



## 6.6 Appendix A

The imposed strain along  $c$  ( $\xi$ ) and the resulting strain in the basal plane ( $\eta$ ) required to ensure zero normal stress within the basal plane are related by the Poisson's ratio for small strains. For large values of  $\xi$ , however, the TOEC's have to be invoked to calculate  $\eta$ .

Consider the mapping between the reference and current configuration of a continuum solid. In the reference configuration, a particle occupies a point  $\mathbf{p}$  with spatial coordinates  $\mathbf{X} = X_1\mathbf{e}_1 + X_2\mathbf{e}_2 + X_3\mathbf{e}_3$ , where  $\mathbf{e}_1, \mathbf{e}_2, \mathbf{e}_3$  is a Cartesian reference triad and  $X_1, X_2, X_3$  are the reference coordinates. Upon deformation of the body, the point originally at  $\mathbf{X}$  is translated by the displacement vector  $\mathbf{u}(X_1, X_2, X_3)$  to its final coordinates  $\mathbf{x}(X_1, X_2, X_3)$ , see Eq. 6.19 .

$$\mathbf{x}(X_1, X_2, X_3) = \mathbf{u}(X_1, X_2, X_3) + \mathbf{X}(X_1, X_2, X_3) \quad (6.19)$$

Based on this description, a deformation gradient is formulated as in Eq. 6.20. The Green-Lagrange strain tensor  $\boldsymbol{\eta}$  then follows from  $\mathbf{F}$  as shown in Eq. 6.21, where  $\mathbf{I}$  denotes the identity matrix.

$$\mathbf{F} = \frac{\partial x_i}{\partial X_j} \quad (6.20)$$

$$\boldsymbol{\eta} = \frac{1}{2} (\mathbf{F}^T \mathbf{F} - \mathbf{I}) \quad (6.21)$$

With the notation now established, the strain energy density can be expanded in terms of the SOEC's, TOEC's and the Green-Lagrange strain as in Eq. 6.22, where  $\rho_0$  represents the mass density in the undeformed state and the terms  $\eta_i$  represent the components of the tensor defined in Eq. 6.21. The symmetry of the SOEC's and TOEC's will be applied in the expansions, which simplifies the resulting expressions considerably.

$$\rho_0 E(\boldsymbol{\eta}) = \frac{1}{2!} \sum_{i,j=1}^6 C_{ij} \eta_i \eta_j + \frac{1}{3!} \sum_{i,j,k=1}^6 C_{ijk} \eta_i \eta_j \eta_k + \dots \quad (6.22)$$

Consider an imposed strain  $\xi$  along the  $c$ -axis of an HCP-metal, initially keeping all other dimensions fixed to the zero strain-state. Consider first the expansion of Eq. 6.22, retaining only terms up to and including the SOEC's (hence, ignoring the TOEC's for now). This gives the energy-expression in Eq. 6.23, in which the symmetry of the SOEC's has been applied. To obtain the equilibrium strain in the basal plane due to the application of  $\xi$ , we perform strain energy-minimization and set  $\bar{\eta} = \eta = \eta_1 = \eta_2$ ,  $\eta_3 = \xi$  and  $\eta_4 = \eta_5 = \eta_6 = 0$  in Eq. 6.23 and solve  $\frac{\partial(\rho_0 E)}{\partial \eta} |_{\xi} = 0$ . We find the equilibrium strain  $\eta = \bar{\eta}$ , given in Eq. 6.24, where the minus-sign signifies the Poisson-contraction in the basal plane.

$$\rho_0 E(\boldsymbol{\eta}) = C_{11} \frac{\eta_1^2}{2} + C_{11} \frac{\eta_2^2}{2} + C_{33} \frac{\xi^2}{2} + C_{44} \frac{\eta_4^2}{2} + C_{44} \frac{\eta_5^2}{2} + \frac{1}{2} (C_{11} - C_{12}) \frac{\eta_6^2}{2} + C_{12} \eta_1 \eta_2 + C_{13} \eta_1 \xi + C_{13} \eta_2 \xi \quad (6.23)$$

$$\eta = \bar{\eta} = -\frac{\xi C_{13}}{C_{11} + C_{12}} \quad (6.24)$$

For large strains, the expansion in Eq. 6.23 is not sufficient and instead, TOEC's have to be included as well. The expansion of the strain energy up to the third order in strain is given in Eq. 6.25, in which the terms  $P$  are given in Eq. 6.26. Note that in Eq. 6.25, the symmetry of the SOEC's and TOEC's has been incorporated to simplify the resulting expression.

$$\begin{aligned} \rho_0 E(\boldsymbol{\eta}) = & C_{11} P_1 + C_{12} P_2 + C_{13} P_3 + C_{33} P_4 + \\ & C_{44} P_5 + C_{111} P_6 + C_{222} P_7 + C_{333} P_8 + \\ & C_{133} P_9 + C_{113} P_{10} + C_{112} P_{11} + C_{123} P_{12} + \\ & C_{144} P_{13} + C_{155} P_{14} + C_{344} P_{15} \end{aligned} \quad (6.25)$$

$$P_1 = \frac{\eta_1^2}{2} + \frac{\eta_2^2}{2} + \frac{\eta_6^2}{4}, \quad (6.26a)$$

$$P_2 = -\frac{\eta_6^2}{4} + \eta_1\eta_2, \quad (6.26b)$$

$$P_3 = \eta_1\eta_3 + \eta_2\eta_3, \quad (6.26c)$$

$$P_4 = \frac{\eta_3^2}{4}, \quad (6.26d)$$

$$P_5 = \frac{\eta_4^2}{2} + \frac{\eta_5^2}{2}, \quad (6.26e)$$

$$P_6 = \frac{\eta_1^3}{6} + \frac{\eta_1\eta_2^2}{2} - \frac{\eta_1\eta_6^2}{4} + \frac{\eta_2\eta_6^2}{4}, \quad (6.26f)$$

$$P_7 = \frac{\eta_2^3}{6} - \frac{\eta_1\eta_2^2}{2} - \frac{\eta_2\eta_6^2}{8} + 3\frac{\eta_1\eta_6^2}{8}, \quad (6.26g)$$

$$P_8 = \frac{\eta_3^3}{6}, \quad (6.26h)$$

$$P_9 = \frac{\eta_1\eta_3^2}{2} + \frac{\eta_2\eta_3^2}{2}, \quad (6.26i)$$

$$P_{10} = \frac{\eta_3\eta_1^2}{2} + \frac{\eta_3\eta_2^2}{2} + \frac{\eta_3\eta_6^2}{4}, \quad (6.26j)$$

$$P_{11} = \frac{\eta_1^2\eta_2}{2} + \frac{\eta_1\eta_2^2}{2} - \frac{\eta_6^2\eta_1}{8} - \frac{\eta_6^2\eta_2}{8}, \quad (6.26k)$$

$$P_{12} = \eta_1\eta_2\eta_3 - \frac{\eta_3\eta_6^2}{4}, \quad (6.26l)$$

$$P_{13} = \frac{\eta_1\eta_4^2}{2} + \frac{\eta_2\eta_5^2}{2} - \frac{\eta_4\eta_5\eta_6}{2}, \quad (6.26m)$$

$$P_{14} = \frac{\eta_2\eta_4^2}{2} + \frac{\eta_1\eta_5^2}{2} + \frac{\eta_4\eta_5\eta_6}{2}, \quad (6.26n)$$

$$P_{15} = \frac{\eta_3\eta_4^2}{2} + \frac{\eta_3\eta_5^2}{2} \quad (6.26o)$$

Given an applied  $\xi$ , we can again find an analytical expression for the Poisson contraction  $\eta = \bar{\eta}$  in terms of  $\xi$  and the SOEC's and TOEC's. The resulting equation that has to be solved is shown in Eq. 6.6. Solving Eq. 6.6 in terms of  $\eta = \bar{\eta} = \eta_1 = \eta_2$  gives the equilibrium strain in the basal plane.

## 6.7 Appendix B

A simple expression for the relations between strains and stresses can be derived for an HCP-structured material that is loaded in tension along the  $c$ -axis, while allowing

for contraction in the basal plane. For this situation, with an applied (Lagrangian) strain  $\eta_3$  along  $c$ , we have  $\eta_1 = \eta_2 = \bar{\eta}$  and  $\eta_3 = \xi$ . Eq. 6.27 expresses the Lagrangian stress tensor in terms of the strain energy and Lagrangian strain tensor [281]. From Eq. 6.27, the Lagrangian stress  $t_{33}$  can be found under the combined strain state currently under investigation, see Eq. 6.28. Further, from Eq. 6.29, we have that  $\boldsymbol{\sigma} = \frac{1}{\det(\mathbf{F})} \mathbf{F} \mathbf{t} \mathbf{F}^T$  which governs the relation between Lagrangian and true stress. This expression can be expanded, with the result given in Eq. 6.30, where  $t_{33}$  is given in Eq. 6.28.

$$t_{ij} = \rho_0 \frac{\partial E}{\eta_{ij}} \quad (6.27)$$

$$t_{33} \Big|_{\eta_4=\eta_5=\eta_6=0} = \eta_1^2 (C_{113} + C_{123}) + \eta_1 (2C_{13} + 2C_{133}\eta_3) + \frac{1}{2} C_{333} \eta_3^2 + C_{33} \eta_3 \quad (6.28)$$

$$t_{ij} = \det(\mathbf{F}) \mathbf{F}^{-1} \boldsymbol{\sigma} (\mathbf{F}^T)^{-1} \quad (6.29)$$

$$\sigma_{33} = \frac{\sqrt{2\xi + 1}}{\sqrt{2\bar{\eta} + 1}} t_{33} \quad (6.30)$$

## Part III

# High-Throughput Approach to Materials Science

## Chapter 7

# High-Throughput Elastic Properties

### 7.1 Foreword

The elastic constant tensor of an inorganic compound provides a complete description of the response of the material to external stresses in the elastic limit. It thus provides fundamental insight into the nature of the bonding in the material, and it is known to correlate with many mechanical properties. Despite the importance of the elastic constant tensor, it has been measured for a very small fraction of all known inorganic compounds, a situation that limits the ability of materials scientists to develop new materials with targeted mechanical responses. To address this deficiency, we present here the largest database of calculated elastic properties for inorganic compounds to date. The database currently contains full elastic information for 1,181 inorganic compounds, and this number is growing steadily. The methods used to develop the database are described, as are results of tests that establish the accuracy of the data. In addition, we document the database format and describe the different ways it can be accessed and analyzed in efforts related to materials discovery and design.

Part of the results presented in this chapter, including the figures and tables, were published by Maarten de Jong, Wei Chen, Tom Angsten, Anubhav Jain, Randy Notestine, Anthony Gamst, Marcel Sluiter, Chaitanya Krishna Ande, Sybrand van der Zwaag, Jose Plata, Cormac Toher, Stefano Curtarolo, Gerbrand Ceder, Kristin Persson and Mark Asta in *Scientific Data*, 2, 2015 [284]. The material is reproduced here with permission of the co-authors and publishers.

## 7.2 Background & Summary

The elastic tensor of a crystalline solid provides a complete description of its response to external forces within the elastic limit. This property is thus one of the most fundamental probes of the nature of the interatomic bonding in a given material system (e.g., [285]). Further, it is known that the elastic tensor correlates with many mechanical and thermal properties, and it is thus a critically important quantity for use in screening in the process of materials discovery and design. For example, since the work of Pugh in the 1950's the ratio of the bulk to shear modulus has been used as a basis to understand and predict trends in the ductility of materials [116, 110, 286, 287, 115, 288, 289, 290]. More recently, extensions of the Pugh analysis have been used to derive descriptors for hardness, in the attempt to discover new materials for hard coating applications, and to guide the search for the elusive inorganic compound with a hardness greater than diamond [110]. Elastic tensors can also be used to screen for materials with targeted thermal properties, as it provides a basis for rapid estimation of trends in heat capacities and thermal conductivities [291, 292, 293, 294]. Knowledge of the full anisotropic elastic tensor can be used in conjunction with mathematical homogenization theories to predict the elastic response of composite materials, and thus guide the design of such materials with targeted stiffnesses [295, 296]. Additionally, an area in which elastic properties find widespread use is geophysics, where acoustic velocities are used for interpretation of seismic data [297, 298].

Despite the importance of the elastic tensor, experimental data for this quantity is available for only a very small subset of all known inorganic compounds. This presents a fundamental bottleneck for the discovery and design of materials with targeted thermal and mechanical properties, or for performing continuum simulations of mechanical response that require elastic moduli as input. Considering only materials for which the full tensor of elastic coefficients is available, the classical works have references that sum up to a total number of around 150 independent systems for which experimental measurements have been compiled [299, 300, 144, 301, 302, 303, 304, 305, 306]. Considering papers that have investigated elastic constants of particular systems, this number might be twice as large, which is a very small fraction of the approximately 30,000 to 50,000 entries for ordered compounds in the inorganic crystal structure database [307, 308, 309]. Among the systems for which experimental data is available are approximately 70 pure elements, with the remainder consisting of binary systems and - to a much smaller extent - ternary systems and a variety of complex minerals. Among the binary materials are solid solutions and compounds, the latter often being ordered intermetallic compounds.

One challenge associated with using published experimental data for elastic moduli is that the spread in the reported values for a given system can be quite large, depending on the details of the experimental conditions and techniques employed. For example, elastic moduli derived from inelastic neutron scattering can be 10 % greater than those derived

from pulse-echo measurements [310]. Differences of over 20 % in reported experimental values for the bulk and shear moduli for the same system have been observed in some cases, such as NiO [311, 312]. Other experimental factors, such as different measurement temperatures [313] and/or the presence of impurity phases, can also lead to variability in reported elastic constants.

Efforts aimed at developing databases of elastic moduli from first-principles computational methods have been undertaken in previous work (e.g. [314, 315]). Such a computational approach provides an advantage that all of the data can be derived in a consistent manner, facilitating comparisons across materials chemistries. In the present work we expand on this approach. Specifically, we present here the to-date largest database of calculated elastic properties of crystalline inorganic compounds, ranging from metals and metallic compounds to semiconductors and insulators. These calculations are part of a high-throughput (HT) effort [15], undertaken within the framework of the Materials Project (MP) [316]. The database of elastic tensors currently consists of over 1,181 materials and is being updated regularly. The elastic properties are obtained using first-principles quantum-mechanical calculations based on Density Functional Theory (DFT). As shown below, the calculated elastic constants are typically within 15 % of experimental values, which represents a smaller scatter than that observed in experimental values in some cases. Pearson ( $r$ ) and Spearman ( $\rho$ ) coefficients indicate that the calculations performed in this work yield elastic properties that show an excellent correlation with experimental values, making the database presented here useful for screening materials with properties based on elastic tensors.

The remainder of the chapter is organized as follows. We first describe our method for calculating elastic constants from DFT in a HT-environment. We then describe verification and validation tests to assess the precision and accuracy of the chosen density functional and the HT algorithms employed in the calculations. Finally, an overview of the structure of the data and a brief description of the results is presented.

## 7.3 Methods

### 7.3.1 Generation of elasticity data

In this launch of the elastic constant database we tabulate results for a subset of 1,181 compounds chosen from those present in the current MP database. This subset includes 2 broad categories: i) metallic and small-band-gap compounds and ii) binary oxides and semiconductor compounds. The first category is taken from the MP-database, under the constraint that 1) the calculated bandgap  $< 0.3$  eV and 2) the energy above the convex hull (decomposition energy [317])  $< 0.5$  eV / atom. These properties have been calculated previously by DFT using the standard HT-procedure and chosen MP parameters suitable



for ground-state energy, lattice structure, and band structure [316, 318]. The constraints are chosen to represent a set of materials that are metallic or near-metallic and energetically stable or near-stable, and yields the majority of the data set (approximately 1,100 systems). For the binary oxides, different selection criteria were used: 1) the bandgap  $> 0.3$  eV and 2) the energy above the convex hull = 0 eV / atom, which yields approximately 100 systems. Furthermore, approximately 20 technologically relevant semiconductors were added to create a representative set of materials.

For these systems we compute the elastic constants using a stress-strain methodology. Specifically, starting from a relaxed structure for each compound, we generate a set of distorted structures, as follows. The Green-Lagrange strain tensor has 6 independent components, each of which is applied independently to every structure, with differing magnitudes, as described in the Workflow section below. For each deformed structure, the  $3 \times 3$  stress tensor is calculated by DFT. If the components of the stress tensor are denoted by  $S_{ij}$  and the components of the Green-Lagrange strain tensor are denoted by  $E_{ij}$ , the constitutive relation within linear elasticity can be written as in Eq. 7.1, which relates stresses to strains via the symmetric elastic matrix, with components  $C_{ij}$ . In Eq. 7.1, the following Voigt-notation is employed: 11  $\mapsto$  1, 22  $\mapsto$  2, 33  $\mapsto$  3, 23  $\mapsto$  4, 13  $\mapsto$  5, 12  $\mapsto$  6.

$$\begin{bmatrix} S_{11} \\ S_{22} \\ S_{33} \\ S_{23} \\ S_{13} \\ S_{12} \end{bmatrix} = \begin{bmatrix} C_{11} & C_{12} & C_{13} & C_{14} & C_{15} & C_{16} \\ C_{12} & C_{22} & C_{23} & C_{24} & C_{25} & C_{26} \\ C_{13} & C_{23} & C_{33} & C_{34} & C_{35} & C_{36} \\ C_{14} & C_{24} & C_{34} & C_{44} & C_{45} & C_{46} \\ C_{15} & C_{25} & C_{35} & C_{45} & C_{55} & C_{56} \\ C_{16} & C_{26} & C_{36} & C_{46} & C_{56} & C_{66} \end{bmatrix} \begin{bmatrix} E_{11} \\ E_{22} \\ E_{33} \\ 2E_{23} \\ 2E_{13} \\ 2E_{12} \end{bmatrix} \quad (7.1)$$

For each of the applied strains  $E_{ij}$ , the full stress tensor is obtained from a DFT calculation in which ionic positions are relaxed. Consequently one row (or equivalently, column) of the elastic matrix is obtained from a linear fit of the calculated stresses over the range of imposed strains. Repeating this procedure for each of the 6 independent strain components, all elements of the elastic modulus tensor can be calculated. The result is a calculated set of  $C_{ij}$  values that can be used to calculate properties such as the bulk modulus  $K$  and the shear modulus  $G$ , as described in Table 7.1. The components of  $C_{ij}$  depend on the choice of coordinate system and lattice vectors, and in this work we have adopted the IEEE standard [319] for all reported tensors.

Table 7.1: Properties derived from the elastic constant matrix in this work, and their corresponding JSON keys and datatypes.

| Property                            | Key                     | Datatype | Unit              | Description                                     | Equation   |
|-------------------------------------|-------------------------|----------|-------------------|---|--|
| Elastic tensor, $C_{ij}$            | elastic_tensor          | array    | GPa               | Elastic tensor (IEEE-format)                    | see main text  |
| Elastic tensor, $C_{ij}$            | elastic_tensor_original | array    | GPa               | Elastic tensor (poscar orientation)             | see main text  |
| Compliance tensor, $s_{ij}$         | compliance_tensor       | array    | GPa <sup>-1</sup> | Tensor, describing elastic behavior             | $s_{ij} = C_{ij}^{-1}$   |
| Bulk modulus, $K_V$                 | K_Voigt                 | number   | GPa               | Upper bound on $K$ for polycrystalline material | $9K_V = (C_{11} + C_{22} + C_{33}) + 2(C_{12} + C_{23} + C_{31})$                                  |
| Bulk modulus, $K_R$                 | K_Reuss                 | number   | GPa               | Lower bound on $K$ for polycrystalline material | $1/K_R = (s_{11} + s_{22} + s_{33}) + 2(s_{12} + s_{23} + s_{31})$                                 |
| Shear modulus, $G_V$                | G_Voigt                 | number   | GPa               | Upper bound on $G$ for polycrystalline material | $15G_V = (C_{11} + C_{22} + C_{33}) - (C_{12} + C_{23} + C_{31}) + 3(C_{44} + C_{55} + C_{66})$    |
| Shear modulus, $G_R$                | G_Reuss                 | number   | GPa               | Lower bound on $G$ for polycrystalline material | $15/G_R = 4(s_{11} + s_{22} + s_{33}) - 4(s_{12} + s_{23} + s_{31}) + 3(s_{44} + s_{55} + s_{66})$ |
| Bulk modulus VRH, $K_{VRH}$         | K_VRH                   | number   | GPa               | Average of $K_R$ and $K_V$                      | $2K_{VRH} = (K_V + K_R)$   |
| Shear modulus VRH, $G_{VRH}$        | G_VRH                   | number   | GPa               | Average of $G_R$ and $G_V$                      | $2G_{VRH} = (G_V + G_R)$   |
| Universal elastic anisotropy, $A^U$ | elastic_anisotropy      | number   | -                 | Description of elastic anisotropy               | $A^U = 5(G_V/G_R) + (K_V/K_R) - 6 \geq 0$  |
| Isotropic Poisson ratio, $\mu$      | poisson_ratio           | number   | -                 | Number, describing lateral response to loading  | $\mu = (3K_{VRH} - 2G_{VRH}) / (6K_{VRH} + 2G_{VRH})$  |

The first-principles results presented in this work are performed using the projector augmented wave (PAW) method [52, 53] as implemented in the Vienna Ab Initio Simulation Package (VASP) [137, 136]. In all calculations, we employ the Perdew, Becke and Ernzerhof (PBE) Generalized Gradient Approximation (GGA) for the exchange-correlation functional [37]. Other parameters employed in our HT-DFT calculations of elastic constants are system-dependent. For the metals and metallic compounds, we employ a cut-off for the plane waves of 700 eV. Further a uniform k-point density of approximately 7,000 per reciprocal atom (pra) is used, which means that the number of atoms per cell multiplied by the number of k-points equals approximately 7,000. For the compounds that contain magnetic elements, a ferromagnetic state is initialized in the calculation. We expect to correctly converge to ferromagnetic and non-magnetic states in this way, but not to anti-ferromagnetic states. This set of parameters results in elastic tensors that are converged to within 5% for 95% of the considered systems. Given the chemical breadth of the compound set - spanning metals, semiconductors and oxides - it is unlikely that one set of parameters performs equally well for all classes of materials. Therefore, to detect anomalies and outliers, tests were designed and corresponding first-principles calculations with higher convergence setting were performed (for more details see the next section). The set of approximately 20 semiconductors is calculated with the same convergence parameters as the metals and metallic compounds with similar resulting convergence. For the binary oxides, a plane wave cut-off of 700 eV is also used, with a k-point density of 1,000 pra. This leads to elastic constants converged to within 5 % for all binary oxides considered in this work. Due to the presence of strongly correlated electrons in some of the oxides, the GGA+U method is employed, with U representing the Hubbard-parameter [320, 321]. The values of U are chosen consistent with those employed in the MP [316, 318].

### 7.3.2 Workflow

In this subsection we describe the workflow for the HT implementation of the stress-strain approach to computing elastic constants described above. We note that the workflow developed for this purpose shares many features in common with that developed for elastic constant-calculations in the Vlab distributed cyberinfrastructure for materials computation [314]. The main difference between the current approach and that described in Ref. [314], is that the focus here is on elastic constants at zero pressure and temperature, whereas the Vlab workflow is developed more generally to consider elastic constants under finite pressures and temperatures, which are particularly important in the context of geophysical applications. The workflow in Ref. [314] thus contains tasks related to the calculations of equations of state and finite-temperature phonon contributions, which are not considered in the present work. The emphasis here is on developing comprehensive databases of elastic moduli across a broad class of inorganic compounds, for materials design applications, and on interfacing the data with the Materials Project (MP) infras-

structure.

Figure 7.1 summarizes the workflow for data generation implemented within the MP HT calculation infrastructure used in the present work. We start from the optimized structures in MP, and perform a tighter structural relaxation, with more stringent convergence parameters in the DFT-calculation. This initial step is necessary since the calculation of elastic constants by the stress-strain method requires a well-converged stress tensor, and the standard HT-settings in the MP, which are optimized for the total energy, are not always sufficient for this purpose. This procedure leads to a structure exhibiting close to zero residual stresses and forces on the atoms.

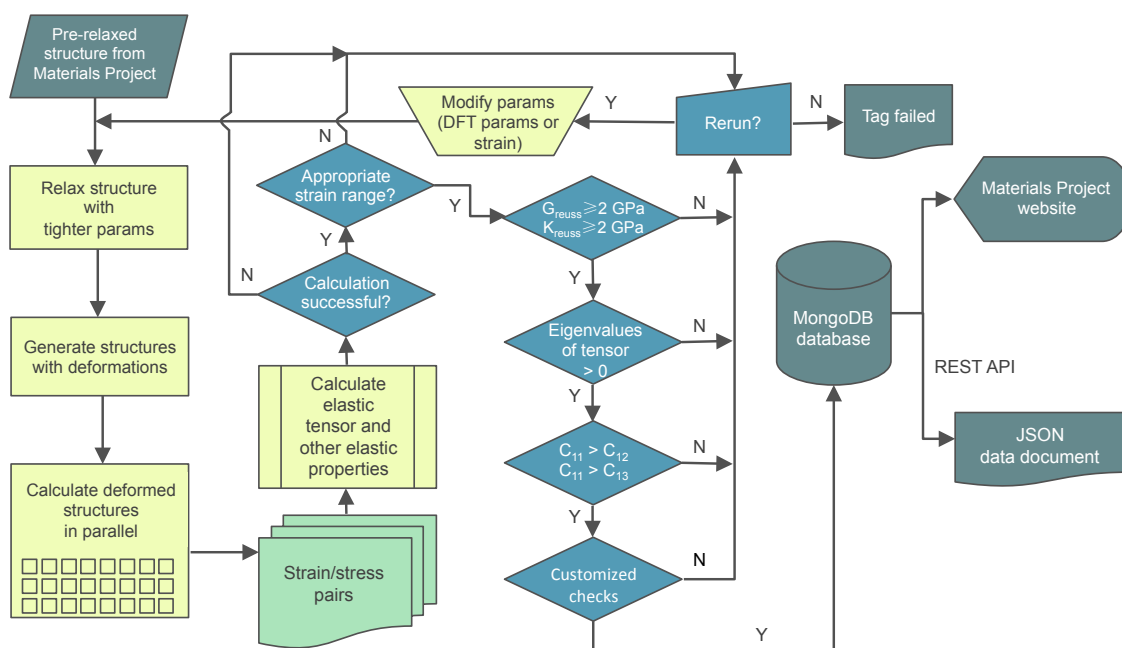


Figure 7.1: High-Throughput calculation scheme. Workflow for calculating and filtering the elastic constants.

The next step is to construct a set of deformed structures, for calculations of the resulting stresses. Each structure in this set is deformed homogeneously by one of the 6 independent components of the strain tensor defined above, with a magnitude chosen over a prescribed range. Similar to previous work (e.g. [322, 313]) in which a stress-strain method for computing elastic tensors has been employed, a maximum strain of 1 % is applied initially to distort the structures. In our experience this value is typically large

enough for most compounds to minimize the numerical noise in the calculation of the stress tensor, but small enough to remain well within the linear-elastic regime. In this initial step we choose four values for the strain magnitude, varying between -1 to 1 %, leading to a set of set of 24 initial deformed structures. First-principles calculations of the stress tensor for each of these structures are performed, including ionic relaxations. The calculation is considered to be unsuccessful if one or more of the single deformation runs fails to converge. In such cases, the calculations are rerun with tighter numerical convergence parameters. In the case of several unsuccessful iterations, a tag to this material is generated indicating that the calculation of the elastic tensor has failed.

Once the 24 stress tensor calculations have been successfully computed, a check is performed to determine whether the range of strains considered is appropriate for deriving the elastic constant tensor using a linear stress-strain relationship. This is done by fitting the elastic constants over different ranges of strain, and examining the sensitivity of the results. We employ the following nomenclature for the chosen ranges of strains investigated:  $\varepsilon_1 = (-1 \%, -0.5 \%, +0.5 \%, +1 \%)$ ,  $\varepsilon_2 = (-0.5 \%, +0.5 \%)$ ,  $\varepsilon_3 = (-0.75 \%, -0.5 \%, +0.5 \%, +0.75 \%)$ , and finally  $\varepsilon_4 = (-1.25 \%, -0.75 \%, +0.75 \%, +1.25 \%)$ . We first fit the elastic constants to the default strain range,  $\varepsilon_1$ , and compare the resulting bulk and shear modulus to those as obtained from a fit to  $\varepsilon_2$ . If the results are within 15 %, we move on to the next step in the workflow using the elastic constants as obtained from the fit to the strain range  $\varepsilon_1$ . If the discrepancies are larger than 15 %, additional stress tensors are calculated for strain values of ( $\pm 0.75\%$ ). We then compare the bulk and shear modulus, as fit from strain ranges  $\varepsilon_2$  and  $\varepsilon_3$ . If the results agree to within 15 %, we progress in the workflow using the elastic constants as fit to the strain range  $\varepsilon_2$ . If again the results disagree, we compare the bulk and shear modulus, fit to  $\varepsilon_1$  and  $\varepsilon_4$ . If these agree to within 15 %, we progress in the workflow using the elastic constants fit to the default strain range  $\varepsilon_1$ . If all of these steps fail, a warning message is generated for the compound, warranting further investigation.

From our initial set of 1,181 materials, we find that in 34 cases, either the bulk modulus and/or the shear modulus are different by over 15 %, depending on whether  $\varepsilon_1$  or  $\varepsilon_2$  is used for fitting the elastic tensor. A refitting of the elastic constants of those systems is performed over the range of strains corresponding to  $\varepsilon_3$ , and the bulk and shear moduli are compared to those as obtained from fitting to  $\varepsilon_2$ . We find that only 20 systems exhibit discrepancies of over 15 %. For the latter systems, we finally compare the bulk and shear moduli as obtained from fitting to  $\varepsilon_1$  and  $\varepsilon_4$ , respectively, finding that only 10 still show discrepancies of over 15 %. Thus, for the vast majority of the cases considered, the default range of strains  $\varepsilon_1$  is found to suffice for calculations of the elastic constants by a stress-strain methodology, and for more than two-thirds of the remaining compounds the additional checks implemented in the workflow lead to identification of an appropriate range of strains to yield reasonable results.

As illustrated in Fig. 7.1, for the systems where the calculation ends successfully and an appropriate range of strains is successfully identified, the elastic tensor results are further checked using various filters, designed to detect possible errors related to the assumption of linear elastic behavior, or other numerical inaccuracies that might occur due to the need for tighter convergence. The filters are designed to reveal physically impossible behavior, which can be indicative of such errors. The filters include: i)  $K_R > 2$  GPa, ii)  $G_R > 2$  GPa, iii) all 6 eigenvalues of the elastic tensor are larger than zero, and iv) Born-Huang stability criteria [323] are obeyed to within a 10 % margin (see below). Note that  $K_R$  and  $G_R$  represent the Reuss-averages of the bulk and shear moduli, respectively [199] (see Table 7.1 for definitions).

Conditions i) and ii) are selected based on an empirical observation that the most compliant known metals have shear and bulk moduli larger than approximately 2 GPa. Hence if our calculations yield results below 2 GPa for either the Reuss averages [199] (a lower bound estimate) of  $K$  or  $G$ , these results might be correct but deserve additional attention. Condition iii) expresses the conditions for mechanical stability of solids under zero stress. If one (or more) of the eigenvalues of the elastic tensor is (are) negative, the compound is mechanically unstable at zero temperature. The effects of finite temperatures may lift the mechanical instability in some systems, such as B2 NiTi [324]. However, negative eigenvalues may also indicate the calculation is erroneous, and hence these cases are flagged for a more detailed investigation. The final set of filters iv) is used to identify elastic tensors that correspond to materials that are mechanically stable but are near an elastic instability. This is done by applying the Born-Huang elastic stability criteria for the appropriate crystal system. As an example for the cubic crystal system, we require that  $C_{11} - C_{12} > 0$ ,  $C_{11} + 2C_{12} > 0$ ,  $C_{44} > 0$ . If one or more of these criteria is violated, one or more of the elastic tensor eigenvalues is negative. To identify compounds that are close to a mechanical instability, we apply a small tolerance to the Born-Huang criteria. As an example, for the case of cubic crystal systems, we check if  $C_{11} > \epsilon C_{12}$  holds true, where  $\epsilon = 1.1$ . We find empirically that when  $C_{11} < \epsilon C_{12}$ , frequently the first-principles calculation was not properly converged or a more accurate PAW potential is required (e.g., including semi-core states). For other crystal systems, similar tests are performed.

For the materials that do not obey one or more of the conditions i)-iv), we investigate the effect of the various convergence parameters in the DFT calculations, and if the results still do not pass the filters, a warning tag is generated warranting further investigation. From the initial set of 1,181 materials, it is found that 97 systems fail to meet criteria i)-iv). In particular, 57 systems are found to be mechanically unstable, 16 systems have Reuss averaged shear or bulk moduli lower than 2 GPa and 19 systems are within a margin  $\epsilon = 1.1$  of being mechanically unstable. For these 97 systems, a new set of calculations is performed using a substantially higher k-point density of approximately

25,000 pra in both structural relaxations and stress-calculations. This set of calculations results in a reduction in the number of systems that do not obey conditions i) - iv) from 97 to 76 systems. Of these, 50 systems are found to be mechanically unstable, 14 systems have Reuss averaged shear or bulk moduli lower than 2 GPa and 12 systems are mechanically stable but within a margin  $\epsilon = 1.1$  of being mechanically unstable. In particular, the pure metals Al and Cu are flagged by the filters in the initial DFT-runs employing lower k-points, since these metals are close to mechanical instability. However, upon increasing the k-points, results improve (this finding was not unexpected since Cu and Al which are known to exhibit complex Fermi surfaces [325]). The filters described above are designed to identify anomalies, and they will likely be refined as our approach evolves and additional validation is performed.

All elastic tensors that have achieved sufficient numerical convergence are inserted into the MP database and reported on the web site. We also store and report on the web-site results for mechanically unstable compounds, but include a warning message to the user. A JSON (JavaScript Object Notation) data document is generated for each reported elastic tensor. This JSON data document is publicly available at the Dryad-repository. We perform the structure generation and data analysis for elastic constant calculations using our open-source materials analysis code pymatgen [326]. The workflow software FireWorks [327] is used to automate the HT calculations and data management.

### 7.3.3 Code availability

The code for calculating elastic constants and related properties is part of the open-source code pymatgen [326]. Pymatgen is released under the MIT (Massachusetts Institute of Technology) License and is freely accessible. The workflow as shown in Fig. 7.1 is powered by the open-source code FireWorks and is released under a modified GPL (GNU General Public License). Also FireWorks can be accessed and used freely.

## 7.4 Data Records

The calculated elastic property data and related metadata of 1,181 materials are publicly available at the Materials Project. The complete data set can be downloaded in a JSON file or via the Materials Project REST API. The Materials Project also provides a convenient web interface that allows searching for materials with particular properties by querying the elastic constant database. In addition, the materials detail pages on the website now include calculated elasticity data when available.

Table 7.2: JSON keys for metadata and their descriptions.

| Key            | Datatype | Description  |
|----------------|----------|--|
| material_id    | string   | IDs for entries in the Materials Project   |
| formula        | string   | Chemical formula   |
| structure      | string   | Relaxed crystal structure represented in Crystallographic Information File (cif) |
| poscar         | string   | relaxed crystal structure represented in poscar-format for VASP calculations     |
| space_group    | number   | Space group number defined by The International Union of Crystallography         |
| volume         | number   | Volume of the relaxed structure in $\text{\AA}^3$                                |
| nsites         | number   | Number of atomic sites for the conventional cell                                 |
| kpoint_density | number   | density of k-points in the first Brillouin zone per reciprocal atom              |

#### 7.4.1 File format

The data set for each material is stored as an individual JSON document. Based on a series of key/value pairs, the JSON format offers a readily parsable yet human readable solution for data exchange. The metadata record for each material includes descriptions of the material (e.g. structure, structure symmetry) and calculation parameters (e.g. k-points density). The JSON keys for the metadata and their descriptions are listed in Table 7.2. Note that the structure is presented both in Crystallographic Information File (cif) and poscar-format. The poscar-format is the standard structure description used by the VASP-code.

#### 7.4.2 Properties

The elastic constants appearing in Eq. 7.1 are calculated by DFT and represent the elastic constants of a single crystal. While single-crystal elastic properties are important as input into higher length-scale modeling of mechanical behavior, we also derive and report several polycrystalline averaged properties. In this work, we calculate for all considered systems the Voigt and Reuss averages of the bulk and shear modulus. The Voigt average provides an upper bound on the elastic moduli of an untextured polycrystalline material whereas the Reuss average provides a lower bound [199]. The experimental quantities will lie between the bounds, with the precise value determined by the detailed orientation of the various grains in the material. Also we provide the empirical VRH-average for the bulk and shear modulus. This empirical average is known to represent the bulk and shear modulus of polycrystalline materials with comparable accuracy as more advanced



polycrystalline homogenization schemes such as those by Hashin and Strickman [328, 295]. Other properties computed in this work are the index of elastic anisotropy [329] and the Poisson ratio in the isotropic approximation. The various derived properties are listed in Table 7.1, including expressions relating these properties to the elements of the single-crystal elastic tensor. The corresponding JSON keys and the datatypes are also listed in Table 7.1. The elastic tensor  $C_{ij}$  is presented in two ways in Table 7.1: i) in the standardized IEEE-format and ii) in the format corresponding to the orientation of the crystal structure as defined in the poscar-key in Table 7.2.

### 7.4.3 Graphical representation of results

A graphical representation of our dataset is presented in Fig. 7.2, which shows a log-log plot of the VRH averaged bulk modulus versus the VRH averaged shear modulus for all materials considered in this work. The orientation of each arrow corresponds to the volume per atom (VPA) of that specific material. The material with the minimum VPA in our dataset is assigned an arrow pointing at 12 o'clock (diamond) and the arrows rotate anti-clockwise towards the materials with the maximum VPA in our dataset at 6 o'clock (barium). The angle of rotation from 12 o'clock to 6 o'clock is proportional to the normalized VPA. The VPA is considered since it is known to correlate well with elastic properties such as bulk modulus [330, 331, 332]. Indeed, Fig. 7.2 illustrates this apparent correlation. Specifically, diamond exhibits the highest bulk and shear moduli of all materials in our database and it also has the smallest VPA among those materials. The more elastically compliant materials in Fig. 7.2 show relatively higher values for the VPA. The color coding in Fig. 7.2 represents the Poisson ratio in the isotropic approximation. Also, two lines of constants  $K_{VRH}/G_{VRH}$  ratio are drawn. As described in the Introduction, this quantity, known as Pugh's ratio [116], has been shown to correlate with ductility in crystalline compounds [116, 110] and is further related to the Poisson ratio [287]. The bar plots show the distribution of materials relative to their respective values for the bulk and shear modulus. The distribution shows that most materials considered, lie in the region around 80 and 190 GPa for the shear modulus and bulk moduli, respectively. Thus, this diagram distills several well-known results in the field of elasticity and illustrates them through a large amount of data.

## 7.5 Technical Validation

### 7.5.1 Verification of computational methodology

To verify proper implementation of HT version of the stress-strain method described above, detailed comparisons have been undertaken between the data derived from this approach and independent computational results obtained in the present work using alternative methods, or published previously by other authors using the same DFT ap-

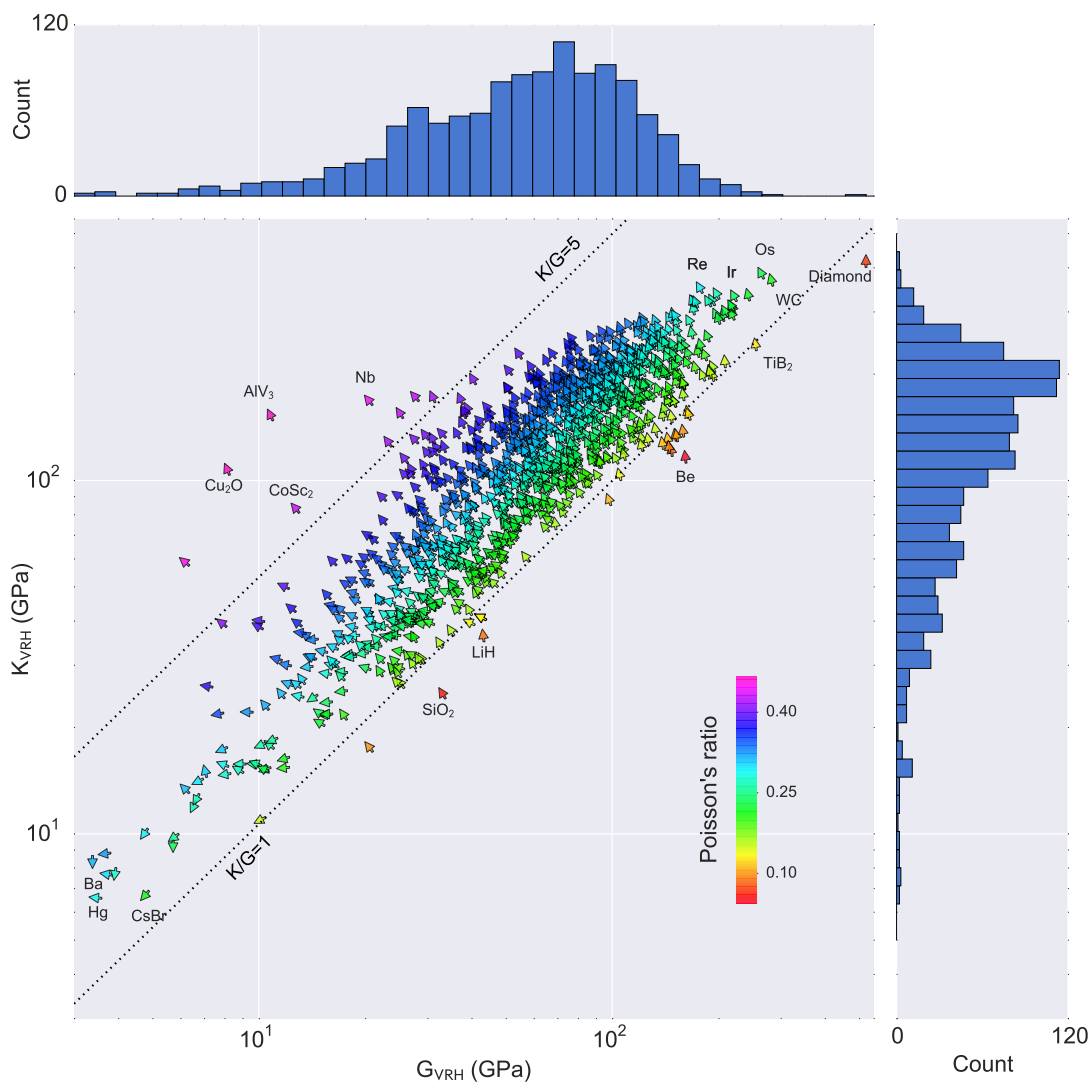


Figure 7.2: Distribution of calculated volume per atom, Poisson ratio, bulk modulus and shear modulus. Vector field-plot showing the distribution of the bulk and shear modulus, Poisson ratio and atomic volume for 1,181 metals, compounds and non-metals. Arrows pointing at 12 o'clock correspond to minimum volume-per-atom and move anti-clockwise in the direction of maximum volume-per-atom, which is located at 6 o'clock. Bar plots indicate the distribution of materials in terms of their shear and bulk moduli.

proximations. Such comparisons have been undertaken for a subset of systems that are representative of the material types in the database. Overall, the comparisons yield agreement at the level of approximately 5%, with a few exceptions, as described below.

Considering first insulator compounds, the  $C_{ij}$  values obtained here for  $\alpha$ -Al<sub>2</sub>O<sub>3</sub> are all within 2% of the results reported in Ref. [313] using the same DFT approximations, combined with a similar stress-strain method. The present  $\alpha$ -Al<sub>2</sub>O<sub>3</sub> results are also within 3% of the values for all  $C_{ij}$  components obtained from a numerical differentiation of the energy versus strain using Wien2K [333, 334], and within 5% of the results for all components obtained by energy differentiation methods derived from Quantum Espresso [193] and reported in Ref. [335]. It should be noted that for  $\alpha$ -Al<sub>2</sub>O<sub>3</sub> the  $C_{14}$  component obtained in this work has a sign opposite to that reported in [335]. In fact, the sign of  $C_{14}$  in  $\alpha$ -Al<sub>2</sub>O<sub>3</sub> has been a source of controversy in other previous theoretical and experimental studies [335, 313, 336]. However, as discussed in [335], the ambiguity in choosing the Cartesian reference coordinate system for trigonal materials with R centering type is the likely cause of these discrepancies. For cubic Y<sub>2</sub>O<sub>3</sub> the present results for each of the  $C_{ij}$  components are within 10% of those reported from the stress-strain calculations performed within in GGA in [336] (the largest discrepancy is found for the  $C_{12}$  component). For  $\beta$ -Si<sub>3</sub>N<sub>4</sub> the present results agree to within 5 % of those reported in the same publication [336]. For the polar wurtzite ZnO compound, the results obtained in the present work agree to within 8% for  $C_{44}$ , and within 2 % for all other moduli, with the values obtained by Wu *et al.* [75] using the same DFT approximations, and an approach that employs density-functional perturbation theory to compute internal displacement contributions.

We have also conducted a number of comparisons between the present results and other theoretical calculations for metallic and small-band-gap systems. We have compared results obtained using our HT methodology with those derived from a method that fits the calculated total energy as a function of volume-conserving strains, as developed by Mehl *et al.* [322, 337]. The present HT stress-strain methodology yields results within 4% of those obtained from this energy versus strain method for BCC Lithium and FCC Aluminum. Further, the elastic constant tensor components for orthorhombic TiB, reported from full-potential-linear-augmented-plane-wave GGA calculations, along with total energy differentiation methods [338], are within 5% for of the values obtained here for all  $C_{ij}$  components, with the exception of  $C_{44}$  (reported as  $C_{66}$  in [338]), which is within 15%.

As described in the previous section, consistency checks are built into the HT-workflow employed in the present work to ensure that the range of strains employed in the fit of the stress-strain relations are appropriate. The dependence of calculated elastic constants on the range of strains considered has been examined in detail in previous work, e.g. [335]. The authors of Ref. [335] employ an energy versus strain method, using sixth-order polynomial fits of the energy to a strain range of up to 8 %. The authors conclude that for

small deformations, the best results are obtained by low-order polynomial fits, and that the stress-strain approach is more accurate in the sense that only first-order derivatives are required, in which case smaller distortions are required. This is consistent with the findings in this work, where a maximum strain of 1 % is found to provide reliable results for over 97 % of the compounds considered, using a linear stress-strain fit. To investigate this issue further we have performed detailed tests similar to those in Ref. [335] for a select number of systems. Strains in the range of 1 % to 8 % were applied and the stresses and strains fit using  $n$ -th order polynomials, where  $n$  ranges from 1 to 4. In particular for KBr, which is one of the most elastically compliant materials in the database, we found changes of less than 2 % in the bulk and shear moduli, as the strain was varied from 1 % to 8 %, regardless of the order of the polynomial. For diamond, the stiffest materials in our database, one might expect relatively strong non-linear behavior of the stress with strain, even for small strains. However, also for diamond we find that the bulk and shear moduli vary by less than 2 % as the strain is varied and the polynomial order ranges from 1 to 4. Overall, the tests described in this and the previous section suggest that the stress-strain approach and the range of strains considered in its application, yield reliable results for the vast majority of the compounds considered in the development of the current database.

### 7.5.2 Validation through comparison to experimental measurements

A comprehensive literature review was performed to compile measured elastic constant tensors, for comparison with the present calculations, in order to establish the expected accuracy of the calculated results. In this comparison we consider only experimental sources that report the full elastic tensor, rather than only the bulk or shear modulus, so that a systematic comparison with the calculated elastic tensors can be made. In total, 104 systems are used in the comparison, including oxides and semiconductors [310, 312, 339, 340, 341, 342, 343, 344, 299, 144, 345, 346] and metals and metallic compounds [347, 348, 349, 350, 351, 352, 299, 144, 353, 302]. In the comparison, we make use of the Voigt-Reuss-Hill average for  $K$  and  $G$  (denoted by  $K_{VRH}$  and  $G_{VRH}$ , respectively), which is the arithmetic mean of the Voigt and Reuss bounds [199]. See also Table 7.1 for their definitions. The shear ( $G_{VRH}$ ) and bulk ( $K_{VRH}$ ) moduli of these 104 systems are compared by calculating the VRH-average from the experimentally measured and calculated tensors. In addition a Euclidean difference norm [354], normalized by the magnitude of the calculated elastic tensor, is used to probe errors relative to the mean elastic constants:  $\|C_{ij}^{exp} - C_{ij}^{calc}\| \cdot \|C_{ij}^{calc}\|^{-1}$ , where the definition of the norm is given as  $\|C_{ij}\|_E = \left( \text{tr} \left[ C_{ij}^T C_{ij} \right] \right)^{0.5}$ . In this expression,  $C_{ij}$  represents the elastic tensor (in matrix form) as defined in Eq. 7.1.

The comparison of calculated and experimental values for  $K_{VRH}$  and  $G_{VRH}$  are

shown in Fig. 7.3 and 7.4, respectively. In each plot, lines are shown indicating relative differences between computation and experiment of  $\pm 15\%$ . As can be seen, the agreement between experiment and calculation is generally within this threshold, although there are some outliers. Specifically, in the case of the bulk modulus a discrepancy between experiment and calculations larger than 15 % is found for 16 systems (in order of absolute deviation, from low to high): Na, Tl, Pb, Ca, CsI, Nd, Yb, YZn, Cd, Mg<sub>2</sub>Sn, Ge, Pt, CaAl<sub>2</sub>, Au, Co, CdAu. The first 11 in the list disagree with experiment by less than 10 GPa. For the shear modulus, a discrepancy between experiment and calculations larger than 15 % is found for 15 systems (in order of absolute deviation, from low to high): KI, Ca, CsI, KBr, CdSe, Tl, Cd, GaSb, GaAs, Ge, CdAu, Y<sub>2</sub>O<sub>3</sub>, Au, Cr<sub>3</sub>Si, MnSi. The first 6 in the list disagree with experiment by less than 10 GPa. These larger discrepancies may be due to errors in the calculations, the experimental measurements or a combination of both. Note that most of the systems displaying greater than 15 % discrepancy between calculations and measurements are those with relatively low bulk and shear moduli, see the insets in Figs. 7.3 and 7.4. Similarly, we find for the quantity  $\|C_{ij}^{exp} - C_{ij}^{calc}\| \cdot \|C_{ij}^{calc}\|^{-1}$  most of the systems show discrepancies below 20 %, with the largest discrepancies found for the systems with the smallest values of  $\|C_{ij}^{calc}\|$ . For these systems with relatively small elastic moduli, the discrepancies may be due to the larger effect of the numerical errors in the calculations on the relative precision of the calculated elastic tensors.

Other factors that might contribute to discrepancies are temperature variations: DFT provides a zero-temperature description of the state of the material, whereas many experiments are done at room temperature. While such temperature variations are typically relatively small below room temperature, in some systems this effect can be large. For example, in previous experimental studies of single-crystal Nb<sub>3</sub>Sn, the value of  $(C_{11}-C_{12})$  starts at 140 GPa and decreases to zero as temperature decreases from 300 to 32 K [348]. Our calculated results for Nb<sub>3</sub>Sn at 0 K show a mechanical instability with  $C_{11}$  slightly less than  $C_{12}$ . Thus, these mechanical instabilities can contain useful information indicating potentially anomalous mechanical properties or shear instabilities at low temperature. Methods have been implemented in the literature to predict the temperature dependence of the elastic constants from first-principles [355, 356], and implementation of such approaches represents a future extension of the database. The elastic constants reported in this work represent the zero-temperature limit of the isothermal moduli, whereas experimentally it is often the adiabatic elastic tensor that is measured; however, the differences between these two types of elastic constants are typically small [357]. From the computational perspective, we have found that for some elements, PAW potentials exhibiting a different number of electrons as valence states can significantly affect the calculated elastic properties. This is the case for the elements V, Ti and Nb. Also, some of the systems listed above exhibit antiferromagnetic states. These states are both temperature and strain dependent, and resolving these details in HT DFT-calculations of elastic constants is challenging and the topic of current work that is expected to impact future releases of the database.

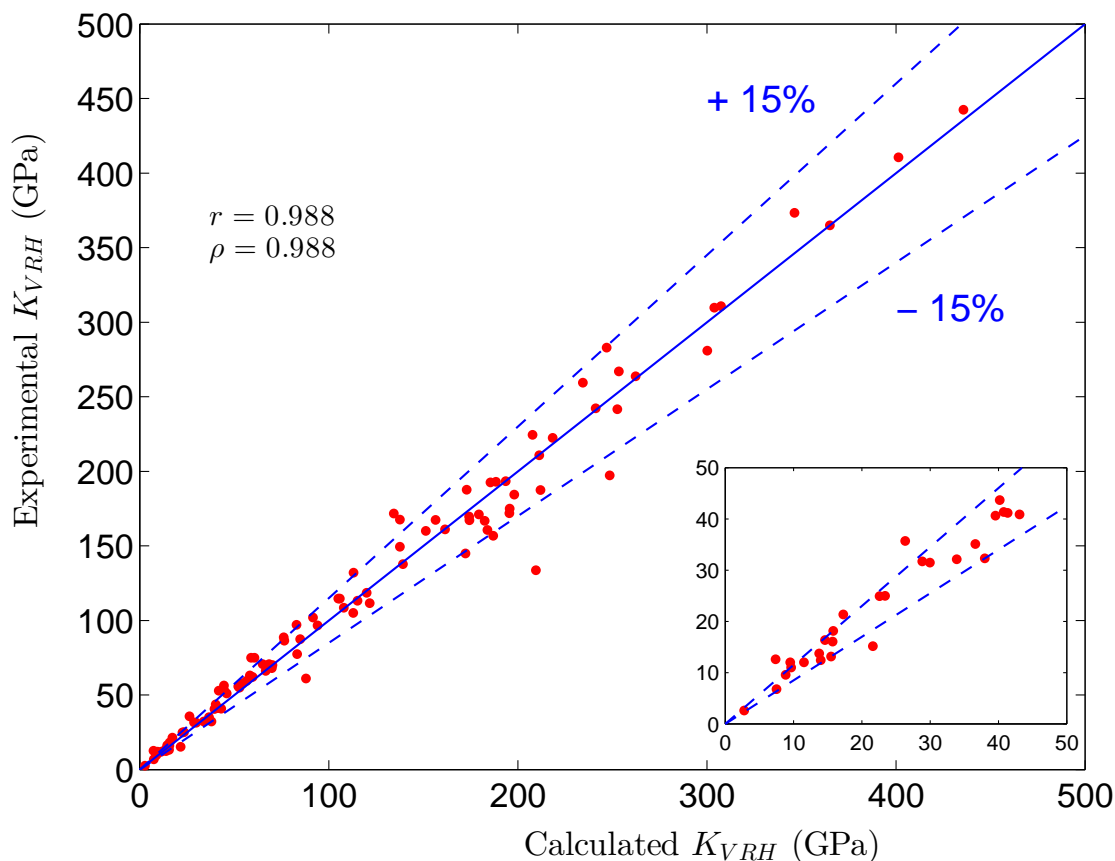


Figure 7.3: Plot of experimental vs. calculated bulk moduli. Comparison of experimental and calculated bulk moduli for a selected set of systems, with calculated Pearson correlation coefficient  $r$  and Spearman correlation coefficient  $\rho$  reported.

For the purpose of using the elastic constant database in the context of materials discovery, it is useful to characterize the correlation between the calculated and measured elastic quantities. For this purpose we again consider the values for  $K_{VRH}$  and  $G_{VRH}$ , and calculate the Pearson and Spearman correlation coefficients ( $r$  and  $\rho$ , respectively). Also computed are 95% bootstrap-based confidence intervals for the correlations. The lower (LB) and upper (UB) bounds of these confidence intervals are presented as ([LB, UB]). For the bulk modulus, the Pearson and Spearman correlation coefficients are 0.988 ([0.978, 0.994]) and 0.988 ([0.973, 0.993]), respectively. For the shear modulus, we find values of 0.994 ([0.985, 0.998]) and 0.982 ([0.955, 0.993]) for the Pearson and Spearman

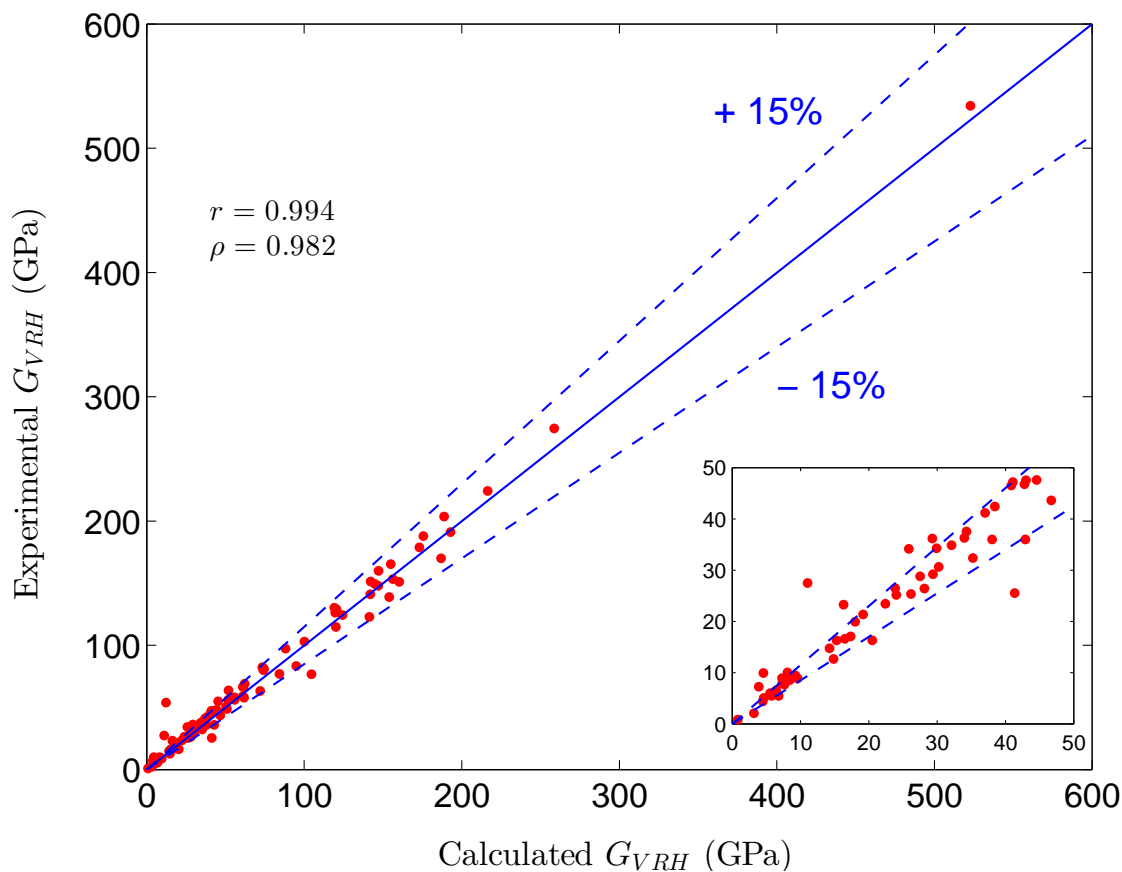


Figure 7.4: Plot of experimental vs. calculated shear moduli. Comparison of experimental and calculated shear moduli for a selected set of systems, with calculated Pearson correlation coefficient  $r$  and Spearman correlation coefficient  $\rho$  reported.

correlation coefficients, respectively. These values suggest that the measured and calculated values for bulk and shear moduli are strongly linearly associated and also, a high monotone association exists.

## 7.6 Usage Notes

The database presented here represents the to-date largest collection of consistently calculated or measured elastic tensors for crystalline inorganic materials. We anticipate that this dataset, and the methods provided for querying it, will provide a useful tool in fundamental and application-related studies of inorganic compounds. We expect,

in particular, that the database will be useful for efforts aimed at materials discovery and design, in the search for and optimization of materials with targeted mechanical and thermal properties. For the first time, researchers will be able to query existing compounds from the database by specifying desired elastic properties, for example a maximum value of the shear modulus with minimum elastic anisotropy. For compounds that are currently not in the database, future extensions of this work will be a web interface where MP-users will be able to calculate elastic properties on demand, by uploading a file describing the crystallography of the material of interest. Techniques such as data mining and machine learning can be used to reveal fundamental trends in the elastic properties of compounds, and guide the screening of potentially interesting materials for target properties.



## Chapter 8

# High-Throughput Discovery of New Piezoelectrics

### 8.1 Foreword

Piezoelectric materials are used in numerous applications requiring a coupling between electrical fields and mechanical strain. Despite the technological importance of this class of materials, for only a small fraction of all inorganic compounds which display compatible crystallographic symmetry, has piezoelectricity been characterized experimentally or computationally. In this chapter we employ first-principles calculations based on density functional perturbation theory to compute the piezoelectric tensors for nearly a thousand compounds, thereby increasing the available data for this property by more than an order of magnitude. The results are compared to select experimental data to establish the accuracy of the calculated properties. The details of the calculations are also presented, along with a description of the format of the database developed to make these computational results publicly available. In addition, the ways in which the database can be accessed and applied in materials development efforts are described.

Part of the results presented in this chapter, including the figures and tables, were published by Maarten de Jong, Wei Chen, Henry Geerlings, Mark Asta and Kristin Persson in *Scientific Data*, 2, 2015 [358]. The material is reproduced here with permission of the co-authors and publishers.

### 8.2 Background & Summary

Piezoelectricity is a reversible physical process that occurs in some materials whereby an electric moment is generated upon the application of a stress. This is often referred to as the direct piezoelectric effect. Conversely, the indirect piezoelectric effect

refers to the case when a strain is generated in a material upon the application of an electric field [359]. Today, piezoelectric materials are integral to numerous applications and devices that exploit this effect, and form the basis for a multi-billion dollar worldwide market [360, 361]. Examples are found in high voltage and power applications, actuators, sensors, motors, atomic force microscopes, energy harvesting devices and medical applications. These technologies all rely on the conversion of voltage to mechanical deformation or vice versa.

The mathematical description of piezoelectricity relates the strain (or stress) to the electric field via a third order tensor. This tensor describes the response of any piezoelectric bulk material, when subjected to an electric field or a mechanical load. The Hecke-mann diagram (Fig. 8.1) [359] conveniently describes how mechanical and electrical properties of solids are related. The piezoelectric response of a material can be described using different piezoelectric constants, reflecting various derivatives of thermodynamic functions. Of particular interest to this work are the isothermal piezoelectric stress constants (abbreviated in the rest of this chapter as simply piezoelectric constants), defined in full tensor notation as  $e_{ijk}^T = \left( \frac{\partial D_i}{\partial \varepsilon_{jk}} \right)_{E,T} = - \left( \frac{\partial \sigma_{jk}}{\partial E_i} \right)_{\varepsilon,T}$ , where  $D$ ,  $E$ ,  $\varepsilon$ ,  $\sigma$  and  $T$  represent the electric displacement field, the electric field, the strain tensor, the stress tensor and the temperature, respectively. In this work, Voigt-notation is employed for brevity so that the relations for the piezoelectric constants read  $e_{ij}^T = \left( \frac{\partial D_i}{\partial \varepsilon_j} \right)_{E,T} = - \left( \frac{\partial \sigma_j}{\partial E_i} \right)_{\varepsilon,T}$ . The Voigt-notation will be explained below in more detail. We note that the most commonly used piezoelectric constants appearing in the (experimental) literature are the piezoelectric strain constants, usually denoted by  $d_{ijk}$ . These can be readily related to the constants  $e_{ijk}$  if the elastic compliances  $s_{lmjk}^{ET}$  (at constant electric field and temperature) of the materials are known [362]:  $d_{ijk}^T = e_{ilm} s_{lmjk}^{ET}$ . In particular, the piezoelectric strain constants can be expressed thermodynamically as [359]  $d_{kij}^T = \left( \frac{\partial \varepsilon_{ij}}{\partial E_k} \right)_{\sigma,T} = \left( \frac{\partial D_k}{\partial \sigma_{ij}} \right)_{E,T}$ .

The complete piezoelectric tensor has been measured or calculated for only a small subset of potential piezoelectric materials. In the main references of compiled materials properties, a total of less than 50 systems can be found for which experimental and/or calculated values for full piezoelectric tensors are available [363, 364, 365, 366, 367, 368, 369, 370, 371, 372, 373, 374, 375, 376, 377, 378, 379, 380]. This represents a small subset of candidate materials, since in principle all materials with a finite bandgap that lack inversion symmetry can exhibit piezoelectric behavior. Hence there are thousands of hitherto unknown potential piezoelectric compounds in the inorganic crystal structure database [307, 308, 309]. Recently, significant effort has been devoted to the development of lead-free piezoelectric materials [381, 382, 383, 384, 385, 386, 387]. However, efficient screening over a wide range of materials chemistries is hindered by the lack of comprehensive experimental data.

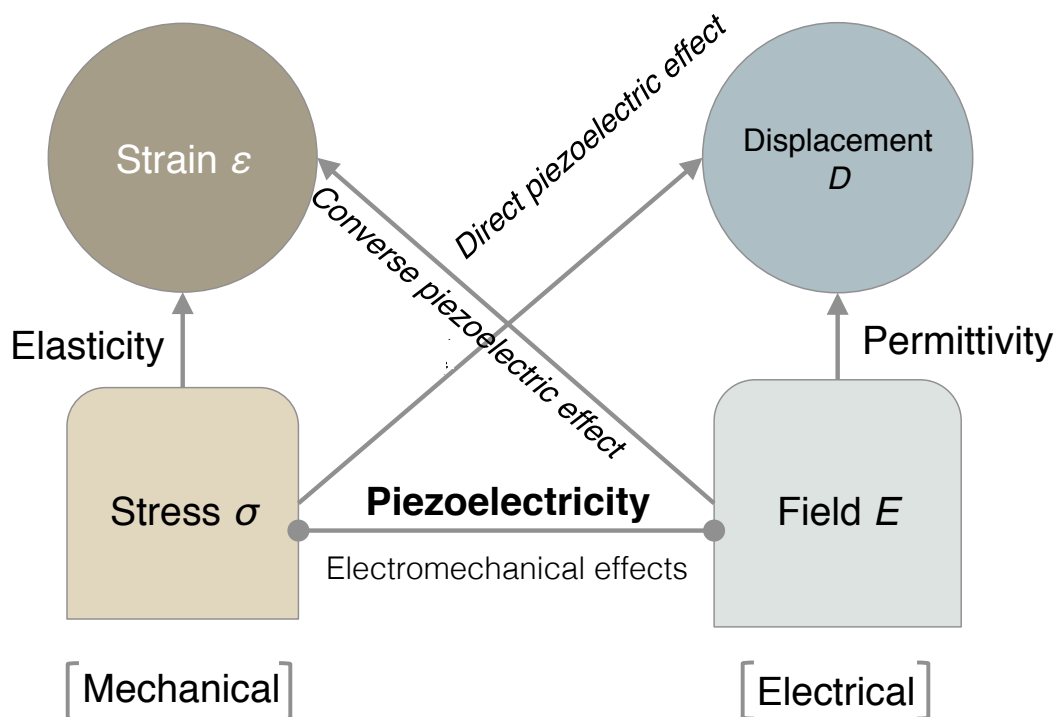


Figure 8.1: Part of a Heckmann diagram, showing the relation between mechanical and electrical properties of solids.

Another challenge associated with the available data for piezoelectric constants is the large variability in the reported values, depending on the details of the experimental or computational techniques employed and/or the conditions under which the experiments are performed. As an example,  $\alpha$ -quartz ( $\text{SiO}_2$ ) is the second most abundant mineral and a commonly employed material in piezoelectric devices. However, its reported piezoelectric constants differ by up to a factor of 3 in magnitude, presumably depending on the experimental conditions [363] and temperature [372, 388]. The same is true for the common mineral  $\text{AlPO}_4$  and elemental Te [363].

In this chapter, we introduce the to-date largest database of consistently calculated piezoelectric tensor properties of dielectric crystalline inorganic compounds. This database supplements our earlier work on elastic constants [284, 115, 288, 290, 190] and contributes to a more complete description of the deformation behavior of solids. Whereas our previous work was limited to describing the relationship between stress and strain in

the absence of electric fields, we now introduce the piezoelectric constants to incorporate this effect. Based on the Heckmann diagram in Fig. 8.1, this addition of piezoelectric constants will significantly increase the applicability of our previous dataset comprising zero-electric field elastic constants [284].

The work presented in this chapter is part of the Materials Project (MP) [316], and aims at employing high-throughput (HT) methods [15, 389] to develop open databases of calculated materials properties for discovery and design. The database of piezoelectric tensors currently consists of 941 materials and efforts are underway to compute more compounds in the near future. The piezoelectric properties are obtained using first-principles quantum-mechanical calculations based on Density Functional Theory (DFT), in particular Density Functional Perturbation Theory (DFPT) [390, 66, 71]. As described below, the calculated piezoelectric constants show a level of agreement with experimental data that is often comparable to the scatter in the measured data itself. It is important to note that in this chapter, intrinsic piezoelectric constants are presented, associated with the bulk, defect-free and strain-free material, at a temperature of 0 K.

The remainder of this chapter is organized as follows. In the next section the methods for materials selection and calculation of piezoelectric constants within an HT approach are described. Subsequently, the results of verification and validation analyses are presented, which establishes the accuracy of our DFT-calculations as well as the HT-algorithms. Finally, the last part of the chapter describes the structure of the data and gives an overview of the results obtained in this study.

## 8.3 Methods

### 8.3.1 Definitions & computational settings

In this work we report calculated values for the proper piezoelectric constants,  $e_{ij}$ , defined as follows:

$$e_{ij}^T = - \left( \frac{\partial \sigma_j}{\partial E_i} \right)_{\epsilon, T}, \quad j \mapsto \{11, 22, 33, 12, 23, 31\}, \quad i \mapsto \{1, 2, 3\} \quad (8.1)$$

where  $\sigma$  denotes the stress tensor and  $E$  denotes the electric field. Also, in the Voigt notation used in this work, pairs of Cartesian directions are contracted as follows: 11  $\mapsto$  1, 22  $\mapsto$  2, 33  $\mapsto$  3, 23, 32  $\mapsto$  4, 13, 21  $\mapsto$  5, 12, 21  $\mapsto$  6. The piezoelectric stress is the sum of the ionic and electronic contributions and the piezoelectric tensor-components as defined in Eq. 8.1 have units C/m<sup>2</sup>.

Note that different matrix-tensor notations exist in the literature. In particular, when mapping the full third order piezoelectric tensor onto a 3  $\times$  6-matrix, factors of 2

pre-multiplying certain constants are sometimes introduced. Specifically, some authors use the convention that  $e_{ijk} = e_{in}$ , when  $n = 1, 2, 3$  and  $2e_{ijk} = e_{in}$ , when  $n = 4, 5, 6$  [359, 391, 370, 392, 393]. In the present work, factors of 2 and  $\frac{1}{2}$  are not introduced in the piezoelectric tensor itself, but rather in the vectors operating on the piezoelectric tensor. Figures 8.2 and 8.3 (discussed in detail below) indicate for different crystal systems and point groups, the form the piezoelectric tensors take, according to the notation employed in this work. It is straightforward to convert to other conventions found in the literature.

The first-principles results presented in this work are performed using the projector augmented wave (PAW) method [52, 53] as implemented in the Vienna Ab Initio Simulation Package (VASP) [137, 136]. In all calculations, we employ the Perdew, Becke and Ernzerhof (PBE) Generalized Gradient Approximation (GGA) for the exchange-correlation functional [37]. A cut-off for the plane waves of 1000 eV is used and a uniform k-point density of approximately 2,000 per reciprocal atom (pra) is employed, which means that the number of atoms per cell multiplied by the number of k-points equals approximately 2,000. For the compounds that contain magnetic elements, a ferromagnetic state is initialized in the calculation. Similarly to our previous work [284], we expect to correctly converge to ferromagnetic and non-magnetic states in this way, but not to anti-ferromagnetic states. Due to the presence of strongly correlated electrons in some of the oxides, the GGA+U method is employed, with U representing the Hubbard-parameter [320, 321]. The values of U are chosen consistent with those employed in MP [316, 318].

We estimate that the choice for plane wave cutoff and kpoints leads to piezoelectric tensors with components that are converged to within approximately 10 % for over 90 % of the considered systems. This is based on careful convergence testing of DFT-results on a representative subset of approximately 25 compounds [363, 364, 365, 366, 367, 368, 369, 370, 371, 372, 373, 374, 375, 376, 377, 378]. Given the large variety of compounds and elements considered in this work, our DFT-parameters cannot be expected to perform equally well for all systems under investigation. Therefore, consistency checks are devised in our HT-infrastructure to detect possible anomalous behavior and errors in the first-principles calculations, similar to those devised for the HT-calculations of the recently published elastic constants [284]. The systems detected as problematic by these checks are recalculated from DFT with improved convergence settings in an attempt to solve the problem (see next next section for more details).

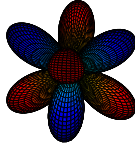
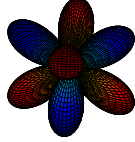
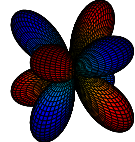
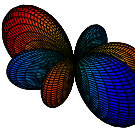

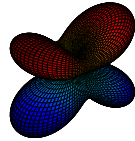
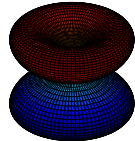
| Crystal system           | Point groups           | Piezoelectric tensor   | Surface representation  |
|--------------------------|------------------------|--|---|
| Cubic                    | $\frac{23}{\bar{4}3m}$ | $\begin{pmatrix} 0 & 0 & 0 & e_{14} & 0 & 0 \\ 0 & 0 & 0 & 0 & e_{14} & 0 \\ 0 & 0 & 0 & 0 & 0 & e_{14} \end{pmatrix}$                       |    |
| Tetragonal               | $\bar{4}2m$            | $\begin{pmatrix} 0 & 0 & 0 & e_{14} & 0 & 0 \\ 0 & 0 & 0 & 0 & e_{14} & 0 \\ 0 & 0 & 0 & 0 & 0 & e_{36} \end{pmatrix}$                       |    |
| Tetragonal               | $\bar{4}$              | $\begin{pmatrix} 0 & 0 & 0 & e_{14} & e_{15} & 0 \\ 0 & 0 & 0 & -e_{15} & e_{14} & 0 \\ e_{31} & -e_{31} & 0 & 0 & 0 & e_{36} \end{pmatrix}$ |    |
| Hexagonal                | $\bar{6}m2$            | $\begin{pmatrix} 0 & 0 & 0 & 0 & 0 & -e_{22} \\ -e_{22} & e_{22} & 0 & 0 & 0 & 0 \\ 0 & 0 & 0 & 0 & 0 & 0 \end{pmatrix}$                     |   |
| Hexagonal                | $\bar{6}$              | $\begin{pmatrix} e_{11} & -e_{11} & 0 & 0 & 0 & -e_{22} \\ -e_{22} & e_{22} & 0 & 0 & 0 & -e_{11} \\ 0 & 0 & 0 & 0 & 0 & 0 \end{pmatrix}$    |  |
| Hexagonal,<br>Tetragonal | $\frac{6mm}{4mm}$      | $\begin{pmatrix} 0 & 0 & 0 & 0 & e_{15} & 0 \\ 0 & 0 & 0 & e_{15} & 0 & 0 \\ e_{31} & e_{31} & e_{33} & 0 & 0 & 0 \end{pmatrix}$             |  |
| Hexagonal,<br>Tetragonal | $\frac{6}{4}$          | $\begin{pmatrix} 0 & 0 & 0 & e_{14} & e_{15} & 0 \\ 0 & 0 & 0 & e_{15} & -e_{14} & 0 \\ e_{31} & e_{31} & e_{33} & 0 & 0 & 0 \end{pmatrix}$  |  |

Figure 8.2: Piezoelectric tensors and symmetry classes considered in this work, part I. Typical representations of the longitudinal piezoelectric modulus in 3D are also shown for each crystal point group.

| Crystal system | Point groups | Piezoelectric tensor  | Surface representation |
|----------------|--------------|---|------------------------|
| Trigonal       | $3m$         | $\begin{pmatrix} 0 & 0 & 0 & 0 & e_{15} & -e_{22} \\ -e_{22} & e_{22} & 0 & e_{15} & 0 & 0 \\ e_{31} & e_{31} & e_{33} & 0 & 0 & 0 \end{pmatrix}$   |                        |
| Trigonal       | $32$         | $\begin{pmatrix} e_{11} & -e_{11} & 0 & e_{14} & 0 & 0 \\ 0 & 0 & 0 & 0 & -e_{14} & -e_{11} \\ 0 & 0 & 0 & 0 & 0 & 0 \end{pmatrix}$   |                        |
| Trigonal       | $3$          | $\begin{pmatrix} e_{11} & -e_{11} & 0 & e_{14} & e_{15} & -e_{22} \\ -e_{22} & e_{22} & 0 & e_{15} & -e_{14} & -e_{11} \\ e_{31} & e_{31} & e_{33} & 0 & 0 & 0 \end{pmatrix}$                     |                        |
| Orthorhombic   | $mm2$        | $\begin{pmatrix} 0 & 0 & 0 & 0 & e_{15} & 0 \\ 0 & 0 & 0 & e_{24} & 0 & 0 \\ e_{31} & e_{32} & e_{33} & 0 & 0 & 0 \end{pmatrix}$  |                        |
| Orthorhombic   | $222$        | $\begin{pmatrix} 0 & 0 & 0 & e_{14} & 0 & 0 \\ 0 & 0 & 0 & 0 & e_{25} & 0 \\ 0 & 0 & 0 & 0 & 0 & e_{36} \end{pmatrix}$  |                        |
| Monoclinic     | $m$          | $\begin{pmatrix} e_{11} & e_{12} & e_{13} & 0 & e_{15} & 0 \\ 0 & 0 & 0 & e_{24} & 0 & e_{26} \\ e_{31} & e_{32} & e_{33} & 0 & e_{35} & 0 \end{pmatrix}$   |                        |
| Monoclinic     | $2$          | $\begin{pmatrix} 0 & 0 & 0 & e_{14} & 0 & e_{16} \\ e_{21} & e_{22} & e_{23} & 0 & e_{25} & 0 \\ 0 & 0 & 0 & e_{34} & 0 & e_{36} \end{pmatrix}$   |                        |
| Triclinic      | $1$          | $\begin{pmatrix} e_{11} & e_{12} & e_{13} & e_{14} & e_{15} & e_{16} \\ e_{21} & e_{22} & e_{23} & e_{24} & e_{25} & e_{26} \\ e_{31} & e_{32} & e_{33} & e_{34} & e_{35} & e_{36} \end{pmatrix}$ |                        |

Figure 8.3: Piezoelectric tensors and symmetry classes considered in this work, part II. Typical representations of the longitudinal piezoelectric modulus in 3D are also shown for each crystal point group.

### 8.3.2 Compound selection and generation of piezoelectricity data

In this work, we present the piezoelectric tensor for a total of 941 compounds. The compounds were selected from the MP database, with certain constraints applied. These constraints are chosen to specifically target compounds that have the possibility of exhibiting piezoelectric behavior, as follows: 1) only structures with space groups 1, 3-9, 16-46, 75-82, 89-122, 143-146, 149-161, 168-174, 177-190, 195-199, 207-220 are allowed (since these space groups lack inversion symmetry), 2) the calculated DFT bandgap  $> 0.1$  eV, 3) the energy above the convex hull (decomposition energy [317])  $< 0.10$  eV / atom, and 4) the number of atoms in the unit cell  $\leq 20$ . These constraints are chosen to identify a set of materials that has the possibility of exhibiting piezoelectric behavior, while being energetically stable or near-stable and having relatively small unit cells. In particular, materials can only exhibit piezoelectric behavior if they lack inversion symmetry and have an electronic bandgap (constraints 1 and 2, respectively). The space group was determined based on the relaxed structures from the MP database.

For these select compounds, the relaxed structures are extracted from the MP-database and used as input for the DFPT-calculation of the piezoelectric constants. However, DFT convergence parameters chosen for structure relaxations, such as the kpoint-density and the plane wave energy cutoff that are optimized for the total energy, are not in general sufficient for the purpose of calculating properties from DFPT, such as phonons and piezoelectric constants. Hence, the DFPT-calculations are performed using more stringent convergence parameters, as required by the Berry-phase approach [72, 394].

### 8.3.3 Workflow

Figure 8.4 illustrates the scheme used for the HT-calculation of the piezoelectric constants from DFT. For each selected structure from the MP database, a DFPT-calculation is first carried out, which directly results in the piezoelectric tensor. To ensure reliable calculated constants, we have devised several consistency checks and filters as part of our workflow. The aim is to detect possible errors in the DFT-calculations and other problems such as unconverged results. These filters largely rely on symmetry considerations. Certain classes of point groups impose constraints on the piezoelectric tensor, such as components being identically equal to zero, or components being equal to each other. For example, within the cubic crystal system, either all piezoelectric constants are equal to zero (for non-piezoelectric cubic compounds) or there is only one independent nonzero piezoelectric constant. An overview of the symmetry constraints for the point groups considered in this work is given in Figs. 8.2 and 8.3.

Our filters take the symmetry considerations above into account and are chosen as



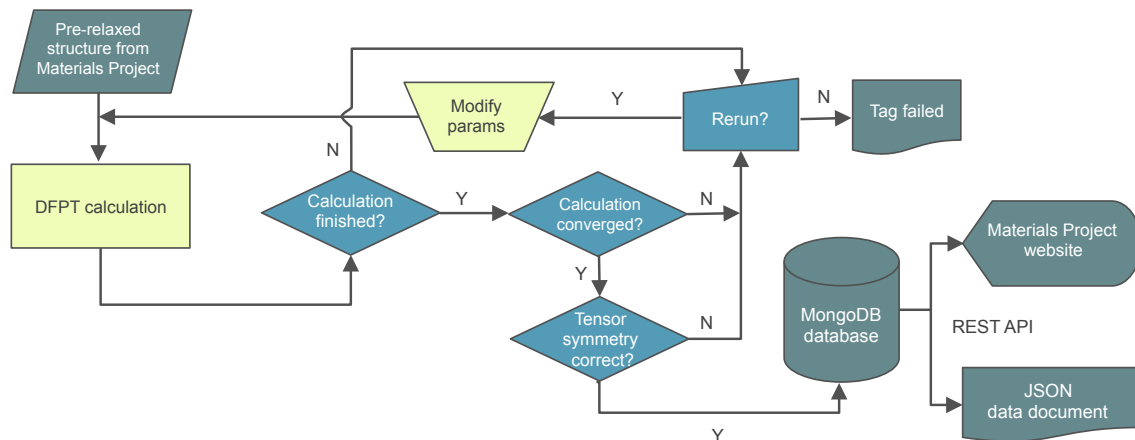


Figure 8.4: Flowchart showing a schematic of the HT-infrastructure for calculating piezoelectric constants, including error-checking steps and database insertions.

follows: (i)  $|e_{ij}| < 0.01 \text{ C/m}^2$  for components that should be identically zero by symmetry (ii) if the point group symmetry imposes that  $e_{ij}$  and  $e_{kj}$  are identical, these should be within 5% in the DFT-calculation and (iii)  $\|e_{ij}\|_{\max} < 5 \text{ C/m}^2$ . Conditions (i) and (ii) are simply employed to check if the symmetry of the crystal structure is approximately represented in the calculated piezoelectric tensor. The notation  $\|e_{ij}\|_{\max}$  in filter (iii) denotes the maximum attainable absolute value of the longitudinal piezoelectric modulus, experienced by the crystal in any direction. For example, as the orientation of the  $E$ -field with respect to the crystal is varied, the response of the crystal in the direction of the  $E$ -field can be measured and this can be repeated for all possible directions.  $\|e_{ij}\|_{\max}$  corresponds to the maximum longitudinal piezoelectric response that is measured among all directions.

Figures 8.2 and 8.3 provide surfaces with the longitudinal magnitude of the piezoelectric modulus for various crystal symmetries. As an example, for cubic crystals the maximum longitudinal piezoelectric modulus  $\|e_{ij}\|_{\max}$  occurs in the  $\langle 111 \rangle$  family of directions, as indicated in Figures 8.2 and 8.3 and also shown in Fig. 8.5 for the specific case of cubic LaOF. These directions where  $\|e_{ij}\|_{\max}$  occurs are indicated in this work by  $v_{\max}$ . The reason for including filter (iii) involving  $\|e_{ij}\|_{\max}$  is that the most potent class of currently known piezoelectric materials, lead zirconate titanate (PZT's), exhibit maximum absolute piezoelectric tensor components in the range of approximately  $6\text{-}12 \text{ C/m}^2$  [371, 395, 396, 397], the precise values depending on the details such as grain size, temperature etc. Calculations that yield values in that range are not necessarily wrong, but deserve additional attention due to the relatively large magnitudes.

For materials that do not pass filters (i)-(iii) an additional DFPT-calculation is

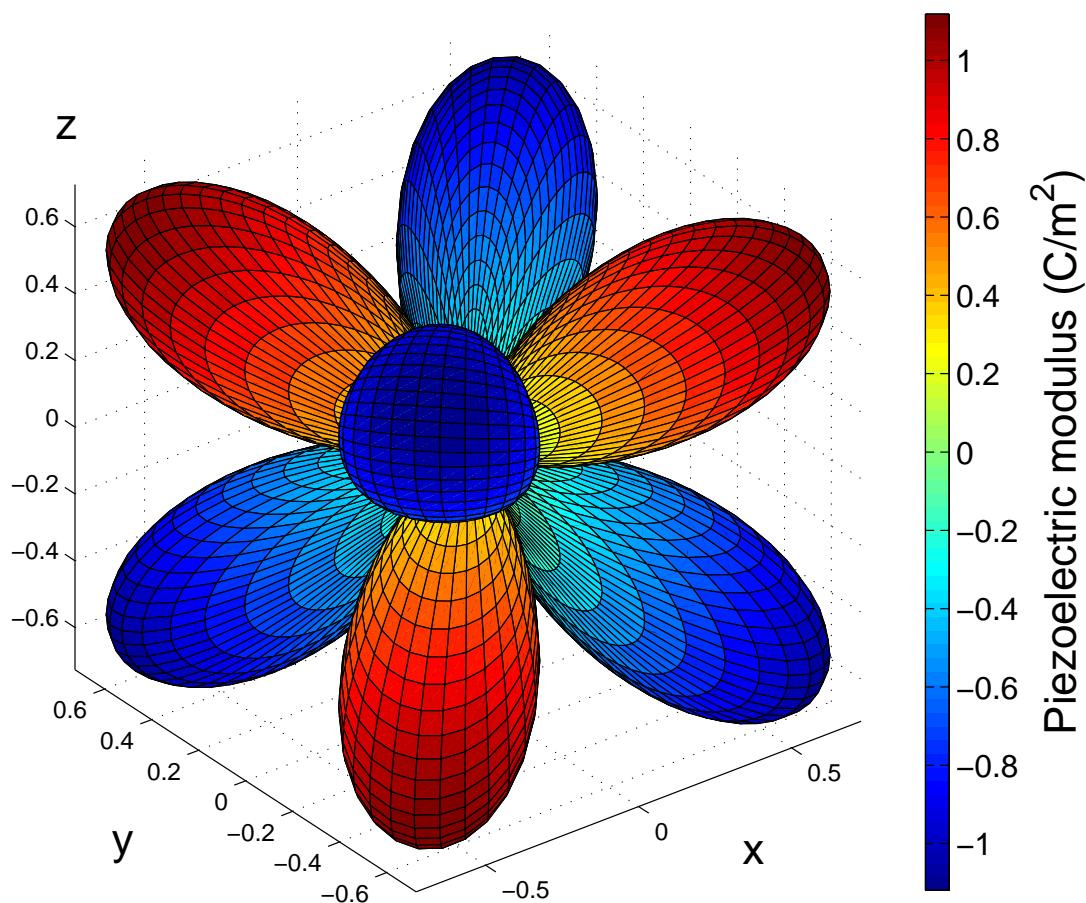


Figure 8.5: Visualization of the piezoelectric tensor: directional dependence of the longitudinal piezoelectric constant in cubic LaOF. Note that the maximum and minimum piezoelectric constants,  $\|e_{ij}\|_{\max}$ , occur for the  $\langle 111 \rangle$  family of crystallographic directions.

performed with more stringent convergence parameters. This is similar to our approach taken for validating the DFT-calculations of elastic constants [284]. If the filters are still not passed after this calculation, a warning tag is attached to that specific compound. In some cases, when the initial DFPT-calculation fails, it is also rerun with more stringent parameters in an attempt to converge the calculation. If it fails a second time, a tag indicating a failed calculation is attached. From the initial set of 941 materials, it is found that 134 materials are flagged by one or more of the filters (i)-(iii). In particular, for 123 compounds we find that filters (i) and/or (ii) are violated, indicating problems with the

symmetry of the piezoelectric tensor. In addition, of the 941 compounds considered, 11 systems exhibit a piezoelectric modulus  $\|e_{ij}\|_{\max} > 5 \text{ C/m}^2$  and therefore are flagged by filter (iii). For these systems, we repeat the DFPT-calculation of the piezoelectric tensor with an increased k-point density. It is found that this reduces the number of systems that do not pass the filters from 123 down to 81. For the remaining compounds, a warning message is generated on the MP website.

Each piezoelectric tensor that passes the filters is symmetrized according to the point group-symmetry and subsequently inserted into the MP database, see Fig. 8.4. It is also reported on the MP website. Furthermore, all currently available data can be downloaded from the Dryad-repository (Data Citation 1). There, it is available as a JSON (JavaScript Object Notation) data document. The data analysis is performed using our open-source materials analysis code pymatgen [326]. The HT calculations are automated using the FireWorks workflow software [327, 398].

### 8.3.4 Code availability

The proprietary VASP-code is used in this work for the calculation of piezoelectric constants. The filters and symmetrization and analysis code for the piezoelectric constants are implemented in pymatgen [326]. Pymatgen is released under the MIT (Massachusetts Institute of Technology) License and is freely accessible. Further, the open-source code MTEX [399, 400, 401, 402] is used to generate the 3D-representation of the piezoelectric tensors. This code operates on most versions of the widely used MATLAB-software package. The workflow depicted in Fig. 8.4 is implemented in FireWorks, which is released free of charge under a modified GPL (GNU General Public License).

## 8.4 Data records

The calculated piezoelectricity data and the associated metadata of all 941 materials are freely available at the website of the Materials Project, and the Materials API [403] can be used to download the data. The complete set of data is also available as a JSON file and can be found in the Dryad-repository. It is possible to query materials with certain piezoelectric properties on the MP website via a dedicated web interface. The MP website also includes dedicated details pages for each compound, giving an overview of its calculated properties to date as well as the calculation parameters.

### 8.4.1 File format

Metadata is associated with each material and contains information regarding some of the properties of the material, such as crystal structure (space groups, point

Table 8.1: JSON keys for metadata and their descriptions.

| Key            | Datatype | Description  |
|----------------|----------|--|
| material_id    | string   | IDs for entries in the Materials Project   |
| formula        | string   | Chemical formula   |
| structure      | string   | Relaxed crystal structure represented in Crystallographic Information File (cif) |
| poscar         | string   | relaxed crystal structure represented in poscar-format for VASP calculations     |
| space_group    | number   | Space group number defined by The International Union of Crystallography         |
| point_group    | string   | Point group in Hermann-Mauguin notation  |
| volume         | number   | Volume of the relaxed structure in $\text{\AA}^3$                                |
| nsites         | number   | Number of atomic sites for the conventional cell                                 |
| kpoint_density | number   | density of k-points in the first Brillouin zone per reciprocal atom              |

groups), a unique MP-ID for structure identification and several DFT calculation parameters such as k-point density. The data for each of the calculated materials is stored as a JSON document. The JSON format is comprised of hierarchical key-value pairs. Table 8.1 lists for each of these properties the JSON key, datatype and a short description. To retain consistency with the database of elastic constants, we present the structure of each piezoelectric compound in two ways: (i) Crystallographic Information File (cif) and (ii) poscar-format. The poscar-format is the structure-description as used in the VASP-code and this can be converted into other formats using pymatgen.

### 8.4.2 Properties

The piezoelectric tensor reported in this work corresponds to a single crystal. For the elastic constants, polycrystalline isotropic averages of the bulk and shear constants can be derived from the single crystal 4th-order elastic tensor [199, 295, 115]. For the 3rd-order piezoelectric tensor, however, an isotropic averaging scheme is not convenient, as it will yield isotropic averages equal to zero [365]. Hence in this work, we report the piezoelectric tensor in matrix form, together with several properties that are expected to be of use to the community, see Table 8.2. The piezoelectric tensor  $e_{ij}$  as presented in this work (see Table 8.2) is expressed in the standardized IEEE-format [319], corresponding to the notation as shown in Figures 8.2 and 8.3. Note that the symmetrized piezoelectric tensors are presented in this work, obeying the point group symmetry of each of the compounds. We further report  $\|e_{ij}\|_{\max}$ , which was defined earlier as the maximum longitudinal piezo-

electric modulus of the compound in any crystallographic direction (see Fig. 8.5). The associated crystallographic direction is also reported, which corresponds to the direction of the  $E$ -field that leads to the maximum normal stress in that same direction. Finally, the symmetry information of each compound is included (space and point groups) since these are closely related to piezoelectric properties.

Table 8.2: Properties related to the piezoelectric tensor in this work, and their corresponding JSON keys and datatypes.

| Property                                   | Key                  | Datatype | Unit             | Description  |
|--|----------------------|----------|------------------|--|
| Piezoelectric tensor, $e_{ij}$             | piezoelectric_tensor | array    | C/m <sup>2</sup> | Tensor, describing piezoelectric behavior (IEEE-format)                    |
| Piezoelectric modulus, $\ e_{ij}\ _{\max}$ | eij_max              | number   | C/m <sup>2</sup> | Maximum longitudinal piezoelectric modulus                                 |
| Crystallographic direction, $v_{\max}$     | v_max                | array    | -                | Crystallographic direction, corresponding to maximum piezoelectric modulus |

### 8.4.3 Graphical representation of results

Our dataset is presented graphically in Fig. 8.6, where the maximum piezoelectric modulus  $\|e_{ij}\|_{\max}$  for 941 compounds is plotted in a pie-chart, which also shows the point group symmetry-classes considered in this work (see also Figures 8.2 and 8.3). The results in Fig. 8.6 are broken up by the 7 crystal systems, which are further subdivided into the point groups that can exhibit piezoelectric behavior.

From Fig. 8.6 it follows that a large fraction of the compounds are located near the center of the chart, which indicates relatively weak piezoelectric behavior ( $\lesssim 1 \text{ C/m}^2$ ) of  $\|e_{ij}\|_{\max}$ . On the other hand, we find that 17 % of the compounds in the dataset satisfy  $\|e_{ij}\|_{\max} \geq 1 \text{ C/m}^2$  and 5 % satisfies  $\|e_{ij}\|_{\max} \geq 3$ , indicating relatively large piezoelectric behavior. Our HT-calculations confirm high (intrinsic) piezoelectric constants for compounds such as  $\text{PbTiO}_3$ ,  $\text{BaNiO}_3$ ,  $\text{RbTaO}_3$  and  $\text{SrHfO}_3$ , some of which are indicated in Fig. 8.6. We further identify a set of potent piezoelectric compounds that (to the best of our knowledge) have not yet been confirmed experimentally or computationally in the literature. Examples are  $\text{VFeSb}$ ,  $\text{Li}_4\text{WO}_5$ ,  $\text{LiMnO}_2$ ,  $\text{NaBiS}_2$  and a few dozen others that are present in Fig. 8.6, but not explicitly indicated. The identification of these compounds, exhibiting interesting piezoelectric behavior, can hopefully contribute to the search for novel new piezoelectric materials. Of particular interest is also how different synthesis techniques can affect the intrinsic piezoelectric response, as shown in Fig. 8.6, by changing for example the grain size, the impurity concentration, and by introducing defects. In fact, the most widely-used piezoelectric compounds today are based on lead zirconate titanate (PZT's). Their high piezoelectric response stems from a careful tuning of the chemical composition to a region that is near a morphotropic phase boundary [404, 405, 406, 407]. In this work, the effect on the piezoelectric properties of alloying to create solid solutions is not considered, however, the intrinsic piezoelectric moduli such as shown in Fig. 8.6 may provide a convenient starting point in the process of searching for new piezoelectrics.

## 8.5 Technical validation and verification

### 8.5.1 Verification of computational methodology

Verification of the current HT implementation for calculating piezoelectric constants by the DFPT Berry phase-approach is undertaken through comparison of the present results to those obtained in the literature. Comparisons are made with work in the literature using similar DFT-methods but alternative implementations of DFPT or a finite strain-based method rather than DFPT. As an example, for the wurtzite-compound  $\text{AlN}$ , we calculate  $e_{33} = 1.46 \text{ C/m}^2$  and  $e_{31} = -0.58 \text{ C/m}^2$  which is within 10 % of the values reported elsewhere, obtained using GGA as well, but with a different implementation of DFPT and slightly different convergence parameters [408]. Similar or better levels of

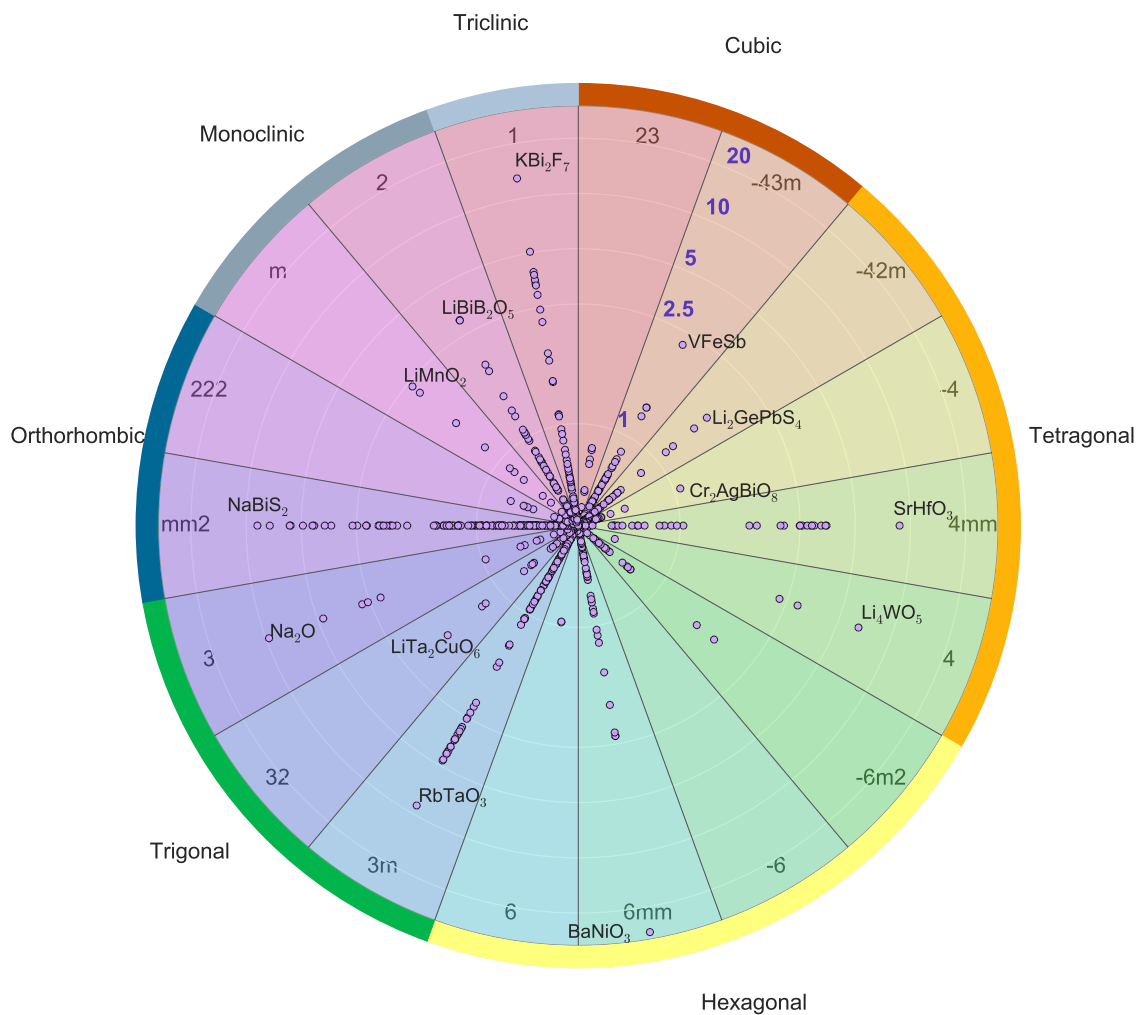


Figure 8.6: A graphical representation of the piezoelectric dataset, currently comprising of 941 materials. A series of concentric circles indicate constant values of the maximum longitudinal piezoelectric modulus,  $\|e_{ij}\|_{\max}$ . Concentric circles corresponding to moduli  $\|e_{ij}\|_{\max}$  of 1, 2.5, 5, 10 and 20  $C/m^2$  are indicated explicitly in the figure. The compounds are broken up according to the crystal system and the different point group symmetry-classes considered in this work.



agreement are obtained for the compounds GaN and InN [408] and several (wurtzite) oxides with piezoelectric behavior such as BeO and ZnO [366]. For the ternary oxide PbTiO<sub>3</sub>, we compare our calculated piezoelectric constants to those calculated from DFPT and a finite strain method [371]. For all 3 components of the piezoelectric tensor, we find agreement to within 15% for both the DFPT and finite strain-calculations. We further compare our calculated piezoelectric constants to those reported in the literature [409] for BiAlO<sub>3</sub>. We find that for the constants  $e_{31}$ ,  $e_{33}$  and  $e_{15}$ , the agreement is within 15-20 %. For the smallest modulus of the tensor,  $e_{21}$ , the agreement is worse, as it differs by approximately a factor 2.5, however the absolute difference is similar to that found for the other components. Even though the method employed in [409] is also based on DFPT and uses GGA-PBE, it employs a Troullier-Martins norm-conserving pseudopotential methodology [51] to describe electron-ion interaction, which differs from the PAW method used in the current approach. We expect that the discrepancy in  $e_{21}$  may be caused by this difference.

Based on the comparisons performed as part of this work, we find that the level of agreement between the piezoelectric constants calculated from our HT-methodology and those obtained in the literature using alternative methods, generally show agreement to within approximately 15-20 %. This level of agreement is consistent with that found in the literature, comparing piezoelectric constants calculated from DFT, e.g. [366, 410].

### 8.5.2 Validation through comparison to experimental measurements

In order to gauge the expected accuracy of the calculated results, an extensive comparison with reported experimental piezoelectric constants was performed. To achieve consistency with the calculations, we consider comparisons only with measurements that report the complete piezoelectric tensor, rather than just a subset of components. This leads to a comparison for 36 systems, and over 75 independent piezoelectric tensor components. The systems for which data from the literature is taken range from well-known semiconductors such as GaAs and InAs to binary compounds such as ZnO, ZnTe and oxides of the form XYO<sub>3</sub> or XYO<sub>2</sub> such as SnTiO<sub>3</sub>, LiNbO<sub>3</sub> and LiGaO<sub>2</sub>.

The comparison of calculated and experimental values for the piezoelectric constants are shown in Fig. 8.7. The points represent the quantity  $\|e_{ij}\|_{\max}$ , which represent the maximum attainable piezoelectric response (over all crystallographic directions) and is derived directly from the calculated and experimentally determined piezoelectric tensors. In the plot, lines are shown indicating relative differences between computation and experiment of  $\pm 25\%$ . A threshold of 25 % is chosen since this represents a typical discrepancy between experiment and calculation for the case of piezoelectric constants. Note that this is true in particular for compounds with relatively large piezoelectric constants. The inset of Fig. 8.7 shows that for values below roughly 0.4 C/m<sup>2</sup>, percentage errors are

much larger. The same trend was observed in our recent work on elastic constants [284], although for piezoelectric constants, the discrepancies between our DFT-calculations and experiments tend to be larger. Discrepancies between experiment and calculation of over 25 % are identified for 16 systems, which are (in order from high to low discrepancies): ZnS, GaP, InP, BeO, BP, CdTe, InAs, SiBiO, InSb, GaSb, AlSb, GaAs, CdS, BN, AlN and CuCl.

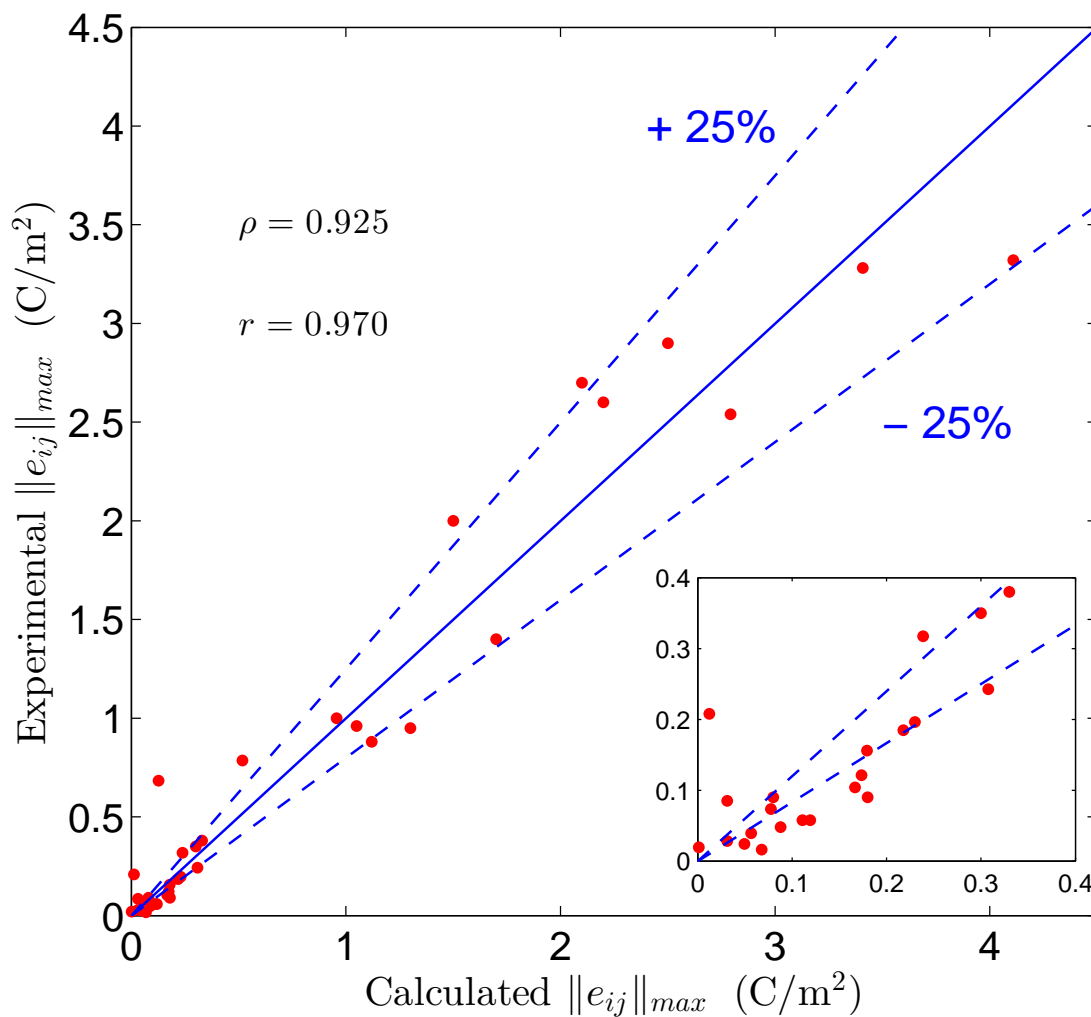


Figure 8.7: Comparison of experimental and calculated piezoelectric constants ( $\|e_{ij}\|_{max}$ ) for a selected set of systems, with calculated Pearson correlation coefficient  $r$  and Spearman correlation coefficient  $\rho$  reported.

There are several other factors that can contribute to discrepancies between calculations and the experiments. First of all, our DFT-calculations provide a description of the materials that is strictly only valid at a temperature of 0K. However, most experiments are done at room temperature or elevated temperatures. Temperature can have a significant effect on the measured piezoelectric response of materials. For example, for lead zirconate, the absolute values of the piezoelectric constants were reported to increase by as much as 46 % as temperature increases from -55 C° to 85C° [411]. Similar temperature dependence was found in other work for lead titanate [412]. In addition to temperature effects, it should be noted that our calculations probe only the intrinsic contribution to the piezoelectric behavior of materials, assuming a perfectly ordered bulk crystal. Hence, extrinsic effects associated with defects and grain size are not considered; grain size is known to influence piezoelectric properties in some compounds such as BaTiO<sub>3</sub> [413].

We further note that piezoelectric coefficients can be strongly affected by variations in lattice constants. This has been established in the literature based on detailed investigations for a number of systems [414, 415, 416]. For example, in some piezoelectric compounds such as PbTiO<sub>3</sub> and BaTiO<sub>3</sub>, hydrostatic pressures of less than 1 GPa can lead to variations in the piezoelectric tensor components of up to 50 % [417, 418]. We observed a similar effect where the choice of either the LDA or GGA approximation to the exchange-correlation energy led to differences in the predicted lattice constants by 1-2 %, with an associated change in the piezoelectric constants of as much as 40 %. In this work, GGA-PBE is used for the piezoelectric calculations to obtain consistency with other data tabulated in the Materials Project. We further found that for compounds containing specific elements, different piezoelectric constants were obtained, depending on how many electrons were used as valence states. This is especially true for the early transition metals such as Sc, Ti, V and Nb, for which piezoelectric components can differ by up to several percent, depending on the details of the PAW-potential. Consistent with the framework of MP, for elements such as these, semi-core states are included in the calculations.

In order to obtain a statistical measure of how well the measured and calculated piezoelectric constants,  $\|e_{ij}\|_{\max}$ , agree, we compute the Pearson ( $r$ ) and Spearman ( $\rho$ ) correlation coefficients. These quantities provide insight into how strongly the measured and calculated piezoelectric constants are linearly associated and monotonely associated, respectively. We find that  $\rho = 0.925$  and  $r = 0.970$ . This implies that the measured and calculated values for the maximum longitudinal piezoelectric constants exhibit a strong linear association and also, a high monotone association exists. This makes the database particularly useful for screening and datamining of structure-chemistry correlations in piezoelectrics.

## 8.6 Usage Notes

In this work, we present a database of calculated intrinsic piezoelectric constants for 941 inorganic crystalline compounds, for use in the design and development of piezoelectric materials and devices. Specifically, we expect this database to enable searches for new, previously unknown, piezoelectric materials or as an aid in screening for replacement candidates for currently known interesting piezoelectric materials such as  $\text{PbTiO}_3$ . Our database allows researchers to search through a large pool of compounds and select those with certain target piezoelectric responses, for example a tensile strain larger than some threshold value upon the application of a given electric field. In addition, researchers can query the database and screen for materials obeying 'composite constraints', for example a combination of desired piezoelectric response, elastic properties and mass density. These features are expected to be of interest to researchers working in a variety of fields, such as piezoelectricity, elasticity and thermodynamic properties. Similar to the previous work on elastic constants, as part of the future work on piezoelectric constants, a web interface will be implemented in which MP-users can request calculated piezoelectric constants for compounds that have not been considered yet up to now. Other possible future work includes the use of statistical methods such as machine learning on the current database to better understand the structure-chemistry descriptors that give rise to interesting behavior (e.g. high piezoelectric constants). Eventually, techniques such as those may assist the accelerated search for new materials with unprecedented piezoelectric properties.

Part IV

**Concluding Remarks**

## Chapter 9

# Summary, Conclusions and Future Work

This chapter starts by summarizing the results that are presented in the dissertation, along with the conclusions. Subsequently, suggestions for future work are made, related to rhenium replacement, data mining and machine learning, and the discovery of new piezoelectric materials and high-ductility alloys.

### 9.1 Summary and Conclusions

Part I of this dissertation describes the introduction and background of the work presented here, along with some of the fundamentals of DFT, which is the workhorse of most of the research described in this dissertation. The SQS method and various other ways of modeling disorder in solids are also described in Part I. Part II of this dissertation concerns a study of intrinsic ductility in elemental Re, Re-alloys and HCP transition metals in general. Particular attention is paid to elastic properties, twinning energetics, ideal strength, their relation to intrinsic ductility and their dependence on  $d$ -band filling. Finally, part III of the dissertation explores high-throughput calculations. The largest databases to-date of piezoelectric and elastic tensor properties are introduced, along with the computational methods used for data generation, validation and verification.

The work presented in this dissertation establishes a the dependence of the structural, elastic and energetic properties of Re-based alloys on the  $d$ -band filling. The structural and elastic properties calculated by DFT are shown to be in excellent agreement with experiments for pure Re. It is found that decreasing the  $d$ -band filling of Re by alloying leads to an increase in the  $c/a$  ratio, whereas increasing the  $d$ -band filling tends to decrease the  $c/a$  ratio. The bulk ( $K$ ) and shear ( $G$ ) moduli of Re-based alloys show roughly parabolic behavior with  $d$ -band filling, attaining maximum values slightly to the

right of Re. The simple intrinsic ductility parameter proposed by Pugh [116] involves the ratio of  $K$  and  $G$ ,  $D = K/G$ . It is shown in this dissertation that when Re is alloyed with transition-metal elements to its left, the intrinsic ductility  $D$  increases, whereas elements to the right decrease  $D$ , leading to intrinsically more brittle alloys. Further, it is shown that for pure Re, the shear modulus is particularly isotropic and alloying with elements either to the left or right in the periodic table leads to a more anisotropic shear modulus. Results on the energetics of Re-based alloys are presented as well in this dissertation. It is shown that Re-based alloys with transition-metal solutes to the right of Re in the periodic table tend to have negative heats of solution (with the exception of the noble metals). On the other hand, solutes to the left of Re yield alloys with positive heats of solution. The trends in structural, elastic and energetic properties of Re-rich alloys with  $d$ -band filling can be rationalized based on well-established tight-binding models. The dependence on  $d$ -band filling of the bulk and shear moduli of Re-alloys and the pure transition metals is very similar. Further, the trends in the structural parameters can be rationalized by invoking canonical  $d$ -band theory and considering the change of the hopping integrals in and out of the basal plane with  $d$ -band filling. Similarly, the energetics of Re-based alloys can be rationalized by canonical  $d$ -band theory.

It is further shown in this dissertation that Re and Tc exhibit a very low  $\{11\bar{2}1\}$  TB energy, compared to what may be expected based on their shear moduli and the shear moduli of other HCP transition metals. DFT calculations indicate that among all HCP transition metals, only Re and Tc energetically favor the  $\{11\bar{2}1\}$  TB, whereas all others favor the  $\{10\bar{1}1\}$  orientation. The  $\{11\bar{2}1\}$  TB takes anomalously low values only for Re and Tc and this is referred to as the “twin-energy anomaly”. Calculations based on SQS, VCA and CPA all show that decreasing the  $d$ -band filling further lowers the  $\{11\bar{2}1\}$  TB energy, whereas increasing the  $d$ -band filling increases the  $\{11\bar{2}1\}$  TB energy. This is in stark contrast to for example the  $\{10\bar{1}1\}$  TB energy which shows the opposite behavior with  $d$ -band filling and is overall much more inert to alloying. DFT calculations also show that the basal-surface energy of Re-based alloys varies very little with alloying. Based on the TB energies  $\gamma_t$  and the surface energies  $\gamma_s$ , a second intrinsic ductility parameter formulated by Yoo [17] can be evaluated, namely  $D = \gamma_s/\gamma_t$ . This intrinsic ductility parameter indicates that alloying Re with transition-metal solutes to its left in the periodic table increases ductility, whereas solutes to the right lead to more brittle alloys. This behavior is mainly governed by the  $\{11\bar{2}1\}$  TB and the large change of its energy with variations in  $d$ -band filling. Interestingly, the ductility parameters by Pugh and Yoo yield qualitatively similar results, despite their different physical underpinnings. Experimental studies on deformed Re indirectly confirm the computational findings presented in this work. First, EBSD studies show that elemental Re deforms almost exclusively by twinning of the type  $\{11\bar{2}1\}$  and a high density of these deformation twins is observed, leading to a high ductility. Second, deformed Re-W alloys show an even higher density of  $\{11\bar{2}1\}$  twins. Both these experimental observations are consistent with the DFT calculations. It is further shown that the

origins of the twin-energy anomaly occurring for the  $\{11\bar{2}1\}$  TB are rooted in the detailed atomic structure of the TB plane. The  $\{11\bar{2}1\}$  TB is unique in the sense that it exhibits icosahedral nearest-neighbor structural units on its twin plane, which are absent in the other twins studied in this dissertation. These same icosahedral units are the fundamental building blocks of TCP compounds, which are stabilized at  $d$ -band fillings slightly below Re. These icosahedral units form the basis of rationalizing the twin-energy anomaly and the  $d$ -band filling behavior. For elemental Re, HCP is the stable phase, however various TCP's, partly made up from icosahedral units are metastable and close in energy at that  $d$ -band filling. This leads to the low energy of the structurally similar  $\{11\bar{2}1\}$  TB at the  $d$ -band filling of Re. In addition, TCP's are stabilized as the  $d$ -band filling is lowered w.r.t. Re, e.g. by alloying with W. This is consistent with the findings presented in this dissertation that the  $\{11\bar{2}1\}$  TB shows a pronounced stabilization as the  $d$ -band filling is lowered from Re. Finally, the discovery of the twin-energy anomaly and the new insights in the role of  $d$ -band filling are employed to suggest replacement candidates for Re. Several Ru-based alloys are proposed that contain no Re or small concentrations of Re, but yield  $\{11\bar{2}1\}$  TB energies close to Re, with presumably comparable intrinsic ductility.

Part of the work in this dissertation involves the calculation of planar defect energies in substitutionally disordered alloys. The fundamental challenge of such calculations is that the disordered nature of the alloy has to be represented in a relatively small supercell that is amenable to first-principles DFT calculations, employing periodic boundary conditions. In order for a small supercell to be a proper representation for a large disordered system, atoms have to be distributed on the atomic sites in such a way to minimize spurious correlations. The SQS approach addresses this problem and distributes atoms on sites in such a way to approximate the random atomic correlation functions as closely as possible. Bulk properties have been studied extensively with the SQS approach, however this is not true for planar defects. In this dissertation, a new method based on SQS is presented that is used to calculate planar-defect energies in substitutionally disordered alloys. It is based on averaging the planar defect energy over all possible locations within a given supercell. Classical potentials based on the EAM method are used to validate the proposed method for the Ti-Al system. It is shown that by performing an average over less than 10 planes of a medium-sized SQS (between approximately 50 and 80 atoms), the random planar defect energies can be approximated to within several %. Hence, the proposed SQS method to calculate planar-defect energies using an averaging procedure is computationally feasible in DFT, while resulting in accuracy to within a few %. This method is used extensively in the work presented in this dissertation to calculate twin and surface energies in Re-based alloys. For example, the results related to the energetics of  $\{11\bar{2}1\}$  twin energies in Re-Ta, Re-W, Re-Os and Re-Ir alloys are calculated using this method.

Ideal-strength calculations are employed in this dissertation to shed more light on the intrinsic ductility and ideal failure mechanisms of HCP transition metals and Re in



particular. Intrinsic ductility is characterized by the occurrence of an elastic shear instability before a tensile instability as the material is loaded up to failure. This is analogous to a situation in which dislocation glide occurs before crack nucleation, resulting in ductile behavior in a real material. In this dissertation, ideal-strength calculations are performed on all HCP transition metals and these are categorized as either intrinsically brittle or ductile. In particular, Re is the HCP transition metal with the highest shear modulus that fails in shear rather than tension when pulled along the  $c$ -axis. The ideal deformation behavior of alloys is studied by using the virtual crystal approximation. Approximate ranges of  $d$ -band filling are mapped out in which intrinsically ductile behavior occurs, which yields rough guidelines for the design of ductile transition-metal alloys. It is further shown that Re, although being intrinsically ductile, is close to the region in which intrinsically brittle behavior occurs, at slightly higher  $d$ -band fillings in the direction of Os.

The ideal deformation behavior and intrinsic ductility of HCP transition metals and alloys is put on a physical foundation in this dissertation by employing a simple interpretation in terms of second and third-order elastic constants. The elastic instability of a solid under stress is a function of its elastic constants in the deformed configuration as well as the applied stress. The eigenvalues of the Wallace tensor govern elastic stabilities and the corresponding eigenvectors indicate the type of (in)stability, e.g. a shear or a tensile instability. An HCP material loaded uniaxially in tension along the  $c$ -axis will normally contract in the basal plane as a consequence, but retains its crystal symmetry (only the axial ratio changes). Therefore, the Wallace tensor exhibits a high degree of symmetry and its eigenvalues can be calculated analytically. By expressing the eigenvalues in terms of the applied strain, the second and third-order elastic constants, stability criteria are formulated as a function of the applied strain along the  $c$ -axis. In addition, new insights into intrinsically ductile vs. brittle behavior are obtained. HCP metals with high shear moduli  $C_{44}$  tend to have high ideal strengths and fail in a brittle mode. On the other hand, ductile metals tend to have low shear moduli, while also exhibiting lower ideal strengths. These observations can be directly rationalized by invoking the eigenvalues of the Wallace tensor. Some HCP metals and alloys such as Re exhibit high shear moduli  $C_{44}$  but nevertheless fail in shear. The Wallace eigenvalues show this is due to a delicate trade-off between second and third-order elastic constants, in particular a high  $C_{33}$  and a largely negative  $C_{344}$ .

The remaining part of this dissertation concerns high-throughput calculations, which is a relatively new, upcoming field in materials science and engineering. This branch of research is motivated by the observation that for only a fraction (typically less than 1 %) of all 50,000-70,000 known inorganic crystalline compounds in nature, basic properties such as elasticity, band gaps, thermal conductivity, electrical conductivity, heat of formation, piezoelectricity etc. are known. This lack of data impedes the optimization of existing materials and the discovery of new materials with certain target properties. Two chapters in this dissertation are dedicated to combating this bottleneck in materials science by em-

ploying high-throughput calculations based on DFT. Chapter 7 describes high-throughput calculations of elastic properties, and Chapter 8 deals with piezoelectric properties.

It is estimated that the experimental full elastic tensor is known for only approximately 150 inorganic crystalline compounds, which is only 0.25 % of all known compounds in nature. In this work, a database of calculated elastic tensor properties is presented that (at the time of writing) consists of over 2,200 compounds. The database consists of various different types of compounds: unaries, binaries, ternaries and quaternaries, metals and non-metals, crystal systems ranging from triclinic to cubic and conventional unit cell sizes ranging from 2 to approximately 50 atoms. All compounds considered for the calculations are within a few meV/atom of the convex hull. This ensures that only energetically feasible structures are considered. Each compound is run through an automated workflow that first performs a structural relaxation and subsequently imposes different distortions to the lattice vectors, followed by DFT calculations of the stress tensors. The elastic constants are then determined from a linear least-squares fit. The workflow also ensures that unconverged DFT calculations are filtered out and it subjects the elastic tensor to a number of tests to ensure the quality of the elastic-constant data. In particular, tests are carried out regarding mechanical stability and to check if the tensor symmetry obeys the symmetry of the underlying crystal. Further, comparisons of the calculated bulk and shear moduli to experiments are done for over 100 compounds and the results of the DFT calculations are compared to those obtained by slightly different techniques. Our calculations and experiments typically agree to within 15 % and also the comparisons with other techniques yield excellent agreement. All the elastic-constant data is made available online <https://materialsproject.org/> and can be conveniently queried and used for applications such as data mining. The full elastic tensor is reported in Voigt notation as a  $6 \times 6$  matrix, together with Voigt and Reuss limits on the bulk and shear moduli and various other properties that are derived from the elastic tensor.

The high-throughput calculations on piezoelectric materials are motivated in part by the very limited experimental data that is available, but primarily by recent efforts in the community to discover novel lead-free alternatives to currently used piezoelectrics such as PZT's. DFPT is used to calculate the piezoelectric tensor of a selected set of compounds. The compound selection for the high-throughput calculations is designed to specifically target materials that have the potential to exhibit piezoelectric behavior. Two fundamental requirements for piezoelectric behavior in materials exist: i) the compound has to lack inversion symmetry and ii) the compound has to exhibit a nonzero electronic band gap. These constraints lead to several thousands of compounds that have the possibility to exhibit piezoelectric behavior. Compounds are selected for the DFPT calculations based on these criteria, together with a maximum distance to the convex hull. Similar to the elastic-constant calculations, a workflow is used to automate the process of the calculations. The calculated piezoelectric tensor is subjected to similar symmetry tests

as for the elastic constants. Comparisons of the calculated piezoelectric moduli to experiments are performed for nearly 40 compounds and a reasonable agreement to within typically 25-30 % is found. All the piezoelectric-constant data is made available online <https://materialsproject.org/> for over 900 compounds. The full tensor is presented as a  $3 \times 6$  matrix in Voigt notation and the maximum longitudinal piezoelectric modulus is reported as a convenient way to screen for potentially interesting candidates for PZT replacement. In the work presented in this dissertation, several promising novel piezoelectric materials are unveiled that may serve as a starting point for further optimization by tuning their composition and microstructure.

## 9.2 Directions of Future Work

This section discusses some suggestions for future work based on the results and methodology presented in this dissertation.

### 9.2.1 High-Entropy alloys for Rhenium replacement

The relationship between various twin energies and  $d$ -band filling is emphasized in this dissertation and a link to intrinsic ductility is established. In terms of Re replacement, Ru based alloys with similar  $d$ -band filling as Re are proposed as viable alternatives, however it remains a challenge to synthesize such alloys as HCP solid solutions, without introducing second phases. Also, even though Ru alloys are more cost effective than Re, the price is still high and also for Ru the worldwide supply is limited. Therefore, an interesting future direction is to look at the possibility of high-entropy alloys [419, 420, 421] for Re replacement. These alloys can be designed to contain 5 or 6 elements at approximately equiatomic concentrations in such a way that the overall  $d$ -band filling coincides with that of the twin-energy anomaly, while stabilizing the HCP phase. Preferably, widely available metals such as Ta, W, Mo, Ti, Nb, Mn, Co, Ni and Cu would be used in these high-entropy alloys to accomplish significant cost savings. A potential problem in this approach is the lowering of the melting temperature of such high-entropy alloys compared to Re. More work is required to look for a proper balance between stability of the HCP phase, twin energy and cost.

### 9.2.2 Data Mining and Machine Learning

The databases of elastic and piezoelectric properties introduced as part of this dissertation lead to previously inaccessible opportunities for understanding, optimizing and discovering materials. By mining the data and applying machine-learning techniques, models can be developed that estimate e.g. elastic properties based on a small set of descriptors, which combined capture most of the underlying physics describing a given property. On one hand, this leads to a practical advantage of being able to estimate elastic constants

for materials in a split second, rather than having to perform a series of DFT calculations. On the other hand, the machine-learning models may provide new physical insights into elastic and piezoelectric properties and can be used for the optimization of materials for certain target properties.

In particular, the database of elastic constants may be used in conjunction with machine learning to screen for classes of novel ductile compounds by employing simple intrinsic ductility parameters. One avenue is to use Pugh's intrinsic ductility parameter, however this works primarily for comparing systems belonging to the same crystal system and it may prove difficult to interpret results across different crystal systems. Another interesting future approach is to use the elastic tensors and Stroh's sextic formalism to calculate anisotropic dislocation-energy prefactors, from which dislocation core radii may be estimated [422, 423, 424, 425]. Compounds with anomalously large dislocation cores and those exhibiting anomalously low shear moduli can be singled out efficiently using data mining and machine learning for a more detailed investigation. Such materials are of high interest, given their potential for high ductility. The database of elastic constants is expected to keep growing significantly in the future and other potential areas of application include thermoelectrics, materials with low thermal conductivity and high-hardness materials.

The database of piezoelectric properties is expected to provide support in the future to ongoing efforts to discover new lead-free piezoelectrics. In fact, in this dissertation several high-potential piezoelectrics are proposed that were previously unknown. Although these new piezoelectrics are unlikely to be competitive with PZT's in their current form, they may provide an excellent starting point for future research. From a computational side, the effect of alloying on the intrinsic piezoelectric response can be studied straightforwardly with DFPT calculations with the aim of finding optimum composition scenarios. Experimentally, the proposed piezoelectrics can be synthesized and extrinsic effects such as defects, solutes, grain size and temperature on the piezoelectric response can be studied. In this way, a concerted effort of high-throughput calculations on one hand and experimental efforts on the other hand may lead to the discovery and synthesis of new piezoelectric materials that are free of lead. Given the subtle nature of piezoelectricity, it may prove difficult to build accurate machine-learning models for this property, however there is a potential for success, particularly as the current database expands in the future.

# Bibliography

- [1] Josiah Willard Gibbs. The collected works of J. Willard Gibbs, volume 1. Yale University Press, 1957.
- [2] Josiah Willard Gibbs. On the equilibrium of heterogeneous substances. American Journal of Science, 1(96):441–458, 1878.
- [3] Max von Laue. Roentgenstrahl-interferenzen, volume 6. Akad. VerlagGes., 1960.
- [4] WH Bragg and WL Bragg. The reflection of x-rays by crystals. Proceedings of the Royal Society of London. Series A, Containing Papers of a Mathematical and Physical Character, pages 428–438, 1913.
- [5] William L Bragg and Ei J Williams. The effect of thermal agitation on atomic arrangement in alloys. Proceedings of the Royal Society of London. Series A, Containing Papers of a Mathematical and Physical Character, pages 699–730, 1934.
- [6] William Hume-Rothery. Xcv. the metallic state. The London, Edinburgh, and Dublin Philosophical Magazine and Journal of Science, 4(25):1017–1045, 1927.
- [7] Nicholas Metropolis and Stanislaw Ulam. The monte carlo method. Journal of the American statistical association, 44(247):335–341, 1949.
- [8] Ryoichi Kikuchi. A theory of cooperative phenomena. Physical review, 81(6):988, 1951.
- [9] P. Hohenberg and W. Kohn. Inhomogeneous electron gas. Phys. Rev., 136:B864–B871, Nov 1964.
- [10] Walter Kohn and Lu Jeu Sham. Self-consistent equations including exchange and correlation effects. Physical Review, 140(4A):A1133, 1965.
- [11] Gerard Paul M Leyson, William A Curtin, Louis G Hector Jr, and Christopher F Woodward. Quantitative prediction of solute strengthening in aluminium alloys. Nature materials, 9(9):750–755, 2010.

- [12] Zhaoxuan Wu and WA Curtin. The origins of high hardening and low ductility in magnesium. Nature, 526(7571):62–67, 2015.
- [13] Xiangyang Huang, Graeme J Ackland, and Karin M Rabe. Crystal structures and shape-memory behaviour of niti. Nature materials, 2(5):307–311, 2003.
- [14] LN Oliveira, EKV Gross, and W Kohn. Density-functional theory for superconductors. Physical review letters, 60(23):2430, 1988.
- [15] Stefano Curtarolo, Gus LW Hart, Marco Buongiorno Nardelli, Natalio Mingo, Stefano Sanvito, and Ohad Levy. The high-throughput highway to computational materials design. Nature materials, 12(3):191–201, 2013.
- [16] G Ceder and K Persson. How supercomputers will yield a golden age of materials science. Scientific American, Dec, 2013.
- [17] MH Yoo. Slip, twinning, and fracture in hexagonal close-packed metals. Metallurgical Transactions A, 12(3):409–418, 1981.
- [18] Daan Frenkel and Berend Smit. Understanding molecular simulation: from algorithms to applications, volume 1. Academic press, 2001.
- [19] Hussein M Zbib. Introduction to discrete dislocation dynamics. Springer, 2012.
- [20] Gilbert Strang and George J Fix. An analysis of the finite element method, volume 212. Prentice-Hall Englewood Cliffs, NJ, 1973.
- [21] F Roters, P Eisenlohr, L Hantcherli, DD Tjahjanto, TR Bieler, and Dierk Raabe. Overview of constitutive laws, kinematics, homogenization and multiscale methods in crystal plasticity finite-element modeling: Theory, experiments, applications. Acta Materialia, 58(4):1152–1211, 2010.
- [22] Franz Roters, Martin Diehl, Philip Eisenlohr, and Dierk Raabe. Crystal plasticity modeling. Microstructural Design of Advanced Engineering Materials, pages 41–67, 2013.
- [23] Nele Moelans, Bart Blanpain, and Patrick Wollants. An introduction to phase-field modeling of microstructure evolution. Calphad, 32(2):268–294, 2008.
- [24] Z.K. Liu and Y.A. Chang. Evaluation of the thermodynamic properties of the re–ta and re–w systems. Journal of alloys and compounds, 299(1):153–162, 2000.
- [25] Jan-C Carlen and Boris D Bryskin. Rhenium-a unique rare metal. MATERIAL AND MANUFACTURING PROCESS, 9(6):1087–1104, 1994.

- [26] Ivor E Campbell, DM Rosenbaum, and BW Gonser. The availability, recovery and properties of rhenium metal. Journal of the Less Common Metals, 1(3):185–191, 1959.
- [27] A Wrona, M Staszewski, M Czepelak, M Woch, M Kamińska, M Osadnik, and D Kołacz. Properties of rhenium-based master alloys prepared by powder metallurgy techniques. Archives of Materials Science and Engineering, 45(2):95–101, 2010.
- [28] Paul J Fink, Joshua L Miller, and Douglas G Konitzer. Rhenium reduction—alloy design using an economically strategic element. JOM, 62(1):55–57, 2010.
- [29] Erwin Schrödinger. An undulatory theory of the mechanics of atoms and molecules. Physical Review, 28(6):1049, 1926.
- [30] Max Born and Robert Oppenheimer. Zur quantentheorie der molekeln. Annalen der Physik, 389(20):457–484, 1927.
- [31] SH Vosko, LI Wilk, and M Nusair. Accurate spin-dependent electron liquid correlation energies for local spin density calculations: a critical analysis. Canadian Journal of physics, 58(8):1200–1211, 1980.
- [32] Paul AM Dirac. Note on exchange phenomena in the thomas atom. In Mathematical Proceedings of the Cambridge Philosophical Society, volume 26, pages 376–385. Cambridge Univ Press, 1930.
- [33] David M Ceperley and BJ Alder. Ground state of the electron gas by a stochastic method. Physical Review Letters, 45(7):566, 1980.
- [34] J. P. Perdew and Alex Zunger. Self-interaction correction to density-functional approximations for many-electron systems. Phys. Rev. B, 23:5048–5079, May 1981.
- [35] John P Perdew and Yue Wang. Accurate and simple analytic representation of the electron-gas correlation energy. Physical Review B, 45(23):13244, 1992.
- [36] John P Perdew and Wang Yue. Accurate and simple density functional for the electronic exchange energy: Generalized gradient approximation. Physical review B, 33(12):8800, 1986.
- [37] John P Perdew, Kieron Burke, and Matthias Ernzerhof. Generalized gradient approximation made simple. Physical review letters, 77(18):3865, 1996.
- [38] John P Perdew, Adrienn Ruzsinszky, Jianmin Tao, Viktor N Staroverov, Gustavo E Scuseria, and Gábor I Csonka. Prescription for the design and selection of density functional approximations: More constraint satisfaction with fewer fits. The Journal of chemical physics, 123(6):062201, 2005.

- [39] Jianmin Tao, John P Perdew, Viktor N Staroverov, and Gustavo E Scuseria. Climbing the density functional ladder: Nonempirical meta-generalized gradient approximation designed for molecules and solids. Physical Review Letters, 91(14):146401, 2003.
- [40] Axel D Becke. A new mixing of hartree-fock and local density-functional theories. The Journal of Chemical Physics, 98(2):1372–1377, 1993.
- [41] John P Perdew, Matthias Ernzerhof, and Kieron Burke. Rationale for mixing exact exchange with density functional approximations. The Journal of Chemical Physics, 105(22):9982–9985, 1996.
- [42] Carlo Adamo and Vincenzo Barone. Toward reliable density functional methods without adjustable parameters: The pbe0 model. The Journal of chemical physics, 110(13):6158–6170, 1999.
- [43] Aliaksandr V Krukau, Oleg A Vydrov, Artur F Izmaylov, and Gustavo E Scuseria. Influence of the exchange screening parameter on the performance of screened hybrid functionals. The Journal of chemical physics, 125(22):224106–224106, 2006.
- [44] Jochen Heyd, Gustavo E Scuseria, and Matthias Ernzerhof. Hybrid functionals based on a screened coulomb potential. The Journal of Chemical Physics, 118(18):8207–8215, 2003.
- [45] C Stampfl and CG Van de Walle. Density-functional calculations for iii-v nitrides using the local-density approximation and the generalized gradient approximation. Physical Review B, 59(8):5521, 1999.
- [46] A Van de Walle and G Ceder. Correcting overbinding in local-density-approximation calculations. Physical Review B, 59(23):14992, 1999.
- [47] Richard M Martin. Electronic structure: basic theory and practical methods. Cambridge university press, 2004.
- [48] Leonard Kleinman and DM Bylander. Efficacious form for model pseudopotentials. Physical Review Letters, 48(20):1425, 1982.
- [49] D. R. Hamann, M. Schlüter, and C. Chiang. Norm-conserving pseudopotentials. Phys. Rev. Lett., 43:1494–1497, Nov 1979.
- [50] Mike C Payne, Michael P Teter, Douglas C Allan, TA Arias, and JD Joannopoulos. Iterative minimization techniques for ab initio total-energy calculations: molecular dynamics and conjugate gradients. Reviews of Modern Physics, 64(4):1045, 1992.
- [51] Norman Troullier and José Luís Martins. Efficient pseudopotentials for plane-wave calculations. Physical review B, 43(3):1993, 1991.



- [52] P. E. Blöchl. Projector augmented-wave method. Phys. Rev. B, 50:17953–17979, Dec 1994.
- [53] G. Kresse and D. Joubert. From ultrasoft pseudopotentials to the projector augmented-wave method. Phys. Rev. B, 59:1758–1775, Jan 1999.
- [54] Hans Hellmann and Dirk Andrae. Hans Hellmann: Einführung in die Quantenchemie: Mit biografischen Notizen von Hans Hellmann jr. Springer-Verlag, 2015.
- [55] Richard Phillips Feynman. Forces in molecules. Physical Review, 56(4):340, 1939.
- [56] OH Nielsen and Richard M Martin. Quantum-mechanical theory of stress and force. Physical Review B, 32(6):3780, 1985.
- [57] OH Nielsen and Richard M Martin. First-principles calculation of stress. Physical Review Letters, 50(9):697, 1983.
- [58] Paul Ziesche, J Gräfenstein, and Ole Holm Nielsen. Quantum-mechanical stress and a generalized virial theorem for clusters and solids. Physical Review B, 37(14):8167, 1988.
- [59] CG Broyden. A new method of solving nonlinear simultaneous equations. The Computer Journal, 12(1):94–99, 1969.
- [60] DD Johnson. Modified broyden’s method for accelerating convergence in self-consistent calculations. Physical Review B, 38(18):12807, 1988.
- [61] Erik Bitzek, Pekka Koskinen, Franz Gähler, Michael Moseler, and Peter Gumbsch. Structural relaxation made simple. Physical review letters, 97(17):170201, 2006.
- [62] K Kunc and RM Martin. Ab definitio calculation of structure and lattice dynamics of gaas. In Ab Initio Calculation of Phonon Spectra, pages 65–99. Springer, 1983.
- [63] GP Srivastava and K Kunc. Phonon dispersion in the (110) direction: a testing ground for phenomenological models of germanium. Journal of Physics C: Solid State Physics, 21(29):5087, 1988.
- [64] Siqing Wei and MY Chou. Ab initio calculation of force constants and full phonon dispersions. Physical review letters, 69(19):2799, 1992.
- [65] RM Sternheimer. Electronic polarizabilities of ions from the hartree-fock wave functions. Physical Review, 96(4):951, 1954.
- [66] Stefano Baroni, Stefano De Gironcoli, Andrea Dal Corso, and Paolo Giannozzi. Phonons and related crystal properties from density-functional perturbation theory. Reviews of Modern Physics, 73(2):515, 2001.

- [67] Xavier Gonze and J-P Vigneron. Density-functional approach to nonlinear-response coefficients of solids. Physical Review B, 39(18):13120, 1989.
- [68] Xavier Gonze. Perturbation expansion of variational principles at arbitrary order. Physical Review A, 52(2):1086, 1995.
- [69] Xavier Gonze and Changyol Lee. Dynamical matrices, born effective charges, dielectric permittivity tensors, and interatomic force constants from density-functional perturbation theory. Physical Review B, 55(16):10355, 1997.
- [70] M Veithen, Xavier Gonze, and Ph Ghosez. Nonlinear optical susceptibilities, raman efficiencies, and electro-optic tensors from first-principles density functional perturbation theory. Physical Review B, 71(12):125107, 2005.
- [71] Xavier Gonze. Adiabatic density-functional perturbation theory. Physical Review A, 52(2):1096, 1995.
- [72] R D King-Smith and David Vanderbilt. Theory of polarization of crystalline solids. Physical Review B, 47(3):1651, 1993.
- [73] Raffaele Resta. Theory of the electric polarization in crystals. Ferroelectrics, 136(1):51–55, 1992.
- [74] Raffaele Resta. Macroscopic polarization in crystalline dielectrics: the geometric phase approach. Reviews of modern physics, 66(3):899, 1994.
- [75] Xifan Wu, David Vanderbilt, and David Hamann. Systematic treatment of displacements, strains, and electric fields in density-functional perturbation theory. Physical Review B, 72(035105), 2005.
- [76] Paul Soven. Coherent-potential model of substitutional disordered alloys. Physical Review, 156(3):809, 1967.
- [77] L Bellaiche and David Vanderbilt. Virtual crystal approximation revisited: Application to dielectric and piezoelectric properties of perovskites. Physical Review B, 61(12):7877, 2000.
- [78] Lothar Nordheim. Zur elektronentheorie der metalle. i. Annalen der Physik, 401(5):607–640, 1931.
- [79] Ping Sheng and Bart van Tiggelen. Introduction to Wave Scattering, Localization and Mesoscopic Phenomena. Taylor & Francis, 2007.
- [80] ZW Lu, S-H Wei, and Alex Zunger. Large lattice-relaxation-induced electronic level shifts in random cu 1- x pd x alloys. Physical Review B, 44(7):3387, 1991.

- [81] GM Stocks and H Winter. Self-consistent-field-korringa-kohn-rostoker-coherent-potential approximation for random alloys. Zeitschrift für Physik B Condensed Matter, 46(2):95–98, 1982.
- [82] A Bansil. Coherent-potential and average t-matrix approximations for disordered muffin-tin alloys. i. formalism. Physical Review B, 20(10):4025, 1979.
- [83] A Bansil. Coherent-potential and average t-matrix approximations for disordered muffin-tin alloys. ii. application to realistic systems. Physical Review B, 20(10):4035, 1979.
- [84] P Ravindran, PA Korzhavyi, H Fjellvåg, and A Kjekshus. Electronic structure, phase stability, and magnetic properties of  $\text{La}_{1-x}\text{Sr}_x\text{CoO}_3$  from first-principles full-potential calculations. Physical Review B, 60(24):16423, 1999.
- [85] JM Sanchez. Cluster expansions and the configurational energy of alloys. Physical review B, 48(18):14013, 1993.
- [86] Juan M Sanchez, Francois Ducastelle, and Denis Gratias. Generalized cluster description of multicomponent systems. Physica A: Statistical Mechanics and its Applications, 128(1):334–350, 1984.
- [87] Alex Zunger, S.-H. Wei, L. G. Ferreira, and James E. Bernard. Special quasirandom structures. Phys. Rev. Lett., 65:353–356, Jul 1990.
- [88] S.-H. Wei, L. G. Ferreira, James E. Bernard, and Alex Zunger. Electronic properties of random alloys: Special quasirandom structures. Phys. Rev. B, 42:9622–9649, Nov 1990.
- [89] Gerhard Inden. Atomic ordering. Materials science and technology, 1991.
- [90] Gus LW Hart and Rodney W Forcade. Algorithm for generating derivative structures. Physical Review B, 77(22):224115, 2008.
- [91] Gus LW Hart and Rodney W Forcade. Generating derivative structures from multi-lattices: Algorithm and application to hcp alloys. Physical Review B, 80(1):014120, 2009.
- [92] Gus LW Hart, Lance J Nelson, and Rodney W Forcade. Generating derivative structures at a fixed concentration. Computational Materials Science, 59:101–107, 2012.
- [93] A Van de Walle, P Tiwary, M De Jong, DL Olmsted, M Asta, A Dick, D Shin, Y Wang, L-Q Chen, and Z-K Liu. Efficient stochastic generation of special quasirandom structures. Calphad, 42:13–18, 2013.

- [94] Chao Jiang, C Wolverton, Jorge Sofo, Long-Qing Chen, and Zi-Kui Liu. First-principles study of binary bcc alloys using special quasirandom structures. Physical Review B, 69(21):214202, 2004.
- [95] C Wolverton and V Ozoliņš. First-principles aluminum database: Energetics of binary al alloys and compounds. Physical Review B, 73(14):144104, 2006.
- [96] Ferenc Tasnádi, Magnus Odén, and Igor A Abrikosov. Ab initio elastic tensor of cubic ti 0.5 al 0.5 n alloys: dependence of elastic constants on size and shape of the supercell model and their convergence. Physical Review B, 85(14):144112, 2012.
- [97] Johann von Pezold, Alexey Dick, Martin Friák, and Jörg Neugebauer. Generation and performance of special quasirandom structures for studying the elastic properties of random alloys: Application to al-ti. Physical Review B, 81(9):094203, 2010.
- [98] ZW Lu, S-H Wei, and Alex Zunger. Electronic structure of ordered and disordered cu 3 au and cu 3 pd. Physical Review B, 45(18):10314, 1992.
- [99] KC Hass, LC Davis, and Alex Zunger. Electronic structure of random al 0.5 ga 0.5 as alloys: Test of the “special-quasirandom-structures” description. Physical Review B, 42(6):3757, 1990.
- [100] N Troullier and José Luís Martins. Efficient pseudopotentials for plane-wave calculations. ii. operators for fast iterative diagonalization. Physical Review B, 43(11):8861, 1991.
- [101] Martin Fuchs and Matthias Scheffler. Ab initio pseudopotentials for electronic structure calculations of poly-atomic systems using density-functional theory. Computer Physics Communications, 119(1):67–98, 1999.
- [102] Stephen Wolfram. Cellular automata and complexity: collected papers, volume 1. Addison-Wesley Reading, 1994.
- [103] GEOPOLITICAL BIZ S.L.U. Rhenium strategic information. <http://www.geopolitical.biz/strategische-metalle.html>. Accessed: 2015-10-25.
- [104] Zongrui Pei, Li-Fang Zhu, Martin Friák, Stefanie Sandlöbes, Johann von Pezold, HW Sheng, Chris Peter Race, Stefan Zaefferer, Bob Svendsen, Dierk Raabe, et al. Ab initio and atomistic study of generalized stacking fault energies in mg and mg–y alloys. New Journal of Physics, 15(4):043020, 2013.
- [105] S Sandlöbes, M Friák, S Zaefferer, A Dick, S Yi, D Letzig, Z Pei, L-F Zhu, J Neugebauer, and D Raabe. The relation between ductility and stacking fault energies in mg and mg–y alloys. Acta Materialia, 60(6):3011–3021, 2012.

- [106] S Sandlöbes, Z Pei, Martin Friák, L-F Zhu, F Wang, S Zaefferer, D Raabe, and J Neugebauer. Ductility improvement of mg alloys by solid solution: Ab initio modeling, synthesis and mechanical properties. Acta Materialia, 70:92–104, 2014.
- [107] Petr Lazar and Raimund Podloucky. Ductility and magnetism: An ab-initio study of nial–fe and nial–mn alloys. Intermetallics, 17(9):675–679, 2009.
- [108] Liang Qi and DC Chrzan. Tuning ideal tensile strengths and intrinsic ductility of bcc refractory alloys. Physical review letters, 112(11):115503, 2014.
- [109] Lorenz Romaner, Claudia Ambrosch-Draxl, and Reinhard Pippan. Effect of rhenium on the dislocation core structure in tungsten. Physical review letters, 104(19):195503, 2010.
- [110] Haiyang Niu, Xing-Qiu Chen, Peitao Liu, Weiwei Xing, Xiyue Cheng, Dianzhong Li, and Yiyi Li. Extra-electron induced covalent strengthening and generalization of intrinsic ductile-to-brittle criterion. Scientific reports, 2, 2012.
- [111] Michael C Gao, Ömer N Doğan, Paul King, Anthony D Rollett, and Michael Widom. The first-principles design of ductile refractory alloys. JOM Journal of the Minerals, Metals and Materials Society, 60(7):61–65, 2008.
- [112] M. Cyrot and F. Cyrot-Lackmann. Energy of formation of binary transitional alloys. Journal of Physics F: Metal Physics, 6:2257, 1976.
- [113] F. Cyrot-Lackmann. Sur le calcul de la cohésion et de la tension superficielle des métaux de transition par une méthode de liaisons fortes. Journal of Physics and Chemistry of Solids, 29(7):1235–1243, 1968.
- [114] J. Friedel and JM Ziman. The physics of metals. Cambridge University Press, New York, 1969). This model was further elaborated on by DG Pettifor, “Solid State Physics, 40:43, 1969.
- [115] Maarten de Jong, David L Olmsted, Axel van de Walle, and Mark Asta. First-principles study of the structural and elastic properties of rhenium-based transition-metal alloys. Physical Review B, 86(22):224101, 2012.
- [116] SF Pugh. Xcii. relations between the elastic moduli and the plastic properties of polycrystalline pure metals. The London, Edinburgh, and Dublin Philosophical Magazine and Journal of Science, 45(367):823–843, 1954.
- [117] UV Waghmare, E. Kaxiras, and MS Duesbery. Modeling brittle and ductile behavior of solids from first-principles calculations. Computer Simulation of Materials at Atomic Level, pages 545–564, 2000.

- [118] N. Bernstein and EB Tadmor. Tight-binding calculations of stacking energies and twinnability in fcc metals. Physical Review B, 69(9):094116, 2004.
- [119] MH Yoo, JR Morris, KM Ho, and SR Agnew. Nonbasal deformation modes of hcp metals and alloys: role of dislocation source and mobility. Metallurgical and Materials Transactions A, 33(3):813–822, 2002.
- [120] Peter Gumbsch. Modelling brittle and semi-brittle fracture processes. Materials Science and Engineering: A, 319:1–7, 2001.
- [121] A Fallahi and A Ataei. Effects of crystal orientation on stress distribution near the triple junction in a tricrystal  $\gamma$ -tial. Materials Science and Engineering: A, 527(18):4576–4581, 2010.
- [122] Desmond Tromans. Elastic anisotropy of hcp metal crystals and polycrystals. Int. J. Res. Rev. Appl. Sci, 6(4):462–483, 2011.
- [123] AT Churchman. Deformation mechanisms and work hardening in rhenium. TRANSACTIONS OF THE AMERICAN INSTITUTE OF MINING AND METALLURGICAL ENGINEERS, 218(2):262–270, 1960.
- [124] GA Geach, RA JEFFERY, and E. Smith. The deformation characteristics of rhenium single crystals. In Rhenium: papers presented at the Symposium on Rhenium of the Electrothermics and Metallurgy Division of the Electrochemical Society, May 3 and 4, 1960, Chicago, Illinois, page 84. Elsevier Pub. Co., 1962.
- [125] RA Jeffery and E Smith. Deformation twinning in rhenium single crystals. Philosophical Magazine, 13(126):1163–1168, 1966.
- [126] DJ Bacon and V. Vitek. Atomic-scale modeling of dislocations and related properties in the hexagonal-close-packed metals. Metallurgical and Materials Transactions A, 33(3):721–733, 2002.
- [127] Michael J Mehl, Dimitrios A Papaconstantopoulos, Nicholas Kioussis, and M Herbranson. Tight-binding study of stacking fault energies and the rice criterion of ductility in the fcc metals. Physical Review B, 61(7):4894, 2000.
- [128] James R Rice and Glenn E Beltz. The activation energy for dislocation nucleation at a crack. Journal of the Mechanics and Physics of Solids, 42(2):333–360, 1994.
- [129] James R Rice. Dislocation nucleation from a crack tip: an analysis based on the peierls concept. Journal of the Mechanics and Physics of Solids, 40(2):239–271, 1992.
- [130] Tianshu Li, JW Morris Jr, N Nagasako, S Kuramoto, and DC Chrzan. “ideal” engineering alloys. Physical review letters, 98(10):105503, 2007.

- [131] DM Clatterbuck, DC Chrzan, and JW Morris. The ideal strength of iron in tension and shear. Acta Materialia, 51(8):2271–2283, 2003.
- [132] D Roundy, CR Krenn, Marvin L Cohen, and JW Morris Jr. The ideal strength of tungsten. Philosophical Magazine A, 81(7):1725–1747, 2001.
- [133] CR Krenn, D Roundy, JW Morris, and Marvin L Cohen. Ideal strengths of bcc metals. Materials Science and Engineering: A, 319:111–114, 2001.
- [134] Shigenobu Ogata, Ju Li, Yoji Shibutani, and Sidney Yip. Ab initio study of ideal shear strength. In IUTAM Symposium on Mesoscopic Dynamics of Fracture Process and Materials Strength, pages 401–410. Springer, 2004.
- [135] Miroslav Černý and Jaroslav Pokluda. Ideal tensile strength of cubic crystals under superimposed transverse biaxial stresses from first principles. Physical Review B, 82(17):174106, 2010.
- [136] G. Kresse and J. Furthmüller. Efficient iterative schemes for *ab initio* total-energy calculations using a plane-wave basis set. Phys. Rev. B, 54:11169–11186, Oct 1996.
- [137] G. Kresse and J. Hafner. *Ab initio* molecular dynamics for liquid metals. Phys. Rev. B, 47:558–561, Jan 1993.
- [138] D. M. Ceperley and B. J. Alder. Ground state of the electron gas by a stochastic method. Phys. Rev. Lett., 45:566–569, Aug 1980.
- [139] Hendrik J. Monkhorst and James D. Pack. Special points for brillouin-zone integrations. Phys. Rev. B, 13:5188–5192, Jun 1976.
- [140] M. Methfessel and A. T. Paxton. High-precision sampling for brillouin-zone integration in metals. Phys. Rev. B, 40:3616–3621, Aug 1989.
- [141] M. Moakher and A.N. Norris. The closest elastic tensor of arbitrary symmetry to an elasticity tensor of lower symmetry. Journal of Elasticity, 85(3):215–263, 2006.
- [142] Ferenc Tasnádi, M. Odén, and Igor A. Abrikosov. *Ab initio* elastic tensor of cubic  $\text{Ti}_{0.5}\text{Al}_{0.5}\text{N}$  alloys: Dependence of elastic constants on size and shape of the supercell model and their convergence. Phys. Rev. B, 85:144112, Apr 2012.
- [143] J.T. Browaeys and S. Chevrot. Decomposition of the elastic tensor and geophysical applications. Geophysical Journal International, 159(2):667–678, 2004.
- [144] Gene Simmons, Herbert Wang, et al. Single crystal elastic constants and calculated aggregate properties, chapter 1, pages 1–100. Mass., MIT Press, 1971.

- [145] D. Tromans. Elastic anisotropy of hcp metal crystals and polycrystals. International Journal of Research and Reviews in Applied Sciences, 6(4):462 – 483, 2011.
- [146] M. Methfessel, C. O. Rodriguez, and O. K. Andersen. Fast full-potential calculations with a converged basis of atom-centered linear muffin-tin orbitals: Structural and dynamic properties of silicon. Phys. Rev. B, 40:2009–2012, Jul 1989.
- [147] M.B. Lv, Y. Cheng, Y.Y. Qi, G.F. Ji, and C.G. Piao. Elastic properties and phonon dispersions of rhenium in hexagonal-close-packed structure under pressure from first principles. Physica B: Condensed Matter, 2011.
- [148] Gerd Steinle-Neumann, Lars Stixrude, and Ronald E. Cohen. First-principles elastic constants for the hcp transition metals fe, co, and re at high pressure. Phys. Rev. B, 60:791–799, Jul 1999.
- [149] L. Hedin and BI Lundqvist. Explicit local exchange-correlation potentials. Journal of Physics C: Solid state physics, 4:2064, 1971.
- [150] John P. Perdew, Kieron Burke, and Matthias Ernzerhof. Generalized gradient approximation made simple. Phys. Rev. Lett., 77:3865–3868, Oct 1996.
- [151] Lars Fast, J. M. Wills, Börje Johansson, and O. Eriksson. Elastic constants of hexagonal transition metals: Theory. Phys. Rev. B, 51:17431–17438, Jun 1995.
- [152] E. Wimmer, H. Krakauer, M. Weinert, and A. J. Freeman. Full-potential self-consistent linearized-augmented-plane-wave method for calculating the electronic structure of molecules and surfaces: o<sub>2</sub> molecule. Phys. Rev. B, 24:864–875, Jul 1981.
- [153] Yogesh K. Vohra, Steven J. Duclos, and Arthur L. Ruoff. High-pressure x-ray diffraction studies on rhenium up to 216 gpa (2.16 mbar). Phys. Rev. B, 36:9790–9792, Dec 1987.
- [154] L.G. Liu, T. Takahashi, and W.A. Bassett. Effect of pressure and temperature on the lattice parameters of rhenium. Journal of Physics and Chemistry of Solids, 31(6):1345–1351, 1970.
- [155] T.S. Duffy, G. Shen, D.L. Heinz, J. Shu, Y. Ma, H.K. Mao, R.J. Hemley, and A.K. Singh. Lattice strains in gold and rhenium under nonhydrostatic compression to 37 gpa. Physical Review B, 60(22):15063, 1999.
- [156] M.H. Manghnani, K. Katahara, and E.S. Fisher. Ultrasonic equation of state of rhenium. Physical Review B, 9(4):1421, 1974.



- [157] PS Rudman. Lattice parameters of some hcp binary alloys of rhenium and osmium: Re-w, re-ir, re-pt os-ir, os-pt. Technical report, Battelle Memorial Inst., Columbus, Ohio, 1967.
- [158] Michal Jahnátek, Ohad Levy, Gus L. W. Hart, Lance J. Nelson, Roman V. Chepulskii, J. Xue, and Stefano Curtarolo. Ordered phases in ruthenium binary alloys from high-throughput first-principles calculations. Phys. Rev. B, 84:214110, Dec 2011.
- [159] O. Levy, M. Jahnátek, R.V. Chepulskii, G.L.W. Hart, and S. Curtarolo. Ordered structures in rhenium binary alloys from first-principles calculations. Journal of the American Chemical Society, 2011.
- [160] T. Qin, R. Drautz, and DG Pettifor. Binding-energy relations and equations of state for the 4d and 5d transition metals. Physical Review B, 78(21):214108, 2008.
- [161] J.A. Moriarty and M. Widom. First-principles interatomic potentials for transition-metal aluminides: Theory and trends across the 3d series. Physical Review B, 56(13):7905, 1997.
- [162] V. Ozoliņš and M. Körling. Full-potential calculations using the generalized gradient approximation: Structural properties of transition metals. Physical Review B, 48(24):18304, 1993.
- [163] A.P. Sutton, M.W. Finnis, D.G. Pettifor, and Y. Ohta. The tight-binding bond model. Journal of Physics C: Solid State Physics, 21:35, 1988.
- [164] MW Finnis, AT Paxton, DG Pettifor, AP Sutton, and Y. Ohta. Interatomic forces in transition metals. Philosophical Magazine A, 58(1):143–163, 1988.
- [165] D.G. Pettifor and R. Podloucky. The structures of binary compounds. ii. theory of the pd-bonded ab compounds. Journal of Physics C: Solid State Physics, 19:315, 1986.
- [166] DG Pettifor. Theory of energy bands and related properties of 4d transition metals. i. band parameters and their volume dependence. Journal of Physics F: Metal Physics, 7:613, 1977.
- [167] JM Wills, O. Eriksson, P. Söderlind, and AM Boring. Trends of the elastic constants of cubic transition metals. Physical review letters, 68(18):2802–2805, 1992.
- [168] J.H. Rose and H.B. Shore. Elastic constants of the transition metals from a uniform electron gas. Physical Review B, 49(17):11588, 1994.
- [169] M. Morinaga, T. Nambu, J. Fukumori, M. Kato, T. Sakaki, Y. Matsumoto, Y. Torisaka, and M. Horihata. Effect of surface imperfections on the ductility of pure chromium. Journal of materials science, 30(4):1105–1110, 1995.

- [170] W.A. Harrison. Elementary electronic structure. World Scientific Pub Co Inc, 1999.
- [171] John Wyrill Christian. The Theory of Transformations in Metals and Alloys (Part I+ II). Newnes, 2002.
- [172] John Wyrill Christian and Subhash Mahajan. Deformation twinning. Progress in Materials Science, 39(1):1–157, 1995.
- [173] MH Yoo and JK Lee. Deformation twinning in hcp metals and alloys. Philosophical Magazine A, 63(5):987–1000, 1991.
- [174] Ke Lu, Lei Lu, and S Suresh. Strengthening materials by engineering coherent internal boundaries at the nanoscale. Science, 324(5925):349–352, 2009.
- [175] Yongjun Tian, Bo Xu, Dongli Yu, Yanming Ma, Yanbin Wang, Yingbing Jiang, Wentao Hu, Chengchun Tang, Yufei Gao, Kun Luo, et al. Ultrahard nanotwinned cubic boron nitride. Nature, 493(7432):385–388, 2013.
- [176] JF Nie, YM Zhu, JZ Liu, and Xi-Ya Fang. Periodic segregation of solute atoms in fully coherent twin boundaries. Science, 340(6135):957–960, 2013.
- [177] JJ Fundenberger, MJ Philippe, F Wagner, and C Esling. Modelling and prediction of mechanical properties for materials with hexagonal symmetry (zinc, titanium and zirconium alloys). Acta materialia, 45(10):4041–4055, 1997.
- [178] S Zaefferer. A study of active deformation systems in titanium alloys: dependence on alloy composition and correlation with deformation texture. Materials Science and Engineering: A, 344(1):20–30, 2003.
- [179] YB Chun, SK Hwang, MH Kim, SI Kwun, and SW Chae. Effect of mo addition on the crystal texture and deformation twin formation in zr-based alloys. Journal of nuclear materials, 295(1):31–41, 2001.
- [180] A Rohatgi, KS Vecchio, and GT Gray III. The influence of stacking fault energy on the mechanical behavior of cu and cu-al alloys: Deformation twinning, work hardening, and dynamic recovery. Metallurgical and Materials Transactions A, 32(1):135–145, 2001.
- [181] EL Hall and SC Huang. Stoichiometry effects: on the deformation of binary tial alloys. Journal of Materials Research, 4(03):595–602, 1989.
- [182] Ch V Kopetskij, MM Myshlyaev, NI Novokhatskaya, and VA Yukhanov. Investigation into plastic deformation of rhenium monocrystals. Fizika Metallov i Metallovedenie, 1975.

- [183] J Kacher and M Minor. Twin boundary interactions with grain boundaries investigated in pure rhenium. Acta Materialia, xx(x):xx–yy, 2014.
- [184] BD Bryskin and FC Danek. Powder processing and the fabrication of rhenium. JOM, 43(7):24–26, 1991.
- [185] C Berne, A Pasturel, M Sluiter, and B Vinet. Ab initio study of metastability in refractory metal based systems. Physical review letters, 83(8):1621, 1999.
- [186] MHF Sluiter. Some observed bcc, fcc, and hcp superstructures. Phase Transitions, 80(4-5):299–309, 2007.
- [187] MHF Sluiter. Lattice stability prediction of elemental tetrahedrally close-packed structures. Acta materialia, 55(11):3707–3718, 2007.
- [188] B Seiser, T Hammerschmidt, AN Kolmogorov, R Drautz, and DG Pettifor. Theory of structural trends within 4 d and 5 d transition metal topologically close-packed phases. Physical Review B, 83(22):224116, 2011.
- [189] Thomas Hammerschmidt, Ralf Drautz, and David G Pettifor. Atomistic modelling of materials with bond-order potentials. International Journal of Materials Research, 100(11):1479–1487, 2009.
- [190] Maarten de Jong, J Kacher, MHF Sluiter, L Qi, DL Olmsted, A van de Walle, JW Morris Jr, AM Minor, and M Asta. Electronic origins of anomalous twin boundary energies in hexagonal close packed transition metals. Physical Review Letters, 115(6):065501, 2015.
- [191] 9 S Mahajan and DF Williams. Deformation twinning in metals and alloys. International Metallurgical Reviews, 18(2):43–61, 1973.
- [192] BA Bilby and AG Crocker. The theory of the crystallography of deformation twinning. In Proceedings of the Royal Society of London A: Mathematical, Physical and Engineering Sciences, volume 288, pages 240–255. The Royal Society, 1965.
- [193] Paolo Giannozzi, Stefano Baroni, Nicola Bonini, Matteo Calandra, Roberto Car, Carlo Cavazzoni, Davide Ceresoli, Guido L Chiarotti, Matteo Cococcioni, Ismaila Dabo, et al. Quantum espresso: a modular and open-source software project for quantum simulations of materials. Journal of Physics: Condensed Matter, 21(39):395502, 2009.
- [194] Hubert Ebert, Diemo Koedderitzsch, and Jan Minar. Calculating condensed matter properties using the kkr-green’s function method-recent developments and applications. Reports on Progress in Physics, 74(9):096501, 2011.

- [195] Brent L Adams, Stuart I Wright, and Karsten Kunze. Orientation imaging: the emergence of a new microscopy. Metallurgical Transactions A, 24(4):819–831, 1993.
- [196] G Kresse and J Hafner. Ab initio molecular dynamics for liquid metals. Physical Review B, 47(1):558, 1993.
- [197] G Kresse and J Furthmüller. Efficient iterative schemes for ab initio total-energy calculations using a plane-wave basis set. Physical Review B, 54(16):11169, 1996.
- [198] G Kresse and J Furthmüller. Efficiency of ab-initio total energy calculations for metals and semiconductors using a plane-wave basis set. Computational Materials Science, 6(1):15–50, 1996.
- [199] Richard Hill. The elastic behaviour of a crystalline aggregate. Proceedings of the Physical Society. Section A, 65(5):349, 1952.
- [200] David L Olmsted, Stephen M Foiles, and Elizabeth A Holm. Survey of computed grain boundary properties in face-centered cubic metals: I. grain boundary energy. Acta Materialia, 57(13):3694–3703, 2009.
- [201] NJ Lane, SI Simak, AS Mikhaylushkin, IA Abrikosov, L Hultman, and MW Barsoum. First-principles study of dislocations in hcp metals through the investigation of the  $(11\bar{2}1)$  twin boundary. Phys. Rev. B, 84:184101, Nov 2011.
- [202] Su-Huai Wei and Alex Zunger. Giant and composition-dependent optical bowing coefficient in GaIn alloys. Physical review letters, 76(4):664, 1996.
- [203] AG Khachaturyan, SM Shapiro, and S Semenovskaya. Adaptive phase formation in martensitic transformation. Physical Review B, 43(13):10832, 1991.
- [204] F Ducastelle and F Cyrot-Lackmann. Moments developments and their application to the electronic charge distribution of d bands. Journal of Physics and Chemistry of Solids, 31(6):1295–1306, 1970.
- [205] F Ducastelle and F Cyrot-Lackmann. Moments developments: II. application to the crystalline structures and the stacking fault energies of transition metals. Journal of Physics and Chemistry of Solids, 32(1):285–301, 1971.
- [206] DG Pettifor, B Seiser, ER Margine, AN Kolmogorov, and R Drautz. Size versus electronic factors in transition metal carbide and tcp phase stability. Philosophical Magazine, 93(28-30):3907–3924, 2013.
- [207] R Phillips and AE Carlsson. Universal stabilizing mechanism for transition-metal polytetrahedrally packed phases. Physical Review B, 42(6):3345, 1990.

- [208] JA Moriarty. Density-functional formulation of the generalized pseudopotential theory. iii. transition-metal interatomic potentials. Physical Review B, 38(5):3199, 1988.
- [209] AP Sutton. Electronic structure of materials. Oxford University Press, 1993.
- [210] L Capolungo and IJ Beyerlein. Nucleation and stability of twins in hcp metals. Physical Review B, 78(2):024117, 2008.
- [211] IJ Beyerlein and CN Tomé. A probabilistic twin nucleation model for hcp polycrystalline metals. Proceedings of the Royal Society A: Mathematical, Physical and Engineering Science, 466(2121):2517–2544, 2010.
- [212] James R Rice and Robb Thomson. Ductile versus brittle behaviour of crystals. Philosophical Magazine, 29(1):73–97, 1974.
- [213] Robb Thomson. Intrinsic ductility criterion for interfaces in solids. Physical Review B, 52(10):7124, 1995.
- [214] Robb Thomson and AE Carlsson. Intrinsic ductility criterion for materials. Philosophical Magazine A, 70(5):893–903, 1994.
- [215] SJ Zhou, AE Carlsson, and Robb Thomson. Crack blunting effects on dislocation emission from cracks. Physical review letters, 72(6):852, 1994.
- [216] James R. Rice. Dislocation nucleation from a crack tip: An analysis based on the peierls concept. Journal of the Mechanics and Physics of Solids, 40(2):239 – 271, 1992.
- [217] Donald J Siegel. Generalized stacking fault energies, ductilities, and twinnabilities of ni and selected ni alloys. Applied Physics Letters, 87(12):121901–121901, 2005.
- [218] Donald J Siegel. Alloying contributions to twinnability in nickel: Testing the rule of thumb. In APS Meeting Abstracts, volume 1, page 26002, 2005.
- [219] Shigenobu Ogata, Ju Li, and Sidney Yip. Energy landscape of deformation twinning in bcc and fcc metals. Physical Review B, 71(22):224102, 2005.
- [220] S Kibey, JB Liu, DD Johnson, and H Sehitoglu. Predicting twinning stress in fcc metals: Linking twin-energy pathways to twin nucleation. Acta Materialia, 55(20):6843–6851, 2007.
- [221] PJH Denteneer and W van Haeringen. Stacking-fault energies in semiconductors from first-principles calculations. Journal of Physics C: Solid State Physics, 20(32):L883, 1987.

- [222] Zongrui Pei, Martin Friák, Stefanie Sandlöbes, Roman Nazarov, Bob Svendsen, Dierk Raabe, and Jörg Neugebauer. Rapid theory-guided prototyping of ductile mg alloys: from binary to multi-component materials. New Journal of Physics, 17(9):093009, 2015.
- [223] J Hartford, B Von Sydow, G Wahnström, and BI Lundqvist. Peierls barriers and stresses for edge dislocations in pd and al calculated from first principles. Physical Review B, 58(5):2487, 1998.
- [224] Benjamin Paul Burton, Axel van de Walle, and Harold T. Stokes. First principles phase diagram calculations for the octahedral-interstitial system zro x, 0|x| 1/2. Journal of the Physical Society of Japan, 81(1):014004, 2011.
- [225] Yunguo Li and Pavel A Korzhavyi. Interactions of point defects with stacking faults in oxygen-free phosphorus-containing copper. Journal of Nuclear Materials, 462:160–164, 2015.
- [226] KR Limmer, JE Medvedeva, DC Van Aken, and NI Medvedeva. Ab initio simulation of alloying effect on stacking fault energy in fcc fe. Computational Materials Science, 99:253–255, 2015.
- [227] Moshior Rahaman, VI Razumovskiy, Börje Johansson, and AV Ruban. Temperature dependence of stacking-fault and anti-phase boundary energies in al sc from ab initio calculations. Philosophical Magazine, 93(25):3423–3441, 2013.
- [228] Mahesh Chandran and SK Sondhi. First-principle calculation of stacking fault energies in ni and ni-co alloy. Journal of Applied Physics, 109(10):103525, 2011.
- [229] Afshin Abbasi, Alexey Dick, Tilmann Hickel, and Jörg Neugebauer. First-principles investigation of the effect of carbon on the stacking fault energy of fe–c alloys. Acta Materialia, 59(8):3041–3048, 2011.
- [230] Andrei Reyes-Huamantinco, Peter Puschnig, Claudia Ambrosch-Draxl, Oleg E Peil, and Andrei V Ruban. Stacking-fault energy and anti-invar effect in fe-mn alloy from first principles. Physical Review B, 86(6):060201, 2012.
- [231] Levente Vitos, J-O Nilsson, and Börje Johansson. Alloying effects on the stacking fault energy in austenitic stainless steels from first-principles theory. Acta Materialia, 54(14):3821–3826, 2006.
- [232] Song Lu, Qing-Miao Hu, Börje Johansson, and Levente Vitos. Stacking fault energies of mn, co and nb alloyed austenitic stainless steels. Acta Materialia, 59(14):5728–5734, 2011.

- [233] Alexey Dick, Tilmann Hickel, and Jörg Neugebauer. The effect of disorder on the concentration-dependence of stacking fault energies in fe1-xmnx—a first principles study. steel research international, 80(9):603–608, 2009.
- [234] Onur Güvenç, Franz Roters, Tilmann Hickel, and Markus Bambach. Icme for crash-worthiness of twip steels: From ab initio to the crash performance. JOM, 67(1):120–128, 2015.
- [235] Wo Kohn and N Rostoker. Solution of the schrödinger equation in periodic lattices with an application to metallic lithium. Physical Review, 94(5):1111, 1954.
- [236] J Korringa. On the calculation of the energy of a bloch wave in a metal. Physica, 13(6):392–400, 1947.
- [237] S Crampin, DD Vvedensky, and R Monnier. Stacking fault energies of random metallic alloys. Philosophical Magazine A, 67(6):1447–1457, 1993.
- [238] K Wildberger, R Zeller, and PH Dederichs. Screened kkr-green’s-function method for layered systems. Physical Review B, 55(15):10074, 1997.
- [239] K Wood and JB Pendry. Layer method for band structure of layer compounds. Physical Review Letters, 31(23):1400, 1973.
- [240] JM MacLaren, S Crampin, DD Vvedensky, and JB Pendry. Layer korringa-kohn-rostoker technique for surface and interface electronic properties. Physical Review B, 40(18):12164, 1989.
- [241] Fu-Yang Tian, Nan-Xian Chen, Lorand Delczeg, and Levente Vitos. Interlayer potentials for fcc (111) planes of pd–ag random alloys. Computational materials science, 63:20–27, 2012.
- [242] TC Schulthess, PEA Turchi, A Gonis, and T-G Nieh. Systematic study of stacking fault energies of random al-based alloys. Acta materialia, 46(6):2215–2221, 1998.
- [243] IA Abrikosov and Hans Lomholt Skriver. Self-consistent linear-muffin-tin-orbitals coherent-potential technique for bulk and surface calculations: Cu-ni, ag-pd, and au-pt random alloys. Physical Review B, 47(24):16532, 1993.
- [244] Wei Li, Song Lu, Qing-Miao Hu, Se Kyun Kwon, Börje Johansson, and Levente Vitos. Generalized stacking fault energies of alloys. Journal of Physics: Condensed Matter, 26(26):265005, 2014.
- [245] Shuo Huang, Wei Li, Song Lu, Fuyang Tian, Jiang Shen, Erik Holmström, and Levente Vitos. Temperature dependent stacking fault energy of fecrconimn high entropy alloy. Scripta Materialia, 108:44–47, 2015.

- [246] Maarten de Jong, J. Kacher, M. H. F. Sluiter, L. Qi, D. L. Olmsted, A. van de Walle, J. W. Morris, A. M. Minor, and M. Asta. Electronic origins of anomalous twin boundary energies in hexagonal close packed transition metals. Phys. Rev. Lett., 115:065501, Aug 2015.
- [247] Rajendra R Zope and Yu Mishin. Interatomic potentials for atomistic simulations of the ti-al system. Physical Review B, 68(2):024102, 2003.
- [248] JR Morris, J Scharff, KM Ho, DE Turner, YY Ye, and MH Yoo. Prediction of a  $\{1122\}$  hcp stacking fault using a modified generalized stacking-fault calculation. Philosophical Magazine A, 76(5):1065–1077, 1997.
- [249] Y Minonishi, S Ishioka, M Koiwa, and S Mobozumi. The structure of  $\{1121\}$  twin boundaries in hcp crystals. physica status solidi (a), 71(1):253–258, 1982.
- [250] AG Crocker.  $\{11\ 1\}$  twinning. Philosophical Magazine, 8(91):1077–1081, 1963.
- [251] Andriy O Lyakhov, Artem R Oganov, Harold T Stokes, and Qiang Zhu. New developments in evolutionary structure prediction algorithm uspeX. Computer Physics Communications, 184(4):1172–1182, 2013.
- [252] Colin W Glass, Artem R Oganov, and Nikolaus Hansen. Uspex—evolutionary crystal structure prediction. Computer Physics Communications, 175(11):713–720, 2006.
- [253] Artem R Oganov and Colin W Glass. Evolutionary crystal structure prediction as a tool in materials design. Journal of Physics: Condensed Matter, 20(6):064210, 2008.
- [254] Gus LW Hart, Volker Blum, Michael J Walorski, and Alex Zunger. Evolutionary approach for determining first-principles hamiltonians. Nature materials, 4(5):391–394, 2005.
- [255] Volker Blum, Gus LW Hart, Michael J Walorski, and Alex Zunger. Using genetic algorithms to map first-principles results to model hamiltonians: Application to the generalized ising model for alloys. Physical Review B, 72(16):165113, 2005.
- [256] A Van de Walle, M Asta, and G Ceder. The alloy theoretic automated toolkit: A user guide. Calphad, 26(4):539–553, 2002.
- [257] Axel van de Walle. Multicomponent multisublattice alloys, nonconfigurational entropy and other additions to the alloy theoretic automated toolkit. Calphad, 33(2):266–278, 2009.
- [258] L Darrell Whitley, Timothy Starkweather, and D’Ann Fuquay. Scheduling problems and traveling salesmen: The genetic edge recombination operator. In ICGA, volume 89, pages 133–40, 1989.



- [259] Erik Metsanurk, A Tamm, A Caro, Alvo Aabloo, and Mattias Klintonberg. First-principles study of point defects at a semicoherent interface. Scientific reports, 4, 2014.
- [260] Anthony Kelly and Norman Hillas Macmillan. Strong solids. Oxford University Press, Walton Street, Oxford OX 2 6 DP, UK, 1986., 1986.
- [261] Hao Wang and Mo Li. Estimate of the maximum strength of metallic glasses from finite deformation theory. Physical review letters, 111(6):065507, 2013.
- [262] D. M. Clatterbuck, C. R. Krenn, Marvin L. Cohen, and J. W. Morris. Phonon instabilities and the ideal strength of aluminum. Phys. Rev. Lett., 91:135501, Sep 2003.
- [263] Liang Qi and D.C. Chrzan. Tuning ideal tensile strengths and intrinsic ductility of bcc refractory alloys. Phys. Rev. Lett., 112:115503, Mar 2014.
- [264] NH Macmillan. The ideal strength of solids. In Atomistics of fracture, pages 95–165. Springer, 1983.
- [265] Hao Wang and Mo Li. The elastic stability, bifurcation and ideal strength of gold under hydrostatic stress: an ab initio calculation. Journal of Physics: Condensed Matter, 21(45):455401, 2009.
- [266] D. Roundy, C. R. Krenn, Marvin L. Cohen, and J. W. Morris. Ideal shear strengths of fcc aluminum and copper. Phys. Rev. Lett., 82:2713–2716, Mar 1999.
- [267] Xiaoqing Li, Stephan Schönecker, Jijun Zhao, Börje Johansson, and Levente Vitos. Ideal strength of random alloys from first principles. Phys. Rev. B, 87:214203, Jun 2013.
- [268] M Šob, LG Wang, and V Vitek. Theoretical tensile stress in tungsten single crystals by full-potential first-principles calculations. Materials Science and Engineering: A, 234:1075–1078, 1997.
- [269] Frederick Milstein and Somchart Chantasiriwan. Theoretical study of the response of 12 cubic metals to uniaxial loading. Phys. Rev. B, 58:6006–6018, Sep 1998.
- [270] Lin Fu, Quan Zhang, and Bi Yu Tang. First-principles study on the ideal strengths of typical hcp metals. In Advanced Materials Research, volume 476, pages 2523–2529. Trans Tech Publ, 2012.
- [271] Duane C Wallace. Thermodynamics of crystals. Courier Corporation, 1998.
- [272] John R Ray. Elastic constants and statistical ensembles in molecular dynamics. Computer physics reports, 8(3):109–151, 1988.

- [273] Jinghan Wang, Sidney Yip, SR Phillpot, and Dieter Wolf. Crystal instabilities at finite strain. Physical Review Letters, 71(25):4182, 1993.
- [274] Jinghan Wang, Ju Li, Sidney Yip, Simon Phillpot, and Dieter Wolf. Mechanical instabilities of homogeneous crystals. Physical Review B, 52(17):12627, 1995.
- [275] R Ramji Rao and R Srinivasan. The third order elastic constants and the pressure derivatives of the second order elastic constants of magnesium. physica status solidi (b), 31(1):K39–K42, 1969.
- [276] R Ramji Rao. Anderson-grüneisen parameter  $\delta$  of some hexagonal metals and mgo from third-order elastic-constant data. Physical Review B, 10(10):4173, 1974.
- [277] RFS Hearmon. Third-order'elastic coefficients. Acta Crystallographica, 6(4):331–340, 1953.
- [278] MF Rose and RT Ramsey. Higher order elastic constants in hcp crystals. physica status solidi (b), 25(1):103–108, 1968.
- [279] Fausto G Fumi. Third-order elastic coefficients of crystals. Physical Review, 83(6):1274, 1951.
- [280] Fausto G Fumi. Third-order elastic coefficients in trigonal and hexagonal crystals. Physical Review, 86(4):561, 1952.
- [281] Michał Łopuszyński and Jacek A Majewski. Ab initio calculations of third-order elastic constants and related properties for selected semiconductors. Physical Review B, 76(4):045202, 2007.
- [282] Hao Wang and Mo Li. Ab initio calculations of second-, third-, and fourth-order elastic constants for single crystals. Physical Review B, 79(22):224102, 2009.
- [283] Hao Wang and Mo Li. Nonlinear theoretical formulation of elastic stability criterion of crystal solids. Physical Review B, 85(10):104103, 2012.
- [284] Maarten de Jong, Wei Chen, Thomas Angsten, Anubhav Jain, Randy Notestine, Anthony Gamst, Marcel Sluiter, Chaitanya Krishna Ande, Sybrand van der Zwaag, Jose J Plata, et al. Charting the complete elastic properties of inorganic crystalline compounds. Scientific Data, 2, 2015.
- [285] DG Pettifor. Theoretical predictions of structure and related properties of intermetallics. Materials science and technology, 8(4):345–349, 1992.
- [286] Karl Gschneidner, Alan Russell, Alexandra Pecharsky, James Morris, Zhehua Zhang, Thomas Lograsso, David Hsu, CH Chester Lo, Yiyang Ye, Aaron Slager, et al. A family of ductile intermetallic compounds. Nature materials, 2(9):587–591, 2003.

- [287] George Neville Greaves, AL Greer, RS Lakes, and T Rouxel. Poisson's ratio and modern materials. Nature materials, 10(11):823–837, 2011.
- [288] Maarten de Jong, Sybrand van der Zwaag, and Marcel Sluiter. Ab-initio modeling of metastable precipitation processes in aluminum 7xxx alloys. International Journal of Materials Research, 103(8):972–979, 2012.
- [289] Z Mao, W Chen, DN Seidman, and C Wolverton. First-principles study of the nucleation and stability of ordered precipitates in ternary Al-Sc-Li alloys. Acta Materialia, 59(8):3012–3023, 2011.
- [290] Maarten De Jong, Rangan K Dutta, Marcel HF Sluiter, Alexis G Miroux, Sybrand van der Zwaag, Jilt Sietsma, and Pedro EJ Rivera Diaz Del Castillo. First-principles and genetic modelling of precipitation sequences in aluminium alloys. Solid State Phenomena, 172:285–290, 2011.
- [291] G Jeffrey Snyder and Eric S Toberer. Complex thermoelectric materials. Nature materials, 7(2):105–114, 2008.
- [292] David G Cahill, Susan K Watson, and Robert O Pohl. Lower limit to the thermal conductivity of disordered crystals. Physical Review B, 46(10):6131, 1992.
- [293] David R Clarke. Materials selection guidelines for low thermal conductivity thermal barrier coatings. Surface and Coatings Technology, 163:67–74, 2003.
- [294] J Feng, B Xiao, J Chen, Y Du, J Yu, and R Zhou. Stability, thermal and mechanical properties of PtAl compounds. Materials & Design, 32(6):3231–3239, 2011.
- [295] Zvi Hashin and S Shtrikman. A variational approach to the theory of the elastic behaviour of multiphase materials. Journal of the Mechanics and Physics of Solids, 11(2):127–140, 1963.
- [296] TI Zohdi and P Wriggers. Aspects of the computational testing of the mechanical properties of microheterogeneous material samples. International Journal for Numerical Methods in Engineering, 50(11):2573–2599, 2001.
- [297] Bijaya B Karki, Lars Stixrude, and Renata M Wentzcovitch. High-pressure elastic properties of major materials of earth's mantle from first principles. Reviews of Geophysics, 39(4):507–534, 2001.
- [298] Orson L Anderson, Edward Schreiber, Robert C Liebermann, and Naohiro Soga. Some elastic constant data on minerals relevant to geophysics. Reviews of Geophysics, 6(4):491–524, 1968.
- [299] DF Nelson. Landolt-Börnstein, Numerical data and functional relationships in science and technology, group III/Vol 29a, 1992.

- [300] William F Gale and Terry C Totemeier. Smithells metals reference book. Butterworth-Heinemann, 2003.
- [301] RFS Hearmon. The elastic constants of anisotropic materials. Reviews of Modern Physics, 18(3):409, 1946.
- [302] K Tanaka and M Koiwa. Single-crystal elastic constants of intermetallic compounds. Intermetallics, 4:S29–S39, 1996.
- [303] Morihiko Nakamura. Elastic constants of some transition-metal-disilicide single crystals. Metallurgical and Materials Transactions A, 25(2):331–340, 1994.
- [304] RJ Schiltz Jr and JF Smith. Elastic constants of some MA12 single crystals. Journal of Applied Physics, 45(11):4681–4685, 1974.
- [305] YP Varshni. Temperature dependence of the elastic constants. Physical Review B, 2(10):3952, 1970.
- [306] H Yasuda, T Takasugi, and M Koiwa. Elasticity of Ni-based L12-type intermetallic compounds. Acta metallurgica et materialia, 40(2):381–387, 1992.
- [307] G Bergerhoff and ID Brown. Crystallographic databases. International Union of Crystallography, Chester, pages 77–95, 1987.
- [308] Alec Belsky, Mariette Hellenbrandt, Vicky Lynn Karen, and Peter Luksch. New developments in the inorganic crystal structure database (ICSD): accessibility in support of materials research and design. Acta Crystallographica Section B: Structural Science, 58(3):364–369, 2002.
- [309] Wahyu Setyawan, Romain M Gaume, Stephanie Lam, Robert S Feigelson, and Stefano Curtarolo. High-throughput combinatorial database of electronic band structures for inorganic scintillator materials. ACS combinatorial science, 13(4):382–390, 2011.
- [310] M. M. Beg and S. M. Shapiro. Study of phonon dispersion relations in cuprous oxide by inelastic neutron scattering. Phys. Rev. B, 13:1728–1734, Feb 1976.
- [311] P.V. Du Plessis, S.J. van Tonder, and L. Alberts. Elastic constants of a NiO single crystal: I (Magnetic transitions). Journal of Physics C Solid State Physics, 4:1983–1987, October 1971.
- [312] Naoya Uchida and Shoichi Saito. Elastic constants and acoustic absorption coefficients in MnO, CoO, and NiO single crystals at room temperature. J. Acoust. Soc. Am., 51(5):1602–1605, 1972.

- [313] Shunli Shang, Yi Wang, and Zi-Kui Liu. First-principles elastic constants of  $\alpha$  and  $\theta$ -Al<sub>2</sub>O<sub>3</sub>. Applied Physics Letters, 90(10):–, 2007.
- [314] Pedro RC Da Silveira, Cesar RS da Silva, and Renata M Wentzcovitch. Metadata management for distributed first principles calculations in vlab-a collaborative cyberinfrastructure for materials computation. Computer Physics Communications, 178(3):186–198, 2008.
- [315] Cesar RS Da Silva, Pedro RC da Silveira, Bijaya Karki, Renata M Wentzcovitch, Paul A Jensen, Evan F Bollig, Marlon Pierce, Gordon Erlebacher, and David A Yuen. Virtual laboratory for planetary materials: System service architecture overview. Physics of the Earth and Planetary Interiors, 163(1):321–332, 2007.
- [316] Anubhav Jain, Shyue Ping Ong, Geoffroy Hautier, Wei Chen, William Davidson Richards, Stephen Dacek, Shreyas Cholia, Dan Gunter, David Skinner, Gerbrand Ceder, et al. Commentary: The Materials Project: A materials genome approach to accelerating materials innovation. APL Materials, 1(1):011002, 2013.
- [317] Dane Morgan, Gerbrand Ceder, and Stefano Curtarolo. High-throughput and data mining with ab initio methods. Measurement Science and Technology, 16(1):296, 2005.
- [318] A. Jain. The Materials Project. <https://materialsproject.org/>. Accessed: 2014-09-30.
- [319] IEEE IEEE. IEEE standard on piezoelectricity. ANSI/IEEE Std 176-1987, pages 0–1, 1988.
- [320] Vladimir I Anisimov, Jan Zaanen, and Ole K Andersen. Band theory and mott insulators: Hubbard u instead of stoner i. Physical Review B, 44(3):943, 1991.
- [321] SL Dudarev, GA Botton, SY Savrasov, CJ Humphreys, and AP Sutton. Electron-energy-loss spectra and the structural stability of nickel oxide: An LSDA + U study. Physical Review B, 57(3):1505, 1998.
- [322] Michael J. Mehl, Barry M. Klein, and Dimitri A. Papaconstantopoulos. Intermetallic Compounds: Principles and Practice, volume 1, chapter 9. John Wiley and Sons, 1994.
- [323] Max Born and Kun Huang. Dynamical Theory of Crystal Lattices Oxford Classic Texts in the Physical Sciences. Clarendon Press, Oxford, 1988.
- [324] Xiangyang Huang, Claudia Bungaro, Vitaliy Godlevsky, and Karin M Rabe. Lattice instabilities of cubic NiTi from first principles. Physical Review B, 65(1):014108, 2001.

- [325] B Grabowski, T Hickel, F Kormann, and J Neugebauer. DFT-based materials and steel design at finite temperatures. Technical report, Lawrence Livermore National Laboratory (LLNL), Livermore, CA, 2011.
- [326] Shyue Ping Ong, William Davidson Richards, Anubhav Jain, Geoffroy Hautier, Michael Kocher, Shreyas Cholia, Dan Gunter, Vincent L Chevrier, Kristin A Persson, and Gerbrand Ceder. Python materials genomics (pymatgen): A robust, open-source python library for materials analysis. Computational Materials Science, 68(0):314 – 319, 2013.
- [327] A. Jain. Fireworks workflow software. <http://pythonhosted.org/FireWorks>. Accessed: 2014-09-30.
- [328] Chi-Sing Man and Mojia Huang. A simple explicit formula for the Voigt-Reuss-Hill average of elastic polycrystals with arbitrary crystal and texture symmetries. Journal of Elasticity, 105(1-2):29–48, 2011.
- [329] Shivakumar I Ranganathan and Martin Ostoja-Starzewski. Universal elastic anisotropy index. Physical Review Letters, 101(5):055504, 2008.
- [330] Orson L Anderson and John E Nafe. The bulk modulus-volume relationship for oxide compounds and related geophysical problems. Journal of Geophysical Research, 70(16):3951–3963, 1965.
- [331] Marvin L Cohen. Calculation of bulk moduli of diamond and zinc-blende solids. Physical Review B, 32(12):7988, 1985.
- [332] Efthimios Kaxiras. Atomic and electronic structure of solids. Cambridge University Press, 2003.
- [333] Karlheinz Schwarz and Peter Blaha. Solid state calculations using wien2k. Computational Materials Science, 28(2):259–273, 2003.
- [334] Karlheinz Schwarz, Peter Blaha, and GKH Madsen. Electronic structure calculations of solids using the wien2k package for material sciences. Computer Physics Communications, 147(1):71–76, 2002.
- [335] Rostam Golesorkhtabar, Pasquale Pavone, Jürgen Spitaler, Peter Puschnig, and Claudia Draxl. Elastic: A tool for calculating second-order elastic constants from first principles. Computer Physics Communications, 184(8):1861–1873, 2013.
- [336] Hongzhi Yao, Lizhi Ouyang, and Wai-Yim Ching. Ab initio calculation of elastic constants of ceramic crystals. Journal of the American Ceramic Society, 90(10):3194–3204, 2007.

- [337] Michael J Mehl and Dimitrios A Papaconstantopoulos. Applications of a tight-binding total-energy method for transition and noble metals: Elastic constants, vacancies, and surfaces of monatomic metals. Physical Review B, 54(7):4519, 1996.
- [338] K.B. Panda and K.S. Ravi Chandran. First principles determination of elastic constants and chemical bonding of titanium boride (tib) on the basis of density functional theory. ActaMaterialia, 54(6):1641 – 1657, 2006.
- [339] W. L. Bond, W. P. Mason, and H. J. McSkimin. Elastic and electromechanical coupling coefficients of single-crystal barium titanate. Phys. Rev., 82:442–443, May 1951.
- [340] M. Lee and R.S. Gilmore. Single crystal elastic constants of tungsten monocarbide. Journal of Materials Science, 17(9):2657–2660, 1982.
- [341] F. Chu, Ming Lei, S.A. Maloy, J.J. Petrovic, and T.E. Mitchell. Elastic properties of C40 transition metal disilicides. ActaMaterialia, 44(8):3035 – 3048, 1996.
- [342] Morihiko Nakamura. Elastic constants of some transition- metal- disilicide single crystals. Metallurgical and Materials Transactions A, 25(2):331–340, 1994.
- [343] Ali Sumer and J. F. Smith. Elastic constants of single crystal CaMg<sub>2</sub>. Journal of Applied Physics, 33(7):2283–2286, 1962.
- [344] Carl F. Cline, Harold L. Dunegan, and Glenn W. Henderson. Elastic constants of hexagonal BeO, ZnS, and CdSe. Journal of Applied Physics, 38(4):1944–1948, 1967.
- [345] PR Son and RA Bartels. CaO and SrO single crystal elastic constants and their pressure derivatives. Journal of Physics and Chemistry of Solids, 33(4):819–828, 1972.
- [346] H Ogi, N Nakamura, M Hirao, and H Ledbetter. Determination of elastic, anelastic, and piezoelectric coefficients of piezoelectric materials from a single specimen by acoustic resonance spectroscopy. Ultrasonics, 42(1):183–187, 2004.
- [347] K. Tanaka and M. Koiwa. Single-crystal elastic constants of intermetallic compounds. Intermetallics, 4, Supplement 1(0):S29 – S39, 1996.
- [348] K. R. Keller and J. J. Hanak. Ultrasonic measurements in single-crystal NbSn. Phys. Rev., 154:628–632, Feb 1967.
- [349] Y. Wu and W. Hu. Elastic and brittle properties of the B2-MgRE (RE = Sc, Y, Ce, Pr, Nd, Gd, Tb, Dy, Ho, Er) intermetallics. The European Physical Journal B, 60(1):75–81, 2007.

- [350] Jiong Wang, Shun-Li Shang, Yi Wang, Zhi-Gang Mei, Yong-Feng Liang, Yong Du, and Zi-Kui Liu. First-principles calculations of binary al compounds: Enthalpies of formation and elastic properties. Calphad, 35(4):562 – 573, 2011. World Round Robin Seminar 2010.
- [351] Yao-Ping Xie, Zhi-Yong Wang, and Z.F. Hou. The phase stability and elastic properties of MgZn<sub>2</sub> and Mg<sub>4</sub>Zn<sub>7</sub> in Mg-Zn alloys. Scripta Materialia, 68(7):495 – 498, 2013.
- [352] H. Yasuda, T. Takasugi, and M. Koiwa. Elasticity of Ni-based L12-type intermetallic compounds. Acta Metallurgica et Materialia, 40(2):381 – 387, 1992.
- [353] GW Shannette and JF Smith. Single crystalline elastic constants of MgZn<sub>2</sub>. Scripta Metallurgica, 3(1):33–35, 1969.
- [354] Rouzbeh Shahsavari, Roland J-M Pellenq, and Franz-Josef Ulm. Empirical force fields for complex hydrated calcio-silicate layered materials. Physical Chemistry Chemical Physics, 13(3):1002–1011, 2011.
- [355] Shun-Li Shang, Hui Zhang, Yi Wang, and Zi-Kui Liu. Temperature-dependent elastic stiffness constants of  $\alpha$ - and  $\theta$ -Al<sub>2</sub>O<sub>3</sub> from first-principles calculations. Journal of Physics: Condensed Matter, 22(37):375403, 2010.
- [356] Zhongqing Wu and Renata M Wentzcovitch. Quasiharmonic thermal elasticity of crystals: an analytical approach. Physical Review B, 83(18):184115, 2011.
- [357] Göran Grimvall. Thermophysical properties of materials. Elsevier, 1999.
- [358] Maarten de Jong, Wei Chen, Henry Geerlings, Mark Asta, and Kristin Aslaug Persson. A database to enable discovery and design of piezoelectric materials. Scientific Data, 2, 2015.
- [359] John Frederick Nye. Physical properties of crystals. Clarendon press, 1985.
- [360] E Koray Akdogan, Mehdi Allahverdi, and Ahmad Safari. Piezoelectric composites for sensor and actuator applications. Ultrasonics, Ferroelectrics, and Frequency Control, IEEE Transactions on, 52(5):746–775, 2005.
- [361] R Bansevicius, S Telksnytė, G Janušas, and A Palevičius. Hybrid numerical-experimental investigation of two-degree-of-freedom piezoelectric positioning actuator. Mechanics, 17(2):182–186, 2011.
- [362] R W Munn and R J Newham. Thermodynamics of internal strain in perfect crystals. III. piezoelectric and related properties. Journal of Physics C: Solid State Physics, 7(5):848, 1974.



- [363] Donald Frederick Nelson. Low frequency properties of dielectric crystals, volume 29. Springer, 1993.
- [364] K Sakata, T Takenaka, and Y Naitou. Phase relations, dielectric and piezoelectric properties of ceramics in the system  $(\text{Bi}_{0.5}\text{Na}_{0.5})\text{TiO}_3\text{-PbTiO}_3$ . Ferroelectrics, 131(1):219–226, 1992.
- [365] Jiang Yu Li. The effective electroelastic moduli of textured piezoelectric polycrystalline aggregates. Journal of the Mechanics and Physics of Solids, 48(3):529–552, 2000.
- [366] Jun Xin, Yanqing Zheng, and Erwei Shi. Piezoelectricity of zinc-blende and wurtzite structure binary compounds. Applied Physics Letters, 91(11):112902, 2007.
- [367] Annie Beya-Wakata, Pierre-Yves Prodhomme, and Gabriel Bester. First-and second-order piezoelectricity in III-V semiconductors. Physical Review B, 84(19):195207, 2011.
- [368] Fabio Bernardini, Vincenzo Fiorentini, and David Vanderbilt. Spontaneous polarization and piezoelectric constants of III-V nitrides. Physical Review B, 56(16):R10024, 1997.
- [369] Vitaly Yuryevich Topolov and Christopher R Bowen. Effective electromechanical properties in piezo-composites. Electromechanical Properties in Composites Based on Ferroelectrics, pages 11–41, 2009.
- [370] A W Warner, M Onoe, and G A Coquin. Determination of elastic and piezoelectric constants for crystals in class (3m). The Journal of the Acoustical Society of America, 42(6):1223–1231, 1967.
- [371] Zhigang Wu and Ronald E Cohen. Pressure-induced anomalous phase transitions and colossal enhancement of piezoelectricity in  $\text{PbTiO}_3$ . Physical Review Letters, 95(3):037601, 2005.
- [372] R. Bechmann. Elastic and piezoelectric constants of alpha-quartz. Phys. Rev., 110:1060–1061, Jun 1958.
- [373] G R Jones, I M Young, J W Burgess, C O'Hara, and R W Whatmore. The growth and piezoelectric properties of  $\text{Te}_2\text{V}_2\text{O}_9$  (for surface acoustic wave device application). Journal of Physics D: Applied Physics, 13(11):2143, 1980.
- [374] Hassel Ledbetter, Hirotsugu Ogi, and Nobutomo Nakamura. Elastic, anelastic, piezoelectric coefficients of monocrystal lithium niobate. Mechanics of Materials, 36(10):941–947, 2004.

- [375] R Leć and W Soluch. The elastic, piezoelectric, dielectric and acoustic properties of  $\text{LiIO}_3$  crystals. In Ultrasonics Symposium, 1977, pages 389–392. IEEE, 1977.
- [376] Tomoaki Yamada, Hiroshi Iwasaki, and Nobukazu Niizeki. Piezoelectric and elastic properties of  $\text{LiTaO}_3$ : Temperature characteristics. Japanese Journal of Applied Physics, 8(9):1127, 1969.
- [377] Satoshi Nanamatsu, Kikuo Doi, and Masao Takahashi. Piezoelectric, elastic and dielectric properties of  $\text{LiGaO}_2$ . Japanese Journal of Applied Physics, 11(6):816, 1972.
- [378] Z Li, S-K Chan, M H Grimsditch, and E S Zouboulis. The elastic and electromechanical properties of tetragonal  $\text{BaTiO}_3$  single crystals. Journal of Applied Physics, 70(12):7327–7332, 1991.
- [379] Jun Kuwata, Kenji Uchino, and Shoichiro Nomura. Phase transitions in the  $\text{Pb}(\text{Zn}_{1/3}\text{Nb}_{2/3})\text{O}_3\text{-PbTiO}_3$  system. Ferroelectrics, 37(1):579–582, 1981.
- [380] Tomoaki Karaki, Kang Yan, Toshiyuki Miyamoto, and Masatoshi Adachi. Lead-free piezoelectric ceramics with large dielectric and piezoelectric constants manufactured from  $\text{BaTiO}_3$  nano-powder. Japanese Journal of Applied Physics, 46(2L):L97, 2007.
- [381] M Demartin Maeder, D Damjanovic, and N Setter. Lead free piezoelectric materials. Journal of Electroceramics, 13(1-3):385–392, 2004.
- [382] R E Jaeger and L Egerton. Hot pressing of potassium-sodium niobates. Journal of the American Ceramic Society, 45(5):209–213, 1962.
- [383] B Noheda, D E Cox, G Shirane, J A Gonzalo, L E Cross, and S E Park. A monoclinic ferroelectric phase in the  $\text{Pb}(\text{Zr}_{1-x}\text{Ti}_x)\text{O}_3$  solid solution. arXiv preprint cond-mat/9903007, 1999.
- [384] Elizabeth A Wood. Polymorphism in potassium niobate, sodium niobate, and other  $\text{ABO}_3$  compounds. Acta Crystallographica, 4(4):353–362, 1951.
- [385] Rickard Armiento, Boris Kozinsky, Geoffroy Hautier, Marco Fornari, and Gerbrand Ceder. High-throughput screening of perovskite alloys for piezoelectric performance and thermodynamic stability. Physical Review B, 89(13):134103, 2014.
- [386] Eric Cross. Materials science: Lead-free at last. Nature, 432(7013):24–25, 2004.
- [387] Thomas R Shrout and Shujun J Zhang. Lead-free piezoelectric ceramics: Alternatives for PZT? Journal of Electroceramics, 19(1):113–126, 2007.
- [388] Richard K Cook and Pearl G Weissler. Piezoelectric constants of alpha- and beta-quartz at various temperatures. Physical Review, 80(4):712, 1950.

- [389] Cormac Toher, Jose J. Plata, Ohad Levy, Maarten de Jong, Mark Asta, Marco Buongiorno Nardelli, and Stefano Curtarolo. High-throughput computational screening of thermal conductivity, debye temperature, and grüneisen parameter using a quasiharmonic debye model. Phys. Rev. B, 90:174107, Nov 2014.
- [390] Stefano Baroni, Paolo Giannozzi, and Andrea Testa. Green’s-function approach to linear response in solids. Physical Review Letters, 58(18):1861, 1987.
- [391] RT Smith and FS Welsh. Temperature dependence of the elastic, piezoelectric, and dielectric constants of lithium tantalate and lithium niobate. Journal of applied physics, 42(6):2219–2230, 1971.
- [392] CS Brown, RC Kell, R Taylor, and LA Thomas. Piezoelectric materials, a review of progress. Component Parts, IRE Transactions on, 9(4):193–211, 1962.
- [393] A Ballato. Basic material quartz and related innovations. In Piezoelectricity, pages 9–35. Springer, 2008.
- [394] Ivo Souza, Jorge Íñiguez, and David Vanderbilt. First-principles approach to insulators in finite electric fields. Physical Review Letters, 89(11):117602, 2002.
- [395] Takeshi Yoshimura and Susan Trolier-McKinstry. Growth and piezoelectric properties of Pb (Yb<sub>1/2</sub> Nb<sub>1/2</sub>)O<sub>3</sub>-PbTiO<sub>3</sub> epitaxial films. Journal of Applied Physics, 92(7):3979–3984, 2002.
- [396] Takeshi Yoshimura and Susan Trolier-McKinstry. Transverse piezoelectric properties of epitaxial pb (Yb<sub>1/2</sub> Nb<sub>1/2</sub>) O<sub>3</sub>-PbTiO<sub>3</sub> (50/50) films. Journal of Crystal Growth, 229(1):445–449, 2001.
- [397] Susan Trolier-McKinstry and Peter Muralt. Thin film piezoelectrics for MEMS. Journal of Electroceramics, 12(1-2):7–17, 2004.
- [398] Anubhav Jain, Shyue Ping Ong, Wei Chen, Bharat Medasani, Xiaohui Qu, Michael Kocher, Miriam Brafman, Guido Petretto, Gian-Marco Rignanese, Geoffroy Hautier, Daniel Gunter, and Kristin A. Persson. Fireworks: a dynamic workflow system designed for high-throughput applications. Concurrency and Computation: Practice and Experience, 2015.
- [399] F Bachmann, Ralf Hielscher, and Helmut Schaeben. Texture analysis with MTEX–free and open source software toolbox. Solid State Phenomena, 160:63–68, 2010.
- [400] R Hielscher and H Schaeben. A novel pole figure inversion method: specification of the MTEX algorithm. Journal of Applied Crystallography, 41(6):1024–1037, 2008.

- [401] David Mainprice, Ralf Hielscher, and Helmut Schaeben. Calculating anisotropic physical properties from texture data using the MTEX open-source package. Geological Society, London, Special Publications, 360(1):175–192, 2011.
- [402] David Mainprice, Florian Bachmann, Ralf Hielscher, and Helmut Schaeben. Descriptive tools for the analysis of texture projects with large datasets using MTEX: strength, symmetry and components. Geological Society, London, Special Publications, 409:SP409–8, 2014.
- [403] Shyue Ping Ong, Shreyas Cholia, Anubhav Jain, Miriam Brafman, Dan Gunter, Gerbrand Ceder, and Kristin A Persson. The Materials Application Programming Interface (API): A simple, flexible and efficient API for materials data based on Representational State Transfer (REST) principles. Computational Materials Science, 97:209–215, 2015.
- [404] Muhtar Ahart, Maddury Somayazulu, RE Cohen, P Ganesh, Przemyslaw Dera, Hokyung Mao, Russell J Hemley, Yang Ren, Peter Liermann, and Zhigang Wu. Origin of morphotropic phase boundaries in ferroelectrics. Nature, 451(7178):545–548, 2008.
- [405] Xiao-hong Du, Jiehui Zheng, Uma Belegundu, and Kenji Uchino. Crystal orientation dependence of piezoelectric properties of lead zirconate titanate near the morphotropic phase boundary. Applied Physics Letters, 72(19):2421–2423, 1998.
- [406] R J Zeches, M D Rossell, J X Zhang, A J Hatt, Q He, C-H Yang, A Kumar, C H Wang, A Melville, C Adamo, et al. A strain-driven morphotropic phase boundary in BiFeO<sub>3</sub>. Science, 326(5955):977–980, 2009.
- [407] Richard E Eitel, Clive A Randall, Thomas R Shrout, Paul W Rehrig, Wes Hackenberger, and Seung-Eek Park. New high temperature morphotropic phase boundary piezoelectrics based on Bi (Me) O<sub>3</sub>–PbTiO<sub>3</sub> ceramics. Japanese Journal of Applied Physics, 40(10R):5999, 2001.
- [408] Agostino Zoroddu, Fabio Bernardini, Paolo Ruggerone, and Vincenzo Fiorentini. First-principles prediction of structure, energetics, formation enthalpy, elastic constants, polarization, and piezoelectric constants of AlN, GaN, and InN: Comparison of local and gradient-corrected density-functional theory. Physical Review B, 64(4):045208, 2001.
- [409] Chenliang Li, Chaoying Wang, Decai Ma, and Baolai Wang. Strain-induced improvements on piezoelectric and nonlinear optical properties of BiAlO<sub>3</sub>. Materials Research Express, 1(3):036301, 2014.
- [410] Priya Gopal and Nicola A Spaldin. Polarization, piezoelectric constants, and elastic constants of ZnO, MgO, and CdO. Journal of Electronic Materials, 35(4):538–542, 2006.

- [411] R A Wolf and S Trolier-McKinstry. Temperature dependence of the piezoelectric response in lead zirconate titanate films. Journal of Applied Physics, 95(3):1397–1406, 2004.
- [412] Fei Li, Zhuo Xu, Xiaoyong Wei, and Xi Yao. Determination of temperature dependence of piezoelectric coefficients matrix of lead zirconate titanate ceramics by quasi-static and resonance method. Journal of Physics D: Applied Physics, 42(9):095417, 2009.
- [413] P Zheng, J L Zhang, Y Q Tan, and C L Wang. Grain-size effects on dielectric and piezoelectric properties of poled BaTiO<sub>3</sub> ceramics. Acta Materialia, 60(13):5022–5030, 2012.
- [414] G Vaschenko, D Patel, C S Menoni, N F Gardner, J Sun, W Götz, C N Tomé, and B Clausen. Significant strain dependence of piezoelectric constants in In<sub>x</sub> Ga<sub>1-x</sub>N/GaN quantum wells. Physical Review B, 64(24):241308, 2001.
- [415] C Daumont, W Ren, I C Infante, S Lisenkov, J Allibe, C Carrétéro, S Fusil, E Jacquet, T Bouvet, F Bouamrane, et al. Strain dependence of polarization and piezoelectric response in epitaxial BiFeO<sub>3</sub> thin films. Journal of Physics: Condensed Matter, 24(16):162202, 2012.
- [416] Shan-Tao Zhang, Alain Brice Kounga, Emil Aulbach, Wook Jo, Torsten Granzow, Helmut Ehrenberg, and Jürgen Rödel. Lead-free piezoceramics with giant strain in the system Bi<sub>0.5</sub>Na<sub>0.5</sub>TiO<sub>3</sub>-BaTiO<sub>3</sub>-K<sub>0.5</sub>Na<sub>0.5</sub>NbO<sub>3</sub>. II. Temperature dependent properties. Journal of Applied Physics, 103(3):-, 2008.
- [417] Naohiko Yasuda, Tomokazu Banno, Kazuhiko Fujita, Hidehiro Ohwa, Mituyoshi Matushita, Yohachi Yamashita, Makoto Iwata, and Yoshihiro Ishibashi. Pressure dependence of piezoelectric properties of a Pb (Mg<sub>1/3</sub>Nb<sub>2/3</sub>) O<sub>3</sub>-PbTiO<sub>3</sub> binary system single crystal near a morphotropic phase boundary. Journal of Physics: Condensed Matter, 18(32):7659, 2006.
- [418] Junjie Gao, Zhuo Xu, Fei Li, Chonghui Zhang, Yi Liu, Gaomin Liu, and Hongliang He. The hydrostatic pressure dependence of the piezoelectric properties for the barium titanate and lead titanate crystals: Thermodynamic analysis. Journal of Applied Physics, 109(11):114111, 2011.
- [419] J-W Yeh, S-K Chen, S-J Lin, J-Y Gan, T-S Chin, T-T Shun, C-H Tsau, and S-Y Chang. Nanostructured high-entropy alloys with multiple principal elements: Novel alloy design concepts and outcomes. Advanced Engineering Materials, 6(5):299–303, 2004.

- [420] Jien Wei Yeh, Yu Liang Chen, Su Jien Lin, and Swe Kai Chen. High-entropy alloys—a new era of exploitation. In Materials Science Forum, volume 560, pages 1–9. Trans Tech Publ, 2007.
- [421] GUO Sheng and Chain Tsuan LIU. Phase stability in high entropy alloys: formation of solid-solution phase or amorphous phase. Progress in Natural Science: Materials International, 21(6):433–446, 2011.
- [422] AN Stroh. Dislocations and cracks in anisotropic elasticity. Philosophical magazine, 3(30):625–646, 1958.
- [423] Ao N Stroh. A theory of the fracture of metals. Advances in Physics, 6(24):418–465, 1957.
- [424] MH Yoo. Dislocation model for twinning and fracture and its application to hcp metals. Technical report, Oak Ridge National Lab., TN (USA), 1979.
- [425] Emmanuel Clouet. Screw dislocation in zirconium: An ab initio study. Physical Review B, 86(14):144104, 2012.